Advances in Atom and Single Molecule Machines
Series Editor: Christian Joachim

Leonhard Grill
Christian Joachim *Editors*

Imaging and Manipulating Molecular Orbitals

Proceedings of the 3rd AtMol International Workshop, Berlin 24–25 September 2012



Advances in Atom and Single Molecule Machines

Series Editor

Christian Joachim

Editorial Board

- L. Grill
- F. Jelezko
- D. Martrou
- T. Nakayama
- G. Rapenne
- F. Remacle
- K. Ohmori

For further volumes: http://www.springer.com/series/10425

Leonhard Grill · Christian Joachim Editors

Imaging and Manipulating Molecular Orbitals

Proceedings of the 3rd AtMol International Workshop, Berlin 24–25 September 2012



Editors
Leonhard Grill
Department of Physical Chemistry
Fritz-Haber-Institute of the
Max-Planck-Society
Berlin
Germany

Christian Joachim GNS CNRS Toulouse Cedex France

ISSN 2193-9691 ISSN 2193-9705 (electronic) ISBN 978-3-642-38808-8 ISBN 978-3-642-38809-5 (eBook) DOI 10.1007/978-3-642-38809-5

Springer Heidelberg New York Dordrecht London

Library of Congress Control Number: 2013940442

© Springer-Verlag Berlin Heidelberg 2013

This work is subject to copyright. All rights are reserved by the Publisher, whether the whole or part of the material is concerned, specifically the rights of translation, reprinting, reuse of illustrations, recitation, broadcasting, reproduction on microfilms or in any other physical way, and transmission or information storage and retrieval, electronic adaptation, computer software, or by similar or dissimilar methodology now known or hereafter developed. Exempted from this legal reservation are brief excerpts in connection with reviews or scholarly analysis or material supplied specifically for the purpose of being entered and executed on a computer system, for exclusive use by the purchaser of the work. Duplication of this publication or parts thereof is permitted only under the provisions of the Copyright Law of the Publisher's location, in its current version, and permission for use must always be obtained from Springer. Permissions for use may be obtained through RightsLink at the Copyright Clearance Center. Violations are liable to prosecution under the respective Copyright Law. The use of general descriptive names, registered names, trademarks, service marks, etc. in this publication does not imply, even in the absence of a specific statement, that such names are exempt from the relevant protective laws and regulations and therefore free for general use.

While the advice and information in this book are believed to be true and accurate at the date of publication, neither the authors nor the editors nor the publisher can accept any legal responsibility for any errors or omissions that may be made. The publisher makes no warranty, express or implied, with respect to the material contained herein.

Printed on acid-free paper

Springer is part of Springer Science+Business Media (www.springer.com)

Preface

This book encompasses contributions of the third AtMol Workshop in Berlin, September 2012. AtMol is a 4-year research project funded by the European Commission's ICT-FET programme. It was launched on 1 January 2011 with the objective to construct the first ever complete molecular chip where common microelectronic functionalities are brought and encapsulated at the atomic scale. The core of a molecular chip will make use of the extraordinary properties of individual molecules and surface atomic wires, regarding both their chemical and quantum electronic characteristics that should be of practical use and appealing to future information technologies (IT) manufacturing.

Real space imaging of the electronic cloud of a single atom or molecule is now of prime importance in the field of quantum information transmission, manipulation and storage and in the field of single-molecule mechanics. Also, the intramolecular electronic and magnetic phenomena inside a single molecule are of fundamental scientific interest. This AtMol workshop brought for the first time research groups from all around the world together, working on the theory or experiments on the spatial extension (associated with electronic spectroscopy) of the electronic cloud of a single atom or molecule. When possible, the maps recorded or reconstructed by Fourier Transform can be interpreted on the basis of the spin-orbitals entering in the Slater determinants decomposition of the electronic quantum states of a single atom or molecule. Depending on the used experimental and calculation techniques, the relation between the obtained data and the mathematical concept of orbitals was vividly debated. Manipulation techniques to change the spatial distribution or quantum properties by interacting with single molecules were also discussed.

This workshop was open for contributors in the fields of single atom and single molecule imaging using, for example, the FEM, TEM, Photoemission, Attosecond Tomography, NC-AFM or LT- STM instruments. It was the occasion to celebrate the first recording of the image of a single molecule by E. Müller 60 years ago in Berlin-Dahlem, the precise location of this third AtMol workshop (see Fig. 1).

vi Preface

The topics reported in this book form one of the scientific backgrounds required for building up the future of calculators and memory as recognized at the European Commission level. We thank the ICT-FET programme and A*STAR of Singapore for the financial support in organizing this third workshop, and Springer Verlag and its staff members for the publication of this book.

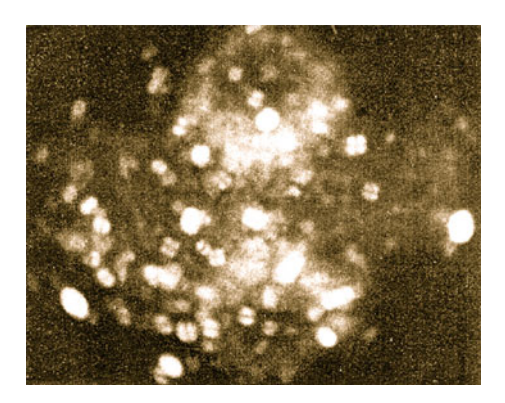


Fig. 1 The first ever recorded image of a few isolated molecules in real space by Erwin W. Müller in 1950 with a Field Emission Microscope. The imaged molecules are Cu-Phthalocyanines deposited on a broad tungsten tip with about a 200 nm radius of curvature. This image was first submitted on 7 August 1950 and published in the journal Zeitschrift für Naturforschung 5a, 473 (1950). At that time E. Müller was at the Kaiser-Wilhelm-Institut für Physikalische Chemie und Elektrochemie in Berlin. Before this direct space image, these molecules were only known indirectly via a Fourier analysis of the Röntgen X-Ray diffraction pattern of a crystal of Cu-Phthalocyanine molecules as obtained for the first time by J.M. Robertson in 1935 (J. Chem. Soc, 615 (1935))

Contents

Part I FEM	
Observations of Individual Cu-Phthalocyanine Molecules Deposited on Nano-Tips in the Field Emission Microscope	3
High Voltage STM Imaging of Single Copper Phthalocyanine C. Manzano, WH. Soe and C. Joachim	15
Part II STEM	
Motional Analysis of a Single Organic Molecule by TEM Using Nanocarbon Materials: Scope of Atomic Level Imaging and Spectroscopy	29
Part III Photo-Emission (PE)	
Imaging Orbitals by Ionization or Electron Attachment: The Role of Dyson Orbitals B. Mignolet, T. Kùs and F. Remacle	41
Part IV LT-UHV-STM	

Mapping the Electronic Resonances of Single Molecule

We-Hyo Soe, Carlos Manzano and Christian Joachim

57

viii Contents

Manipulation and Spectroscopy of Individual Phthalocyanine Molecules on InAs(111)A with a Low-Temperature Scanning Tunneling Microscope	69
Electronic Structure and Properties of Graphen Nanoribbons: Zigzag and Armchair Edges	81
Imaging and Manipulation of Molecular Electronic States on Metal Surfaces with Scanning Tunneling Microscopy Robin Ohmann, Lucia Vitali and Klaus Kern	91
SPM Imaging of Trinaphthylene Molecular States on a Hydrogen Passivated Ge(001) Surface	105
Part V STM Theory and Image Interpretation	
Simulations of Constant Current STM Images of Open-Shell Systems	117
Electronic Transmission Through a Single Impurity in a Multi-configuration Scattering Matrix Approach	137
Electron Transport Through a Molecular Junction Using a Multi-configurational Description	159
Visualizing Electron Correlation in Molecules Using a Scanning Tunneling Microscope: Theory and Ab Initio Prediction	181
Part VI NC-AFM	
Submolecular Resolution Imaging of C_{60} : From Orbital Density to Bond Order	195

Part I FEM

Observations of Individual Cu-Phthalocyanine Molecules Deposited on Nano-Tips in the Field Emission Microscope

Moh'd Rezeq, Christian Joachim, Ma Han Lwin and Francisco Ample Navarro

Abstract Using a field emission microscope (FEM), the first image ever of isolated individual molecules was reported in the 1950s. At that time, the Cu-Phthalocyanine (Cu-Pc) molecule was imaged in different configurations, namely two- and four-leaf patterns. These various apparent shapes were linked to the location of the molecule on particular atomic planes of the relatively quite large FEM tip apex used at that time. We report here on how the fabrication of an extremely sharp FEM tip with an apex of the size of the molecule to be imaged provides a unique opportunity to study the behavior of one molecule at a time on the tip apex. Preliminary data are presented where two adsorption states have been observed according to the electronic cloud FEM images of the molecule. Since the atomic structure of the tip can be determined first from a field ion microscope image, the interaction of the molecule with tip apex surface atoms, and thus the molecule adsorption conformation can be readily determined.

M. Rezeq (⊠)

Khalifa University of Science Technology and Research (KUSTAR), POB 127788, Abu Dhabi, UAE

e-mail: mohd.rezeq@kustar.ac.ae

C. Joachim · F. A. Navarro

Institute of Materials Research and Engineering, Agency for Science, Technology and Research (A*STAR), 3 Research Link, 117602 Singapore, Singapore

C. Joachim

Nanoscience Group and MANA Satellite, CEMES/CNRS, 29 Rue Marvig, BP 94347, 31055 Toulouse Cedex, France

M. H. Lwin

Formerly of IMRE, Singapore, Singapore

L. Grill and C. Joachim (eds.), *Imaging and Manipulating Molecular Orbitals*, Advances in Atom and Single Molecule Machines, DOI: 10.1007/978-3-642-38809-5_1, © Springer-Verlag Berlin Heidelberg 2013

1 Introduction

The remarkable invention of the field emission microscope (FEM) in 1936 by Muller enabled him some years later to turn it into a potential instrument for imaging individual molecules. He actually reported the first images of a single isolated organic molecule, namely a phthalocyanine molecule, in 1950 [1].

The observation of Metal-Phthalocyanine (M-Pc) molecules in the FEM was then reported in several places [2-5]. The thermal vapor deposition of M-Pc molecules on the tip surface usually results in a random distribution of these molecules all over the tip apex area with different shapes. The apparent shapes of the molecule have been classified into two main groups, quadrates which mostly settle on the closely packed (110) planes and doublets that can be seen on the other planes, like (111) and (112). Some other shapes, a doughnut-like shape, have been rarely observed [1–5]. The stability of the molecule on the tip surface has been studied, mainly for the four-leaf pattern. It was found that some molecules disappear gradually during the imaging process at a fixed applied voltage where the remaining molecules are considered the most stable ones; although the majority of the four-leaf molecules and some of the doublets have been found to disappear upon the removal of the applied voltage and turning it back up again. Moreover, the quadruplets can disappear by just increasing or decreasing the applied voltage. It has also been observed that some doublets appear on different sizes and brightness. The various molecular shapes, sizes, brightness, and stabilities indicate different adsorption states on the tip surface. Gomer et al. [2] used I-V measurements to estimate the ionization potential to be 7 V. They found that the images are not the result of diffraction patterns' superposition, but rather are the results of electron optic effects. Emission measurements of molecules adsorbed on clean tungsten show irregularities of 5–10 Å exist on the cleanest surfaces. The work by Morikawa et al. [4] involved the deposition of H₂-, Fe-, Co-, Ni- and Cu-Pc at liquid nitrogen temperature. They observed four- and two-leaf patterns in a FEM image of a tungsten tip. Most of the four-leaf patterns have been seen on (110) planes. Two-leaf patterns appeared evenly on the whole tip with no preference. Whereas for Co-Pc, almost all the observed molecule images show up only two-leafs. They also found that the adsorption state of Co-Pc two-leaf patterns is the same as the other M-PC molecules with four-leaf patterns. The two-leaf patterns in Co-Pc are stable as the four-leaf patterns in other M-Pc molecules. Nevertheless, the reason for the difference in the appearance between Co-Pc and other M-Pc molecules is not yet understood.

However, the broad tip surfaces that have been used in these images allow the accommodation of a large number of molecules at the same time. Therefore, only statistical information about the molecular adsorption states on the tip surface was possible to obtain.

Reducing the tip size to a very small apex, in the range of the molecular size [6–11], enables the selection of only one molecule to be studied at a time. The atomic structure of the apex is precisely characterized in the field ion microscope

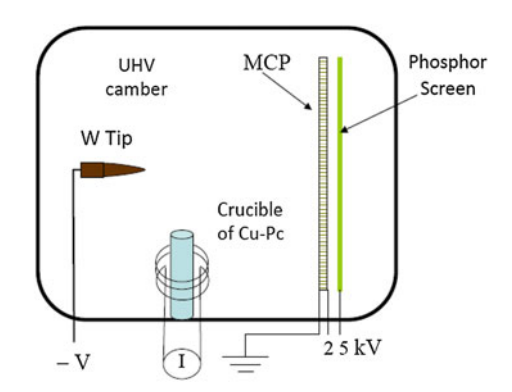
prior to the molecular deposition process, for an accurate estimate of the molecule location on the tip surface [10, 11]. However, we have observed new states of molecular adsorption that introduce a new insight into the molecular interaction with the surface under the influence of a high electric field. We have found that a flat molecule on the surface can exhibit single, double, triple, and quadrate leaf patterns. In another case, we found that the two-leaf pattern is quite stable and does not convert to other shapes. Furthermore, these doublets do not disappear upon the decrease or increase of the applied voltage. For this stable case the current–voltage data have been taken after the deposition of a single molecule. The I–V plots for the individual molecule have shown unconventional behavior that does not fit in Fowler–Nordheim theory.

The advantages of using an ultrasharp tip for molecular characterization can be summarized as follows: (1) An optimum magnification of the molecule can be obtained. (2) The applied voltage will be a direct function of the field emission from the molecule, as no other parts of the tip will contribute to the field emission current. (3) As the field emission is restricted to one molecule the effect of this molecule on the metal work function can be readily extracted. (4) As the molecule is confined to a small substrate area the position of the molecule on the surface can be estimated with a high precision.

2 Experimental Setup and Molecule Images

The typical field ion and FEM setup [12] is used to shape and characterize the tip [10, 11]. A crucible with Cu-Pc molecule is placed at a normal angle and 20 mm below the tip, whereas the latter faces the screen at a distance 35 mm away, as schematically depicted in Fig. 1. The crucible is embraced by a heating loop from a tungsten wire but does not touch the outside wall of the crucible; this is meant for thermal radiation heating of the crucible. The heating coil and crucible were outgassed several times before the actual molecular vapor deposition.

Fig. 1 The schematic of the FIM setup showing the position of the crucible, which is used for molecular deposition on the tip apex



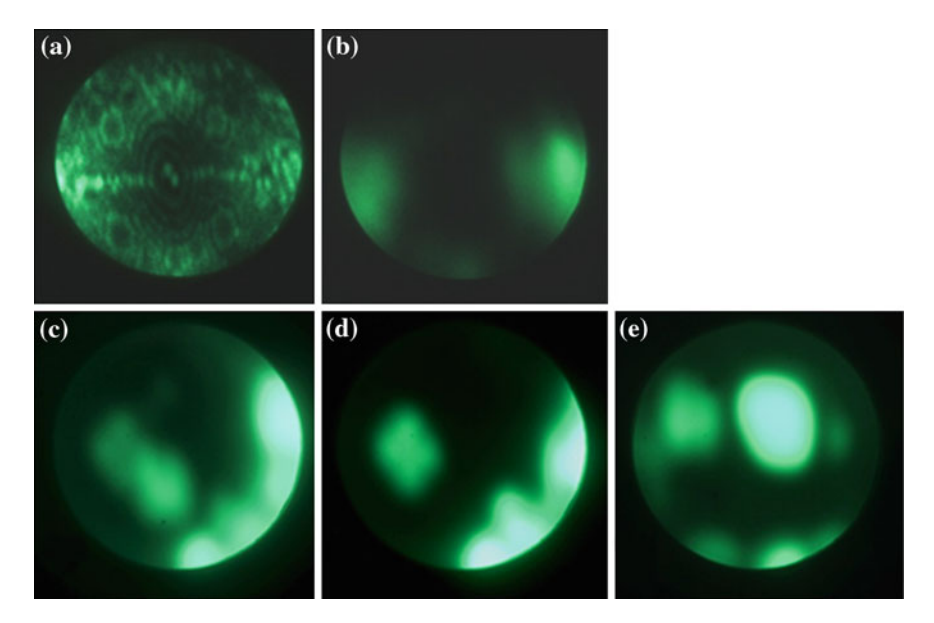


Fig. 2 a Atomically clean tip apex of a radius around 13 nm, at 8.4 kV, before the deposition of Cu-Pc molecules. **b** The electron field emission from the same tip apex, at −700 V. **c**−**e** FEM pictures after the deposition of Cu-Pc molecules

Then the tip was atomically cleaned in the FIM by the common field evaporation process, as in Fig. 1a, at 8.4 kV. Later, the tip bias was reversed and the field emission was obtained at -700 V, as in Fig. 1b, at liquid nitrogen temperature (Fig. 2).

Subsequently, the tip voltage was lowered to 1 k V and the molecules were deposited at a filament current 3.5 A for 60 s, while the tip was kept at the liquid nitrogen temperature. The high electric field at the tip, during the deposition mechanism, tends to attract molecules not only to the side that is exposed to the crucible but also to the tip center as we see in Fig. 1c, at -500 V. The bright area, bottom-right, is the area that is facing the crucible where a large amount of molecules are accumulated. In the same FEM image we can see two Cu-Pc of (four-leaf pattern) molecules at (110) plane. After a short time, the top molecule disappeared and the most stable one sitting on the (110) surface is left with well resolved four-leaf structure, as in Fig. 1(d). Increasing the field further led to the removal of the center four-leaf molecule and to the diffusion of other molecules from the periphery of the tip, the bright area, as in Fig. 5e at -520 V.

Later, the tip was sharpened using the field assisted nitrogen etching process [10]. The nano-tip size can be estimated by computationally reproducing the atomic structure of the apex, as was done previously in several places [10, 11]. Our approach here, for the characterization of a single molecule, is to reduce the size of the tip to around 1–2 nm in radius and then obtain a field emission of the clean

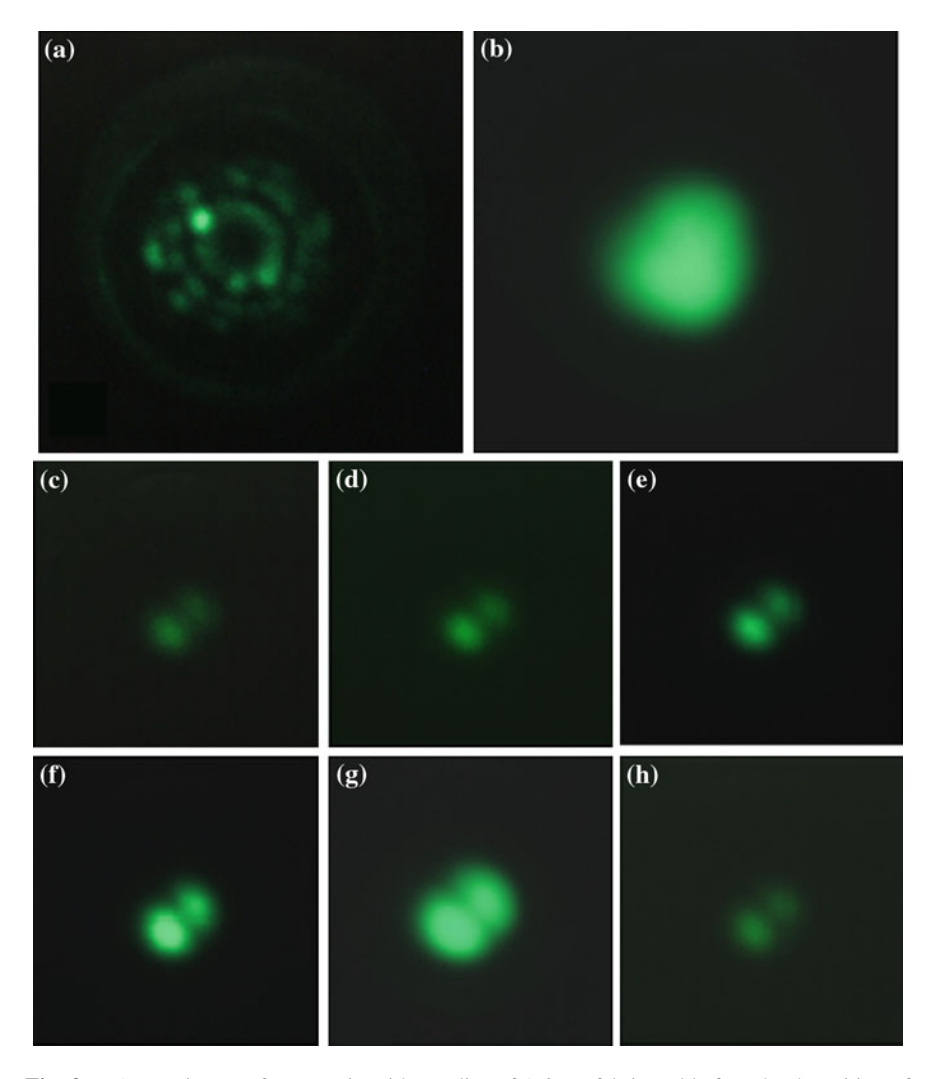


Fig. 3 a A FIM image of a nano-tip with a radius of 1.6 nm fabricated before the deposition of Cu-Pc. **b** A FEM image for the same tip. **c**-**h** A stable two-fold leaf pattern, the shape or position of the pattern does not change upon increase and subsequent decrease of the applied voltage

surface before the molecular deposition. The FIM image of the ultrasharp tip is presented in Fig. 3a, at 4.4 kV and estimated to be 1.6 nm in radius, where the electron field emission from the nano-tip apex is imaged in Fig. 3b, at -500 V. We aim from the FEM of a clean tip to be able to distinguish between the FEM of the molecule and that before the molecular deposition. This is because we will not be able to see any field emission from the tip background after the molecule is deposited, since the field emission will be completely dominated by the molecule.

We present two interesting cases that highlight the molecular adsorption states. The first case is the extremely stable two-leaf configuration. The molecule is deposited at the established current, time, field, and temperature parameters, i.e., I = 3.6 A, t = 60 s, V = 160 V, T = LN. Subsequently, and after increasing the voltage gradually from the initial adsorption field the two-fold pattern appeared at a voltage = -360 V, which is much lower than the threshold FEM value of the same tip before the molecular deposition as mentioned above, i.e., -500 V. This two-leaf pattern only showed an increase in the brightness upon increasing the applied voltage and vice versa. The FEM patterns at different voltages are shown in Fig. 3c-h. We mean here by stability that the molecule does not vibrate or evolve to other shapes as we will see in the next case. In this particular adsorption state the two almost identical leafs are quite stable over a long period of time, more than an hour, and very stable upon increasing or decreasing the applied voltage. Furthermore, the molecule does not disappear even after the removal of the electric field and turning the voltage back up to the imaging values, as in Fig. 3c, where V = 365 V and I = 13.21 nA, and in Fig. 3d, where V = 365 V and I = 13.22 nA. We have also noticed that the field emission current from the molecule is quite stable and reversible with the applied voltage. This is obvious in Fig. 3e and h, where identical FEM patterns were obtained at 380 V before reaching the highest voltage 440 V in Fig. 3g, and after decreasing the voltage to the same value (380 V). The FE currents were also measured directly at these two cases and were 13.64 and 13.84 nA, respectively, whereas the current at 440 V was 17.32 nA. In fact, this outstanding stability and reversibility in field emission patterns can be rarely seen, even for clean nano-tips.

Later, the tip was atomically cleaned by field desorption of the adsorbed molecules and other contaminates until the atomic structure of the tip is recovered as in Fig. 4a, and its FEM profile in Fig. 4b, where the applied voltages were 4.4 kV and -500 V, respectively, which are similar to those of the initial nano-tip. Then the molecule was deposited again at the same setting parameters. We found that the Cu-Pc molecule in this second case exhibits different features that vary between single, two, three, and four leafs and some intermediate cases, as in Fig. 4c–k. In fact, these results represent an example from several experiments that show the same behavior. We also noticed that some leafs appear with different FEM intensities. More importantly, we noticed that the doublet pattern appeared in different orientations as in Fig. 4f, g, k. This suggests that the appearance of various patterns is determined by the binding state between the molecular segments and the surface atoms of the tip, as we will try to explain by models in the Sect. 3

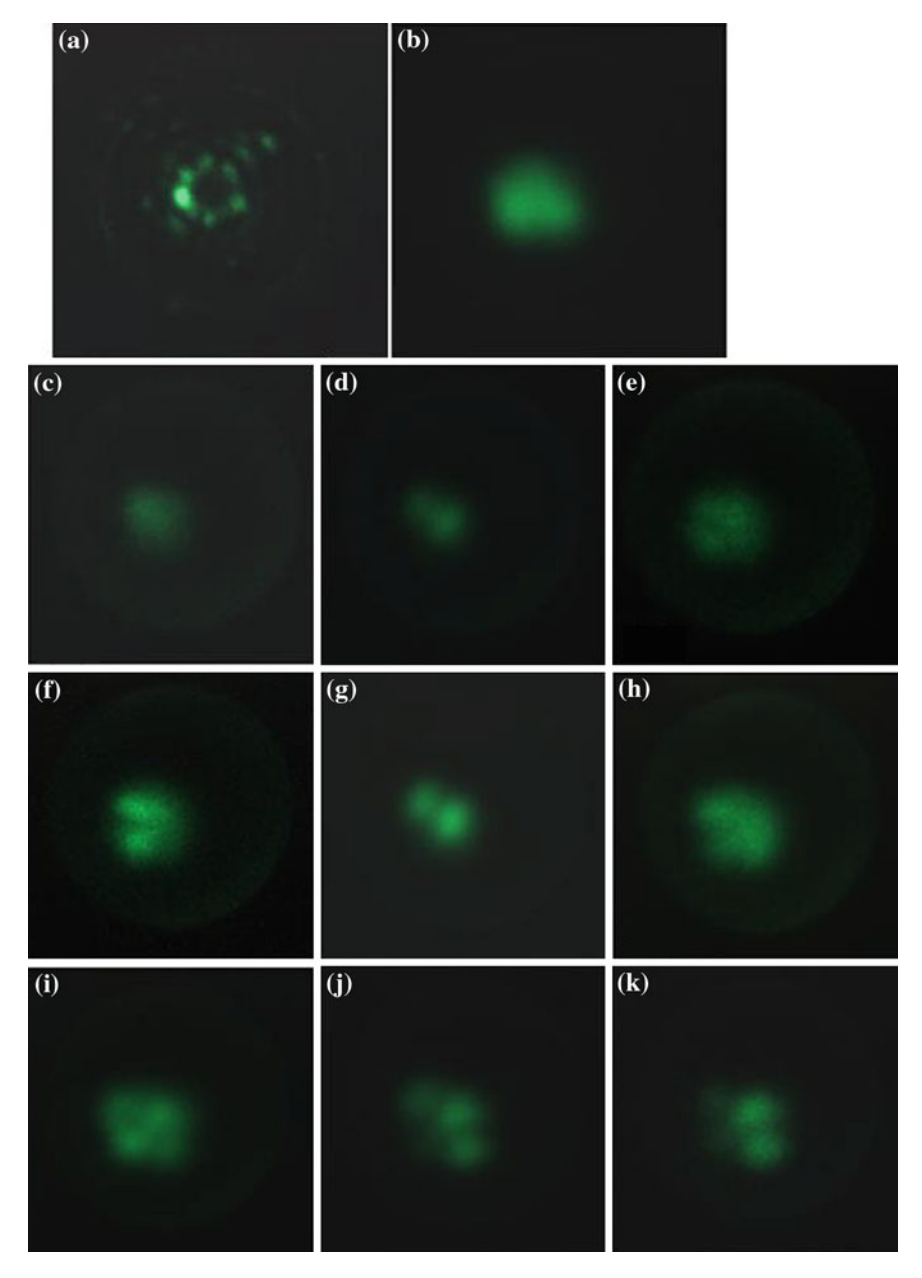


Fig. 4 a A FIM image of the clean nano-tip. b The FEM of the same nano-tip just before the molecular depositions. c-k FEM patterns of the same Cu-Pc molecule

3 Current Voltage Emission Characteristics Through the Molecule

The I–V data have been taken for the above stable doublet case, in Fig. 3, after the deposition of the Cu-Pc molecule, these data are plotted in Fig. 5. The electric current here is measured directly from the tip using a pico-ammeter with an internal voltage source. Two main decisive behaviors can be recognized. First, the relatively high current at small voltages compared to previous studies, which accounts for the ultrasharp tip base fabricated with the nitrogen etching method. The I–V curves do not fit the known Fowler–Nordheim theory, where ln(I/V²) versus V is linear, but they rather fit the modified field emission theory by Yuasa et al. [13], as we see in Fig. 5a, b. They found that $I/V^3 \propto \exp(-A/V)$, where A is a constant, thus ln(I/V³) versus V is linear. This is also consistent with previous studies which showed that the tip apex maximum electric field, and thus the tunneling current, is a function of the radius of the tip base [14]. Second, it has also been observed that at low current, and below the imaging FE current, the molecular FE current starts at a threshold voltage higher than that of a clean tip and then the current enhances dramatically as the voltage increases, as can be seen in Fig. 6. This indicates that the molecule at low electric field tends to retard the field emission from the surface Fermi electrons into the vacuum. When the electric field becomes high enough at the molecule the resonance tunneling enhances significantly due to the small barrier behind the molecule which results in an enhanced field emission. This enhancement of the field emission accounts for the observation of the FEM image at a lower voltage than needed for a clean tip in the previous both cases. However, more analysis will be needed and it is worth designating a separate and detailed study for these phenomenal behaviors.

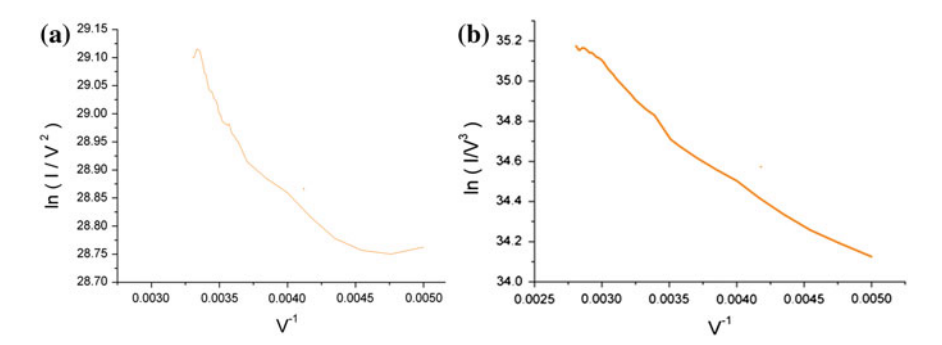


Fig. 5 a A plot of $\ln (I/V^2)$ versus (1/V) for a single Cu-Pc molecule deposited on a nano-tip surface. **b** A plot of $\ln (I/V^3)$ versus (1/V) for a single Cu-Pc molecule deposited on a nano-tip surface

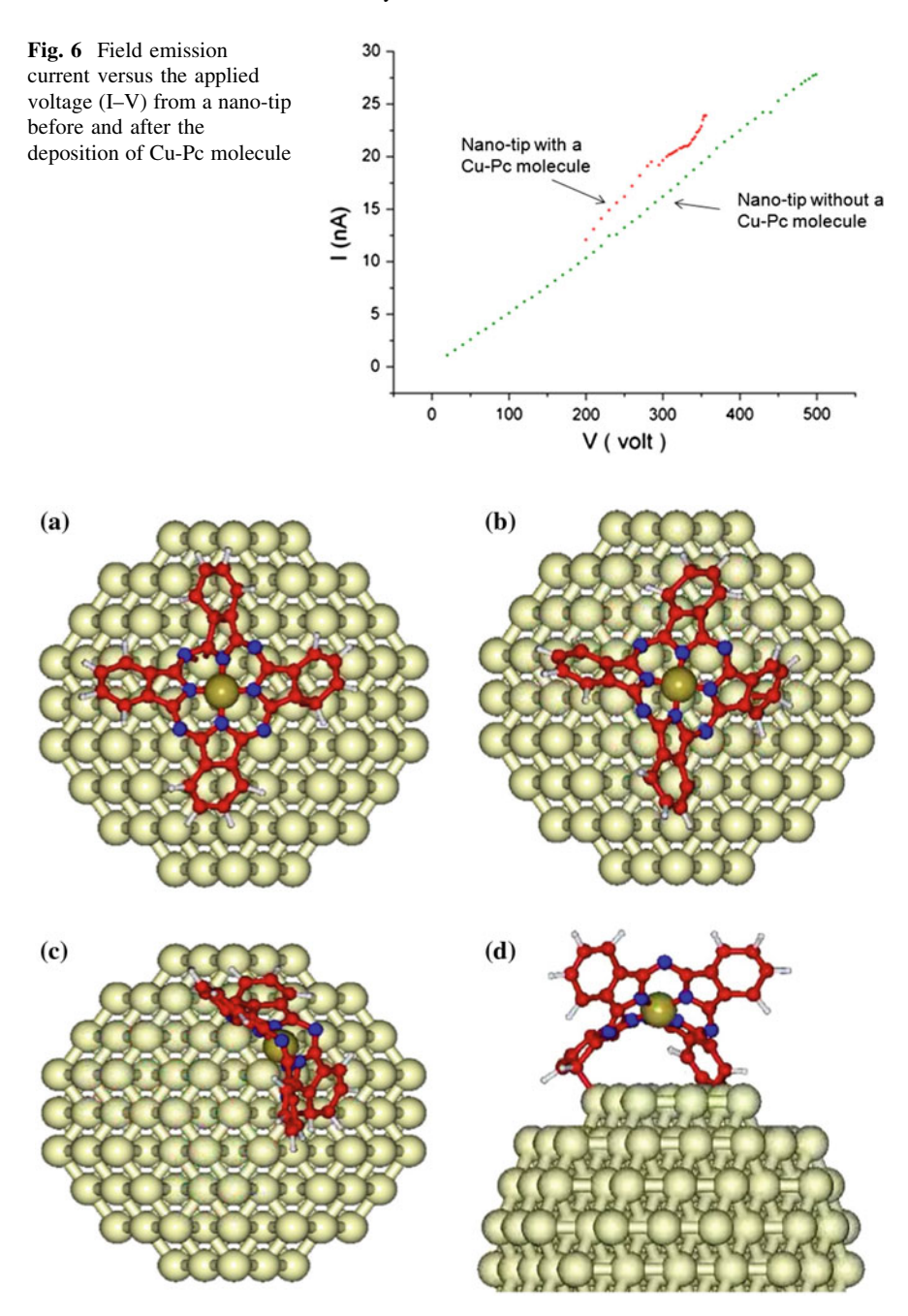


Fig. 7 a A Cu-Pc molecule with four arms sitting on the nano-tip apex of (110) plane. b Some arms are detached from the nano-tip surface. c The molecule diffused slightly from the original position. d Side view of the tip showing the Cu-Pc molecule standing on two arms and the other two arms are detached from the surface

4 Computer Simulation of the Molecule Adsorption on the Nano-Tip Apex

Molecular dynamics simulations were done to understand the behavior of a single Cu-Pc molecule deposited on the tungsten nano-tip (with radius = 1.6 nm and (110) crystal orientation) by means of the ASED+ program [15]. The semi-empirical atom superposition and electronic delocalization molecule orbital (ASED-MO) approach were used to describe the chemical bonds of the molecule and its interactions with the tungsten tip. Our calculations showed that chemical bonds between the molecule and the tungsten tip are rather of a physisorbed nature during the adsorption on the tip surface. The simulations showed multiple conformations of the Cu-Pc molecule on the tungsten nano-tip, as shown in Fig. 7a–d. In these configurations, the molecule can be attached to the surface by the four arms but in some cases, some arms can be detached from the surface. That would explain the observation of different number of bumps when the electric field is emitted through the molecule. Also, the diffusion of the molecule over the tip was observed in the simulations, as in Fig. 7c.

5 Conclusion

We have demonstrated that the fabrication of extremely sharp tips with an apex in the range of 1–2 nm is an ideal method for imaging and characterizing single molecules in the FEM. We have shown that the appearance of the Cu-Pc molecules is not linked to particular atomic planes, but rather to the adsorption state on the surface. This accounts for the observation of single, double, triple, and quadrate FEM patterns for the same Cu-Pc molecule. We have also observed strong, doublet state where the molecule does not change shape upon decreasing or increasing the applied voltage and the field emission current from the molecule is fairly reversible. A computer simulation for the various molecular adsorption states on the tip apex has been presented.

References

- 1. Muller, E.W.: Die Sichtbarmachung einzelner Atome und Moleküle im Feldelektronenmikroskop. Z. Naturforsch. **5a**, 473 (1950)
- 2. Gomer, R., Speer, D.A.: Molecular images with the projection microscope. The ionization potential of Zinc Phthalocyanine. J. Chem. Phys. 21, 73 (1953)
- Mellmed, A.J., Muller, E.W.: Study of molecular patterns in the field emission microscope.
 J. Chem. Phys. 29, 1037 (1958)
- Morikawa, H., Okamoto, K.: Field emission microscope observations of H₂- and metal-Phthalocyanines. Jpn J. Appl. Phys. 35, 4486 (1996)

- 5. Morikawa, H., Okamoto, K., Iwatsu, F., Terao, T.: Jpn. J. Appl. Phys. 36, L583–L586 (1997)
- Fink, H.-W.: Mono-atomic tips for scanning tunneling microscopy. IBM J. Pres. Develp. 30, 460 (1986)
- 7. Binh, V.T., Purcell, S.T., Semet, V., Feschet, F.: Nanotips and nanomagnetism. Appl. Surf. Sci. 130–132, 803 (1998)
- 8. Kuo, H.S., Hwang, I.S., Fu, T.Y., Wu, J.Y., Cheng, C.C., Tsong, T.T.: Perpetration and characterization of single-atom tips. Nano Lett. **4**, 2379 (2004)
- 9. Kuo, H.-S., Hwang, I.S., Fu, T.-Y., Hwang, Y.-S., Lu, Y.-H., Lin, Ch-Y, Hou, J.-L., Tsong, T.T.: A single-atom sharp iridium tip as an emitter of gas field ion sources. Nanotechnology **20**, 335701 (2009)
- Rezeq, M., Pitters, J., Wolkow, R.: Tungsten nanotip fabrication by spatially controlled fieldassisted reaction with nitrogen. J. Chem. Phys. 124, 204716 (2006)
- 11. Rezeq, M., Joachim, C.: Nanotip technology for scanning probe microscopy. In: Tomczak, N., Johnson, G.K. (eds.) Scanning probe microscopy. World Scientific, Singapore (2011)
- 12. Muller, W., Tsong, T.T.: Field ion microscopy: Principles and applications. American Elsevier, Amsterdam (1969)
- 13. Yuasa, K., Shimoi, A., Ohba, I., Oshima, C.: Modified Fowler–Nordheim field emission formulae from a non-planar emitter model. Surf. Sci. **50**, 18 (2002)
- Rezeq, M.: Finite element simulation and analytical analysis for nano field emission sources that terminate with a single atom: A new perspective on nanotips. Appl. Surf. Sci. 258, 1750 (2011)
- 15. Ample, F., Joachim, C.: The chemisorption of polyaromatic hydrocarbons on Si (1 0 0) H dangling bonds. Surf. Sci. **602**, 1563 (2008)

High Voltage STM Imaging of Single Copper Phthalocyanine

C. Manzano, W.-H. Soe and C. Joachim

Abstract In this chapter experiments done to investigate the scanning tunneling microscope (STM) imaging at near field emission voltages of single Copper Phthalocyanine (CuPc) molecules deposited on Au(111) are presented. An imaging bias voltage range is explored exceeding the standard tunneling imaging conditions going from the threshold of the tunneling junction barrier up to — 10.0 V. At this voltage regime current transmitted through the tip-molecule-substrate junction is made not only of tunneling electrons but also of electrons overcoming the tunneling barrier and behaving like free electrons. Our interpretation of the process, enabling the visualization of the electronic cloud of single organic molecules under these conditions, is presented.

1 Introduction

In Chap. 1 the *far field* electron emission imaging technique known as Field Emission Microscopy (FEM) [1] was thoroughly described. The possibility of imaging molecules in real space is, however, not only restricted to the use of high electric fields. In a Scanning Tunneling Microscope (STM) bias voltages of a few volts (± 2.0 V) giving access to electronic states near the substrate's Fermi level are normally used to take images of low-resistance surfaces and molecules or adsorbates deposited on them.

C. Manzano (⋈) · W.-H. Soe

IMRE, Agency for Science, Technology and Research (A*STAR), 3 Research Link 117602 Singapore, Singapore

e-mail: garciac@a-star.edu.sg

C. Joachim

CEMES/CNRS, Pico Lab, 29 Rue Marvig, BP 94347 31055 Toulouse Cedex, France

16 C. Manzano et al.

In a STM, the near field optics element of the microscope is a metal probe which is brought in close proximity, down to few angstroms, to a conductive surface until a current passing through the sample and tip, due to an applied bias voltage between them, set as a control parameter is measured. This current which passes through a potential barrier, whose width is determined by the tip-sample distance separation, is known as the tunneling current and is named after the quantum tunneling effect making possible its occurrence. Normally, an image of a selected substrate and adsorbates is obtained by scanning the tip above the substrate surface using an active feedback loop while applying voltages in between the sample and STM tip of a few volts ($\pm 2.0 \text{ V}$). In this research work, we have gone further and explored whether it is possible to image single molecules beyond the typical voltage range ($\pm 2.0 \text{ V}$) of standard tunneling STM imaging conditions by using even higher voltages exceeding the work function of either the tungsten STM tip or the Au(111) crystal used as a substrate in these experiments. STM images acquired under these conditions are considered to be taken in the near field emission regime.

For using FEM to image organic molecules, the appropriate trade-off between FEM's operation parameters, i.e., emission voltage and electrode-screen distance, needs to be determined and set in order to preserve the integrity of the metal tip electrode as well as to avoid breaking the molecule to be observed. For that purpose, voltages below the metal tip breakdown voltage [2] are selected in combination with the tip-screen distance, with values falling within the area below the voltage breakdown curve shown in Fig. 1, to concurrently keep the molecule undamaged and obtain the best molecule image resolution. Actually, by decreasing these parameters down to their lowest limit, so that the voltage in between the FEM electrodes is of few volts and their distance separation is of few angstroms, we would end up with an experimental conformation resembling an STM. Likewise, an STM tunneling junction can be considered the analog of a FEM setup with the scanning STM tip functioning as a mobile single pixel screen and the sample acting as the emitting electrode. In principle, by using the appropriate experimental parameters, i.e., tip-sample distance and high enough voltages, an STM should be able to image in the near field emission mode.

Low voltage (±2.0 V) imaging parameters are standard and commonly used in STM-based investigations. On the contrary, STM imaging in the near field emission regime has been less explored. Early STM electron spectroscopy experiments investigating conductance spectra taken using voltages within the near field emission regime showed the existence of distinctively spaced resonances in the electron spectra [3–5]. These resonances were previously predicted by Gundlach [6] and are thought to arise due to resonant tunneling through electronic states resulting from a Fabry–Perot cavity confinement, formed by the asymmetric energy potential formed in the tunneling junction produced by the high electric fields applied in between the electrodes, see Fig. 2.

The existence of these high differential conductance Gundlach resonances, also known as field emission resonances (FER), has made possible to STM image large wide gap semiconductor surfaces like C(001) [7] whose energy band gap is

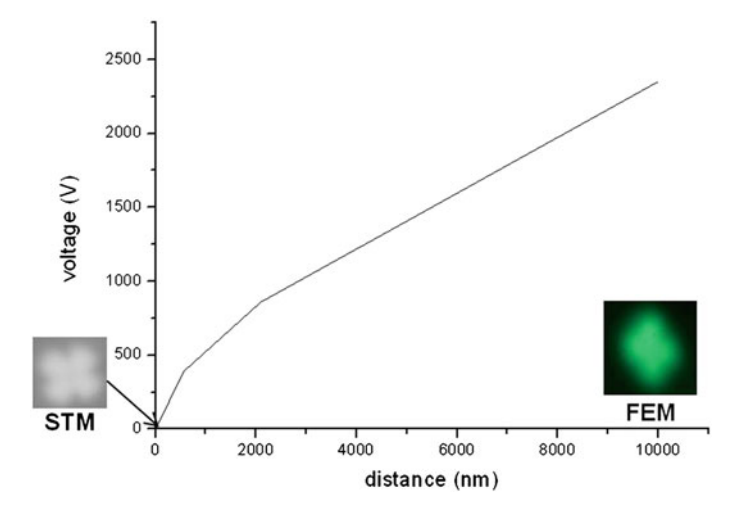


Fig. 1 Breakdown voltage curve showing the maximum voltage that can be applied between FEM electrodes at a given electrode distance separation before any of them gets damaged. For single molecule, FEM imaging the best trade-off between voltages in the area below this curve and the electrodes distance is selected to ensure that electrodes and molecules remain undamaged and to get the best image resolution. In principle, by setting the appropriate parameters it would be possible to get images using field emission electrodes in the far and near fields with either a FEM or an STM. Images of single CuPc taken using FEM and STM at these different imaging regimes are also shown (CuPc FEM image courtesy of Mohamed Rezeq)

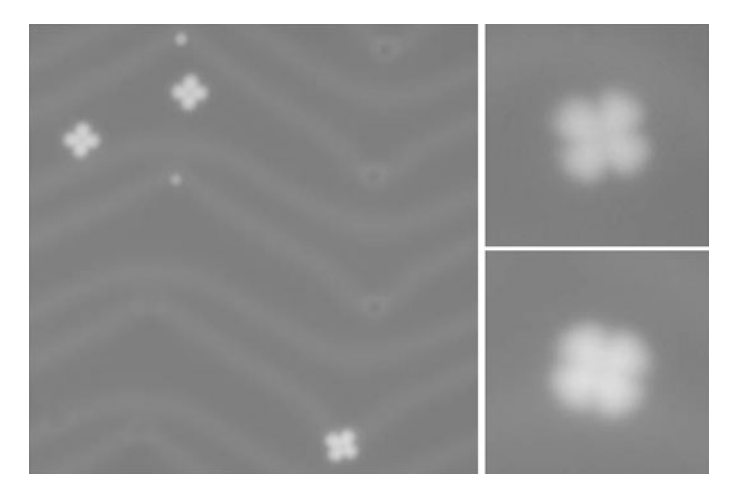


Fig. 2 Topographic STM image showing single CuPc molecules deposited on Au(111), the characteristic "herringbone" surface reconstruction of Au(111) is also observed (image size: 24×24 nm). The top and bottom images at the left correspond to CuPc molecule images taken at -2.0 and 2.0 V, respectively (image size: 4.5×4.5 nm)

18 C. Manzano et al.

 $\sim\!7.0$ V. Carbon dimer lines of the topmost layer of a diamond surface are imaged with near atomic resolution by setting the STM bias voltage at the value corresponding to the first resonance maxima in C(001) dZ/dV spectra, which is above the C(001) conduction band edge. The same FER imaging approach has also been used to investigate the dynamics of surface electrons in metal surfaces and alkali metal clusters [8, 9]. We are not aware of any research work intentionally targeting the FER imaging of single molecules.

To explore the STM imaging of single molecules, through the whole voltage range, the model molecule CuPc was selected. An Au(111) crystal was used as a substrate in these experiments since it has been already reported that CuPc as well as other molecules like Pentacene and Starphene upon sublimation on Au(111) are physisorbed [10]. Likewise, CuPc adsorption state on Au(111) results in electronically weakly coupled CuPc molecules, whose electronic structure is minimally modified and allows at the same time access to well-separated electronic resonances in the transmission spectra of the tunnel junction.

A submonolayer of CuPc molecules was deposited on a clean Au(111) crystal via free evaporation from a quartz crucible heated to 623 K with the Au(111) substrate held at \sim 473 K. Thereafter, the sample was cooled down with liquid helium and transferred to the STM system. Before the molecule deposition the substrate was cleaned after undergoing several cycles of sputtering and annealing. All the STM experiments were done using a Createc low temperature STM operating at a base pressure of at least 8×10^{-11} mbar and \sim 7 K. Standard tunneling spectroscopy methods were also used to measure differential conductance (dI/dV) spectra.

2 Experiments and Results

STM images taken after CuPc/Au(111) sample preparation show that CuPc molecules adsorbed on terraces and also at step edges, see Fig. 2, the characteristic surface reconstruction of Au(111) is also observed. In low voltage STM topographic images of isolated single CuPc molecules taken using voltages from +2.0 to -2.0 V, a CuPc appears like a symmetric four-lobed cross without any intramolecular features being discernible, characteristic images taken within that range are shown in Fig. 2. A comprehensive analysis of CuPc molecular electronic states, upon adsorbtion on Au(111), was done by measuring the tunneling junction transmission resonances using tunneling spectroscopy and also by mapping the differential conductance at selected voltages. The results and findings of that investigation are reported in another chapter of this book.

So far, we have shown STM images taken with bias voltages set within standard imaging conditions characteristic of the tunneling regime ($\pm 2.0~V$) in which the whole current passing through the tip and sample is made of tunneling electrons, as shown in the diagram in Fig. 3. These imaging parameters are standard and commonly used in STM-based investigations.

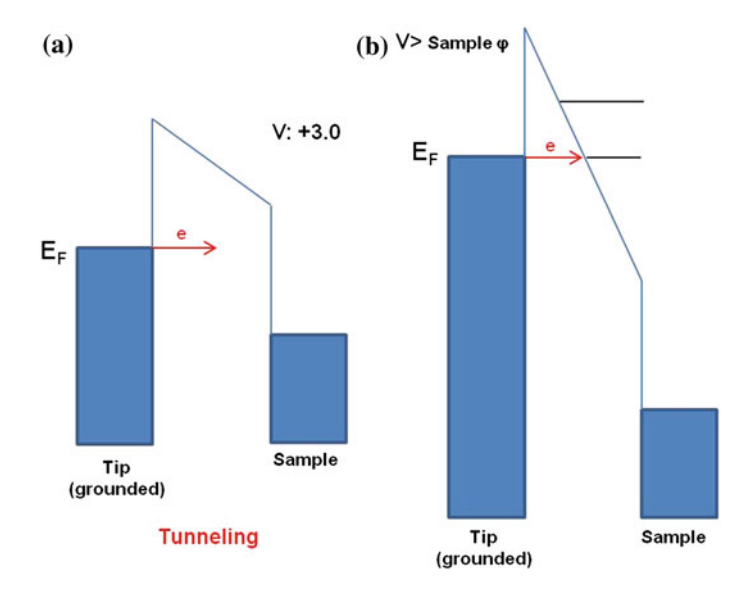


Fig. 3 a Schematics showing the electron tunneling through a potential barrier from the STM tip to the sample for standard tunneling bias conditions. **b** Potential barrier diagram showing the existence of electron confinement due to the potential deformation resulting from applying voltages within the STM junction above the sample's work function. Resonant tunneling through the electronic states in the near field emission regime gives rise to Gundlach resonances observed in the dZ/dV spectra

After getting images and dI/dV maps of CuPc using parameters considered to be within the standard tunneling conditions, we proceeded to take images at higher positive and negative voltages with the aim of finding out whether it is possible to image single CuPc molecules using FER imaging without breaking them. The voltage range explored in our investigation is constrained to the maximum voltage range ($\pm 10~\rm V$) attainable by the digital analog converters of the electronic system used to operate our STM instrument.

Z/V and dZ/dV spectra are taken on a bare Au(111) terrace to determine the spectral position of the Gundlach resonances in the tip-substrate tunneling junction used in these experiments, shown in Fig. 4. The spectra are taken with the STM feedback loop active, so that the tunneling current stays constant while a voltage ramp is applied. Because the feedback loop is "ON", the STM piezo tube holding the STM tip adjusts the tip-sample distance or tip height displacements Z to keep the tunneling current constant at the value initially set as a control parameter; the changes in Z are recorded in function of the voltage applied giving rise to the Z/V while concurrently using a lock-in amplifier to obtain the dZ/dV spectra. Both type of spectra recorded at positive voltages present the characteristic high voltage resonances previously observed in other systems. Interestingly, these spectra are easily reproduced regardless of whether the STM tip is fit enough for getting topographic images or not.

C. Manzano et al.

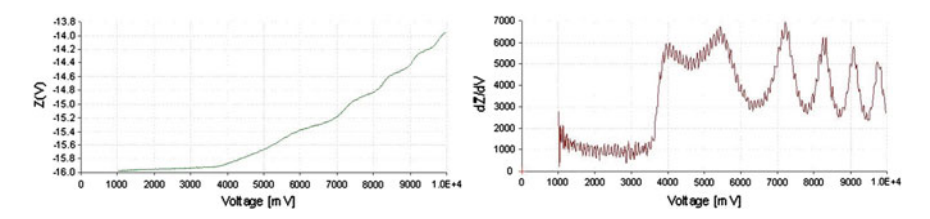


Fig. 4 Z/V and dZ/dV spectra taken at positive voltages from 1.0 to 10.0 V on a bare Au(111) terrace. Both spectra show the existence of Gundlach resonances in the tip-substrate tunneling junction used in these experiments. The spectral position of the resonances was used as a reference in the near field STM imaging of CuPc

After confirming that we are able to identify Gundlach resonances, a sequence of topographic images shown in Fig. 5 was taken starting from 2.5 V and gradually increasing the bias voltage up to about 6.0 V to visualize the CuPc molecule before and after the abrupt differential conductance step-like increase in the dZ/dV in Fig. 4, taking place in between the 3.0 and 4.0 V range. The characteristic cross shape of CuPc is clearly seen at 2.5 V; however, in images taken at about 3.0 V the four lobes become indistinguishable and the molecules are imaged as bright blobs where the molecule's inner structure cannot be recognized. At 4.0 V, already at voltages where tunneling conductance shows a drastic increase in the dZ/dV, a CuPc molecule appears having a bright four-peaked star-like shaped center with four dimmer lobes in between the star peaks. Comparing with CuPc images taken at lower voltages reveals that all features captured at 4.0 V are rotated 45° with respect to the cross-shaped CuPc images; the four peaks of the star-like center appear to arise from the areas in between the lobes of CuPc. When images are taken at 4.6 and 5.5 V which correspond, respectively, to an anti-resonance and a resonance peak in the dZ/dV, the star shape and all other intramolecular features previously observed appear broadened and cannot be easily identified anymore, blurring and overshadowing the overall molecule shape observed at low voltages. Attempts to image CuPc at even slightly higher voltages damaged the molecules as is shown in the last image of Fig. 5, which was taken after trying to image scanning at 6.0 V. The fragmentation of CuPc at these relatively low voltages hindered the realization of further experiments to FER imaging CuPc at the voltages corresponding to the four topmost high voltage resonances appearing in the dZ/dV above 7.0 V in Fig. 4.

Thereafter, the same approach was followed using negative polarity voltages, characteristic Z/V, and dZ/dV spectra taken on a bare Au(111) as shown in Fig. 6. Contrary to spectra taken at positive biases these spectra do not present any sign of Gundlach resonances. It is worth to notice that Gundlach resonances have been observed only in tip-substrate junctions using positive voltage polarities where electrons are emitted and transmitted from the STM tip to the sample. We think that, the absence of Gundlach resonances at negative voltages where electrons move from the sample to the tip is a consequence of the different asymmetric spatial confinement experienced by the emitted electrons, depending on whether

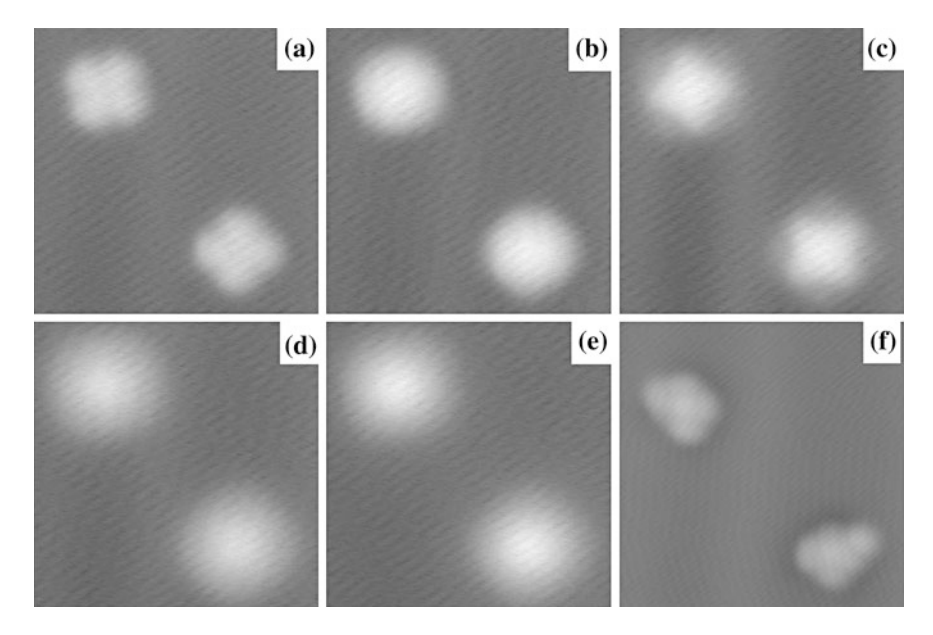


Fig. 5 Sequence of CuPc's STM images taken at positive voltages. **a** The characteristic cross shape of CuPc is clearly seen at 2.5 V. **b** At about 3.0 V, the molecules are imaged as bright blobs where the molecule's inner structure cannot be recognized anymore. **c** At 4.0 V, CuPc appears having a star-like shaped center with four dimmer lobes in between the four star peaks. **d** and **e** Images are taken at 4.6 and 5.5 V, they correspond, respectively, to an anti-resonance and a resonance peak in the dZ/dV, all intramolecular features previously observed appear broadened, blurring, and overshadowing the overall molecule shape observed at low voltages. **f** CuPc molecules damaged after trying to image them scanning at 6.0 V (image size: 6.7 × 6.7 nm)

they are transmitted from the tip to the sample or from the sample to the tip. At positive voltages, the emitted electrons move from the tip toward a planar electrode to the substrate's surface, such tunneling junction acts as an effective Fabry–perot-like cavity giving rise to well-separated electron states. On the contrary, at negative polarities electrons emitted from the sample are transmitted to the tip—a non-planar electrode resulting in a tunneling junction less effective as a cavity and

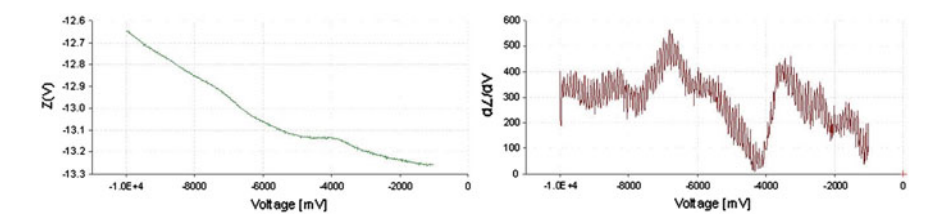


Fig. 6 Z/V and dZ/dV spectra taken at negative voltages from -1.0 to -10.0 V on a bare Au(111) terrace. Contrary to spectra taken at positive voltages these spectra do not show any trace of the Gundlach resonances

C. Manzano et al.

where confinement of the electrons leaving the metal substrate does not take place, as evidenced in the dZ/dV spectra.

In spite of the absence of Gundlach resonances in the dZ/dV spectra, we proceeded to image CuPc at voltages above the tungsten tip work function; the sequence of images taken from -3.0 V up to -10.0 V is shown in Fig. 7. In the images taken using low voltages going from -3.0 V up to -5.0 V, the already well-known characteristic shape of CuPc is visualized, while images taken at higher voltages all the way up to -10.0 V become gradually blurry concomitantly with the voltage rise. Moreover, the images lose resolution, the inner molecule features observed at lower voltages are blurred, and CuPc's four lobes appear broadened making the space in between them undistinguishable. At -10.0 the CuPc image does not resemble anymore the cross-like shape observed at low voltages. What is remarkable, however, is that after this image sequence was taken the CuPc molecule integrity is preserved.

High voltage imaging at negative bias was also done on single Azastarphene molecules deposited on Au(111) showing similar results (see Fig. 8). STM images obtained using tunneling regime parameters show Azastarphene like a three-peaked star-shaped molecule. High voltage images obtained at -9.0 and -10.0 V show likewise in the case of CuPc lower resolution. The three branches of Azastarphene appear broadened and submolecular features that are clearly visible in low voltage images are completely blurred.

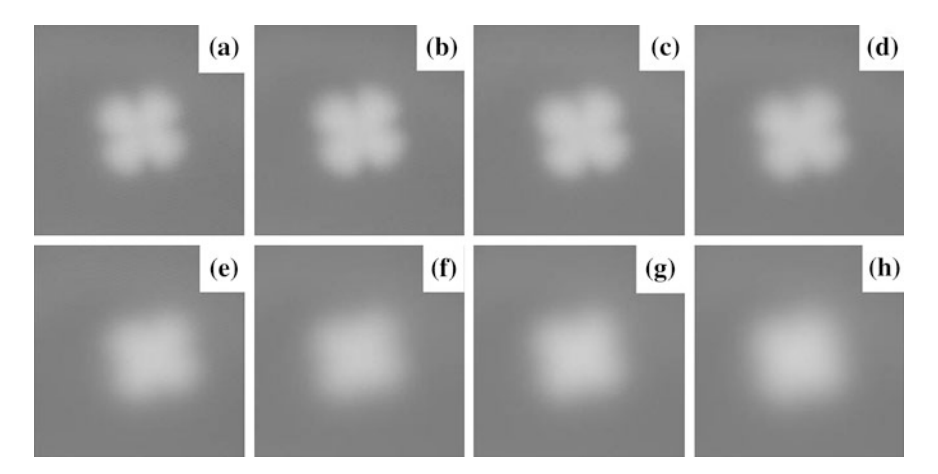


Fig. 7 Sequence of CuPc's STM images taken at negative voltages. *Top row images* (**a**–**d**) were taken at -3.0, -4.0, -5.0 and -6 V, respectively, the characteristic four lobed crossed-like shape of CuPc is visualized. *Bottom row images* (**e**–**h**), taken at -7.0, -8.0, -9.0 and -10.0 V become gradually blurry. CuPc's intramolecular resolution decreases and its four lobes appear broadened making the space in between them undistinguishable (image size: 4.5×4.5 nm)

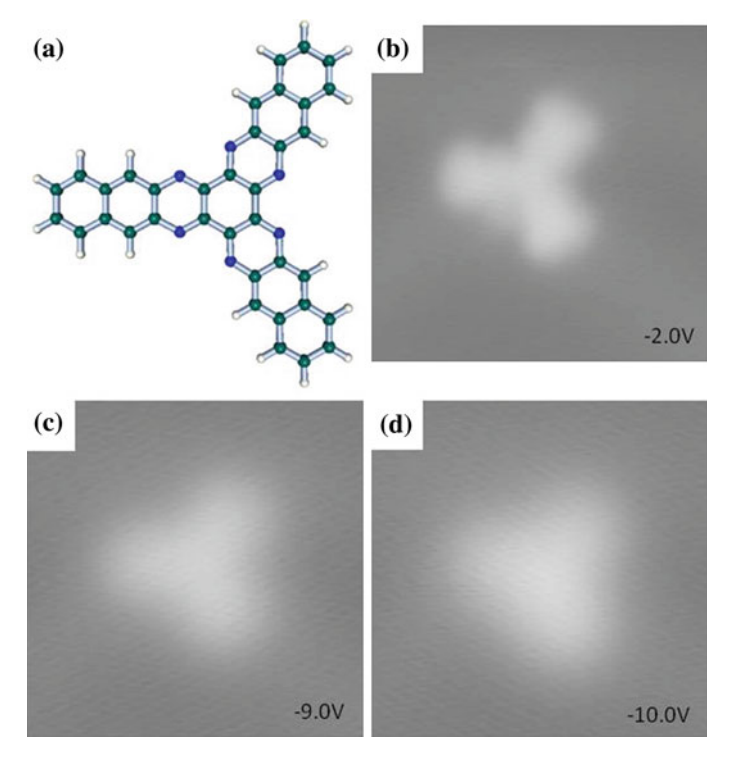


Fig. 8 a Ball and stick model of the Azastarphene molecule. **b** STM image of Azastarphene taken using standard tunneling imaging parameters (\mathbf{c}) and (\mathbf{d}) are images taken in the near field emission regimen, the three lobes of Azastarphene appear broaden and submolecular features in the branches that are clearly visible in low voltage images are completely blurred (image size: $4.5 \times 4.5 \text{ nm}$)

3 Interpretation

To understand and explain the gradual contrast and resolution changes taking place during STM-near field emission imaging, we need to revisit a well-known effect in the wave optics field, the diffraction effect occurring when an optic wave travels through a circular aperture or a pinhole. The wave planes of an incident light beam passing through a circular aperture will be diffracted depending on the aperture diameter and wavelength of the incoming wave. The diffracted wave can be imaged by placing a recording media or screen in front of the aperture. The diffraction due to a circular aperture will form a two-dimensional pattern made of a central bright spot known as Arago spot and evanescent concentric ridges (Fig. 9) [11].

Diffracted waves also broaden spatially when moving and spreading away from the aperture [11], the pattern spatial spreading (W) captured by a screen position at a given distance (X) from the aperture depends on several parameters like the wavelength of the incoming wave planes, the aperture diameter (a), and the screen

C. Manzano et al.

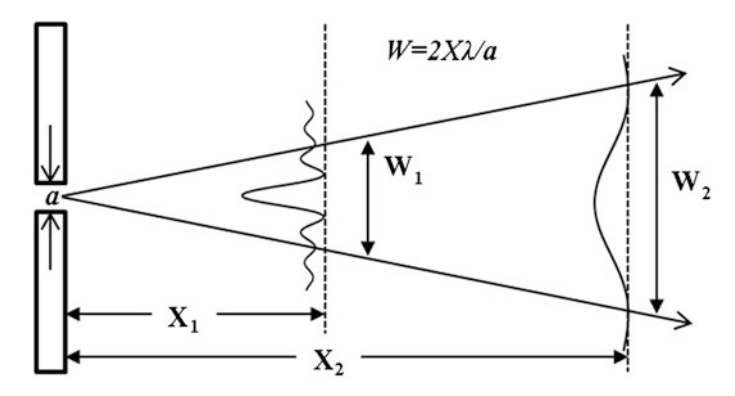


Fig. 9 Sketch showing how diffracted waves broaden spatially, when they spread away from an aperture. The cross-section of the diffraction pattern recorded at two different distances from the aperture shows the diffraction pattern broadening and its intensity attenuation

distance from the aperture (X) and can be approximated by the expression $W = 2X\lambda/a$. An example showing how the diffraction pattern spreads away from the aperture is shown in Fig. 9. The cross-section broadening of the diffraction pattern due to a circular aperture recorded at two different distances is also shown.

Evidently, there is not an actual aperture in the Au(111) surface, however, a molecule adsorbed on the metal substrate modifies locally the substrate's work function lowering the tunneling barrier height [12]. The perturbation of the barrier renders an area with the shape and footprint of the CuPc with a lower barrier height relative to that of Au(111) and in analogy to light waves passing through an aperture the STM tip will detect field emitted electrons passing through an "aperture", whose shape is defined by the CuPc molecule.

The whole sequence of CuPc high voltage images was taken using the constant current mode and as shown before in the Z(V) in Fig. 6 when the feedback loop is active the tip height is adjusted by the STM electronics to keep the current constant; the Z(V) shows that the tip moves away from the substrate commensurately with the voltage. Consequently, CuPc images in that sequence taken at increasing voltages were accordingly also taken at increasing larger tip-molecule distances relative to each other. The blurring and broadening present in the CuPc near field emission images, shown in Fig. 7, are the effects of retracting the STM tip *screen* away from the *aperture* and the sample surface by subsequently increasing the imaging voltage. This is a pure optics-like effect due to the field emitted electrons passing through the CuPc "aperture" that is made more evident by moving the *screen* away from the electrons source.

This hypothesis is reinforced by taking two series of images at tunneling resistances resulting in two image sets, which are shown in Fig. 10, obtained at different tip-substrate distances. By comparing the two series of near field emission images, it can be clearly noticed that the CuPc images taken at the same voltage but larger tip-substrate distances have lower resolution and appear blurred and

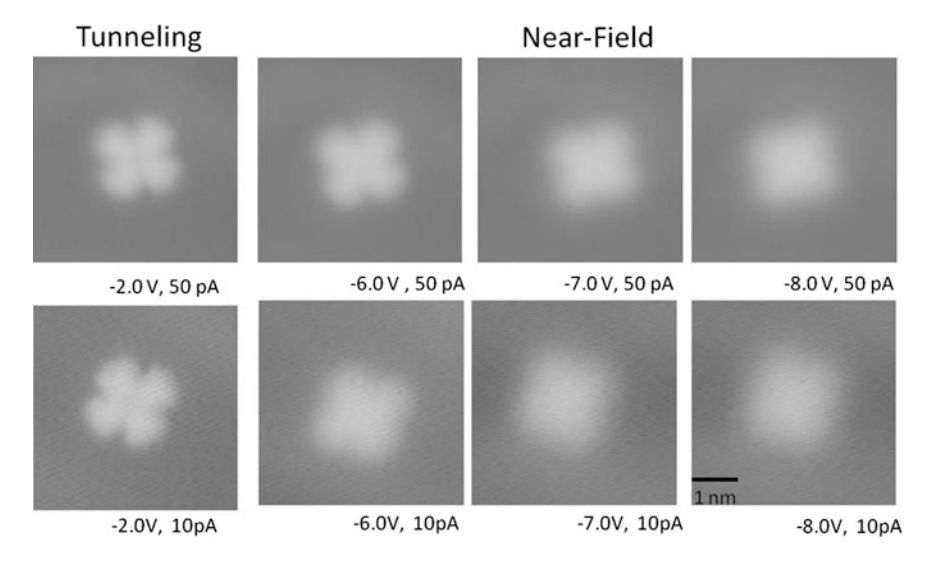


Fig. 10 Sequences of STM images taken at tunneling resistances resulting in two image sets obtained at different tip-substrate distances. The near field emission images show clearly that the CuPc images taken at the same voltage but larger tip-substrate distances have lower resolution and appear blurred and broadened relative to those taken at shorter distances. The images taken using standard tunneling parameters show that the two different tip-substrate distances have no effect in terms of image resolution (image size: $4.5 \times 4.5 \text{ nm}$)

broadened relative to those taken at shorter distances. That optics-like blurring and broadening is only observed in images taken in the near field regime at which STM images are made of the superposition of contributions due to tunneling electrons and field emitted electrons. As shown in the leftmost images in Fig. 10, it is clear that for images taken using low voltages at which the transmitted current through the tunneling junction is made of only tunneling electrons—the two different tip-substrate distances have no effect in terms of image resolution.

4 Conclusion

Low temperature STM experiments were done to investigate the possibility of imaging single CuPc molecules deposited on Au(111) using parameters that exceed the standard ones normally used for STM imaging and lie within the near field emission range. The imaging of single CuPc and Trianthracene molecules using voltages above the tip work function demonstrate that it is possible to use STM near field emission at negative bias voltages without damaging the target molecules.

The blurring and broadening of intramolecular features observed in images taken in the near field emission is analogous to the diffraction pattern broadening

C. Manzano et al.

observed when the diffraction pattern of a light beam passing through a circular aperture spreads away from the aperture. STM near field emission images are made of the superposition of contributions to the measured current due to both tunneling electrons and field emitted electrons. The weight of field emitted electrons contribution showing up in the images as optic-like blurring and broadening will depend not only on the imaging bias voltage but also on the tip-sample distance.

Acknowledgments We acknowledge financial support from the Agency of Science, Technology, and Research (A*STAR) for the Visiting Investigatorship Program (Phase III): AtomTech Project and the European Commission integrated project AtMol.

References

- Melmed, A.J., Muller, E.W.: Study of molecular patterns in the field emission microscope. J. Chem. Phys. 29, 1037 (1958). doi:10.1063/1.1744651
- Boyle, W.S., Kisliuk, P., Germer, L.H.: Electrical breakdown in vacuum. J. Appl. Phys. 26, 720 (1955). doi:10.1063/1.1722078
- 3. Binnig, G., Frank, K.H., Fuchs, H., Garcia, N., Reihl, B., Rohrer, H., Salvan, F., Williams, A.R.: Tunneling spectroscopy and inverse photoemission: image and field states. Phys. Rev. Lett. **55**, 991 (1985). doi:10.1103/PhysRevLett.55.991
- Becker, R.S., Golovchenko, J.A., Swartzentruber, B.S.: Electron interferometry at crystal surfaces. Phys. Rev. Lett. 55, 987 (1985). doi:10.1103/PhysRevLett.55.987
- Kubby, J.A., Wang, Y.R., Greene, W.J.: Fabry-Perot transmission resonances in tunneling microscopy. Phys. Rev. B 43, 9346 (1991). doi:10.1103/PhysRevB.43.9346
- Gundlach, K.H.: Zur Berechnung des Tunnelstroms Durch eine Trapezförmige Potentialstufe. Solid State Electron. 9, 946 (1966). doi:10.1016/0038-1101(66)90071-2
- Bobrov, K., Mayne, A.J., Dujardin, G.: Atomic-scale imaging of insulating diamond through resonant electron injection. Nature 413, 616 (2001). doi:10.1038/35098053
- 8. Pascual, J.I., Corriol, C., Ceballos, G., Aldazabal, I., Rust, H.-P., Horn, K., Pitarke, J.M., Echenique, P.M., Arnau, A.: Role of the electric field in surface electron dynamics above the vacuum level. Phys. Rev. B **75**, 165326 (2007). doi:10.1103/PhysRevB.75.165326
- Stepanow, S., Mugarza, A., Ceballos, G., Gambardella, P., Aldazabal, I., Borisov, A.G., Arnau, A.: Localization, splitting, and mixing of field emission resonances induced by alkali metal clusters on Cu (100). Phys. Rev. B 83, 115101 (2011). doi:10.1103/ PhysRevB.83.115101
- Soe, W.-H., Manzano, C., De Sarkar, A., Chandrasekhar, N., Joachim, C.: Direct observation of molecular orbitals of pentacene physisorbed on Au (111) by scanning tunneling microscope. Phys. Rev. Lett. 102, 176102 (2009). doi:10.1103/PhysRevLett.102.176102
- Pedrotti, F.L., Pedrotti, L.S., Pedrotti, L.M.: Introduction to Optics, 3rd edn. Addison-Wesley, Reading (2006)
- 12. Wu, S.W., Ogawa, N., Nazin, G.V., Ho, W.: Conductance hysteresis and switching in a single-molecule junction. J. Phys. Chem. C 112, 5241 (2008). doi:10.1021/jp7114548

Part II STEM

Motional Analysis of a Single Organic Molecule by TEM Using Nanocarbon Materials: Scope of Atomic Level Imaging and Spectroscopy

Masanori Koshino and Kazutomo Suenaga

Abstract The unique environment of single molecule analysis using nanocarbon materials is discussed in comparison with the conventional analysis of organic crystals by transmission electron microscopy (TEM). The methodology provides motional information of individual molecules in addition to the static images. The observed motions of molecules are mainly triggered by an electron beam used for imaging. A more advanced technique with aberration correctors, a low voltage electron beam, and a bright and atomic size electron probe will contribute to further understand the behaviors and reactions of molecules.

1 Organic Single Molecule Versus Organic Crystal

Our methodology of single molecular analysis is unique in that we utilize nanocarbon materials, such as carbon nanotubes and nanohorns, as a substrate of organic molecules not only for static imaging but also imaging in motion by highresolution transmission electron microscopy (HRTEM). First, we will discuss the unique environment of single molecule analysis in comparison with the conventional analysis used for organic crystals. Then we will discuss the methodology and the cause of the motions from the viewpoint of temperature and electron beam. In the last part, we will briefly introduce the recent advances of atomic imaging and spectroscopy with the perspective of a possible application to the analysis of molecular motions.

Not many organic molecules were reported as a single molecule by HRTEM, in part due to electron beam damage, low signal-to-noise (S/N) ratio, the packing of molecules in the crystal, etc. Microscopic images of organic crystals are

M. Koshino (⋈) · K. Suenaga

Nanotube Research Center, National Institute of Advanced Industrial Science and Technology (AIST), 1-1-1 Higashi, Tsukuba, Ibaraki 3058565, Japan e-mail: m-kosihno@aist.go.jp

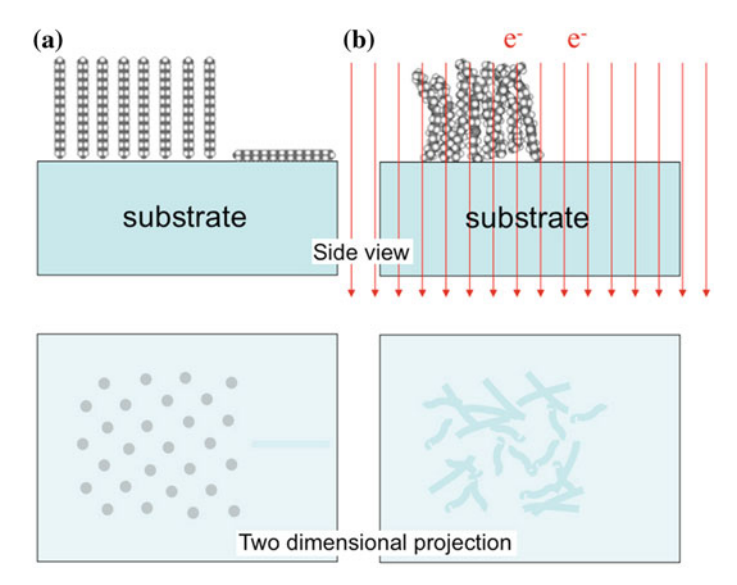


Fig. 1 Illustration of imaging an alkyl chains crystal and its degradation by an electron beam. Alkyl chains vertically aligned (**a** *upper left*) give a strong dot contrast (*lower left*). A single alkyl chain lying on the substrate gives small contrast embedded in the substrate. Under electron beam irradiation (from **a** to **b**), molecules suffer from conformational changes to lose their crystallinity, resulting in intensity decay when one observes its electron diffraction. Information for a single molecule is not available by either imaging or diffraction

sometimes from several molecules forming columnar structures [1], or from a certain direction along the crystal [2]. As the TEM image is the projection of 3D structures into a 2D image, the structure of alkyl chains, for example, could be visualized along their standing direction as dot spots even on a thick supportive substrate (Fig. 1a). When the position of alkyl chains changes their conformations (even without damage to the molecule itself) we can easily see the loss of crystallinity (Fig. 1b). Moreover, an alkyl chain lying on the substrate (right side in Fig. 1a) gives very small contrast, so that it is difficult for us to visualize unless the thickness of the substrate is the order of a few atoms.

2 Putting Molecules Inside Carbon Nanotubes: Method

Putting molecules inside carbon nanotubes provide a unique environment in which to visualize individual molecules [3]; a few groups have applied the method for organic molecules [4–6]. It was, however, not clear whether organic molecules preserve their structural integrity under such high electron doses (>10⁴ electrons nm⁻²), which is general for HRTEM. The crystal of organic materials undergoes a fading of diffraction intensity, as well as the fading of π^* in electron energy-loss

spectroscopy (EELS) [7, 8]. It was, therefore, necessary to examine whether or not the single molecular imaging of organic materials using carbon nanotubes is possible.

Our systematic study proved that some organic molecules can certainly be visualized as a single molecule with their motions under much higher electron doses than those expected for crystal destructions. As a proof of principle study, we designed various organic molecules: Alkyl chains [9, 10], amide bonds [11, 12], pyrene [11], catalytic metals [13], etc., and attached them to an elemental marker and then put them into nanotubes [9, 10, 14]. An example of alkyl chains is illustrated in Fig. 2.

Not only could we distinguish four different types of alkyl chains (Fig. 3a), but we also observed the translational and rotational motions of alkyl chains up to the order of $\sim 10^5$ e nm⁻², which is an electron dose hundreds of times higher than that used for electron diffraction of analogous crystals ($\sim 10^2$ e nm⁻²) [15]. The rotational motion of two separate alkyl chains indicates the structural integrity of the carbon skeleton (Fig. 3b). By assuming hydrogen removal, one can expect the conversion from alkane to alkene (olefin) or to alkyne, which is more active to cross-link together (Fig. 3c). Two separate alkyl chains were observed for quite a while, so that the cross-linking reaction was not confirmed at the electron dose of crystal destruction. Therefore, single organic molecular imaging has been proved

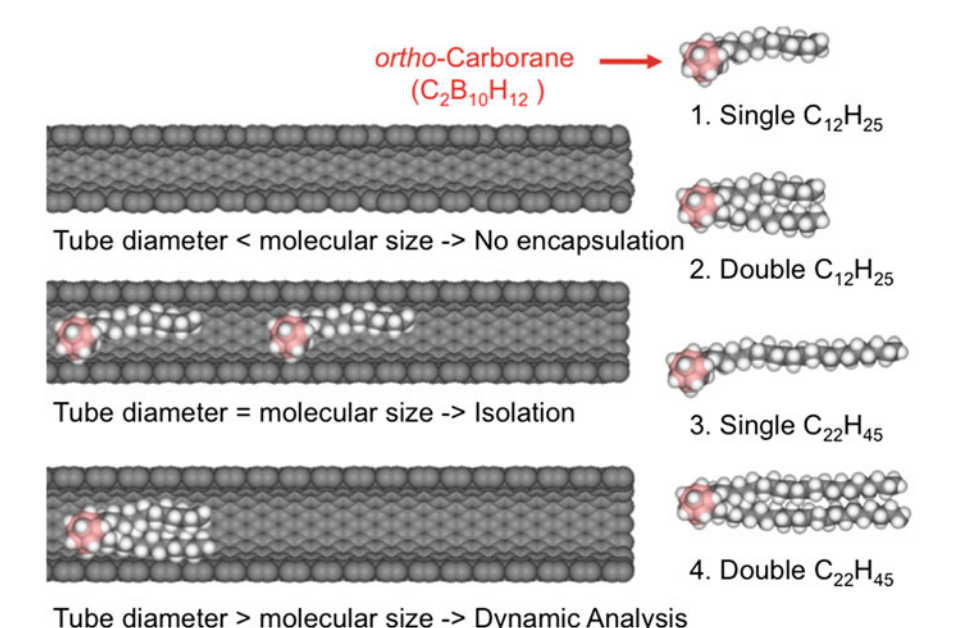


Fig. 2 Encapsulation of organic molecules. Nanotubes are de-capped before use [14]. Organic molecules are encapsulated in either the gas phase or liquid phase. Molecules are isolated and sometimes suitable for its motional analysis

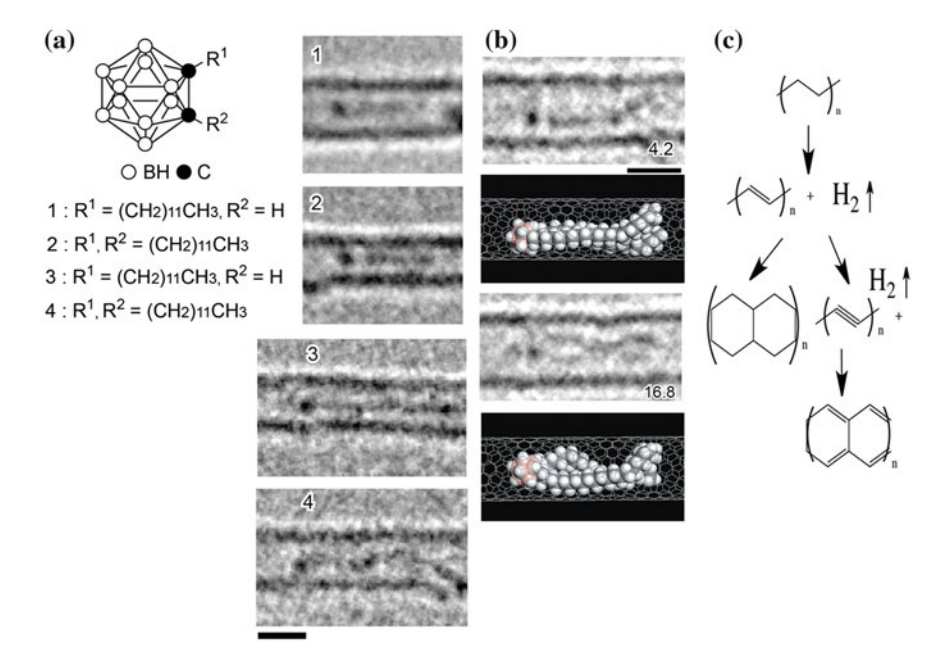


Fig. 3 Single molecule imaging. Experimental TEM images of four different alkyl chains attached to a carborane tag were quantitatively analyzed by their length and by their contrast. (a) Rotational motions of two alkyl chains showed two separate alkyl chains, indicating structural integrity of the carbon skeleton [9]. A hypothesis of hydrogen removal in (c) is less plausible, judged from (b)

possible with the simple encapsulation of molecules into nanotubes or physical adsorption of molecules outside the nanocarbon materials [10, 12, 16], providing with structural and motional information of organic molecules.

3 What Influences Molecular Motions?

The speed of motion was less affected by temperature but was more related to the electron dose used for imaging. We could observe a passage of alkyl chains through a defect hole on the nanotube wall when molecules were placed both at 293 and 4 K [10]. Indeed, the motion of molecules became slightly small at 4 K, compared to higher temperatures [17], but not as exponentially as expected by the Arrhenius plot.

It was the total electron dose, rather than the time interval of recording, that has affected the rotational motion of alkyl chains. A 180 degree of rotational motion of alkyl chain required c.a. 2.9×10^5 e nm⁻², with a time interval of every 2.1 s in which samples were irradiated for 0.5 s and the beam blank was 1.6 s, as

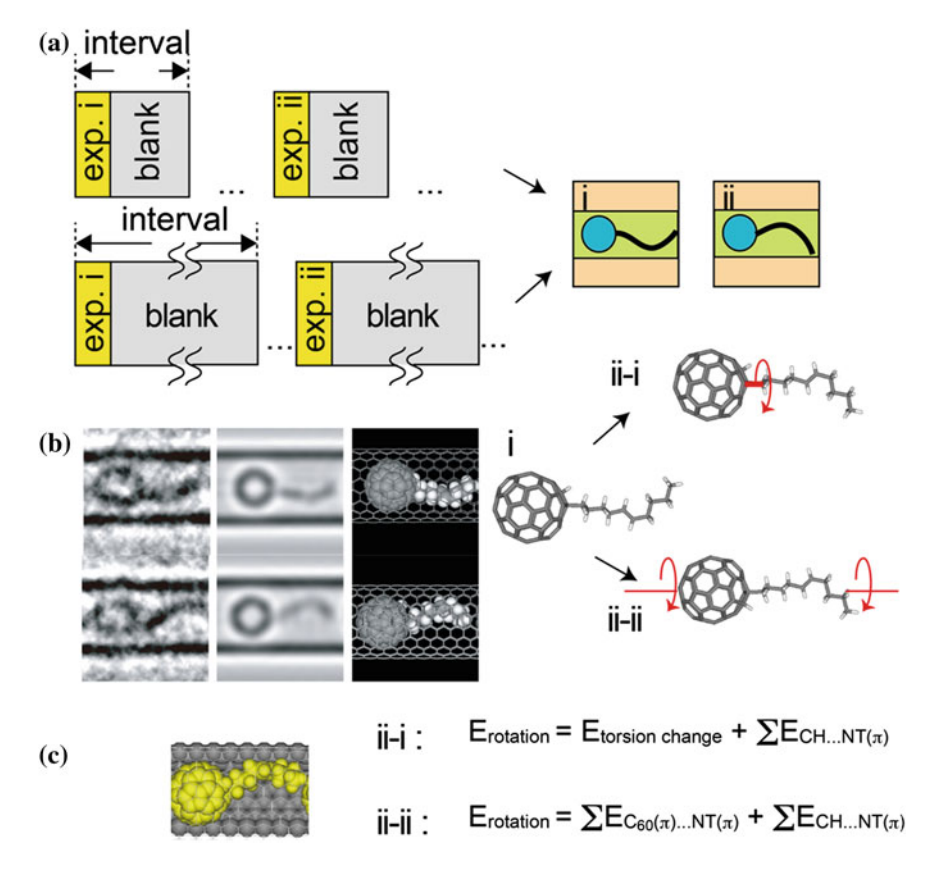


Fig. 4 Schematic images of the recording condition, the rotational motion of the molecule, and the estimation of energy. **a** A recorded series of images with the exposure time + blank time = interval (2.1 s for *upper* and 60 s for *lower*). Similar degrees of rotation indifferent to the time interval but with the same amount of electron doses are seen. **b** An example of a 180° rotation of an alkyl chain [10] with experiments (*left*), simulations (*middle*), and models (*right*) with the time consequence from upper to lower. The motion can be explained by either the torsion along the alkyl chain (i to ii–i) or the rotation of the entire molecule (i to ii–ii). **c** The molecule is tightly contacted to the inner tube wall, as illustrated by the CPK model. The energy required for the observed rotation can be estimated from the energy of torsion and the sum of CH π (NT) interaction (ii–i) or the sum of the energy to overcome individual π (C₆₀) – π (NT) and CH- π (NT) interactions

illustrated by Fig. 4a top and b [10]. When we changed the recording interval from 2.1 to 60 s with the same exposure time of 0.5 s and a blanking time of 59.5 s, we qualitatively saw the same rotational motion of alkyl chains at the same number of slides (Fig. 4a bottom).

How much energy do we need to rotate the alkyl chain (or the entire molecule) inside the nanotube? Experimentally, it is difficult to tell the exact answer because the motions of molecules are rather random. We still obtained the value of 6.7×10^5 e nm⁻² rot⁻¹ at a temperature of 298 K and at 120 kV of accelerating

voltage. We now think of two cases of the energies necessary for the rotation. The first is the energy just to rotate an alkyl chain along the axis between the alkyl chain and fullerene; we call this change "torsion" in convenience as shown in Fig. 4b ii-i. The energy required for the observed rotational motion can thus be explained by the energy required for the torsion in addition to the sum of energies in order to slide the alkyl chain along the nanotube if there are CH (alkyl chain)- π (nanotube, NT) interactions (Fig. 4c ii-i). The maximum energy for the torsion is at most a few kcal/mol and the energy for the sliding is in the same order. The second interpretation of the observed rotational motion is that the entire molecule rotates along the tube axis (Fig. 4b ii-ii). The energy for the rotation will be the sum of the energy to overcome individual $\pi(C_{60}) - \pi(NT)$ and CH- $\pi(NT)$ interactions. For either case, the required energy for 360 degrees of rotation is much less than the energy imparted by the 120 kV incident electron. The motions of molecules observed in the nanotubes are thus the gradual transition from one stable state to another. This is perceived as a partially fixed molecule on the substrate, vibrated by the electron beam to pop into different energy minima.

4 Characterizing the Structure with Atomic Resolution

A more precise answer to the question of molecular motion in terms of orientation with regard to the nanotube will be given by more dedicated experiments using an aberration corrected TEM. We could identify a certain orientation of fullerene molecules [17, 18]. Not only the motional analysis but also the characterization of chemical reactions becomes possible [13, 17]. Mild experimental conditions with low voltage are ideal for the motional analysis of molecules, so that we expect more information available in the near future.

In addition to the TEM study, more recent advances have been found in scanning transmission electron microscopy (STEM) combined with electron energy-loss spectroscopy (STEM-EELS) on the basis of single atomic imaging and spectroscopy. We could successfully discriminate the intrinsic electronic states of individual carbon atoms consisting of a graphene sheet in Fig. 5a-c [19]. Different spectral features of a carbon atom located at the edge or in bulk regions indicate the different energy states related to different coordination numbers (Fig. 5b, c). We could also see the different electronic states of a nitrogen atom adjacent to a single boron vacancy of hexagonal boron nitride (h-BN) [20, 21], as shown in Fig. 5d-f. Due to the delocalization of EELS information, it has been believed impossible to obtain the electronic information from a single atom. Low-voltage microscopy reduces the effect of delocalization, enabling us to provide some evidences of ultimate single atomic analysis of imaging and spectroscopy. The low-voltage microscopy with aberration correction provides more benefits, such as less damage and higher contrast, in addition to the localization of core-loss EELS. Combining this technique to single molecular analysis, we will be able to understand the behavior and properties of a molecule in more detail.

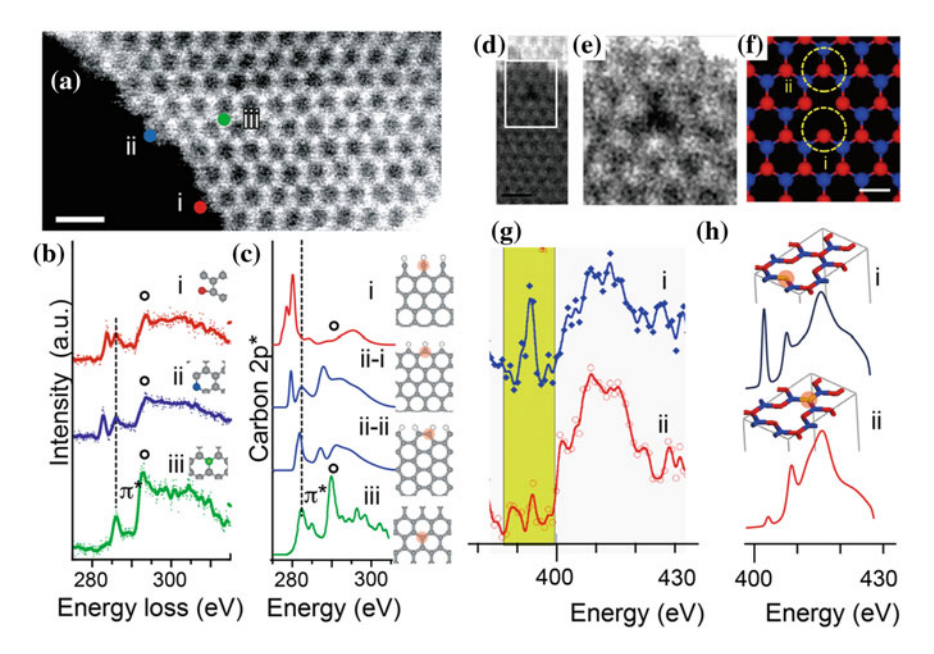


Fig. 5 Single atomic imaging and spectroscopy. The electronic states of edge carbon and bulk carbon of a single graphene sheet ($\bf a$ i–iii) show different EELS fine structures ($\bf b$ i–iii), which are interpreted by theoretical calculation ($\bf c$ DV-X α) [19]. The electronic states of nitrogen atoms in h-BN (*wide view* $\bf d$ and *magnified area* $\bf e$), either adjacent to a boron vacancy (*two coordination* $\bf f$ –i) or surrounded by three boron atoms (*three coordination* $\bf f$ –ii), show different EELS features $\bf g$, which are also interpreted by theoretical calculation ($\bf h$ Wien2 k) [20]

5 Conclusion

Nanocarbon materials play an important role in visualizing a single organic molecule in motion. The reduced reaction rate of a single organic molecule with regard to the imparted electron beam should be due to the different environment from the conventional analysis that deals with crystals or numbers of molecules. By taking advantage of low voltage STEM-EELS, such as less damage, higher contrast, and localization of EELS information, we will very soon be able to understand the behavior and properties of a single molecule as described here.

Acknowledgments A part of the study is supported by Kakenhi from MEXT (23681026 and 22000008), JST-Kenkyu Kasoku, and JST-S-innovation.

References

- Uyeda, N., Kobayashi, T., Ishizuka, K., Fujiyoshi, Y.: High voltage electron microscopy for image discrimination of constituent atoms in crystals and molecules. Chem. Scr. 14, 47–61 (1979)
- Zemlin, F., Reuber, E., Beckmann, E., Zeitler, E., Dorset, D.L.: Molecular resolution electron-micrographs of monolamellar paraffin crystals. Science 229(4712), 461–462 (1985)
- 3. Smith, B.W., Monthioux, M., Luzzi, D.E.: Carbon nanotube encapsulated fullerenes: A unique class of hybrid materials. Chem. Phys. Lett. **315**(1–2), 31–36 (1999)
- Takenobu, T., Takano, T., Shiraishi, M., Murakami, Y., Ata, M., Kataura, H., Achiba, Y., Iwasa, Y.: Stable and controlled amphoteric doping by encapsulation of organic molecules inside carbon nanotubes. Nat. Mat. 2, 683–688 (2003)
- Khlobystov, A.N., Britz, D.A., Briggs, G.A.D.: Molecules in carbon nanotubes. Acc. Chem. Res. 38(12), 901–909 (2005)
- Liu, Z., Koshino, M., Suenaga, K., Mrzel, A., Kataura, H., Iijima, S.: Transmission electron microscopy imaging of individual functional groups of fullerene derivatives. Phys. Rev. Lett. 96(8), 088304 (2006). doi:10.1103/PhysRevLett.96.088304
- Isaacson, M.S.: Inelastic scattering and beam damage of biological molecules. In: Siegel, B.M., Beaman, D.R. (eds.) Physical Aspects of Electron Microscopy and Microbeam Analysis, pp. 247–258. Wiley, New York (1975)
- 8. Koshino, M., Kurata, H., Isoda, S.: Study of structures at the boundary and defects in organic thin films of perchlorocoronene by high-resolution and analytical transmission electron microscopy. Ultramicroscopy **110**(12), 1465–1474 (2010)
- Koshino, M., Tanaka, T., Solin, N., Suenaga, K., Isobe, H., Nakamura, E.: Imaging of single organic molecules in motion. Science 316(5826), 853 (2007). doi:10.1126/science.1138690
- Koshino, M., Solin, N., Tanaka, T., Isobe, H., Nakamura, E.: Imaging the passage of a single hydrocarbon chain through a nanopore. Nat. Nanotech. 3(10), 595–597 (2008)
- Solin, N., Koshino, M., Tanaka, T., Takenaga, S., Kataura, H., Isobe, H., Nakamura, E.: Imaging of aromatic amide molecules in motion. Chem. Lett. 36(10), 1208–1209 (2007). doi:10.1246/cl.2007.1208
- Nakamura, E., Koshino, M., Tanaka, T., Niimi, Y., Harano, K., Nakamura, Y., Isobe, H.: Imaging of conformational changes of biotinylated triamide molecules covalently bonded to a carbon nanotube surface. J. Am. Chem. Soc. 130(25), 7808–7809 (2008). doi:10.1021/ja8022708
- Nakamura, E., Koshino, M., Saito, T., Niimi, Y., Suenaga, K., Matsuo, Y.: Electron microscopic imaging of a single group 8 metal atom catalyzing C-C bond reorganization of fullerenes. J. Amer. Chem. Soc. 14151-14153, 14151-14153 (2011). doi:10.1021/ja203225n
- Kataura, H., Maniwa, Y., Kodama, T., Kikuchi, K., Hirahara, K., Suenaga, K., Iijima, S., Suzuki, S., Achiba, Y., Kratschmer, W.: High-yield fullerene encapsulation in single-wall carbon nanotubes. Synth. Met. 121(1-3), 1195-1196 (2001)
- 15. Reimer, L.: Methods of detection of radiation damage in electron microscopy. Ultramicroscopy **14**(3), 291–303 (1984)
- Liu, Z., Suenaga, K., Iijima, S.: Imaging the structure of an individual c60 fullerene molecule and its deformation process using HRTEM with atomic sensitivity. J. Amer. Chem. Soc. 129(21), 6666–6667 (2007)
- Koshino, M., Niimi, Y., Nakamura, E., Kataura, H., Okazaki, T., Suenaga, K., Iijima, S.: Analysis of the reactivity and selectivity of fullerene dimerization reactions at the atomic level. Nat. Chem. 2(2), 117–124 (2010)
- Sato, Y., Suenaga, K., Okubo, S., Okazaki, T., Iijima, S.: Structures of d5d-c80 and iher3n@c80 fullerenes and their rotation inside carbon nanotubes demonstrated by aberration-corrected electron microscopy. Nano Lett. 7(12), 3704-3708 (2007)
- Suenaga, K., Koshino, M.: Atom-by-atom spectroscopy at graphene edge. Nature 468, 1088–1090 (2010). doi:10.1038/nature09664

- Suenaga, K., Kobayashi, H., Koshino, M.: Core-level spectroscopy of point defects in single layer h-BN. Phys. Rev. Lett. 108(7), 075501 (2012)
- Suenaga, K., Kobayashi, H., Koshino, M.: Single atom imaging and spectroscopy in nanostructured carbon materials. MRS Bull. 37, 36–38 (2012). doi:10.1557/mrs.2011.339

Part III Photo-Emission (PE)

Imaging Orbitals by Ionization or Electron Attachment: The Role of Dyson Orbitals

B. Mignolet, T. Kùs and F. Remacle

Abstract Molecular orbitals are one-electron wave functions computed at a mean field level of approximation in electronic structure theory. Spatially resolved scanning tunneling microscopy (STM) experiments probe the electron density of a species with an extra electron or with a default of one electron, which strictly speaking, corresponds to a Dyson orbital. Dyson orbitals are one-electron wave functions that represent the density of the electron that is removed or attached to the molecule. They provide a correlated view of the wave function of the leaving electron. They are computed as the overlap between the neutral species and the species with a defect of one electron or an extra one. Dyson orbitals correspond to molecular orbitals of the neutral only when there is little electron relaxation in the charged species with respect to the neutral. They also play a crucial role in the interpretation of photoelectron angular distributions. We discuss the properties of Dyson orbitals in pentacene for electron attachment and removal and in C_{60} and LiH with special reference to photoelectron angular distributions and the probing of ultrafast electron dynamics.

1 Introduction

Molecular orbitals (MO) are widely used in the interpretation of low temperature spatially scanning tunneling microscopy (STM) experiments [1–4], angular resolved photoemission spectra [5], and more recently in tomography of orbitals probed by attosecond trains of high harmonics [6–10]. In these three kinds of experiments, the imaging of the molecular orbital is realized by adding or removing an electron to the atom or the molecule. Strictly speaking, the one-electron wave function that is probed is therefore a Dyson orbital (one-electron

Department of Chemistry, B6c, University of Liège, B4000 Liège, Belgium

e-mail: fremacle@ulg.ac.be

B. Mignolet · T. Kùs · F. Remacle (⋈)

quasi particle) [11–14], given by the overlap of the N and the N+1 or N-1 many-electron wave functions of the system:

$$\phi_{\text{cat}}^{D}(\mathbf{r}) = \sqrt{N} \int d\mathbf{r}_{1} ... d\mathbf{r}_{N-1} \Psi_{\text{neut}}^{N}(\mathbf{r}_{1}, ..., \mathbf{r}_{N}) \Psi_{\text{cat}}^{N-1}(\mathbf{r}_{1}, ..., \mathbf{r}_{N-1})$$
(1)

or

$$\phi_{\text{anion}}^{D}(\mathbf{r}) = \sqrt{N+1} \int d\mathbf{r}_{1} ... d\mathbf{r}_{N} \Psi_{\text{neut}}^{N}(\mathbf{r}_{1}, ..., \mathbf{r}_{N}) \Psi_{\text{anion}}^{N+1}(\mathbf{r}_{1}, ..., \mathbf{r}_{N+1})$$
(2)

 $|\Psi^N\rangle$ and $|\Psi^{N\pm 1}\rangle$ are antisymmetrized many-electron wave functions. When electron correlation is taken into account, they are expressed as linear combinations of configurations, each of them being a Slater determinant, \mathbf{D} , built from the occupied MO, $|\varphi_i\rangle$, of the corresponding one-electron Hamiltonian.

The Dyson orbitals in Eqs. (1) and (2) can be expanded in the MO of the neutral:

$$\phi_{\text{cat}}^{D}(\mathbf{r}) = \sum_{i} \varphi_{i}^{\text{neut}} \langle \Psi_{\text{cat}}^{N-1} | \hat{a}_{i} \Psi_{\text{neut}}^{N} \rangle$$

$$\phi_{\text{anion}}^{D}(\mathbf{r}) = \sum_{i} \varphi_{i}^{\text{neut}} \langle \Psi_{\text{neut}}^{N} \hat{a}_{i}^{\dagger} | \Psi_{\text{anion}}^{N+1} \rangle$$
(3)

Where \hat{a}_i^{\dagger} and \hat{a}_i are the operators that add to and remove an electron from the molecular orbital φ_i . The overlap between the wavefunction of the cation and the wavefunction of the neutral where an electron has been removed from the *i*th MO can be expressed as the determinant of the overlap matrix between the occupied MOs of the Slater determinant of the neutral and cation [15].

$$\left\langle \mathbf{\Psi}_{\text{cat}}^{N-1} \middle| \widehat{a}_{i} \mathbf{\Psi}_{\text{neut}}^{N} \right\rangle = \sum_{l} \sum_{m} \frac{c_{l}^{*} c_{m}}{(N-1)!} \left\langle \mathbf{D}_{l}^{\text{cat}} \middle| \widehat{a}_{i} \mathbf{D}_{m}^{\text{neut}} \right\rangle
\frac{\left\langle \mathbf{D}_{l}^{\text{cat}} \middle| \widehat{a}_{i} \mathbf{D}_{m}^{\text{neut}} \right\rangle}{(N-1)!} = \begin{vmatrix} \left\langle \varphi_{1,l}^{\text{neut}} \middle| \varphi_{1,m}^{\text{cat}} \right\rangle & \dots & \left\langle \varphi_{1,l}^{\text{neut}} \middle| \varphi_{N-1,l}^{\text{cat}} \right\rangle \\ \dots & \dots & \dots \\ \left\langle \varphi_{N-1,l}^{\text{neut}} \middle| \varphi_{1,m}^{\text{cat}} \right\rangle & \dots & \left\langle \varphi_{N-1,l}^{\text{neut}} \middle| \varphi_{N-1,m}^{\text{cat}} \right\rangle \end{vmatrix}$$
(4)

Dyson orbitals provide a correlated view of the wavefunction of the leaving electron. In the simple Koopmans picture and for single determinant wavefunctions, Dyson orbitals correspond to the MO of the neutral from which an electron has been removed, or the MO to which an electron has been added. The Koopmans picture is widely used in chemical physics and is valid when there is no extensive electron relaxation upon adding or removing an electron to the system. It also does not take into account the possibility of a nuclear rearrangement induced by ionization or electron attachment. Usually, the Koopmans picture is better for ionization than for electron attachment.

It became recently possible to probe electronic densities upon ionization and electron recombination by analyzing the high harmonic generation obtained by submitting the molecule or the atom to an intense infrared field. [6–10] The central quantity in this analysis is the photoemission dipole between the wave function of the recolliding electron, ϕ_{elec} , and that of the N-1 electron cation, Ψ_{cat}^{N-1} , with that of the neutral, Ψ_{neut}^{N} :

$$\begin{split} \left\langle \Psi_{\text{cat}}^{N-1}, \phi_{\text{elec}} \middle| \mathbf{E}.\mathbf{r} \middle| \Psi_{\text{neut}}^{N} \right\rangle &= \int \mathrm{d}\mathbf{r} \phi_{\text{elec}}(\mathbf{E}.\mathbf{r}) \int \mathrm{d}\mathbf{r}_{2}...\mathrm{d}\mathbf{r}_{N} \Psi_{\text{cat}}^{N-1} \Psi_{\text{neut}}^{N} \\ &= \int \mathrm{d}\mathbf{r} \phi_{\text{elec}}(\mathbf{E}.\mathbf{r}) \phi_{\text{cat-neut}}^{D}(\mathbf{r}) \end{split} \tag{5}$$

The photoionization amplitude is given by the same matrix element. A particularly interesting situation occurs when the wavefunction of the neutral is not that of the ground state, as can be the case when the neutral molecule has been previously excited. We discuss here two different cases: the case when the ionized molecule is in a highly excited state of the neutral, like in the recent report of super atom molecular states (SAMO) in C_{60} [16, 17], and that in which the neutral has been pumped by a short fs pulse to a coherent superposition of states prior to ionization [18–20]. We start by reporting on the Dyson orbitals for electron detachment and attachment in pentacene, [2] with reference to a recent STM study [4].

2 Dyson Orbitals in Pentacene

Soe et al. [4] observed the three highest occupied and the lowest unoccupied MO of pentacene by measuring the differential conductance of a pentacene molecule adsorbed on a metal surface using low temperature spatially resolved scanning tunneling microscopy. We show here that these orbitals also correspond to the Dyson orbitals (that reflect the wavefunction of the outgoing electron) for a transition from the ground state (GS) of the neutral to the ground and excited electronic states (ES) of the cation or of the anion.

The equilibrium geometry of the gas phase neutral pentacene was determined under symmetry constraint (point group D_{2h}) using Density Functional Theory (DFT) with the B3LYP functional and the 6-31 ++G(D, P) basis set as implemented in the suite of quantum chemistry programs Gaussian 09 [21]. For a recent theoretical study on oligoacenes, see Aiga [22]. The isocontours of the highest occupied MO are shown in Fig. 1. We also computed the electronic structure ground state of the cation with the same basis set and functional and found a vertical ionization potential (IP) of 6.18 eV, which is relatively close to the experimental vertical IP of 6.61 \pm 0.02 eV [23]. The isocontours of the MOs of the cation are similar to the ones of the neutral, which shows that the electronic rearrangement is small upon removing an electron from the neutral. In this case,

the Koopmans theorem is expected to work and the Dyson orbital of the ground state looks like the highest occupied molecular orbital (HOMO).

The ten lowest excited states of the cation were computed using time-dependent (TD) DFT and the configuration interaction with single substitutions and perturbative correction (CIS(D)) methods at the equilibrium geometry of the neutral. The excitation energies from the ground to the excited states are reported in Table 1 in addition to the transition that composes the main configuration of a given excited state.

The experimental energy difference between the ground state of the cation and the first/second excited state is about 1.31 and 1.71 eV, respectively [23], which is in good agreement with the TD-DFT computed excitation energies of 1.45 and 1.85 eV for the second and third excited states. As discussed below, the computed first excited state of the cation does not lead to any significant ionization probability from the GS of the neutral. The excitation energies computed in CIS(D) and in Complete Active Space Self-Consistent Field CASSCF(5-6)/6-31G(D) (not reported here) are higher than in TD-DFT but the excited states are built of similar transitions.

We computed the Dyson orbitals of the cation (Fig. 2) with the wavefunction obtained in TD-DFT using Eq. (3). The first Dyson orbital corresponds to the ionization of the GS of the neutral to the GS of the cation. It is almost identical to the HOMO of the neutral, in agreement with the Koopmans theorem, since the electronic relaxation when going from the neutral to the cation is small. In the main electronic configuration of the computed first excited state of the cation, an electron is promoted from the HOMO to the lowest unoccupied molecular orbital (LUMO). The overlap of this wavefunction of the cation with the ground state of the neutral is close to zero since the LUMO is unoccupied in the neutral and the electronic relaxation is low. As can be seen in Fig. 2 there is, however, some density for the Dyson orbital because the first excited state is also composed of other electronic configurations with small weights. Note that this state is not expected to play a role in a photoionization process since the photoionization width is proportional to the square modulus of the Fourier transform of the Dyson

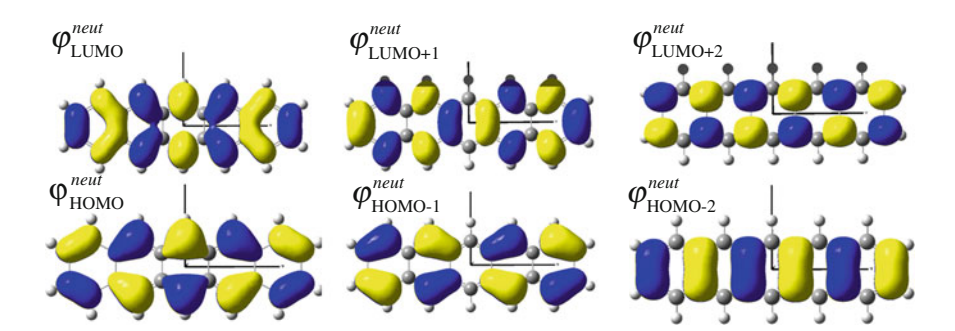


Fig. 1 Amplitude isocontour of the molecular orbitals of pentacene molecule computed at the DFT/B3LYP/6-31 ++G(D,P) with the D_{2h} symmetry

	TD-DFT		CIS(D)	
	Excitation energy (eV)	Transition of the main configuration	Excitation energy (eV)	Transition of the main configuration
1st excited state 2nd excited state 3 rd excited state	1.39 1.45 1.85	$\varphi_{ ext{HOMO}}^{ ext{cat}} o \varphi_{ ext{LUMO}}^{ ext{cat}}$ $\varphi_{ ext{HOMO}-1}^{ ext{cat}} o \varphi_{ ext{HOMO}}^{ ext{cat}}$ $\varphi_{ ext{HOMO}-2}^{ ext{cat}} o \varphi_{ ext{HOMO}}^{ ext{cat}}$	1.75 2.02 2.67	$\begin{array}{c} \varphi_{\text{HOMO-1}}^{\text{cat}} \to \varphi_{\text{HOMO}}^{\text{cat}} \\ \varphi_{\text{HOMO}}^{\text{cat}} \to \varphi_{\text{LUMO}}^{\text{cat}} \\ \varphi_{\text{HOMO-2}}^{\text{cat}} \to \varphi_{\text{HOMO}}^{\text{cat}} \end{array}$

Table 1 Excitation energies and transition of the excited states of the cation computed in TD-DFT and CIS(D)

orbital [Eq. (5)] and will be negligible. In the second and third exited states of the cation, the main configurations correspond to promotion of an electron from the HOMO-1 and HOMO-2 to the HOMO. The Dyson orbital will then be mainly composed of $\varphi^{\text{cat}}_{\text{HOMO-1}}$ and $\varphi^{\text{cat}}_{\text{HOMO-2}}$ for the second and third excited states, respectively.

The agreement of the computed isocontours of the Dyson orbitals with the experimental data of Soe et al. [4] is quite good for the Dyson of the ground state of the cation and the second excited state but is less good for the third excited state.

The differential conductance spectrum of Ref [4] shows peaks corresponding to the HOMO-1 and HOMO-2 at 1.0 and 1.6 V below the peak of the HOMO. The agreement with the computed excitation energies of the cation (Table 1) is rather good, taking into account those are computed for gas phase pentacene and not for the molecule adsorbed on a surface.

The electronic states of the anion have been computed in TD-DFT with the B3LYP functional and the 6-31 ++G(D,P) basis set (Table 2) also at the equilibrium geometry of the neutral. The computed electron affinity is 1.41 eV (experimental value is 1.39 eV [24]). The Dyson orbital for the transition between

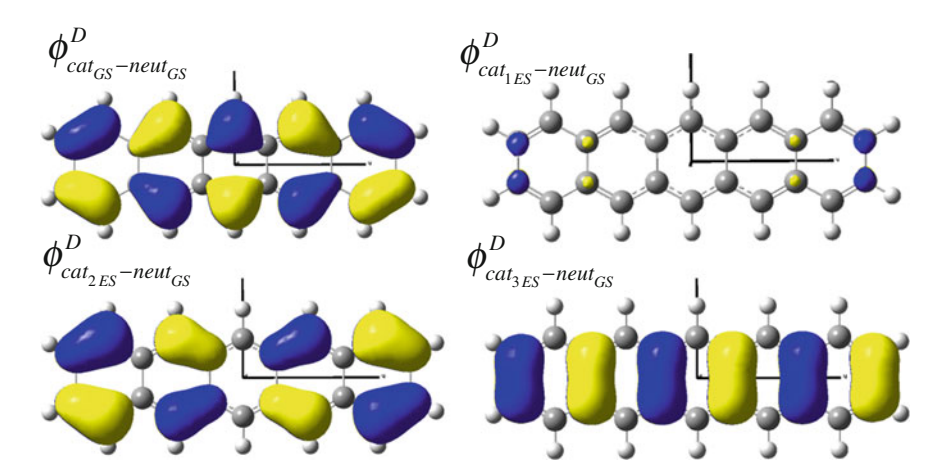


Fig. 2 Amplitude isocontour of Dyson orbitals computed between the ground state of the neutral and the electronic states of the cation using DFT and TD-DFT wavefunctions

DFI				
	TD-DFT			
	Excitation energy (eV)	Transition of the main configuration		
First excited state	1.33	$arphi_{ ext{HOMO}}^{ ext{anion}} ightarrow arphi_{ ext{LUMO}}^{ ext{anion}}$		
Second excited state	1.53	$arphi_{ m HOMO}^{ m anion} ightarrow arphi_{ m LUMO}^{ m anion}$		
Third excited state	1.73	$arphi_{ m HOMO}^{ m anion} ightarrow arphi_{ m LUMO}^{ m anion}$		

Table 2 Excitation energies and transition of the excited states of the anion computed in TD-DFT

the GS of the neutral and the GS of anion corresponds to the LUMO and is in good agreement with the measured data. The Dyson of the first excited state (not shown here) is zero because the excited state has its main configuration with two electrons in the LUMO. It is then impossible to have a good overlap with the neutral since the GS of the neutral has no electron in the LUMO. The Dyson orbital to the second excited state of the anion corresponds to the LUMO + 1 of the neutral. The main configuration of the third excited state of the anion is the excitation of an electron from the LUMO to the LUMO + 2. The Dyson orbitals are expected to be composed of the LUMO + 2 of the neutral but due to the electronic rearrangement when going from the neutral to the anion, the Dyson orbital is composed of a linear combination of the LUMO + 4 and LUMO + 7: $\phi_{\text{anion}_{3\text{ES}}-\text{neut}_{GS}}^D = -0.93 \phi_{\text{LUMO}+4}^{\text{neut}} + 0.31 \phi_{\text{LUMO}+7}^{\text{neut}}$ (see Fig. 3).

We showed that there is a good agreement between the molecular densities of pentacene measured by STM experiment of Soe et al. [4] and the computed Dyson orbitals. Similar molecular densities can be generated from the photoelectron spectrum measured in ultraviolet angle-resolved photoelectron spectroscopy [5, 25] of a crystalline pentacene film.

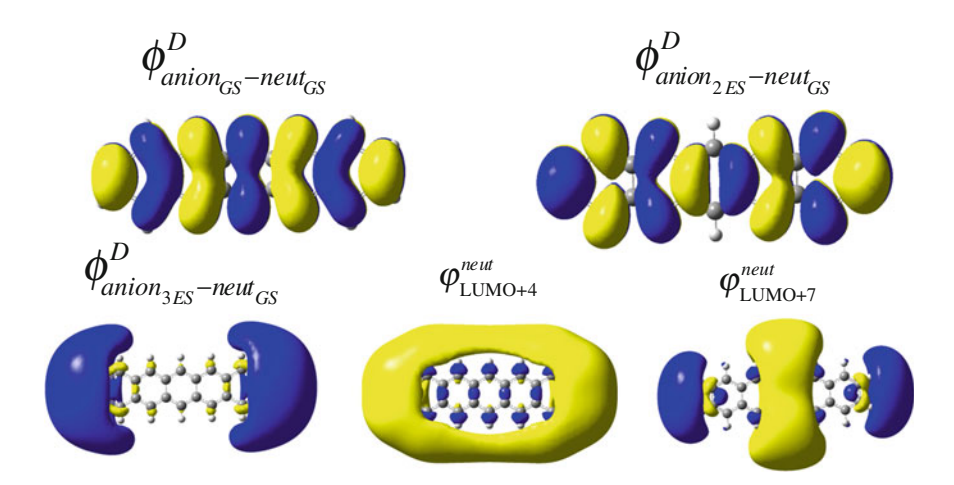


Fig. 3 Amplitude isocontour of LUMO + 4, LUMO + 7 of the neutral and Dyson orbitals computed between the ground state of the neutral and the electronic states of the anion using the DFT and TD-DFT wavefunctions

3 Dyson Orbitals and Super Atomic Molecular Orbital States in C₆₀

In C₆₀, in addition to MO localized close to the C atoms, the spherical potential defined by the carbon cage supports diffuse hydrogenic-like MO called Super Atom MO (SAMO). They were first identified by Petek et al. [26, 27] using low temperature scanning tunneling spectroscopy (LT-STS) of C₆₀ on a Cu surface. SAMOs were also characterized optically, on surfaces [28] and in the gas phase [16, 17]. As for the pentacene molecule discussed above, the cation of C_{60} undergoes very little relaxation compared to the neutral. Therefore, the extended Koopmans picture for ionization is valid and the Dyson orbitals corresponding to the ionization of the SAMO neutral states where an electron is promoted from the HOMO to a SAMO of the neutral are in very good approximation given by the SAMOs directly. The 1s-, p- and d-, and 2s- SAMOs of the neutral C₆₀ are shown in Fig. 4. Isoenergetic to the SAMO states, there are also non-SAMO excited states, where the electron is promoted from the HOMO to a non-occupied non-SAMO orbital, which is characterized by electron density localized close to the C atom cage. Isocontours of such orbitals are also shown in Fig. 4 and the excitation spectrum of the lowest 500 excited state of C₆₀ computed at the TD-DFT/B3LYP/ 6-31+G(d) level is shown in Fig. 5.

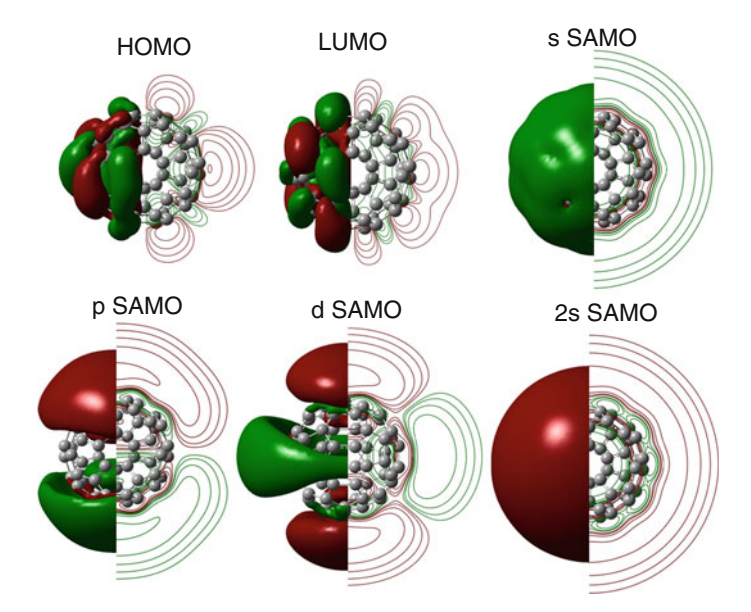
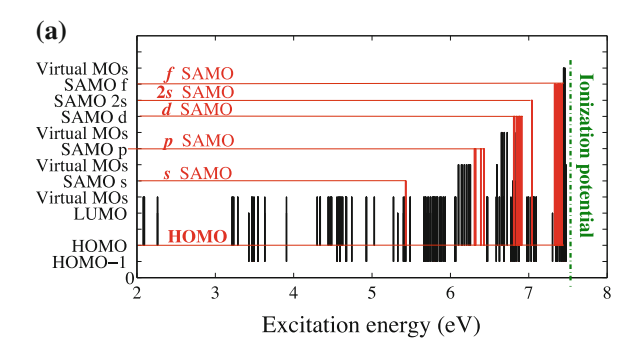


Fig. 4 Isosurface (*left side* of the molecule) and the isocontour (*right side* of the molecule) of the amplitudes of two non-SAMOs (HOMO and LUMO) and four SAMOs. The SAMO s(n=3), p, d_{z2} and 2s(n=4) have their electronic density localized far from the cage while the non-SAMO orbitals such as the HOMO and the LUMO have their electronic densities localized close to the C atoms



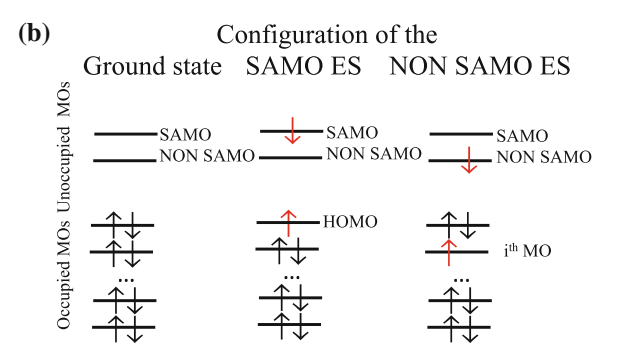


Fig. 5 a Excitation energy of the first 500 excited states of C_{60} . There are only a few SAMO states (*red sticks*) in comparison with the large number of non-SAMO states (*black sticks*). **b** The excited states are built from transitions where an electron is promoted from an occupied MO to an unoccupied MO. The sticks in panel (a) show this excitation where the bottom represents the MO from which the electron is excited and the top is where the electron is promoted. Most of the states are composed of a single excited configuration. When the electron is promoted from the HOMO to a SAMO, then the state is called SAMO excited state

We show in Ref. [17] that because of their completely different spatial localization, the photoionization widths of the SAMO and the non-SAMO states are vastly different. For low kinetic energies near the ionization threshold, in a range 0–2 eV, the SAMO states have one photon ionization width in the femtosecond range while those of the non-SAMO states fall in the piconanosecond range for excitation field strength of 0.01 au $(5.1 \cdot 10^7 \text{ V/cm})$. This explains why the SAMO states and their hydrogenic photoelectron angular distributions (PAD) dominate the photoelectron spectrum [16, 17].

The ionization of the SAMO states of C_{60} provides a picture complementary to that of discussed for the pentacene above. Here, the ionization is from an excited state of the neutral to the GS of the cation, while in the case of the pentacene molecule, the ionization is from the GS of the neutral to an excited state of the cation. We next discussed a time-dependent case, where the optical excitation of the neutral by an ultrashort pulse has prepared a coherent superposition of electronic states.

4 Time-Dependent Dyson Orbitals

The recent advances in the engineering of ultrashort pulses make few cycle photon pulses of duration of a few femtoseconds available for exciting and probing electron dynamics in atoms and molecules in real time. [8, 29–34] When the neutral molecule is excited by an ultrashort UV pulse, one can prepare a coherent superposition of the excited states of the neutral [19, 35–37] that can be probed by sudden XUV ionization before the nuclei dynamics sets in [20]. The PAD reflects the spatial localization of the coherent electronic wave packet built by the ultrashort excitation pulse. More precisely, the PAD is a function of the time-dependent Dyson orbital at the time of ionization, τ:

$$\phi_K^D(\tau) = \sqrt{N} \int \Psi_K^{\text{cat}} \Psi(\tau) d\mathbf{r}_1 \dots d\mathbf{r}_{N-1} = \sum_I c_I(\tau) \phi_{\text{IK}}^D$$
 (6)

where $|\Psi(\tau)\rangle$ is the coherent superposition of field free electronic states of the neutral, $|\Psi_I\rangle$, built by the excitation pulse

$$|\Psi(t)\rangle = \sum_{I} c_{I}(t) |\Psi_{I}\rangle \tag{7}$$

The time-dependent amplitudes $c_I(t)$ are computed solving the time-dependent Schrödinger equation, taking the coupling to the electric field of the excitation pulse into account:

$$i\hbar \frac{d\mathbf{c}(t)}{dt} = (\mathbf{H}_{\text{elec}} - \mathbf{E}(t) \cdot \mu)\mathbf{c}(t)$$
 (8)

where \mathbf{H}_{elec} is the matrix of the electronic Hamiltonian is the basis of field free many-electron states and $\mathbf{E}(t) \times \mu$ is the dipolar coupling term, $\mathbf{E}(t) = \mathbf{E} \exp\left(-(t-t_0)/2\sigma^2\right) \cos(\omega t + \phi)$ is the time profile of the electric field of the excitation pulse and μ the transition dipole moment of the molecule.

Taking the orthogonalization of the plane wave that describes the ionized electron with the electronic states of the neutral into account, the angular resolved photoionization cross-section at the time τ of ionization is given by [20]

$$\frac{d\sigma_{K}(\varepsilon)}{d\Omega} = \frac{8\pi e^{2}\omega}{\varepsilon_{0}c}\rho_{\Omega}(\varepsilon)\left|\left(\left\langle\phi_{K}^{D}(\tau)\middle|\mathbf{r}\middle|\varepsilon_{K,\Omega}\right\rangle - \sum_{i}^{m}\left\langle\phi_{K}^{D}(\tau)\middle|\mathbf{r}\middle|\phi_{i}^{\text{neut}}\right\rangle\left\langle\phi_{i}^{\text{neut}}\middle|\varepsilon_{K,\Omega}\right\rangle\right)\right|^{2}$$

where $|\phi_i\rangle$ are the MO of the neutral. Therefore, the angular resolved photoionization cross-section at different time of ionization τ will reflect the beatings and the spatial localization of the one-electron density matrix $\rho(t)$:

$$\rho(t) = |\Psi(t)\rangle\langle\Psi(t)| = \sum_{i,j} c_i^*(t)c_j(t)\rho_{ij}$$
(9)

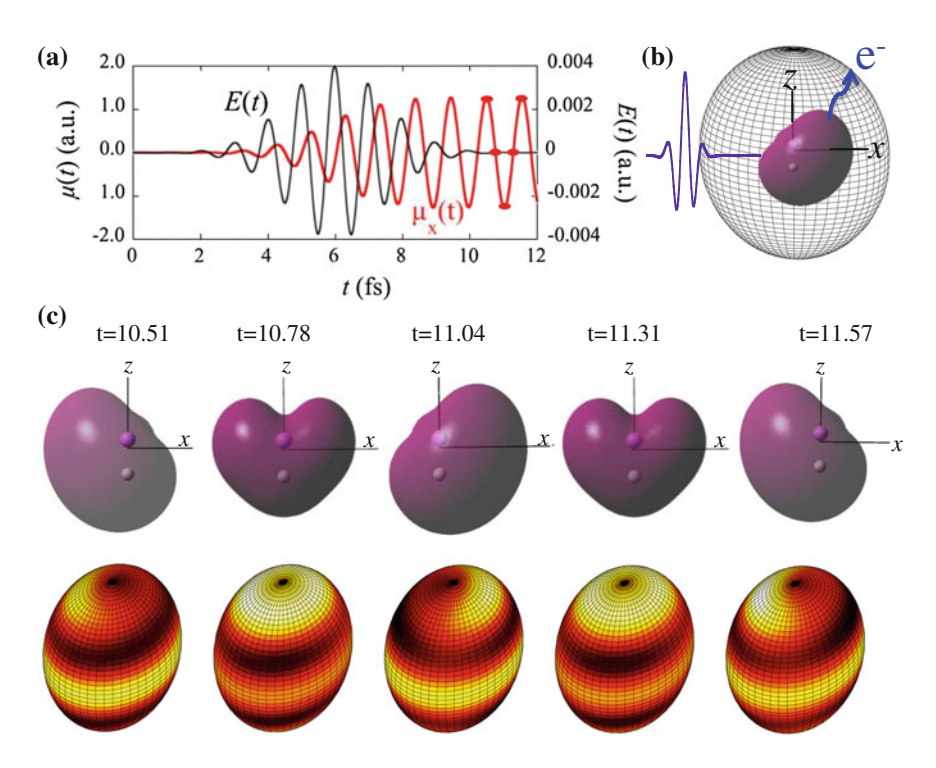
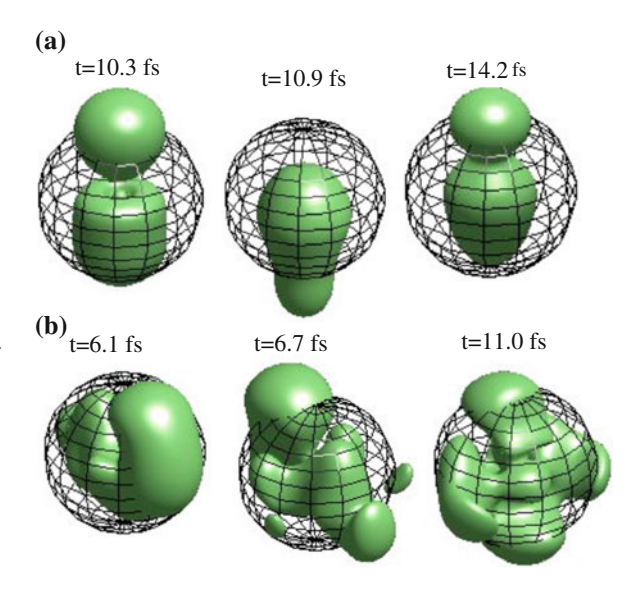


Fig. 6 a Time-dependent variation of the component of the dipole moment perpendicular to the bond axis induced by UV excitation pulse, E(t) ($t_0=250$ a.u., $\omega=0.15$ a.u, and $\sigma=60$ a.u. $\mathbf{E}=0.004$ a.u. and is polarized perpendicularly to the bond axis), applied to an aligned molecule. At the end of the excitation pulse a coherent superposition of the GS and the lowest Π state is built. The red dots represent the time at which the system is probed by sudden photoionization with an XUV pulse ($\omega=0.47$ a.u) polarized along z. b Schematic representation of a pump-probe experiment. The pump pulse builds a superposition of electronic states that are probed by sudden photoionization by an XUV pulse. c) $\rho(t)$ (top) and MFPAD (bottom) computed for minimal and maximal interferences at the times shown by the red spheres on the panel (a). The angular distributions (or MFPAD) of the ionized electron are represented by a sphere where the colors indicate the intensity

Figure 6 shows the PAD and the time-dependent density matrix computed for the LiH molecule excited by UV pulse polarized perpendicular to the bond axis and weak enough not to induce ionization. The excitation pulse builds a superposition of the GS and of the lowest Π state of the neutral that beats with a period of 1.06 fs. These beatings observed in the plane perpendicular to the bond axis are clearly reflected both by $\rho(t)$ and by the PAD probed by sudden photoionization. A basis of 40 electronic states computed in CASSCF with the 6-311++G(2df,2p) basis set [18, 20] is used to describe the purely electronic dynamics induced by the excitation pulse.

One can also directly compute images of the localization of the density of the Dyson orbital in time. In the example shown below, a single pulse is used to excite the molecule and induce ionization. Therefore, a very large band of electronic states

Fig. 7 Density of the time-dependent Dyson orbital (Eq. (6)) in LiH excited by a strong (E = 0.05 a.u.) 1.5 fs UV pump pulse resonant ($\omega = 0.14$ a.u) with the two lowest excited states with a polarization along z (panel a) and x (panel b). A sphere of radius of 10 Å represents the distance at which the electron can be considered ionized and all the density of the Dyson localized outside this sphere will ionize



of the neutral LiH molecule is necessary to describe the electronic dynamics. In this example, the electronic states are computed at the equation-of-motion coupled-cluster model with single and double substitutions (EOM-CCSD) level with an aug-cc-pVQZ basis set to which diffuse functions were added. The electron density in the band of excited electronic states just below the IP is localized so far from the nuclei of the molecule that it can be considered as ionized. The time-dependent Dyson orbital is shown in Fig. 7 for the LiH molecule excited by an ultrashort pulse polarized either perpendicularly or parallel to the bond axis. Due to selection rules, the pulse polarized along the bond axis can only excite Σ states, which generates a motion of the density of the Dyson orbital parallel to the bond. This motion remains rather regular, even for a strong excitation pulse with field strength of 0.05 a.u. On the other hand, an excitation pulse polarized perpendicular to the bond excites a superposition of Σ and Π states, which corresponds to a much more complex electronic motion. The radius of the sphere shown in Fig. 7 is such that one can consider that the electron density localized outside that sphere is ionized.

5 Conclusions

Dyson orbitals play an essential role in various processes that remove or add an electron to a molecule or an atom. We discussed three examples: the Dyson orbitals of the pentacene molecule that correspond to conduction by holes (analog to ionization) and by electrons (analog to electron attachment) in the differential conductance measured by low temperature STM. These Dyson orbitals represent the electronic density when the GS of the neutral molecule is ionized to different

excited states of the cation or of the anion. We then discussed how the properties of the Dyson orbitals of SAMO and non-SAMO states in C_{60} are vastly different, in terms of their localization either far (SAMO) or close to the C atoms of the cage, which leads to very fast ionization rates for SAMO states. Here, the Dyson orbitals correspond to the ionization of an excited state of the neutral to the GS of the cation. Dyson orbitals can also reflect the dynamics of a coherent superposition of states prepared by an ultrashort pulse and we illustrated this case on the LiH molecule.

Acknowledgments We thank C. Joachim and W. H. Soe for stimulating discussions on the pentacene molecule at the occasion of the ATMOL conference in Berlin. We gratefully acknowledge support from the Fonds de la Recherche Fondamentale Collective FRFC 2.4545.12 'Control of attosecond dynamics'. FR is a Director of Research and BM is a PhD fellow of Fonds National de la Recherche Scientifique (FNRS, Belgium). TK acknowledges FNRS for a post-doctoral fellowship (FRFC 2.4545.12).

References

- 1. Gross, L., Moll, N., Mohn, F., Curioni, A., Meyer, G., Hanke, F., Persson, M.: High-resolution molecular orbital imaging using a p-wave STM tip. Phys. Rev. Lett. **107**(8), 086101 (2011)
- Repp, J., Meyer, G., Stojković, S., Gourdon, A., Joachim, C.: Molecules on insulating films: Scanning-tunneling microscopy imaging of individual molecular orbitals. Phys. Rev. Lett. 94(2), 026803 (2005)
- Soe, W.H., Wong, H.S., Manzano, C., Grisolia, M., Hliwa, M., Feng, X.L., Mullen, K., Joachim, C.: Mapping the excited states of single hexa-peri-benzocoronene oligomers. ACS Nano 6(4), 3230–3235 (2012)
- Soe, W.H., Manzano, C., De Sarkar, A., Chandrasekhar, N., Joachim, C.: Direct observation of molecular orbitals of pentacene physisorbed on Au(111) by scanning tunneling microscope. Phys. Rev. Lett. 102(17), 176102 (2009)
- Puschnig, P., Berkebile, S., Fleming, A.J., Koller, G., Emtsev, K., Seyller, T., Riley, J.D., Ambrosch-Draxl, C., Netzer, F.P., Ramsey, M.G.: Reconstruction of molecular orbital densities from photoemission data. Science 326(5953), 702–706 (2009)
- Akagi, H., Otobe, T., Staudte, A., Shiner, A., Turner, F., Dorner, R., Villeneuve, D.M., Corkum, P.B.: Laser tunnel ionization from multiple orbitals in HCl. Science 325(5946), 1364–1367 (2009)
- Itatani, J., Levesque, J., Zeidler, D., Niikura, H., Pepin, H., Kieffer, J.C., Corkum, P.B., Villeneuve, D.M.: Tomographic imaging of molecular orbitals. Nature 432(7019), 867–871 (2004)
- 8. Smirnova, O., Mairesse, Y., Patchkovskii, S., Dudovich, N., Villeneuve, D., Corkum, P., Ivanov, M.Y.: High harmonic interferometry of multi-electron dynamics in molecules. Nature **460**(7258), 972–977 (2009)
- Haessler, S., Caillat, J., Boutu, W., Giovanetti-Teixeira, C., Ruchon, T., Auguste, T., Diveki, Z., Breger, P., Maquet, A., Carre, B., Taieb, R., Salieres, P.: Attosecond imaging of molecular electronic wave packets. Nat. Phys. 6(3), 200–206 (2010)
- Salières, P., Maquet, A., Haessler, S., Caillat, J., Taïeb, R.: Imaging orbitals with attosecond and Ångström resolutions: toward attochemistry? Rep. Prog. Phys. 75(6), 062401 (2012)
- 11. McWeeny, R., Sutcliffe, B.T.: Methods of Molecular Quantum Mechanics, vol. 2. Academic Press, London (1969)

- 12. Deleuze, M., Pickup, B.T., Delhalle, J.: Plane wave and orthogonalized plane wave many-body Green's function calculations of photoionization intensities. Mol. Phys. **83**(4), 655–686 (1994)
- Ortiz, J.V.: Electron propagator theory: an approach to prediction and interpretation in quantum chemistry. Wiley Interdisciplinary Reviews: Computational Molecular Science, 3, 123 (2013)
- Oana, C.M., Krylov, A.I.: Dyson orbitals for ionization from the ground and electronically excited states within equation-of-motion coupled-cluster formalism: Theory, implementation, and examples. J. Chem. Phys. 127(23), 234106–234114 (2007)
- Patchkovskii, S., Smirnova, O., Spanner, M.: Attosecond control of electron correlations in one-photon ionization and recombination. J. Phys. B: At. Mol. Opt. Phys. 45(13), 131002 (2012)
- Johansson, J.O., Henderson, G.G., Remacle, F., Campbell, E.E.B.: Angular-resolved photoelectron spectroscopy of superatom orbitals of fullerenes. Phys. Rev. Lett. 108(17), 173401 (2012)
- 17. Mignolet, B., Johansson, J.O., Campbell, E.E.B., Remacle, F.: Probing rapidly ionizing super-atom molecular orbitals in C60: A computational and fs photoelectron spectroscopy study. Under revision (2013)
- 18. Remacle, F., Levine, R.D.: Attosecond pumping of nonstationary electronic states of LiH: Charge shake-up and electron density distortion. Phys. Rev. A 83(1), 013411 (2011)
- Remacle, F., Nest, M., Levine, R.D.: Laser steered ultrafast quantum dynamics of electrons in LiH. Phys. Rev. Lett. 99, 183902–183904 (2007)
- Mignolet, B., Levine, R.D., Remacle, F.: Localized electron dynamics in attosecond-pulseexcited molecular systems: Probing the time-dependent electron density by sudden photoionization. Phys. Rev. A 86(5), 053429 (2012)
- 21. Frisch, M.J., Trucks, G.W., Schlegel, H.B., Scuseria, G.E., Robb, M.A., Cheeseman, J.R., Scalmani, G., Barone, V., Mennucci, B., Petersson, G.A., Nakatsuji, H., Caricato, M., X. Li, H.P.H., Izmaylov, A.F., Bloino, J., Zheng, G., Sonnenberg, J.L., Hada, M., Ehara, M., Toyota, K., Fukuda, R., Hasegawa, J., Ishida, M., Nakajima, T., Honda, Y., Kitao, O., Nakai, H., Vreven, T., Montgomery, J.A., Jr., J.E.P., Ogliaro, F., Bearpark, M., Heyd, J.J., Brothers, E., Kudin, K.N., Staroverov, V.N., Kobayashi, R., Normand, J., Raghavachari, K., Rendell, A., Burant, J.C., Iyengar, S.S., Tomasi, J., Cossi, M., Rega, N., Millam, J.M., Klene, M., Knox, J.E., Cross, J.B., Bakken, V., Adamo, C., J. Jaramillo, R. Gomperts, R. E. Stratmann, O. Yazyev, A. J. Austin, R. Cammi, C. Pomelli, J. W. Ochterski, R. L. Martin, K. Morokuma, V. G. Zakrzewski, G. A. Voth, P. Salvador, J. J. Dannenberg, S. Dapprich, A. D. Daniels, Ö. Farkas, J., B. Foresman, J. V. Ortiz, J. Cioslowski, Fox., D.J.: Gaussian 09 Revision A.1. (2009)
- 22. Aiga, F.: Theoretical study on oligoacenes and polycyclic aromatic hydrocarbons using the restricted active space self-consistent field method. J. Phys. Chem. A 116(1), 663–669 (2012)
- 23. Schmidt, W.: Photoelectron spectra of polynuclear aromatics. V. Correlations with ultraviolet absorption spectra in the catacondensed series. J. Chem. Phys. **66**(2), 828 (1977)
- Crocker, L., Wang, T., Kebarle, P.: Electron affinities of some polycyclic aromatic hydrocarbons, obtained from electron-transfer equilibria. J. Am. Chem. Soc. 115(17), 7818–7822 (1993)
- Dauth, M., Körzdörfer, T., Kümmel, S., Ziroff, J., Wiessner, M., Schöll, A., Reinert, F., Arita, M., Shimada, K.: Orbital density reconstruction for molecules. Phys. Rev. Lett. 107(19), 193002 (2011)
- 26. Feng, M., Zhao, J., Huang, T., Zhu, X., Petek, H.: The electronic properties of superatom states of hollow molecules. Acc. Chem. Res. **44**(5), 360–368 (2011)
- 27. Feng, M., Zhao, J., Petek, H.: Atom like, hollow-core–bound molecular orbitals of C60. Science 320(5874), 359–362 (2008)
- Dougherty, D.B., Jin, W., Reutt-Robey, J.E., Robey, S.W.: Superatom orbitals of C60 on Ag(111): Two-photon photoemission and scanning tunneling spectroscopy. Phys. Rev. B 84(19), 195435 (2011)

- 29. Corkum, P.B., Krausz, F.: Attosecond science. Nat. Phys. **3**(6), 381–387 (2007)
- Kling, M.F., Vrakking, M.J.J.: Attosecond electron dynamics. Ann. Rev. Phys. Chem. 59, 463–492 (2008)
- 31. Krausz, F., Ivanov, M.: Attosecond physics. Rev. Mod. Phys. 81(1), 163-234 (2009)
- 32. Huismans, Y., Rouzée, A., Gijsbertsen, A., Jungmann, J.H., Smolkowska, A.S., Logman, P.S.W.M., Lépine, F., Cauchy, C., Zamith, S., Marchenko, T., Bakker, J.M., Berden, G., Redlich, B., van der Meer, A.F.G., Muller, H.G., Vermin, W., Schafer, K.J., Spanner, M., Ivanov, M.Y., Smirnova, O., Bauer, D., Popruzhenko, S.V., Vrakking, M.J.J.: Time-resolved holography with photoelectrons. Science 331(6013), 61–64 (2011)
- 33. Gallmann, L., Cirelli, C., Keller, U.: Attosecond science: Recent highlights and future trends. Annu. Rev. Phys. Chem. **63**(1), 447–469 (2012)
- 34. Zhou, X., Ranitovic, P., Hogle, C.W., Eland, J.H.D., Kapteyn, H.C., Murnane, M.M.: Probing and controlling non-born-oppenheimer dynamics in highly excited molecular ions. Nat. Phys. **8**(3), 232–237 (2012)
- 35. Remacle, F., Levine, R.D.: An electronic time scale for chemistry. Proc. Natl. Acad. Sci. USA 103, 6793–6798 (2006)
- 36. Remacle, F., Kienberger, R., Krausz, F., Levine, R.D.: On the feasibility of an ultrafast purely electronic reorganization in lithium hydride. Chem. Phys. **338**, 342–347 (2007)
- 37. Mignolet, B., Gijsbertsen, A., Vrakking, M.J.J., Levine, R.D., Remacle, F.: Stereocontrol of attosecond time-scale electron dynamics in ABCU using ultrafast laser pulses: a computational study. PCCP 13(18), 8331–8344 (2011)

Part IV LT-UHV-STM

Mapping the Electronic Resonances of Single Molecule STM Tunnel Junctions

We-Hyo Soe, Carlos Manzano and Christian Joachim

Abstract In this chapter is presented how the electron probability distributions of molecular states are imaged in real space using scanning tunneling microscopy. Differential tunneling conductance images of selected single molecules taken at voltages corresponding to resonances near the substrate Fermi level were found to be very close to their respective mono-electronic molecular orbitals. In contrast, high-order resonance states images were composed of molecular orbitals components from many states, even though those states lie in a lower energy range.

1 Introduction

Low-temperature scanning tunneling microscope (STM) differential conductance (dI/dV) spectroscopy is a very effective technique to gain access to the low-lying electronic states of a molecule weakly coupled to a surface within an STM tunnel junction. By accessing those states, the electron probability distribution of the ground and first excited states of a pentacene molecule had been imaged in real space [1]. For that purpose, pentacene was electronically decoupled from the metal substrate by an ultrathin insulating layer. The corresponding STM images are found to be very close to pentacene's mono-electronic HOMO (the highest occupied molecular orbital) and LUMO (the lowest unoccupied molecular orbital) maps [1]. To have access to more states and therefore to more molecular orbital (MO) maps, a metal surface where the molecule is physisorbed on the surface of

W.-H. Soe (⋈) · C. Manzano · C. Joachim

IMRE, A*STAR (Agency for Science, Technology and Research), 3 Research Link,

Singapore 117602, Singapore

e-mail: wh-soe@imre.a-star.edu.sg

C. Joachim

CEMES/CNRS, Pico Lab, 29 Rue Marvig BP 94347, Toulouse Cedex 31055, France

58 W.-H. Soe et al.

the STM tunnel junction can be used to reduce the energy gap between STM junction tunneling resonances and also to get more molecular electronic states inside the STM bias voltage range without destroying the molecule.

In this chapter, we first show that aside from the two frontier MOs (HOMO and LUMO), the second (HOMO-1) and third (HOMO-2) occupied MOs of a pentacene molecule lying directly on an Au(111) surface can be imaged [2]. The way to disentangle those MO components from the contribution of higher resonance molecular electronic states will be discussed.

Second, the case of the Cu-phthalocyanine molecule characterized by a double-degenerated LUMO will be presented. An MOs basis set decomposition of the electronic cloud of this molecule does not correspond to the one provided by the STM dI/dV conductance mapping: During scanning, the tip apex-molecular cloud electronic interactions capture the MO components of the molecular electronic states located in the dI/dV energy range as a mixture of different phases and weight contributions [3].

Finally, the hexabenzocoronene molecule and its dimer prepared by an onsurface synthesis on Au(111) were imaged. An extensive theoretical investigation of the tunneling spectra and the dI/dV maps of these molecules demonstrate that a given STM dI/dV electronic resonance results from a complex contribution to the local conductance of many molecular states. This makes difficult to reconstruct an apparent molecular orbital electron probability density map in a straightforward manner using the standard quantum superposition of Slater determinants constructed with those mono-electronic molecular orbitals [4].

2 Pentacene/Au(111)

In the experiments reported here, not only pentacene but also Cu-phthalocyanine and hexabenzocoronene molecules were sublimed on a cleaned Au(111) single crystal substrate at room temperature, after molecule sublimation the samples were cooled down to cryogenic temperatures and transferred to the STM chamber. Most molecules adsorb on the Au(111) reconstructed terraces and at step edges, however, only pentacene molecules physisorbed at herringbone kinks are used for recording spectroscopic data and dI/dV maps, since this is a favorable adsorption site and the molecule is unlikely to move while scanning.

Figure 1a shows a typical dI/dV spectrum detected on a pentacene molecule. Distinct from the Au(111) surface state, it presents several conductance resonances at -900, -1,900, and -2,700 mV and an additional broad peak at +1,300 mV. The constant-current STM dI/dV map of a single pentacene molecule taken at -900 mV as shown in Fig. 1b is almost identical to the free pentacene electron probability distribution of HOMO. Similarly, the maps recorded at -1,900 and +1,300 mV are confirmed as the mono-electronic HOMO-1 and LUMO states of the free pentacene molecule, respectively. Identifying the MO captured in the -2,500 mV dI/dV map is, however, not as straightforward.

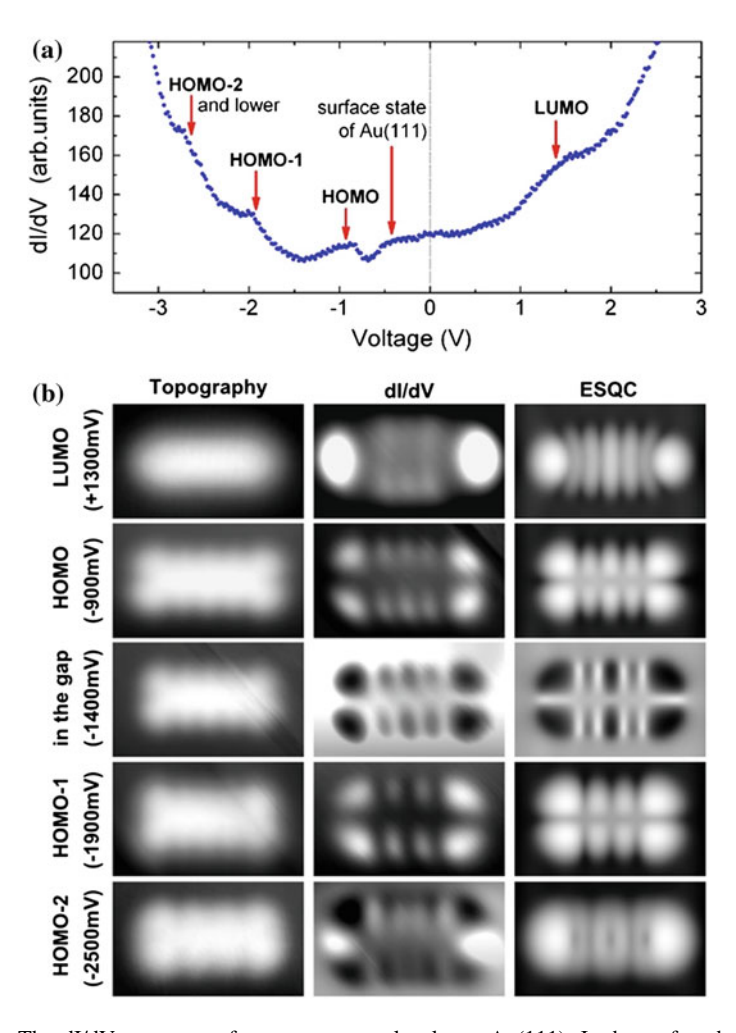


Fig. 1 a The dI/dV spectrum of a pentacene molecule on Au(111). It shows four broad and distinct peaks corresponding to pentacene LUMO in the positive bias side, and its HOMO, HOMO-1, and HOMO-2 in the negative side. The surface state of Au(111) is also observable. **b** The left and center columns are experimental topographic and dI/dV images recorded at voltages indicated by the arrows in (a). The right column displays the corresponding calculated STM images (see the next section for details about STM image calculation), at the monoelectronic states corresponding to the LUMO, HOMO, HOMO-1, and HOMO-2, respectively. The experimentally observed and theoretically calculated images in the gap between the HOMO and HOMO-1 are inserted in between them. All images are 2.5 × 1.5 nm

A consequence of our imaging technique is that the differential conductance remains sensitive to the spatial variation of the inter-electrode electronic coupling across the molecule even at voltages away from a resonance. For instance, a dI/dV image recorded at a higher energy overcoming the -900 mV HOMO resonance is

60 W.-H. Soe et al.

essentially an inverted contrast image of the HOMO map as shown in Fig. 1b. This indicates that for higher lying energies the effective inter-electrode couplings through pentacene remain sensitive to the mono-electronic contributions of its lower energy states. The effects of lower mono-electronic states contributions are more evident in the -2,500 mV dI/dV map which is a very complex intermix made of the HOMO-2, HOMO, and HOMO-1 mono-electronic states and which appear as the superposition of low and high differential conductance features rendering the shape of pentacene. A deconstruction of the experimental dI/dV map recorded at -2,500 mV is proposed in Fig. 2. Each of the HOMO-2, HOMO-1, and HOMO contributions was inverted and weighted as necessary. That deconstruction shows that the HOMO-2 molecular orbital is captured and present in the dI/dV map but overshadowed by the two other lower energy MOs.

Pentacene MO energy levels around frontier MOs are well separated from each other and its states are not degenerate despite being a highly symmetric molecule. In the next section, we will take a close look at what can be observed from a molecule having doubly degenerate MOs.

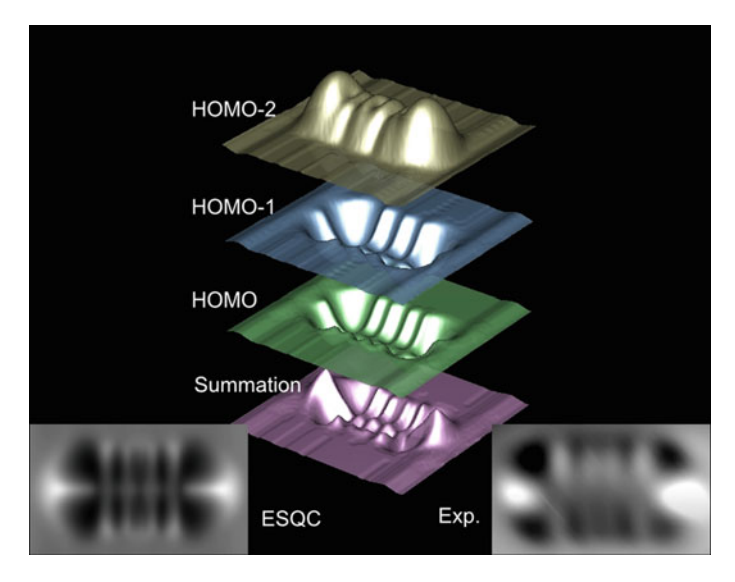


Fig. 2 A three-dimensional representation showing the contribution of resonant and nonresonant states explaining the dI/dV map recorded at -2,500 mV. The three topmost plots were extracted from the theoretical results shown in the right column of Fig. 1b. The plot at the bottom corresponding to the weighted sum of the HOMO-2, HOMO-1, and HOMO shown above. Here resonant state (HOMO-2 in this case) is positive, and nonresonant states (HOMO and HOMO-1) are negative. The image at the bottom-left corner shows the top view of the integrated plot, and the bottom-right image is the corresponding experimental dI/dV map

3 Cu-Phthalocyanine/Au(111)

Figure 3a presents a characteristic experimental dI/dV spectrum obtained on a phenyl-terminal of single Cu-phthalocyanine (CuPc) molecule adsorbed on an Au(111) terrace. Apart from the Au(111) surface state resonance, the main features in this spectrum include a sharp peak at -680 mV and a comparatively broad but higher amplitude peak at +1,300 mV. To obtain more information on the identity of those resonances, their spatial electronic distribution was mapped using the constant current dI/dV mapping technique as shown in Figs. 3b, c.

A usual practice for indexing the resonances in such tunneling spectrum is to calculate the possible electronic probability density maps of the CuPc ground and also of some of its first excited states, and to compare these density maps to the experimental one. CuPc molecular orbitals were calculated using density functional theory (DFT) and the B3LYP functional method, the corresponding MOs iso-surfaces are shown in Figs. 3d-f [5, 6].

The -680 mV resonance can be tentatively assigned as the CuPc ground state since the external crowns of the experimental Fig. 3b and the calculated DFT HOMO Fig. 3d agree reasonably well, even though the lateral expansion of the eight lobes of the crown is not well reproduced by the iso-surface map. A perfect match between a dI/dV map and an iso-density map is not expected here, because the electrons' tunneling processes between the tip and the surface through the CuPc molecule are not included in the DFT molecular orbital calculation. We utilized the mono-electronic elastic scattering quantum chemistry (ESQC) theory [7, 8] at the semi-empirical level to calculate a T(E) mono-electronic transmission spectrum through the junction taking into account the bulk band structure of both the Au substrate and the STM tip. In the ESQC approach, the tunneling junction is considered as a scattering defect made of the Au(111) surface, the adsorbed molecule, and the complete tip apex atomic structure.

The ESQC image calculated at the HOMO energy level conforms well with the 16 maxima of the DFT iso-surface calculated for a CuPc with planar conformation, despite the molecule being strongly chemisorbed on the metal substrate and the constituting atomic orbital components of the HOMO being broadened. To better approach the experimental dI/dV map, the tunnel junction was re-equilibrated electronically by slightly distorting each CuPc wing. In this case, when the tip apex is positioned on a wing end, the T(E) resonance is higher in intensity as compared to the central part of the CuPc molecule, and the eight external lobes of the HOMO are imaged with higher contrast compared to the central part as shown in Fig. 3g.

At the +1,300 mV resonance, the experimental dI/dV and the theoretical DFT iso-surface maps do not show a good match. However, the experimental dI/dV map could be constructed by superposing in real space CuPc's LUMO and LUMO+1 since these two mono-electronic states are actually degenerated. To confirm that the +1,300 mV dI/dV is capturing these degenerated states and can accordingly be composed of their superposition, highly resolved ESQC T(E) spectra were calculated

62 W.-H. Soe et al.

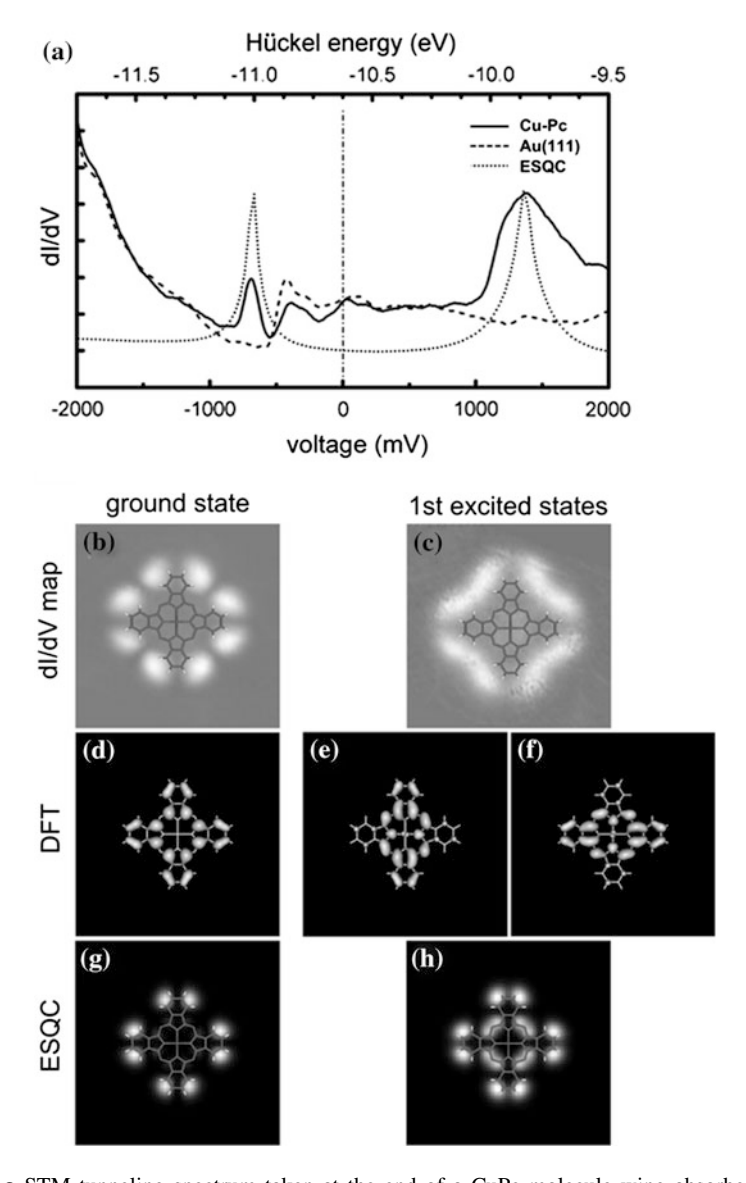
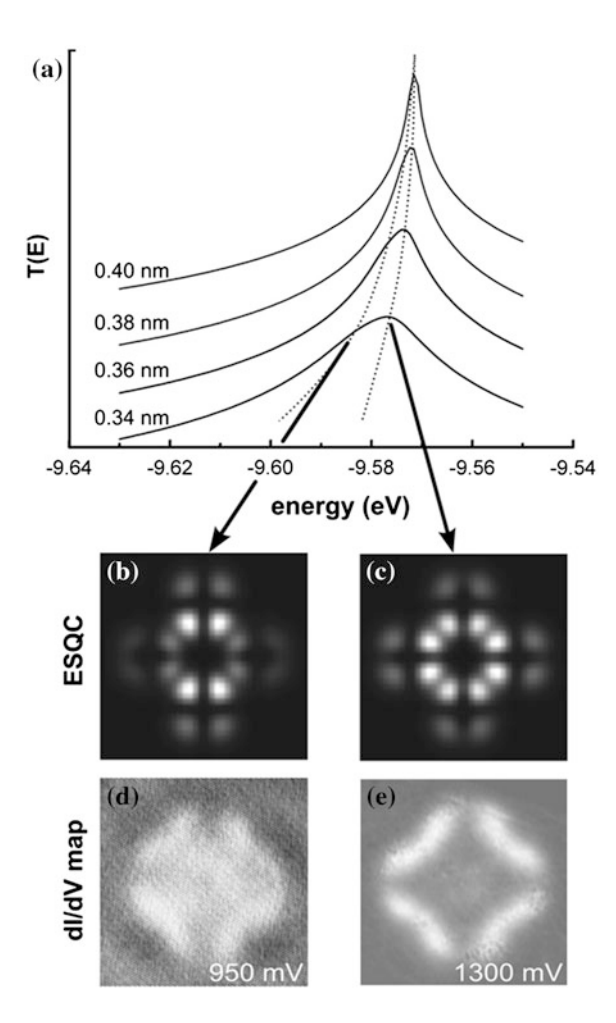


Fig. 3 a STM tunneling spectrum taken at the end of a CuPc molecule wing absorbed on an Au(111) surface, together with the theoretical ESQC T(E) electronic transmission spectrum calculated using the corresponding tunnel junction. Two obvious resonance peaks were observed: A sharp one at negative bias and another at positive bias with broader width and higher intensity. **b–c** The dI/dV maps differential conductance maps scanned at the resonating voltages are given with wire framed molecule models, which show how the experimentally observed electron clouds expand in real space. **d–f** DFT mono-electronic molecular orbitals are computed for a D4h symmetry CuPc. HOMO (**d**) corresponds to the ground state with C4 symmetry, and degenerate LUMO (**e**) and LUMO+1 (**f**) have equivalent C2 symmetries. Calculated ESQC T(E) conductance maps for a slightly deformed molecule having C4v symmetry are also shown in **g–h**, that correspond to the mono-electronic energy levels of HOMO, and degenerate LUMO and LUMO+1, respectively. All image sizes are 3.0×3.0 nm

to cover the energy range of the LUMO states as a function of the molecule—substrate separation. As shown in Fig. 4a, the intensity of the LUMO resonance peak appearing in this energy range decreases and its width broadens by increasing the CuPc-Au(111) surface electronic interaction. The spectra also show that by bringing the molecule closer to the substrate the peak position shifts to lower energies. Moreover, the degenerate LUMO resonance splits into two peaks, a shoulder-like peak emerges at the left side of the main resonance.

CuPc images were calculated at both peaks energy values as presented in Fig. 4b, c. The image calculated at the main peak's energy shows a CuPc rendered by high differential conductance lobes having C4 symmetry features. This image also reproduces well the C4 symmetry arch-like lobes of the experimental 1,300 mV dI/dV map. The image calculated at the shoulder-like peak CuPc shows C2 symmetry. For comparison to this image, an experimental dI/dV map was taken

Fig. 4 a Molecule-surface distance dependence of the LUMO peak. Highly resolved ESQC T(E) resonance splits into two peaks, hence resolving the degeneracy of the LUMO and LUMO+1 due to the different interaction weights of each molecular orbital and the substrate. **b**-**c** T(E) maps calculated for the main and shoulder-like peak positions. These T(E) maps show the symmetry change from C4 (c) to C2 (b) and conform with the transformation shown in the experimental dI/ dV maps in d-e



64 W.-H. Soe et al.

off the 1,300 mV resonance at 950 mV. This CuPc dI/dV map shown in Fig. 4d presents exactly the same C2 symmetry features of the image calculated at the shoulder-like peak in Fig. 4b.

The calculated spectra and images demonstrate that the first excited states of a CuPc molecule adsorbed on Au(111) are composed of at least two MO components, i.e., the degenerate LUMO and LUMO+1, but the ration of the two orbitals contribution in the electron transfer process is not known.

To get a better understanding of the molecular states in the tunnel junction, we will move into a more complex system in the next section.

4 Hexabenzocoronene/Au(111)

Hexabenzocoronene (HBC) is known as a super-benzene molecule [9] where the ground and first excited states are easily decomposed on Slater determinants built up using π orbitals. To see its electron probability distribution, the dI/dV STM imaging of HBC monomer was treated as described previously in this chapter. As presented in Fig. 5, the spatial variation of the electronic transparency of the molecular junction was mapped at two resonances energies, -1,260 and +2,200 mV, which appear in the spectrum taken at the periphery of an HBC molecule. According to the Hohenberg-Kohn theorem, the ground state of an N-electron system can be described by a one-electron density functional [10]. Therefore, a good way to describe the -1,260 mV resonance map is to build up this functional starting from the HOMO component of the mono-electronic HBC ground state. On the other hand, the +2,200 mV resonance originates mainly from two mono-electronic states (corresponding to HBC's degenerate LUMO and LUMO+1) contained in 6 low-lying excited states. To understand the implications of it, the HBC dimer was investigated.

Figure 6a shows the spectra taken at the periphery and the center, betweentwo HBC partners, of an HBC dimer. The former spectrum has only one resonance at +2,250 mV, in contrast, the later captures two pronounced resonances at +2,050 and +2,850 mV. Using the configuration interaction analysis and considering one valence electron excitation [11], 12 excited states have been identified in the +2,250 mV energy range contributing to the molecular junction conductance. They belong to the first six LUMOs of HBC dimer issued from the hybridization of the first three LUMOs of each HBC fragment. To optimize the analysis of the experimental images presented in Fig. 6b, c, each of these six corresponding ESQC STM images was calculated and superposed as shown in Fig. 6e, f. The calculated images have the same features present in the experimental dI/dV maps confirming that the +2,050 and +2,250 mV resonances originate from the electronic interactions between the tip apex and those 12 states. The experimental dI/dV maps arise from the conductance tunnel paths through the molecular states selectively captured by the tip at each energy and position. Similarly, the identified

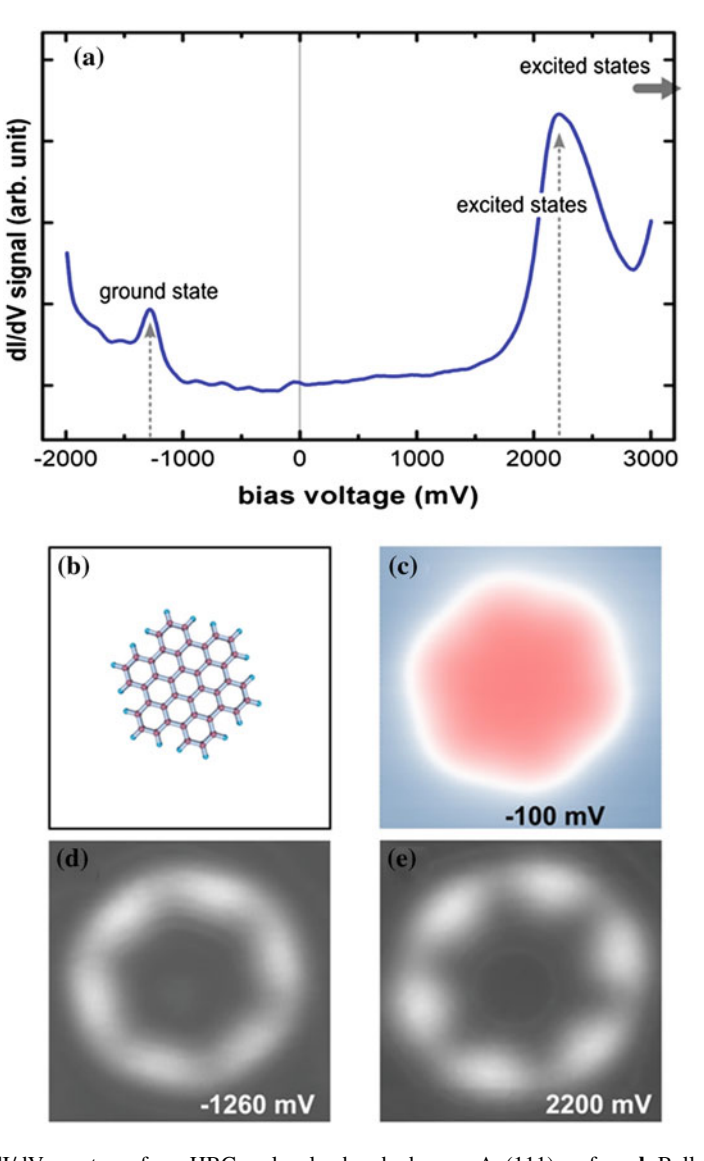


Fig. 5 a dI/dV spectrum for a HBC molecule absorbed on an Au(111) surface. **b** Ball-and-stick model of HBC molecule. **c** Experimental STM topographic image of a single HBC at a nonresonant energy, and \mathbf{d} — \mathbf{e} its dI/dV differential conductance maps taken at the resonant state energies at both polarities. All image sizes are 2.5×2.5 nm

+2,850 mV resonance (Fig. 6d) is composed of at least 6 excited states built up with a large contribution from the LUMO+6 component (Fig. 6g).

Following nomenclature practices commonly used to identify the resonances detected in tunneling electron spectroscopy, the +2,050 mV (and/or +2,250 mV) resonance is the first excited state of HBC dimer and can be identified as its

66 W.-H. Soe et al.

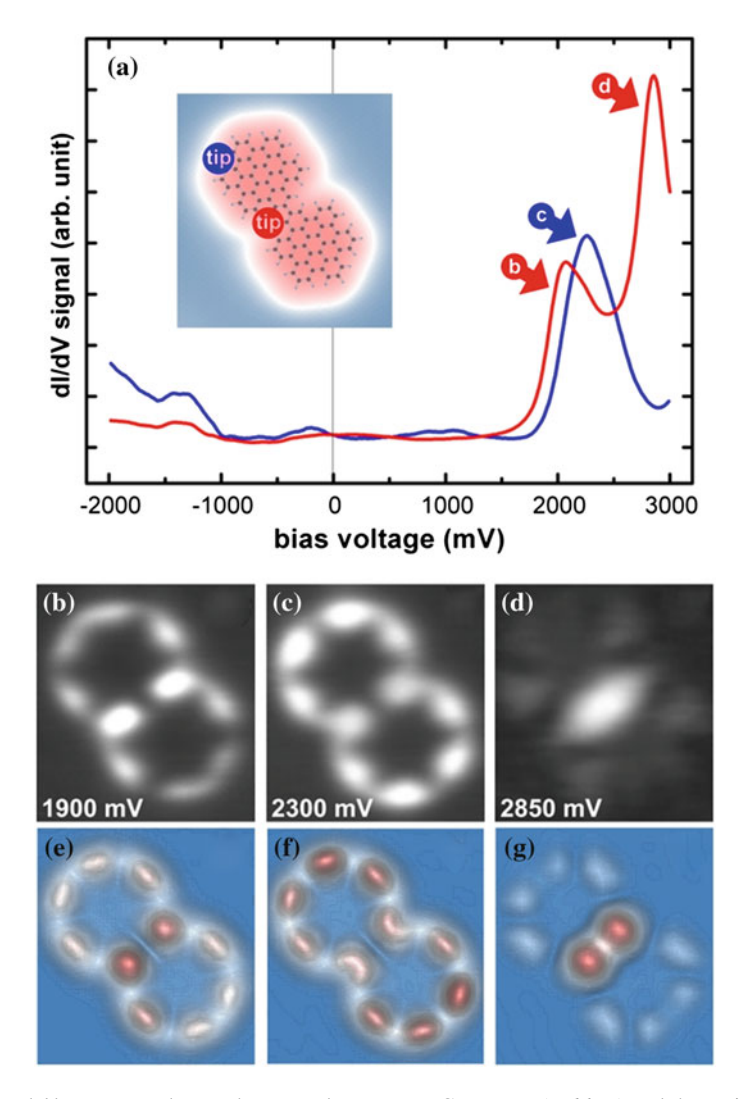


Fig. 6 a dI/dV spectra taken at the center between HBC partners (*red line*) and the periphery of the dimer (*blue line*). Inset shows the topographic image of a HBC dimer and a superimposed ball-and-stick molecular model, the exact tip locations where each spectrum was measured are shown by the corresponding colored dots. **b-d** Experimental dI/dV maps taken at the peak positions labeled in the spectrum, and **e-g** their corresponding optimized ESQC images. All image sizes are 3.2 × 3.2 nm

LUMO, because the MO weight on all of the 12 states captured by this resonance is almost entirely made of the LUMO component. On the contrary, the +2,850 mV resonance cannot be called LUMO+1. As it was shown in the superposition made to calculate the +2,850 mV dI/dV map in Fig. 6g, it is more appropriate to name it the second excited states consisting entirely of LUMO+6.

5 Conclusion

Herein, we have demonstrated that resonances captured in STM dI/dV spectra taken from single molecules can be attributed to specific superposition of molecular states created by the STM measurement itself. These electronic resonances are not simply a linear combination of mono-electronic molecular orbitals, but the result of a mixture of the multi-configuration molecular electronic states and their electronic coupling to the tunnel junction electrodes. Our investigation findings ask for the development of a complete many-body scattering theory of the electrons tunneling through the STM molecule junction.

Acknowledgments This work was supported by A*STAR (the Agency for Science, Technology and Research) funding under project no 1021100072.

References

- Repp, J., Meyer, G., Stojkovie, S.M., Gourdon, A., Joachim, C.: Molecules on insulating films: STM images of individual molecular orbitals. Phys. Rev. Lett. 94, 026803 (2005)
- Soe, W.-H., Manzano, C., De Sarkar, A., Chandrasekhar, N., Joachim, C.: Direct observation
 of molecular orbitals of pentacene physisorbed on Au(111) by scanning tunneling
 microscope. Phys. Rev. Lett. 102, 176102 (2009)
- Soe W.-H., Manzano C., Wong H. S., Joachim C.: Mapping the first electronic resonances of a Cu-phthalocyanine STM tunnel junction. J. Phys.: Condes. Matter 24, 354011 (2012)
- Soe, W.-H., Wong, H.S., Manzano, C., Grisolia, M., Hliwa, M., Feng, X., Mullen, K., Joachim, C.: Mapping the excited states of single hexa-peri-benzocoronene oligomers. ACS Nano 6, 3230 (2012)
- 5. Granovsky A. A.: Fierfly version 7.1.5 http://classic.chem.msu.su/gran/firefly/index.html
- Scmidt, M.W., Baldridge, K.K., Boatz, J.A., Elbert, S.T., Gordon, M.S., Jensen, J.H., Koseki, S., Matsunaga, N., Nguyen, K.A., Su, S., Windus, T.L., Dupuis, M., Montgomery, J.A.: General atomic and molecular electronic structure system. J. Comput. Chem. 14, 1347 (1993)
- 7. Sautet, P., Joachim, C.: Calculation of benzene of rhodium STM images. Chem. Phys. Lett. **185**, 23 (1991)
- 8. Sautet, P., Joachim, C.: Electronic transmission coefficient for the single-impurity problem in the scattering-matrix approach. Phys. Rev. **B38**, 12238 (1988)
- Watson, M.D., Fechtenkotter, A., Mullen, K.: Big is beautiful: "Aromaticity" revisited from the viewpoint of macromolecular and supramolecular benzene chemistry. Chem. Rev. 101, 1267 (2001)
- 10. Hohenberg, P., Kohn, W.: Inhomogeneous electron gas. Phys. Rev. 136, B864 (1964)
- 11. Stewart, J.J.P.: Optimization of parameters for semi-empirical methods V: modification of NNDO approximations and applications to 70 elements. J. Mol. Model. 13, 1173 (2007)

Manipulation and Spectroscopy of Individual Phthalocyanine Molecules on InAs(111)A with a Low-Temperature Scanning Tunneling Microscope

Christophe Nacci, Kiyoshi Kanisawa and Stefan Fölsch

Abstract Single free-base phthalocyanine (H₂Pc), copper phthalocyanine (CuPc), and naphthalocyanine (NPc) molecules on the III-V semiconductor surface InAs(111)A- (2×2) were investigated by cryogenic scanning tunneling microscopy (STM) at 5 K. STM imaging of largely unperturbed frontier orbitals of NPc on InAs(111)A reveals that the molecule is physisorbed. In the adsorbed state, the molecular electronic structure of NPc is preserved to a large extent, indicating a weak electronic coupling to the underlying substrate surface. As a free molecule, H₂Pc is bistable because of an internal hydrogen transfer reaction (tautomerization). When adsorbed on the InAs(111)A surface, H₂Pc experiences rotational fluctuations about its center because of excitations induced by inelastic electron tunneling (IET). STM-based atom and molecule manipulation techniques were used to sterically hinder the molecular rotation by assembling In adatom-molecule complexes, facilitating to probe the hydrogen transfer reaction in a controlled way. STM imaging of the In_{ad}-H₂Pc-In_{ad} complex clearly reveals the presence of a lefthanded and a right-handed conformer, indicating that the H₂Pc tautomerization is left unperturbed by the substrate and the pinning adatoms, and that it can be triggered by the tunneling electrons.

Paul-Drude-Institut für Festkörperelektronik, Hausvogteiplatz 5-7 10117 Berlin, Germany

NTT Basic Research Laboratories, NTT Corporation, Atsugi, Kanagawa 243-0198, Japan

C. Nacci (⋈)

Fritz-Haber-Institut der Max-Planck-Gesellschaft, Abteilung für Physikalische Chemie, Faradayweg 4-6 14195 Berlin, Germany

e-mail: nacci@FHI-berlin.mpg.de

C. Nacci · S. Fölsch

K. Kanisawa

L. Grill and C. Joachim (eds.), *Imaging and Manipulating Molecular Orbitals*, Advances in Atom and Single Molecule Machines, DOI: 10.1007/978-3-642-38809-5_6, © Springer-Verlag Berlin Heidelberg 2013

1 Introduction

The idea to use single organic molecules as functional device components was put forward by Aviram and Ratner [1] as early as 1974 and has triggered immense research effort since then [2–4]. Specifically, it is of interest as to how molecular function can be utilized in an environment compatible with semiconductor materials [5]. In this context, the interaction of an adsorbed molecule with the supporting semiconductor template is a crucial ingredient; it can be vary between strong covalent bonding [5, 6], or even fragmentation [7], in the presence of partially filled surface dangling bonds (such as on bare Si surfaces) and weak coupling on surfaces with fully saturated dangling bonds. In the following, we concentrate on the latter case and employ the experimental technique of cryogenic scanning tunneling microscopy (STM) to investigate how individual switchable molecules can be pinned into place on a semiconductor platform in a manner that leaves their intrinsic switching characteristics undisturbed.

The model system described in this chapter features single surface-supported phthalocyanine (Pc) and naphthalocyanine (NPc) molecules as functional building blocks. STM studies have revealed various intriguing phenomena in Pc molecules adsorbed at metal surfaces and insulating spacer layers, e.g., tautomerization switching [8] and reversible conformational changes [9], as well as the control of the magnetic state of single molecules [10–12]. Here, we study Pc molecules adsorbed on the chemically inert III-V semiconductor surface InAs(111)A and explore their electronic structure by scanning tunneling spectroscopy (STS) and constant-current STM imaging confirming a weak electronic molecule-surface coupling. Furthermore, we analyze rotational fluctuations of the in-plane molecular orientation excited by inelastic electron tunneling (IET). Finally, the technique of atom and molecule manipulation [13] is applied to assemble molecule-adatom complexes in which the IET-induced molecular rotation is suppressed, allowing us to trigger a reversible hydrogen tautomerization reaction and probe the energetics of this molecule-inherent switching function.

2 Results and Discussion

2.1 Experimental Details

The measurements presented in this chapter were performed in an ultra-high vacuum (UHV) STM operated at a temperature of 5 K. A layer 20 nm thick of undoped InAs was grown on an InAs(111)A substrate by molecular beam epitaxy (MBE) [14]. After the MBE growth of the substrate, the surface was capped with an amorphous layer of arsenic and transferred under ambient conditions to the UHV STM system. The As capping layer was removed in UHV by annealing at 630 K, prior to transferring the sample into the microscope cooled to 5 K.

InAs(111)A surfaces prepared in this way show the same features as MBE-grown and in situ investigated samples [15, 16]. The adsorbates free-base phthalocyanine (H_2Pc), copper phthalocyanine (CuPc), and naphthalocyanine (NPc) were purified in crystalline form in UHV by repeated cycles of degassing. Submonolayer coverages ($\sim 1 \times 10^{12}$ molecules per cm²) of molecules were deposited directly into the microscope at sample temperatures below 20 K by sublimation from a tantalum crucible heated to 628 K (H_2Pc and CuPc), and 681 K (NPc), respectively. STS was performed by lock-in technique (10 mV peak-to-peak modulation amplitude at a modulation frequency of 670 Hz). STM images were recorded in constant-current mode with the bias voltage referring to the sample with respect to the STM tip.

2.2 The Substrate Surface: InAs(111)A

The geometric structure of the In-terminated InAs(111)A substrate surface is schematically shown in Fig. 1a. The surface is characterized by a (2×2) Invacancy reconstruction with a rhombic unit cell and a nearest-neighbor In vacancy spacing of $a' = a_0\sqrt{2} = 8.57$ Å $(a_0 = 6.06$ Å, cubic InAs lattice constant). High-resolution STM imaging of the reconstructed InAs surface (Fig. 1b) shows the In surface atoms as protrusions and the In vacancies as depressions [15]. The MBE-grown surface exhibits randomly distributed native In adatoms (In_{ad}), located on top of the In-vacancy sites as shown in Fig. 1c. The In surface vacancy is the only

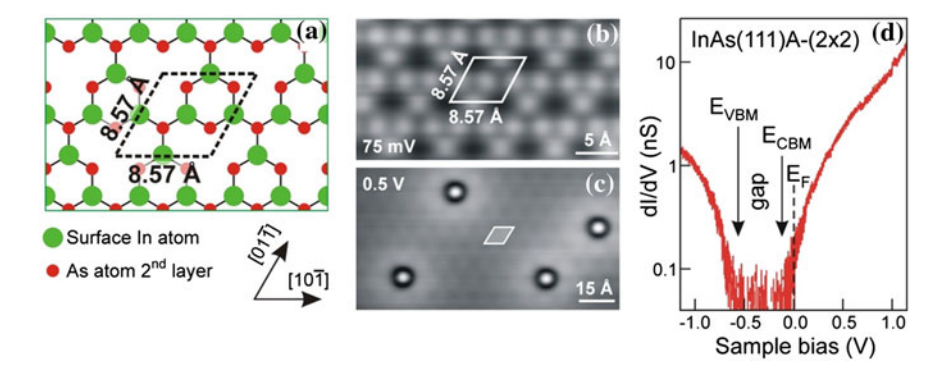


Fig. 1 a Stick-and-ball model of the first two atomic layers of the InAs(111)A surface; the rhombic unit cell is indicated. Constant-current STM images of InAs(111)A (b) at atomic resolution (48 Å \times 24 Å, 3 nA, 75 mV) showing the (2 \times 2) In-vacancy reconstruction with In atoms as protrusions and In vacancies as depressions; and (c) at larger scale (110 Å \times 60 Å, 50 pA, 0.5 V) showing randomly distributed native In adatoms all located at In-vacancy sites. d dI/dV spectrum taken over the surface indicating a band gap of 0.42 eV and the Fermi level pinned in the conduction band; the dI/dV signal is plotted on a logarithmic scale to clearly display the valence and conduction band edges. Ref. [20]

72 C. Nacci et al.

stable adsorption site of In_{ad} atoms, as observed by STM and corroborated by ab initio calculations [17]. The In adatom on InAs(111)A acts as a donor supplying one electron to the conduction band of the substrate and leading to the formation of an electron accumulation layer at the surface [16, 18]. In the empty-state STM image in Fig. 1c, the positive charge state is evident from the bright halo extended around the adatom, which is due to the local downward band bending induced by the donor [19]. Figure 1d shows a differential tunneling conductance (dI/dV) spectrum of the bare surface indicating a band gap of 0.42 eV [20, 21] and a Fermi level pinning $\simeq 0.2$ eV above the conduction band minimum, reflecting the presence of the surface-accumulated electrons [22].

2.3 Naphthalocyanine Molecules on InAs(111)A

The (2×2) -reconstructed InAs(111)A surface is characterized by the presence of completely saturated surface dangling bonds with the In (As) dangling bond states being fully empty (occupied). As a consequence, InAs(111)A is chemically inert. We will see that this property preserves the electronic structure of adsorbed molecules to a large extent and thereby opens up the prospect to explore molecule-inherent functionalities that remain essentially undisturbed in the adsorbed state.

As an example of weak electronic molecule–substrate coupling, we discuss the case of naphthalocyanine (NPc) adsorbed on InAs(111)A. NPc is a planar π -conjugated molecule with D_{2h} symmetry, as illustrated by the structure model in Fig. 2a. In the free molecular state, NPc can undergo a tautomerization reaction in which the two hydrogen atoms in the inner cavity switch from one *trans* conformation to the other, analogous to the cases of free-base phthalocyanine (H₂Pc) [23] and porphyrine [24]. For single NPc molecules adsorbed on thin NaCl insulating films, it was reported that the hydrogen tautomerization can be induced by IET [8]. Figure 2b shows an isolated NPc molecule adsorbed on top of a phase boundary line separating coherent domains of the (2 \times 2) surface reconstruction.

We find that NPc molecules adsorbed on phase boundary lines are more stable during STM imaging compared to those adsorbed on defect-free terraces. In the latter case, the scanning STM tip induces unintentional displacements of the molecule under typical imaging conditions (i.e., tunnel currents in the regime of 40-100 pA and bias voltages $V \in [1.5 \text{ V}, -1.5 \text{ V}]$).

Figure 2c shows a dI/dV spectrum taken on top of a NPc molecule, revealing sharp molecular resonances assigned to the highest occupied (HOMO) and lowest unoccupied (LUMO) molecular orbital states.

Constant-current STM imaging of the NPc molecule at -1.5 V (Fig. 2d) shows a 4-fold symmetric appearance that resembles the DFT-calculated HOMO density in the free molecular state [8]. On the other hand, when imaged at 0.4 V (Fig. 2g), NPc exhibits a 2-fold symmetry, and in this case resembles the DFT-calculated LUMO density derived for the free NPc [8]. When imaged at biases in the regime of the HOMO–LUMO gap (Fig. 2(e, f)), the molecule exhibits a cross-shaped

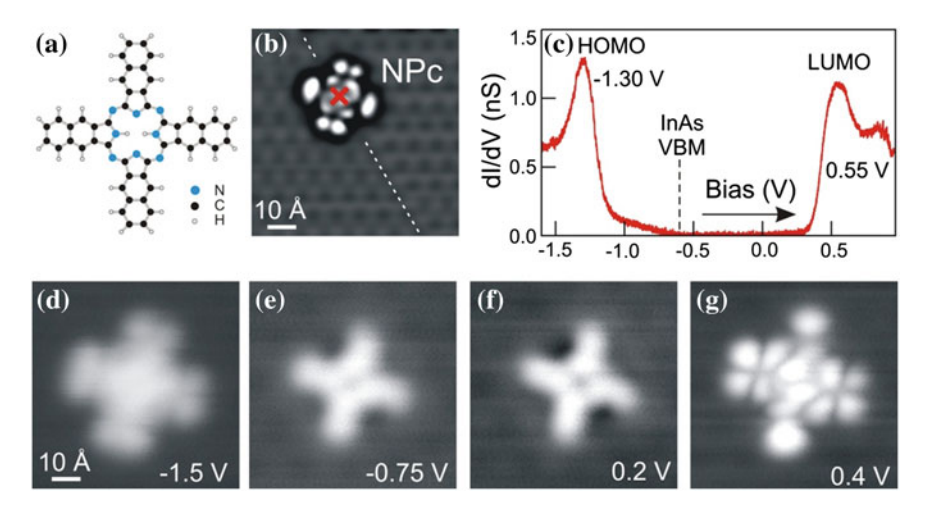


Fig. 2 a Structure model of naphthalocyanine (NPc). **b** STM image (96 Å \times 96 Å, 100 pA, 0.5 V) of a NPc molecule adsorbed on top of a phase boundary line (*dashed line*) and (**c**) dI/dV spectrum taken at disabled feedback loop with the STM tip placed on top of it at the position indicated in (**b**). **d**–**g** STM images of the NPc molecule (**d**) at the energetic positions of the HOMO, (**e**, **f**) at in-gap conditions, and (**g**) in the regime of the LUMO; all the images (**d**–**g**) acquired at 50 pA, 36 Å \times 36 Å. Ref [25]

appearance without internal structure, as previously observed for NPc adsorbed on thin insulating NaCl films [8]. These experimental findings indicate that the NPc molecule is in a physisorbed state on InAs(111)A and experiences only a weak perturbation of its molecular orbitals by the supporting substrate surface [25].

2.4 Free-Base Phthalocyanine Molecules on InAs(111)A

Free-base phthalocyanine (H₂Pc) is the smaller counterpart to NPc having only one benzene unit per molecular extremity, as shown in the structure model in Fig. 3a. When adsorbed on the InAs(111)A surface, the molecule is always centered at an In-vacancy site. STM imaging of the molecule at 0.5 V (Fig. 3b) reveals a uniform protrusion of 3-fold symmetry, suggesting that the molecule undergoes in-plane rotational jumps at a frequency beyond the temporal resolution of the STM imaging process. Three-fold appearance persists at 0.25 V (Fig. 3c). At a further reduced sample bias of 0.175 V, discrete rotational jumps of the molecule about its center can be identified in STM imaging as shown in Fig. 3d.

¹ An upper bound of the tunnel current detection rate is set by the bandwidth of the preamplifier corresponding to 550 Hz. In the constant-current imaging mode, a further reduction may arise from the actual feedback loop setting.

74 C. Nacci et al.

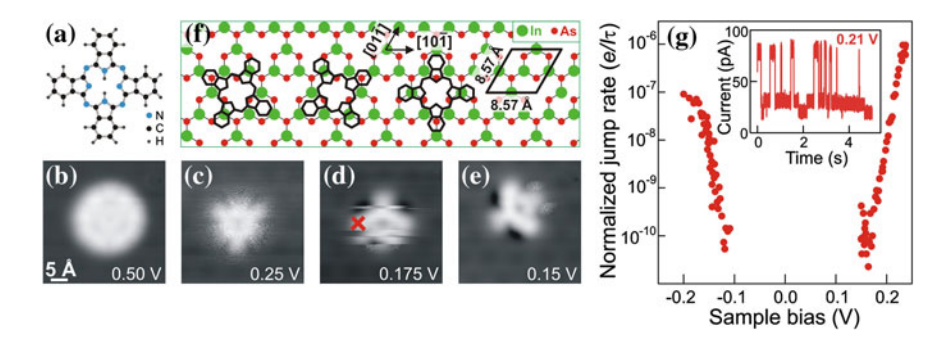


Fig. 3 a Structure model of free-base phthalocyanine (H₂Pc). **b–e** STM images (36 Å × 36 Å) of H₂Pc on InAs(111)A at different bias voltages. At 0.50 V (**b**) and 0.25 V (**c**) the molecule is imaged as a protrusion with 3-fold symmetry due to rapid rotational jumps excited by the tunneling electrons; discrete molecular rotational jumps are discernible at 0.175 V (**d**), while the molecule becomes stable at 0.15 V (**e**). STM images acquired at 25 pA (**b–d**), and 50 pA (**e**). **f** Structure model showing the adsorption geometry of H₂Pc on InAs(111)A with three equivalent rotational orientations. **g** Bias-dependent normalized jump rate $e/I\tau$ (e: electron charge, I: tunnel current, τ : residence time in a given orientation) determined from the time-dependent tunnel current signal (inset) probed at a fixed bias and disabled feedback loop, the tip position is indicated in (**d**). Time spectroscopy set point parameters: 0.175 V, 50 pA. Ref. [14]

Finally, the molecule is stable at a bias of 0.15 V as shown in the STM image in Fig. 3e, revealing the expected cross-shaped appearance.

We find three equivalent adsorption configurations of H_2Pc on InAs(111)A with the molecular extremities parallel/perpendicular to any of the three $\langle 110 \rangle$ in-plane directions as indicated in Fig. 3f. The process of molecular rotation can be probed by time spectroscopy of the tunneling current. In this mode of measurement, the current signal is acquired by keeping the STM tip fixed above the molecule in an off-center position and at disabled feedback loop. In agreement with the three molecular orientations identified by STM imaging, the time-dependent tunnel current signal shows fluctuations among three discrete current levels as indicated in the inset of Fig. 3g.

The STM images in Fig. 3b—e already indicated that the rotational fluctuation of the molecule sensitively depends on the applied sample bias. Figure 3g shows the bias-dependent normalized jump rate, $e/I\tau$ (e: electron charge, I: tunnel current, τ : mean residence time in a given state), which is the probability to induce a molecular in-plane rotational jump per tunneling electron. The data show that the molecular rotation is activated at threshold voltages of about ± 100 mV [14], nearly symmetrical with respect to the Fermi level at V = 0 V.

The observation of a bipolar and nearly symmetrical threshold behavior suggests that the molecular rotation is excited by IET, as reported previously for the current-induced lateral hopping of metal adatoms on metal surfaces [26]. Rotations excited by IET processes were previously reported for molecules adsorbed on metal surfaces [27–30]. To summarize, when the molecule is imaged at bias voltages significantly larger than the activation thresholds, frequent in-plane

rotational jumps are excited, and because of the low temporal resolution of STM, the imaging process averages over all the possible molecular orientations leading to a 3-fold symmetric protrusion (cf. Fig. 3b, c). On the other hand, for bias voltages close to the activation thresholds, the reduced rotational jump rate makes it possible to discern the different molecular orientations with respect to the InAs substrate surface.

We used STM-based atom and molecule manipulation techniques [13] to (1) suppress the rotational fluctuations of the H_2Pc molecule and (2) excite and probe its tautomerization switching in a controlled way. This is illustrated by the STM images in Fig. 4a, b: first, two In_{ad} were positioned at two next nearest-neighbor In-vacancy sites (2a' = 17.14 Å separation) by vertical atom manipulation [20, 31] in the vicinity of an H_2Pc molecule (cf. Fig. 4b). Next, the molecule was repositioned via lateral manipulation and dragged in between the two In_{ad} atoms, see Fig. 4c.

Here, lateral manipulation is enabled by short-range attractive tip-molecule interactions, so that it is possible to move the molecule along the surface by the STM tip. This behavior is similar to our previous findings for the lateral manipulation of SnPc molecules on InAs(111)A [32]. The possibility to perform lateral manipulation is a further consequence of the weak molecule–substrate coupling present in this system.

When pinned between the two In_{ad} atoms, the incorporated H_2Pc molecule shows the expected stable cross-like shape due to the sterical hindrance of the molecular rotation, as evident from the STM image in Fig. 4c. Imaging the In_{ad} - H_2Pc - In_{ad} complex at different sample bias voltages reveals the existence of two conformers of chiral symmetry, as evident from the images in panels (d–g) in Fig. 4 compared to those in panels (h–k). This observation suggests that the two conformers of the H_2Pc tautomerization can be stabilized in the molecule-adatom complex and readily distinguished in constant-current STM images.

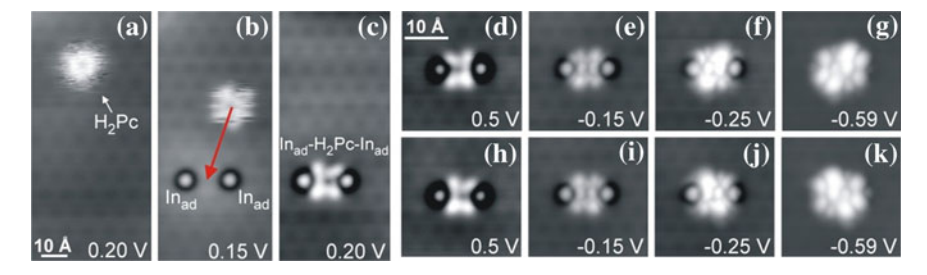


Fig. 4 a–c STM images (46 Å \times 96 Å, 75 pA) showing the stepwise assembly of an In_{ad} – H_2Pc – In_{ad} complex on InAs(111)A; **b** two native In adatoms were repositioned by vertical manipulation to occupy next nearest-neighbor In-vacancy sites in the vicinity of the H_2Pc molecule shown in (a). In (c) the molecule was moved in between the two In_{ad} via lateral manipulation. **d–k** STM imaging of the resulting complex (48 Å \times 48 Å, 50 pA); two rotationally nonequivalent chiral conformations are identified and depicted in panels (**d–g**) and (**h–k**), respectively. Ref [14]

76 C. Nacci et al.

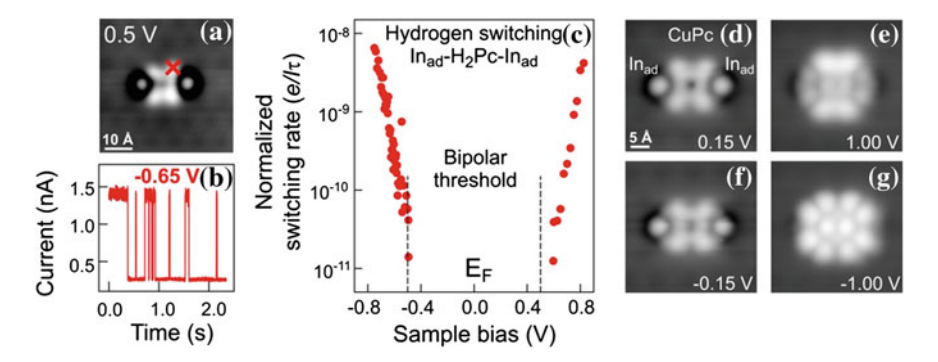


Fig. 5 a–c Hydrogen atom switching within the central cavity of an H_2Pc molecule pinned in between two In_{ad} [14]. b Time-dependent tunneling current signal revealing binary switching with the STM tip position fixed above the molecule as indicated in (a); set point parameters during time spectroscopy: 50 pA, 0.5 V. c Bias-dependent normalized switching rate $e/I\tau$ extracted from the binary tunnel current switching, indicating a nearly symmetrical threshold behavior. d–g STM images (35 Å × 35 Å, 100 pA) of an In_{ad} –CuPc– In_{ad} complex for comparison with the STM images in Fig. 4; consistent with the absence of a tautomerization bistability, the complex involving the CuPc molecule is characterized by only one conformation with twofold symmetry

The complex can be reversibly switched between its two conformers. This is achieved, for example, by placing the STM tip above the molecule, at the position indicated in Fig. 5a, and applying a bias of -0.65 V. The corresponding time-dependent tunnel current signal detected at disabled feedback loop reflects a binary switching between two well-defined current levels with an on/off ratio on the order of 10:1 (Fig. 5b). Also in this case, the bias dependence of the normalized switching rate² (Fig. 5c) suggests an activated switching process that is characterized by threshold energies nearly symmetrical with respect to the Fermi level, now detected at significantly higher bias values of around ± 500 mV [14].

To further verify our experimental observations, we have investigated complexes in which a single CuPc molecule is incorporated in between two In_{ad} atoms. In contrast to H_2Pc , CuPc has D_{4h} symmetry [33] without any tautomeric bistability. Analogous to H_2Pc on InAs(111)A, a CuPc molecule adsorbs on top of an In-vacancy site with the molecular extremities oriented parallel/perpendicular to the $\langle 110 \rangle$ in-plane direction. In addition, CuPc undergoes tunnel current-induced in-plane rotational jumps about its center, as also observed previously for SnPc molecules on InAs(111)A [32]. Thus, the rotational excitation is a generic feature of Pc molecules adsorbed on InAs(111)A. In contrast to the case of H_2Pc —and consistent with the properties of CuPc—time spectroscopy measurements on the In_{ad} —CuPc— In_{ad} complex do not show any indication of binary current switching, along with the presence of only one conformation showing 2-fold symmetry in

² Here, the normalized rate corresponds to the probability per tunneling electron to induce a discrete tautomerization switching event.

STM images, see Fig. 5d–g. Due to this behavior, we interpret the bistability of the In_{ad} – H_2Pc – In_{ad} complex as a consequence of the tautomerization switching of the central molecule.

Final evidence for the presence of tautomerization switching in an adatom-pinned H_2Pc molecule comes from density functional theory (DFT) calculations [14]. The calculations verify: (1) the STM appearance of the complex depending on the tautomerization state of the central molecule and (2) show that the potential energy surface of tautomerization switching is essentially the same as that of the free molecular state [23]. Specifically, the calculated activation barrier along the reaction pathway between the two equivalent *trans* conformations is 0.58 eV [14], in close agreement with the measured thresholds for current-induced switching shown in Fig. 5c. This establishes that the inherent switching properties of the pinned H_2Pc molecule remain undisturbed both by the substrate and the pinning adatoms.

3 Conclusions

The results discussed in this chapter demonstrate that the chemically inert environment provided by the InAs(111)A substrate surface largely preserves the electronic structure of adsorbed molecules. This circumstance is crucial to transfer (unperturbed) molecular functionalities to semiconductor surfaces. Our experimental findings reveal that the STM-imaged frontier orbitals of NPc molecules on InAs(111)A resemble the DFT-derived HOMO and LUMO state densities of the free molecule, indicating that NPc is weakly coupled to the substrate, thus adopting a physisorbed state.

H₂Pc molecules adsorbed on the weakly binding InAs(111)A surface experience molecular rotational jumps about their center, leading to a ternary tunnel current signal detected with the STM tip kept at an off-center position and at constant height. The bias dependence of the normalized jump rate suggests that the in-plane molecular rotation is excited by inelastic electron tunneling. Similarly, current-induced molecular rotations were also observed for CuPc and SnPc molecules showing that this behavior is a general feature of Pc molecules adsorbed on InAs(111)A.

Complexes consisting of a single H_2Pc (or CuPc) molecule and two native In_{ad} atoms were assembled by STM-based manipulation techniques to sterically hinder the molecular rotation. STM imaging of the In_{ad} - H_2Pc - In_{ad} complex reveals the existence of two chiral conformations, reflecting that the incorporated molecule maintains its intrinsic tautomerization bistability. Hence, low-energy excitations of the weakly bound H_2Pc molecule—here an in-plane rotation—can be suppressed and its switching function accessed in a controlled way. These results show that individual molecules with predictable, predefined functions can be stabilized and assembled on semiconductor templates with atomic-scale precision.

78 C. Nacci et al.

Acknowledgments We gratefully acknowledge financial support of this research by the Japanese Agency of Science and Technology, and the German Research Foundation (FO 362/1-3; SFB 658, TP A2).

References

- 1. Aviram, A., Ratner, M.A.: Molecular rectifiers. Chem. Phys. Lett. 29, 277–283 (1974)
- Joachim, C., Gimzewski, J.K., Aviram, A.: Electronics using hybrid-molecular and monomolecular devices. Nature 408, 541–548 (2000)
- Nitzan, A., Ratner, M.A.: Electron transport in molecular wire junctions. Science 303, 1384–1389 (2003)
- 4. Heath, J.R.: Molecular electronics. Annu. Rev. Mater. Res. 39, 1–23 (2009)
- Wolkow, R.A.: Controlled molecular adsorption on silicon: Laying a foundation for molecular electronics. Annu. Rev. Phys. Chem. 50, 413–441 (1999)
- Hamers, R.J., Coulter, S.K., Ellison, M.D., Hovis, S.J., Padowitz, D.F., Schwartz, M.P., Greenlief, C.M., Russel, J.N.: Cycloaddition chemistry of organic molecules with semiconductor surfaces. Acc. Chem. Res. 33, 617–624 (2000)
- Lin, R., Galili, M., Quaade, U.J., Brandbyge, M., Bjørnholm, T., Esposti, A.D., Biscarini, F., Stokbro, K.: Spontaneous dissociation of a conjugated molecule on the Si(100) surface. J. Chem. Phys. 117, 321–330 (2002)
- 8. Liljeroth, P., Repp, J., Meyer, G.: Current-induced hydrogen tautomerization and switching of naphthalocyanine molecules. Science **317**, 1203–1206 (2007)
- 9. Wang Y., Kroeger J., Berndt R., Hofer W.A.: Pushing and pulling a Sn Ion through an adsorbed phthalocyanine molecule. J. Am. Chem. Soc. 131, 3639–3643 (2008)
- Stróżecka, A., Soriano, M., Pascual, J.I., Palacios, J.J.: Reversible change of the spin state in a manganese phthalocyanine by coordination of CO molecule. Phys. Rev. Lett. 109, 147202–147206 (2012)
- 11. Tsukahara, N., Shiraki, S., Itou, S., Ohta, N., Takagi, N., Kawai, M.: Evolution of Kondo resonance from a single impurity molecule to the two-dimensional lattice. Phys. Rev. Lett. **106**, 187201–187205 (2011)
- Brede, J., Atodiresei, N., Kuck, S., Lazić, P., Caciuc, V., Morikawa, Y., Hoffmann, G., Blügel, S., Wiesendanger, R.: Spin- and energy-dependent tunneling through a single molecule with intramolecular spatial resolution. Phys. Rev. Lett. 105, 047204–047207 (2010)
- 13. Stroscio, J.A., Eigler, D.M.: Atomic and molecular manipulation with the scanning tunneling microscope. Science **254**, 1319–1326 (1991)
- Nacci, C., Erwin, S.C., Kanisawa, K., Fölsch, S.: Controlled switching within an organic molecule deliberately pinned to a semiconductor surface. ACS Nano 6(5), 4190–4195 (2012)
- Taguchi, A., Kanisawa, K.: Stable reconstruction and adsorbates of InAs(111)A surface. Appl. Surf. Sci. 252, 5263–5266 (2006)
- Kanisawa, K., Butcher, M.J., Yamaguchi, H., Hirayama, Y.: Imaging of Friedel oscillation patterns of two-dimensionally accumulated electrons at epitaxially grown InAs(111)A surfaces. Phys. Rev. Lett. 86, 3384–3387 (2001)
- 17. Ishimure, N., Akiyama, T., Nakamura, K., Ito, T.: Ab initio-based approach to the reconstruction on InAs(111)A wetting layer grown on GaAs substrate. Physica E **42**, 2731–2734 (2010)
- Kanisawa K., Fujisawa T.: Mechanism of electron accumulation layer formation at the MBEgrown InAs(111)A surface. Hyomen Kagaku 29, 747–757 (2008)
- 19. Stroscio, J.A., Feenstra, R.M., Newns, D.M.: Voltage-dependent scanning tunneling microscopy imaging of semiconductor surfaces. J. Vac. Sci. Technol. A 6, 499–507 (1988)
- Fölsch S., Yang J., Nacci C., Kanisawa K.: Atom-by-atom quantum state control in adatom chains on a semiconductor. Phys. Rev. Lett. 103, 096104–096107 (2009)

- 21. Niimi Y., Kanisawa K., Kojima H., Kambara H., Hirayama Y., Tarucha S., Fukuyama H.: STM/STS measurements of two-dimensional electronics states in magnetic fields at epitaxially grown InAs(111)A surfaces. J. Phys.: Conf. Ser. 61, 874–878 (2007)
- Olsson, L.Ö., Anderrson, C.B.M., Håkansson, M.C., Kanski, J., Ilver, L., Karlsson, U.O.: Charge accumulation at InAs surfaces. Phys. Rev. Lett. 76, 3626–3629 (1996)
- 23. Cortina H., Senent M.L., Smeyers Y.G.: Ab initio comparative study of the structure and properties of H₂-porphyn and H₂-phthalocyanine. The electronic absorption spectra. J. Phys. Chem. **107**, 8968–8974 (2003)
- 24. Völker, S., van der Waals, J.H.: Laser-induced photochemical isomerization of free base porphyrin in an n-octane crystal at 4.2 K. Mol. Phys. **32**, 1703–1718 (1976)
- Münnich G., Albrecht F., Nacci C., Utz M., Schuh D., Kanisawa K., Fölsch S., Repp J.: Probing individual weakly-coupled π-conjugated molecules on semiconductor surfaces. J. Appl. Phys. 112, 034312–034315 (2012)
- 26. Stroscio, J.A., Celotta, R.J.: Controlling the dynamics of a single atom in lateral atom manipulation. Science **306**, 242–247 (2004)
- 27. Stipe B.C., Rezaei M.A., Ho W.: Inducing and viewing the rotational motion of a single molecule. Science **279**, 1907–1909 (1998)
- 28. Matsumoto, C., Kim, Y., Okawa, T., Sainoo, Y., Kawai, M.: Low-temperature STM investigation of acetylene on Pd(111). Surf. Sci. 587, 19–24 (2005)
- Wang W., Shi X., Jin M., Minot C., Van Hove M.A., Collin J.-P., Lin N.: Electron stimulation of internal torsion of a surface-mounted molecular rotor. ACS Nano 4, 4929–4935 (2010)
- Tierney, H.L., Murphy, C.J., Jewell, A.D., Baber, A.E., Iski, E.V., Khodaverdian, H.Y., McGuire, A.F., Klebanov, N., Sykes, E.C.H.: Experimental demonstration of a single-molecule electric motor. Nat. Nanotechnol. 6, 625–629 (2011)
- Yang J., Nacci C., Martínez-Blanco J., Kanisawa K., Fölsch S.: Vertical manipulation of native adatoms on the InAs(111)A surface. J. Phys.: Condens. Matter 24, 354008–354013 (2012)
- 32. Nacci C., Kanisawa K., Fölsch S.: Reversible switching of single tin phthalocyanine molecules on the InAs(111)A. J. Phys.: Condens. Matter **24**, 394004–394008 (2012)
- 33. Day, P.N., Wang, Z., Pachter, R.: Calculation of the structure and absorption spectra of phthalocyanine in the gas phase and in solution. THEOCHEM **455**, 33–50 (1998)

Electronic Structure and Properties of Graphen Nanoribbons: Zigzag and Armchair Edges

Matthias Koch, Francisco Ample, Christian Joachim and Leonhard Grill

Abstract Scanning tunneling microscopy is a very suitable instrument for the local probing and spectroscopic characterization of individual molecules, in our case narrow graphene nanoribbons. The electronic properties of a graphene nanoribbon can be controlled by its edge structure and width. Bottom-up approaches like on-surface synthesis allow the formation of extended conjugated electronic systems. Moreover, they lead to atomically defined edges which are important as structural defects have been predicted to modify the electronic structure. We have used low temperature scanning tunneling microscopy to investigate the formation, adsorption properties, and electronic structure of single graphene nanoribbons. 10,10'-Dibromo-9,9'-bianthryl molecules were used as molecular building blocks to form graphene nanoribbons after linking of the monomers and subsequent cyclodehydrogenation. In addition to intact ribbons, the influence of various defects on the electronic states is also investigated.

1 Introduction

Graphene, a one-atom thick plane of graphite, fascinates scientists all over the world [1, 2]. Starting from exfoliation of graphene [3] by using a scotch tape many scientists investigated the artificial growth of graphene [4–6]. Meanwhile, 30 inch

M. Koch · L. Grill (⊠)

Department of Physical Chemistry, Fritz-Haber-Institute of the Max-Planck-Society, 14195 Berlin, Germany

e-mail: lgr@fhi-berlin.mpg.de

F. Ample · C. Joachim

Institute of Materials Research and Engineering (IMRE), Singapore, Singapore

C. Joachim

Nanosciences Group, CEMES-CNRS, Toulouse, France

L. Grill and C. Joachim (eds.), *Imaging and Manipulating Molecular Orbitals*, Advances in Atom and Single Molecule Machines, DOI: 10.1007/978-3-642-38809-5_7, © Springer-Verlag Berlin Heidelberg 2013

M. Koch et al.

large graphene sheets are produced onto flexible copper substrate by chemical vapor deposition [4]. One of the most discussed properties of graphene is the zero effective mass of the electrons [7]. Their speed of propagation is the Fermi-Dirac velocity, which is in the order of 10⁶ ms⁻¹ [7]. While graphene is semimetallic graphene nanoribbons (GNR), a narrow stripe of graphene, exhibit a gap between the highest occupied molecular orbital (HOMO) and the lowest unoccupied molecular orbital (LUMO) depending on the ribbon width [8, 9]. This semiconducting behavior holds for a GNR with a width less than 10 nm [9]. For the fabrication of room-temperature field effect transistors a band gap larger than 0.5 eV is needed, and therefore a ribbon width of less than 5 nm. Further tuning of the electronic properties of a GNR can be realized by controlling its edge structure [10]. Two different edge geometries exist for GNRs: armchair (Fig. 1a) and zigzag (Fig. 1b), and the corresponding GNRs are termed as armchair GNR and zigzag GNR. Theory predicts edge states for zigzag GNRs close to the Fermi level [11]. These states only exist along the zigzag edges. This shows the importance of the precise control of the edge structure during the fabrication of the GNRs.

Using scanning tunneling spectroscopy to map the native molecular orbitals semiconductors or insulating layers (thus NaCl) are used to decouple the molecule from the substrate [12–14]. The influence of the metal surface on the electronic states of a molecule is not only broadening but also the electronic states are perturbed from the case of the free molecule [14–16]. For example, the HOMO-LUMO gap of a pentacene molecule increases with the thickness of the NaCl layer on a Cu(111) substrate [14].

Additionally to the surface, the tip state has a large influence on the probed electronic structure. In general, the metallic character of the tip is confirmed before recording a dI/dV map, e.g., for Au(111) by measuring the surface state. Sometimes the tip is chemically modified on purpose. By picking up a molecule and attaching it to the tip apex the chemical nature of the tip can be tuned in a controlled way [12, 17]. For example, a pentacene molecule attached to the tip apex improves the resolution [14, 18]. By picking up a CO molecule tunneling occurs through the degenerated π_x and π_y orbitals of the CO molecule. This allows

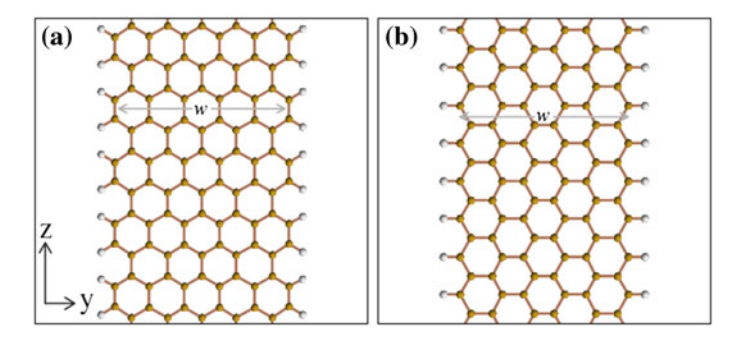


Fig. 1 a GNR with armchair edges. b GNR with zigzag edges. From Yang et al. [9]

to increase the p-wave contributions and, simultaneously, to improve the resolution in a controlled manner [12].

Recently constant-current dI/dV imaging of a pentacene on a bare Au(111) surface was investigated. In comparison to STM-elastic scattering quantum chemistry (ESQC) images, experimentally observed conductance maps were taken at different bias energies. At high bias voltage the molecular orbitals at lower energies contribute to the dI/dV maps [19]. A good agreement between experiment and theory could be reached if this is taken into account during the calculation of the ESQC images.

2 Experiment and Results

The fabrication of GNRs in top-down approaches has been reported many times in literature [20–23]. Narrow GNRs with a width below 5 nm could be produced starting from graphene by a combination of lithography and gas-phase etching chemistry [23]. A different approach opens a carbon nanotube by scanning tunneling microscope lithography [22]. The disadvantage of these techniques is the missing control over the edge structure. As mentioned above this is essential to control its electronic properties. For the investigation of the electronic structure of GNRs it is crucial to fabricate GNRs with smooth edges and a well-defined width. This is problematic for top-down approaches.

On-surface polymerization [24–26], a bottom-up approach, bases on the idea of equipping molecular building blocks with halogen atoms (see Fig. 2). During the activation step the halogen atoms are dissociated from the molecular building block while the remaining molecule stays intact. In the next step the activated molecules, with a free bond in place of the halogen atom, can undergo a covalent link with each other. The advantage of this method is that the precursor molecules define the final structure of the product. This leads, in case of GNRs, automatically to smooth edges and a well-defined width.

The growth of GNRs has been reported first in 2009 by Cai et al. [27]. They sublimated 10,10-dibromo-9,9-bianthryl precursor molecules on a 200 nm Au(111) film on a mica surface. The sample temperature during deposition was

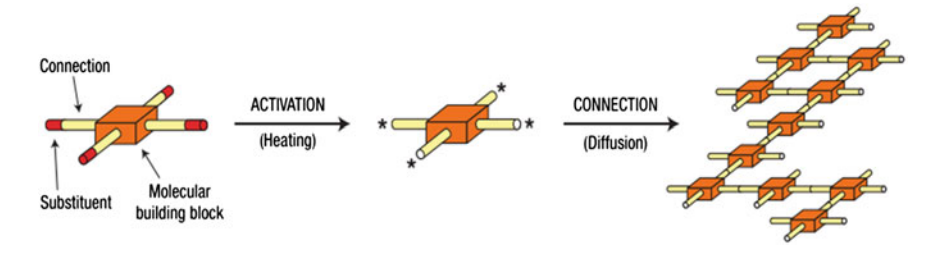


Fig. 2 Schematic model of the bottom-up approach on-surface polymerization. From Grill et al. [24]

84 M. Koch et al.

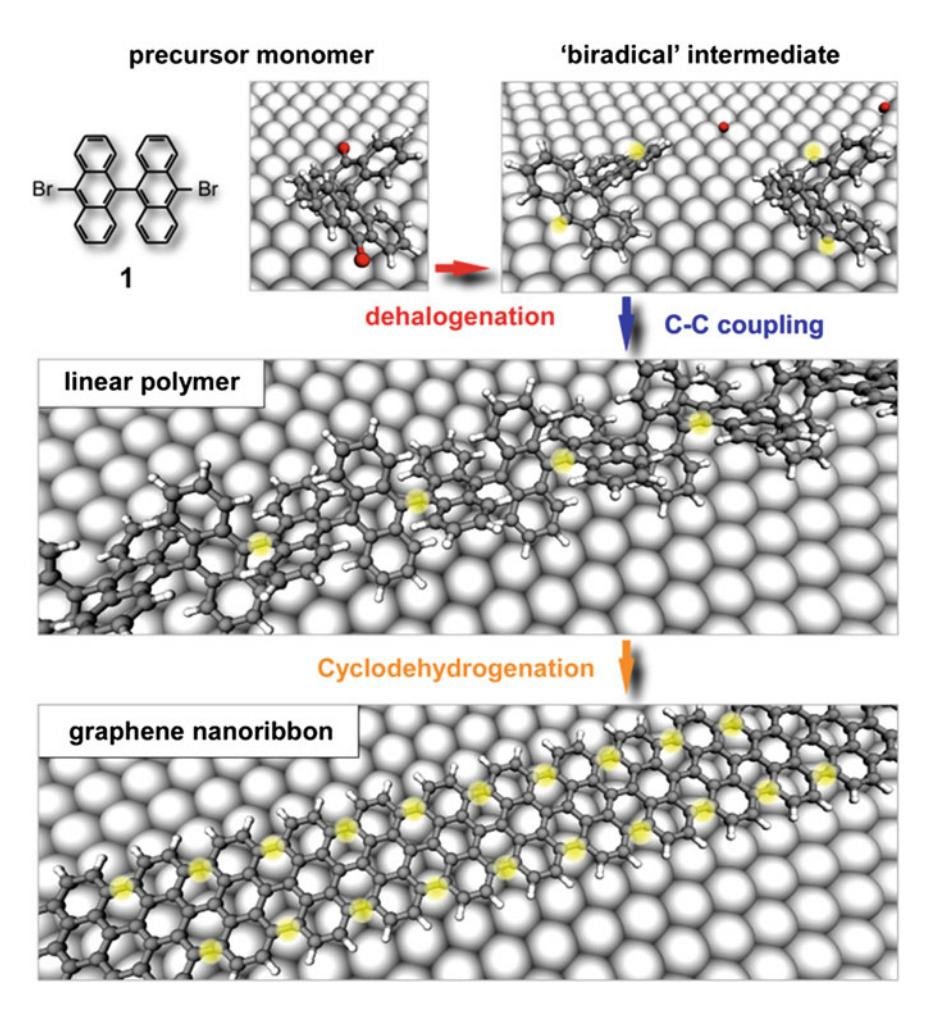


Fig. 3 Schematic model of the GNR fabrication. *1* Chemical structure of 10,10-dibromo-9,9-bianthryl. *Top* Dehalogenation of the precursor molecule. *Middle* Formation of an anthracene oligomer. *Bottom* Cyclodehydrogenation and fabrication of a flat GNR. From Cai et al. [27]

kept at 473 K. At this temperature the activation of the molecule takes place immediately and chains of anthracene are formed (as described in Fig. 3). During the second heating step to 673 K cyclodehydrogenation occurs and a GNR with armchair edges is formed (see Fig. 3). The width of a GNR is 0.74 nm [27].

To study the electronic structure of the GNRs we followed the recipe described above. The 10,10-dibromo-9,9-bianthryl molecules were purchased from the Ruiyuan Group. The Au(111) sample was cleaned by neon ion sputtering and subsequent annealing to 750 K. For deposition a Knudsen cell was used. The temperature of the cell for the period of deposition was ~ 470 K measured by a thermocouple. During the evaporation the sample temperature was kept

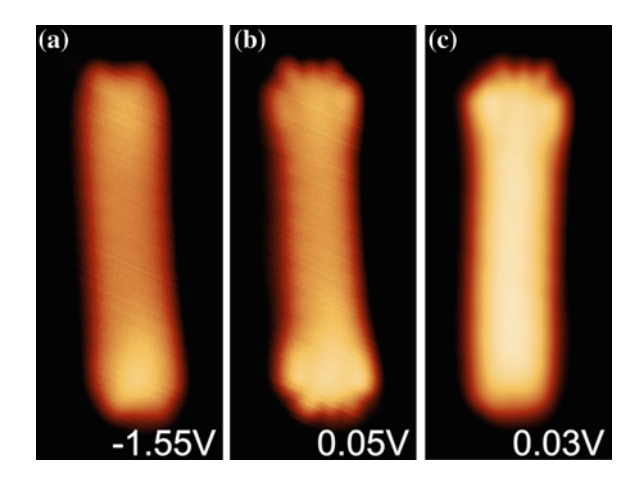
at \sim 470 K. In the following, the surface was annealed to 670 K and cyclodehydrogenation occurred.

All experiments were performed at low temperatures with a Createc scanning tunneling microscopy operating at 10 K. For dI/dV spectroscopy and mapping we used a Stanford Lock-In with a frequency of 610 Hz and an amplitude of 20 mV. The conductance maps were recorded in constant current mode and the bias voltage was applied to the sample. Before measuring a dI/dV curve or a conductance map, the quality of the tip was ensured by probing the position of the surface state at ~ -500 mV [28].

For the investigation of the electronic structure of a GNR we concentrate on single molecules which lay isolated on the surface. The appearance of a GNR depends a lot on the applied bias voltage. At high bias energies the shape of a GNR is rather smooth and without any noticeable structure (Fig. 4a). Taking images at bias voltages between -0.2 and +0.2 V, however, has a huge effect on the silhouette of the ribbon terminus [29]. This points to an electronic (and not a topographic) cause for the appearance. Only in a small bias windows the difference becomes visible. For some GNRs the ribbon end does no longer appear like a rectangular, instead it is fringed (Fig. 4b). But although 33 % of the ribbons show this feature 65 % of the GNRs stay structureless (bottom terminus in Fig. 4c). Additionally, 2 % of the molecules are attributed to a third species as they show a central lobe at the center of the ribbon end. These cases are summarized in Fig. 5.

The reason for the different appearances in STM images is the chemical structure of the ribbon termini (see Fig. 5). Comparing the experimental results with calculated STM images of chemically modified termini shows that most of the molecules on the surface are defected at the end. Only 33 % of the molecules are defect-free and have this feature which occurs in STM images with bias voltages between -0.2 V and +0.2 V (Fig. 5a, d, g). The bright lobe of the third species is probably due to a Bromine atom, which is still attached to the molecule (Fig. 5c, f, i). The most common species, without any feature at low bias voltage,

Fig. 4 a and **b** STM images of the same molecule at different bias energies. **c** STM image of a different species at a low bias voltage. All images are $3 \times 7 \text{ nm}^2$



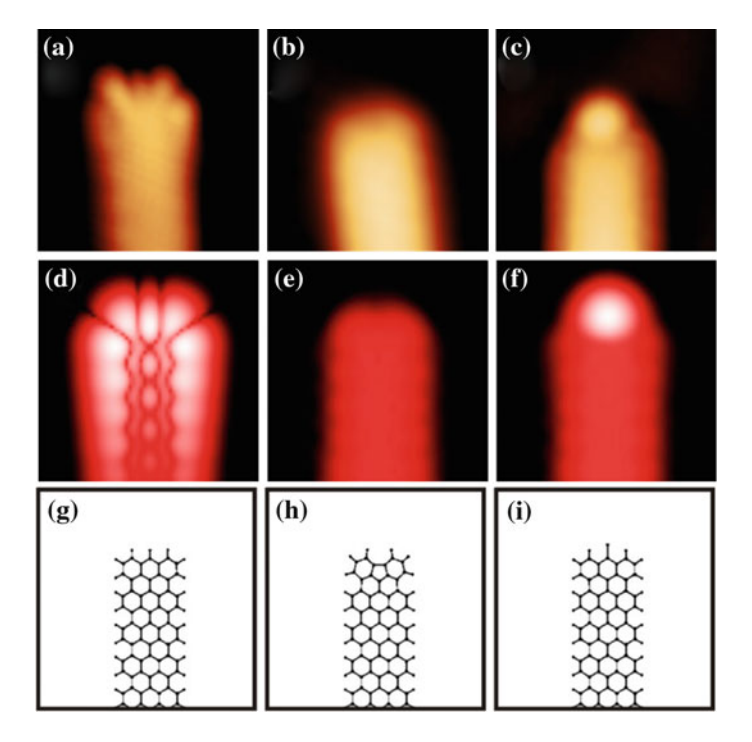


Fig. 5 Appearance of chemical different termini sketched in (**g-i**). *Left* Defect-free GNR (**a**, **d**, **g**). *Middle* GNR with a defect at the terminus (**b**, **e**, **h**). *Right* Not fully activated GNR with Br still connected (**c**, **f**, **i**). (**a–c**) Experimentally obtained STM images ($3 \times 3 \text{ nm}^2$). (**d–f**) ESQC calculated conductance maps ($3 \times 3 \text{ nm}^2$). From Koch et al. [29]

has a defect at the ribbon end (Fig. 5b, e, h). Instead of six carbon atoms, there are only five atoms in the calculation since the carbon atom with the activated bond is missing. This also stops the GNR from further growing as other building blocks can no longer covalently bind to this ribbon. This explains the localization of the defects at the GNR termini and the lack of defects in the inner parts.

3 dI/dV Spectroscopy

The reason for the different shape of the defect-free GNR at low bias voltages is an electronic state located slightly above the Fermi level [11]. This electronic state is resolved in dI/dV spectroscopy as shown in Fig. 6a. Spectra recorded at the ribbon termini exhibit a peak at about 30 mV. This state is localized at the ribbon termini and vanishes at the center of the GNR. For comparison, the defected GNR shows a peak located at the defect-free end while this state is quenched at the defected end (Fig. 6b). The only difference between the two GNRs is the chemical structure of

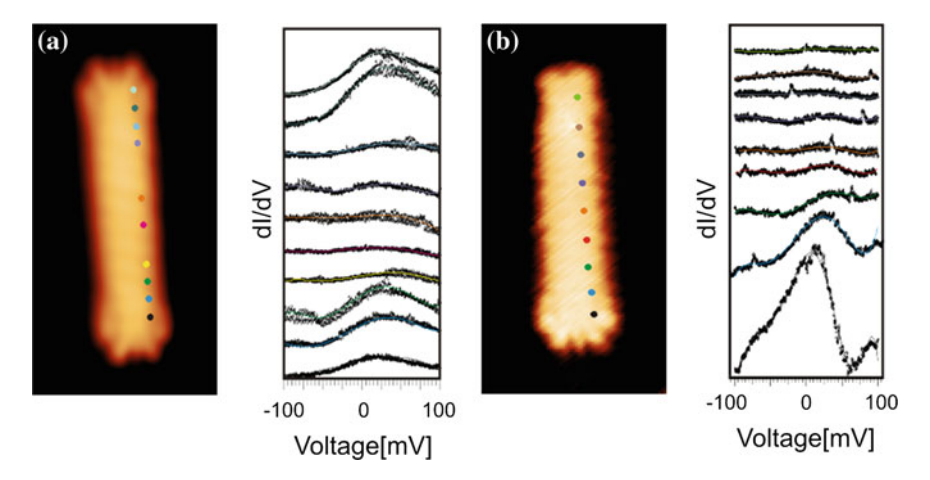
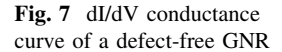
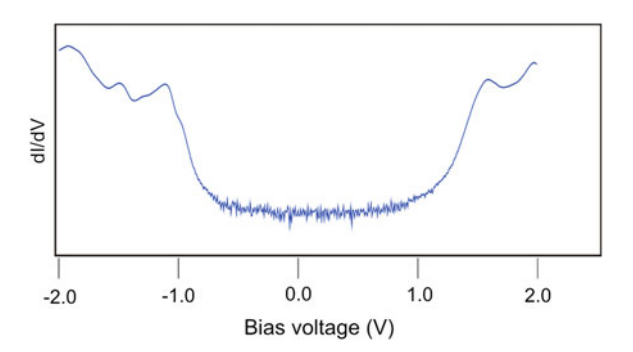


Fig. 6 dI/dV spectroscopy along two GNRs. a Defect-free GNR. b GNR with a defect at the upper terminus

the short edges. In the defect-free case these are zigzag edges while in case of a defect this specific zigzag structure is destroyed. We assign the electronic state to Tamm states [30] which have been predicted by theory [11]. They are located at the zigzag edges and are absent at the armchair edges. The defect of the GNR shown in Fig. 5h and b destroys the zigzag structure of the ribbon end and with this the specific arrangement of the carbon atoms necessary for the Tamm states. The spectroscopic result (Fig. 4b right part) is in very good agreement with this.

Recording a dI/dV spectra for a larger bias window shows us the position of the HOMO and the LUMO (Fig. 7). The HOMO is assigned to a peak located at -1.1 eV and the LUMO is found at +1.6 eV. These GNRs have a HOMO-LUMO gap of 2.7 eV, which is consistent with previous measurements. They report a band gap of 2.8 eV for the same GNRs [31] and HREELS measurements find an electronic transition at 2.6 eV [32]. GW approximations are present with a larger band gap of 3.8 eV [9]. This mismatch between experiment and theory can be explained through the influence of the metal surface on the ribbon [14–16].





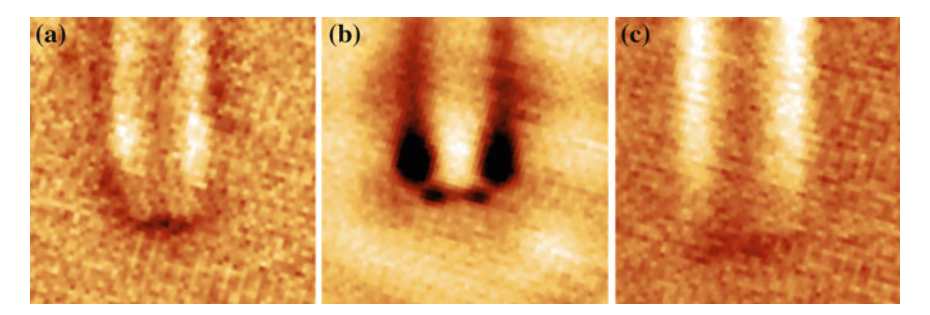


Fig. 8 Conductance maps of the same defect-free GNR at different bias energies $(5 \times 5 \text{ nm}^2)$: $\mathbf{a} = -1.15 \text{ V (HOMO)}, \mathbf{b} + 0.05 \text{ V (Tamm states)}, \mathbf{c} + 1.6 \text{ V (LUMO)}$

4 dI/dV Mapping

We recorded such maps at four different bias voltages which correspond to the HOMO, the Tamm states and the LUMO. To guarantee a metallic tip dI/dV curves on the bare Au(111) substrate are measured before taking a conductance map. The Tamm states are localized at the zigzag edges at ribbon end as we know already from dI/dV spectroscopy. This is visible in the map in Fig. 8b. In contrast the conductance maps taken at -1.15 V (HOMO) show some delocalization along the ribbon edges (Fig. 8a). Also the spatial distribution of the LUMO is delocalized along the armchair edges of the GNR (Fig. 8c).

5 Conclusion

We could show the large influence of small changes in the chemical structure on the electronic states. Only the defect-free ribbon terminus has a Tamm state close to the Fermi level. A small defect at the ribbon end can already destroy the chemical environment necessary for the state to develop. This proves the importance of a defect-free fabrication of GNRs, especially for conductance measurements. Further, we find the HOMO at -1.1 eV and the LUMO at +1.6 eV. This results in a HOMO-LUMO gap of 2.7 eV. From dI/dV spectroscopy we know that the Tamm states close to the Fermi level are localized at the zigzag edges. Conductance maps show a delocalization of the HOMO and the LUMO along the ribbon backbone [29].

Acknowledgments The authors acknowledge financial support from European Projects ART-IST and AtMol and the German Science Foundation DFG (through SFB 658). We also acknowledge the A*STAR Computational Resource Centre (A*CRC) for the computational resources and support.

References

- 1. Geim, A.K.: Graphene: status and prospects. Science 324, 1530 (2009)
- 2. Geim, A.K., Novoselov, K.S.: The rise of graphene. Nat. Mater. 6, 183 (2007)
- 3. Novoselov, K.S., Geim, A.K., Morozov, S.V., Jiang, D., Zhang, Y., Dubonos, S.V., Grigorieva, I.V., Firsov, A.A.: Electric field effect in atomically thin carbon films. Science **306**, 666 (2004)
- Bae, S., Kim, H., Lee, Y., Xu, X., Park, J.-S., Zheng, Y., Balakrishnan, J., Lei, T., Ri Kim, H., Song, Y.I., Kim, Y.-J., Kim, K.S., Ozyilmaz, B., Ahn, J.-H., Hong, B.H., Iijima, S.: Roll-toroll production of 30-inch graphene films for transparent electrodes. Nat. Nano. 5, 574 (2010)
- Kim, K.S., Zhao, Y., Jang, H., Lee, S.Y., Kim, J.M., Kim, K.S., Ahn, J.-H., Kim, P., Choi, J.-Y., Hong, B.H.: Large-scale pattern growth of graphene films for stretchable transparent electrodes. Nature 457, 706 (2009)
- 6. Ohta, T., Bostwick, A., Seyller, T., Horn, K., Rotenberg, E.: Controlling the electronic structure of bilaver graphene. Science **313**, 951 (2006)
- 7. Castro Neto, A.H., Guinea, F., Peres, N.M.R., Novoselov, K.S., Geim, A.K.: The electronic properties of graphene. Rev. Mod. Phys. 81, 109 (2009)
- 8. Han, M.Y., Özyilmaz, B., Zhang, Y., Kim, P.: Energy band-gap engineering of graphene nanoribbons. Phys. Rev. Lett. **98**, 206805 (2007)
- 9. Yang, L., Park, C.-H., Son, Y.-W., Cohen, M.L., Louie, S.G.: Quasiparticle energies and band gaps in graphene nanoribbons. Phys. Rev. Lett. **99**, 186801 (2007)
- Brey, L., Fertig, H.A.: Electronic states of graphene nanoribbons studied with the Dirac equation. Phys. Rev. B 73, 235411 (2006)
- 11. Nakada, K., Fujita, M., Dresselhaus, G., Dresselhaus, M.S.: Edge state in graphene ribbons: Nanometer size effect and edge shape dependence. Phys. Rev. B **54**, 17954 (1996)
- Gross, L., Moll, N., Mohn, F., Curioni, A., Meyer, G., Hanke, F., Persson, M.: Highresolution molecular orbital imaging using a p-wave STM tip. Phys. Rev. Lett. 107, 086101 (2011)
- Makoudi, Y., Palmino, F., Duverger, E., Arab, M., Chérioux, F., Ramseyer, C., Therrien, B., Tschan, M.J.L., Süss-Fink, G.: Nondestructive room-temperature adsorption of 2,4,6-tri(2'-thienyl)-1,3,5-triazine on a Si-B interface: high-resolution STM imaging and molecular modeling. Phys. Rev. Lett. 100, 076405 (2008)
- Repp, J., Meyer, G., Stojkovic, S.M., Gourdon, A., Joachim, C.: Molecules on insulating films: scanning-tunneling microscopy imaging of individual molecular orbitals. Phys. Rev. Lett. 94, 026803 (2005)
- Chavy, C., Joachim, C., Altibelli, A.: Interpretation of STM images: C60 on the gold (110) surface. Chem. Phys. Lett. 214, 569 (1993)
- Neaton, J.B., Hybertsen, M.S., Louie, S.G.: Renormalization of molecular electronic levels at metal-molecule interfaces. Phys. Rev. Lett. 97, 216405 (2006)
- 17. Lagoute, J., Kanisawa, K., Fölsch, S.: Manipulation and adsorption-site mapping of single pentacene molecules on Cu(111). Phys. Rev. B 70, 245415 (2004)
- 18. Lagoute, J., Kanisawa, K., Fösch, S.: Manipulation and adsorption-site mapping of single pentacene molecules on Cu(111). Phys. Rev. B 70, 245415 (2004)
- Soe, W.H., Manzano, C., De Sarkar, A., Chandrasekhar, N., Joachim, C.: Direct observation of molecular orbitals of pentacene physisorbed on Au(111) by scanning tunneling microscope. Phys. Rev. Lett. 102, 176102 (2009)
- Jiao, L., Zhang, L., Wang, X., Diankov, G., Dai, H.: Narrow graphene nanoribbons from carbon nanotubes. Nature 458, 877 (2009)
- Moreno-Moreno, M., Castellanos-Gomez, A., Rubio-Bollinger, G., Gomez-Herrero, J., Agraït, N.: Ultralong natural graphene nanoribbons and their electrical conductivity. Small 5, 924 (2009)
- 22. Tapaszto, L., Dobrik, G., Lambin, P., Biro, L.P.: Tailoring the atomic structure of graphene nanoribbons by scanning tunnelling microscope lithography. Nat. Nano 3, 397 (2008)

90 M. Koch et al.

 Wang, X., Dai, H.: Etching and narrowing of graphene from the edges. Nat. Chem. 2, 661 (2010)

- 24. Grill, L., Dyer, M., Lafferentz, L., Persson, M., Peters, M.V., Hecht, S.: Nano-architectures by covalent assembly of molecular building blocks. Nat. Nano 2, 687 (2007)
- Hla, S.-W., Bartels, L., Meyer, G., Rieder, K.-H.: Inducing all steps of a chemical reaction with the scanning tunneling microscope tip: towards single molecule engineering. Phys. Rev. Lett. 85, 2777 (2000)
- Lafferentz, L., Eberhardt, V., Dri, C., Africh, C., Comelli, G., Esch, F., Hecht, S., Grill, L.: Controlling on-surface polymerization by hierarchical and substrate-directed growth. Nat. Chem. 4, 215 (2012)
- Cai, J., Ruffieux, P., Jaafar, R., Bieri, M., Braun, T., Blankenburg, S., Muoth, M., Seitsonen, A.P., Saleh, M., Feng, X., Mullen, K., Fasel, R.: Atomically precise bottom-up fabrication of graphene nanoribbons. Nature 466, 470 (2010)
- Chen, W., Madhavan, V., Jamneala, T., Crommie, M.F.: Scanning tunneling microscopy observation of an electronic superlattice at the surface of clean gold. Phys. Rev. Lett. 80, 1469 (1998)
- 29. Koch, M., Ample, F., Joachim, C., Grill, L.: Voltage-dependent conductance of a single graphene nanoribbon. Nat. Nano 7, 713 (2012)
- 30. Tamm, I.: Über eine mögliche Art der Elektronenbindung. Phys. Z. Sowjetunion 1, 733 (1932)
- Linden, S., Zhong, D., Timmer, A., Aghdassi, N., Franke, J.H., Zhang, H., Feng, X., Müllen, K., Fuchs, H., Chi, L., Zacharias, H.: Electronic structure of spatially aligned graphene nanoribbons on Au(788). Phys. Rev. Lett. 108, 216801 (2012)
- 32. Bronner, C., Leyssner, F., Stremlau, S., Utecht, M., Saalfrank, P., Klamroth, T., Tegeder, P.: Electronic structure of a subnanometer wide bottom-up fabricated graphene nanoribbon: End states, band gap, and dispersion. Phys. Rev. B 86, 085444 (2012)

Imaging and Manipulation of Molecular Electronic States on Metal Surfaces with Scanning Tunneling Microscopy

Robin Ohmann, Lucia Vitali and Klaus Kern

Abstract Electrically tunable molecules are highly attractive for the construction of molecular devices, such as switches, transistors, or machines. A precise knowledge about their electronic properties, such as molecular states as well as information on how these can be manipulated is thus demanding. Here, we present a scanning tunneling microscopy study of organic molecules on a metal surface. Single 4-[trans-2-(pyrid-4-yl-vinyl)] benzoic acid (PVBA) molecules, as well as artificially constructed metal—organic complexes made of PVBA and one Cu atom and self-assembled metal—organic complexes are investigated. We demonstrate that a chemical bond between a copper atom and coordinating organic molecules adsorbed on a metal surface acts as a variable frequency switch, which can be actuated and probed by means of low-temperature scanning tunneling microscopy. Whereas below a threshold bias voltage the bond is permanently either formed or broken, the bonding state continuously oscillates at higher voltages. The switching rate of the bistable molecular system can be widely tuned from below 1 Hz up to

R. Ohmann () · L. Vitali · K. Kern

Max-Planck-Institut fur Festkörperforschung, Heisenbergstrasse 1 D-70569 Stuttgart, Germany

e-mail: robin.ohmann@nano.tu-dresden.de

R. Ohmann

Institute for Materials Science and Max Bergmann Center of Biomaterials, TU Dresden, D-01062 Dresden, Germany

L. Vitali

Centro de Física de Materiales CFM-MPC, Centro Mixto CSIC-UPV/EHU, San Sebastián E-20018, Spain

L. Vitali

IKERBASQUE, Basque Foundation for Science, Bilbao E-48011, Spain

K. Kern

Institut de Physique de la Matière Condensée, Ecole Polytechnique Fédérale de Lausanne (EPFL), CH-1015 Lausanne, Switzerland

L. Grill and C. Joachim (eds.), *Imaging and Manipulating Molecular Orbitals*, Advances in Atom and Single Molecule Machines, DOI: 10.1007/978-3-642-38809-5_8, © Springer-Verlag Berlin Heidelberg 2013

the kilohertz regime. The quantum yield per tunneling electron to trigger a transition between the two states varies spatially and is related to the local density of states of the bonded and non-bonded configuration.

1 Introduction

Controlling matter at the atomic scale allows to unravel the principles of natural occurring chemical and physical processes and may open pathways for designing components for nanoscale functional devices. Recently, impressive progress has been made in modifying the position, charge state, and conformation of atoms and single molecules adsorbed on a surface by external stimuli such as light [1, 2], temperature [3, 4], electric fields [5, 6], or tunneling electrons [7–17]. For the investigation of such nanoscale systems, the STM has proven to be a versatile tool as it provides a high level of spatial resolution in addressing and modifying adsorbed chemical species and determining their electronic structure. For example, the movement of single adatoms by STM, first demonstrated by Don Eigler and coworkers [18], shows how atoms can be positioned at defined places on the surface. In his case, Xe atoms, deposited on a metal surface, were arranged to display the letters "IBM". Since then, the STM has been utilized for numerous atomic-scale manipulation experiments. Some of which, including also vertical manipulation of adsorbates, are outlined in Ref. [19]. For the lateral manipulation, as used by Eigler, the tip is typically brought close to the adsorbate and then moved along a desired trajectory. Depending on the adsorbate-substrate interaction and the conductance several kinds of movements are distinguished [20]. For example, the adsorbates can be pulled, pushed, rolled, or follow a sliding motion [21].

Another way of manipulation of nanostructures is by simply applying a voltage between tip and sample. The resulting electric field and/or the injected tunneling electrons can lead to a displacement or chemical modification of the adsorbate [7–17, 22]. Manipulation thus reveals information about the interaction of atoms and molecules with each other and the surface. Using the STM allows to explore these mechanisms and the design of new structures, which may serve as a model system. Importantly, the morphology and electronic properties of reactants and products can be accessed by acquiring topographic and conductance maps before and after a reaction was triggered. In the following, the formation and the time-dependent behavior of chemical bonds between a metal adatom and an organic molecule are reported. This overview is based mainly on previously published data by the authors of the chapter [23, 24].

2 Formation of a Metal-Ligand Bond with Cu and PVBA

Metal-ligand bonds are important and frequently observed in nature. Typical examples are metal-organic complexes, where a central metal atom or ion is coordinated by either several molecules and/or by a polydentate ligand, which offers multiple binding sites. Complexes are abundant in the human body, where about one-third of proteins require metal ions to carry out their function. For example the haemoglobin molecule, which is an iron-containing metalloprotein, is responsible for the oxygen transport in the blood. In this case, the central metal atom is held in a heterocyclic ring, known as a porphyrin, coordinated to four Natoms. The bond strength of a metal-ligand bond is larger than pure electrostatic interactions and can be as strong as in covalent bonds. In general, the number of coordinating ligands is given by the electronic properties of the central atom and geometric constraints. In solution or gas phase, two to ninefold coordination are possible. On the surface, the number of ligands and possible binding sites to coordinate to an adsorbed metal atom is reduced. Surface supported coordination has been shown to lead to supramolecular structures [25]. Metal complexes with only one metal-ligand bond were, however, not found in nature. Creating such a structure artificially would be interesting as it provides the basic unit in the formation of metal-organic coordination networks. It is known that the STM can be utilized to form chemical bonds between adsorbates on the surface as has been reported in [26, 27]. In the following, it will be shown that a single coordinated complex can be created by moving a Cu adatom with the tip of an STM toward a PVBA molecule.

The experiments were carried out with a home-built low-temperature scanning tunneling microscope operated at a temperature of 6 K in ultrahigh vacuum. The single crystal Cu(111) was prepared by repeated cycles of Ar^+ ion sputtering and subsequent annealing. 4-[Trans-2-(pyrid-4-yl-vinyl)] benzoic acid (PVBA), which is an organic molecule consisting of two (hetero-)aromatic groups, was evaporated ($T_{cell} = 456$ K) on the clean substrate held at room temperature achieving submonolayer coverage. The single Cu atoms have been obtained by the following procedure: First, the electrochemically etched tungsten tip has been dipped into the Cu surface several times covering the apex of the tip with Cu. Second, the tip was dipped again into the surface, however, in this last step with a high bias voltage (5 V). This resulted in single adatoms on the surface. To verify that indeed the found atoms are Cu, the spectroscopic signature of the adatom was investigated, which showed the characteristic surface state localization peak as described in [28]. Additionally, the topographic height profile was compared with previous measurements on Cu/Cu(111).

In Fig. 1a, a topographic image of a Cu adatom and a PVBA molecule adsorbed on Cu(111) is shown. PVBA appears as two protrusions and one large depression at one end. The protrusions are assigned to the two aromatic groups and the depression is associated with the deprotonated carboxyl side. Hereafter, the term PVBA refers to the deprotonated form. The manipulation of the Cu atom, which

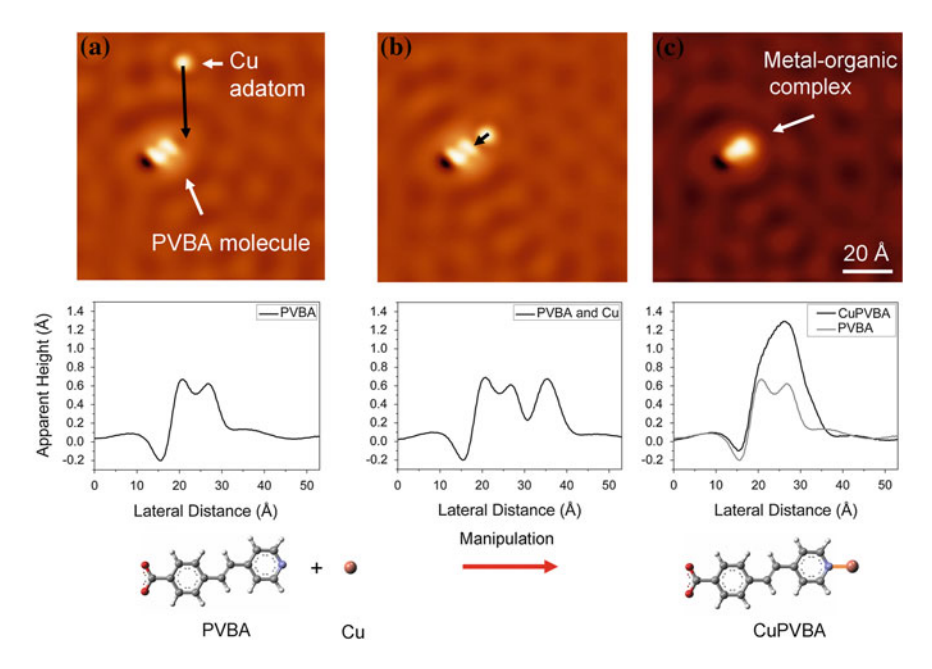


Fig. 1 Formation of a onefold coordinated metal-organic complex using STM for manipulation. **a** Topography image of a PVBA molecule and a Cu adatom. The Cu adatom has been moved by the tip along the *black line*. Its new position is shown in image (**b**). **b** Manipulation of the Cu adatom toward PVBA. **c** A metal-organic complex has been formed as a result of the manipulation. Below the images are line scans across the long axis of the structures. V = 10 mV, I = 0.5 nA for all images (taken from [24])

appears as a round protrusion, has been done by positioning the tip above the Cu adatom, then reducing the tip-adsorbate distance and moving the tip along a desired trajectory under constant current conditions. This caused the adatom to move across the surface. The manipulation pathes are indicated by black lines in Fig. 1a and b. In an initial step, the adatom was moved to the vicinity of the PVBA molecule. In the final step, the adatom was moved toward the N-terminated side of the PVBA molecule. This resulted in the structure shown in Fig. 1c. A strong change in the apparent height is visible (see line profiles along the long axis). The apparent height is increased with respect to the PVBA monomer and only one large protrusion becomes apparent. This cannot simply be explained by a superposition of the apparent height of a single Cu adatom and the PVBA molecule. Instead, the electronic structure of PVBA has been altered indicative of the formation of a chemical bond. For the bond formation no high-voltage pulse was necessary, as has been used for attaching a Au atom to a Pentacene molecule on NaCl/Cu(111) [10]. A close look at the tip height profile during the lateral manipulation of the adatom toward the molecule (see Fig. 2) indicates that at the end a sudden drop in the vertical tip-displacement occurred (marked by red arrows). This is interpreted as lateral jump-to-contact of the adatom toward the

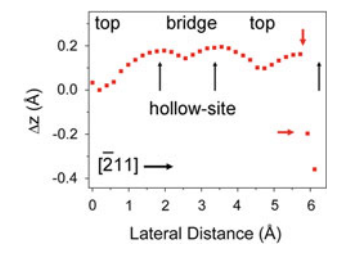


Fig. 2 Tip-displacement profile along the manipulation path (*black line*) in Fig. 1. From the profile the position of the Cu adatom with respect to the substrate can be identified. At the end of the manipulation path, a sudden change of the tip-displacement is visible (indicated by *red arrows*). Manipulation parameters are V = 8 mV, I = 200 nA (G = 0.3 G_0), gain of preamplifier 10^7 V/A and lateral speed of the tip = 30 Å/s (taken from [23])

molecule. The profile of the whole path differs also from the lateral manipulation curves obtained by moving single adatoms [20]. The difference is ascribed to the large conductance $(0.3\ G_0)$ at which the manipulation has been done, suggesting a different movement of the adatom similar to the movement of a Co atom on Cu(111) reported in [29]. Knowing the orientation of the molecule with respect to the substrate [30], the lateral manipulation path is assigned along one of the $[\bar{2}11]$ -high symmetry directions. From the positions at which the maxima and minima in the height profile occur, one can deduce the position of the Cu adatom during the manipulation with respect to the substrate. The strongest minima are assigned to a top site, the maxima to hollow sites, and the intermediate minimum to a bridge site. Based on the above assignment, the Cu adatom just before contact formation jumps from one hollow site toward the final position. The final position is a hollow site, which is suggested by the DFT calculations of the adsorption model of CuPVBA [23]. The average distance between the occurrence of the jump and the estimated position of the

N-atom of the PVBA molecule is $3.0\pm0.5\text{Å}$. This is slightly larger than the Cu–N bond distance of 1.91 Å. Attractive forces acting between the Cu atom and the N-terminated side of the PVBA may be responsible for this.

3 Actuated Transitory Metal-Ligand Bond as Tunable Electromechanical Switch

Chemical reactions typically result into well-defined chemical bonds between reactants. In the last section, Cu atoms were mechanically moved toward the PVBA to form a CuPVBA complex mimicking a chemical reaction. This caused a substantial change in the electronic structure of the single components compared to the product [11, 26, 27]. Other structures created by manipulating adsorbates on a surface by means of STM have been reported in literature. The reactants were

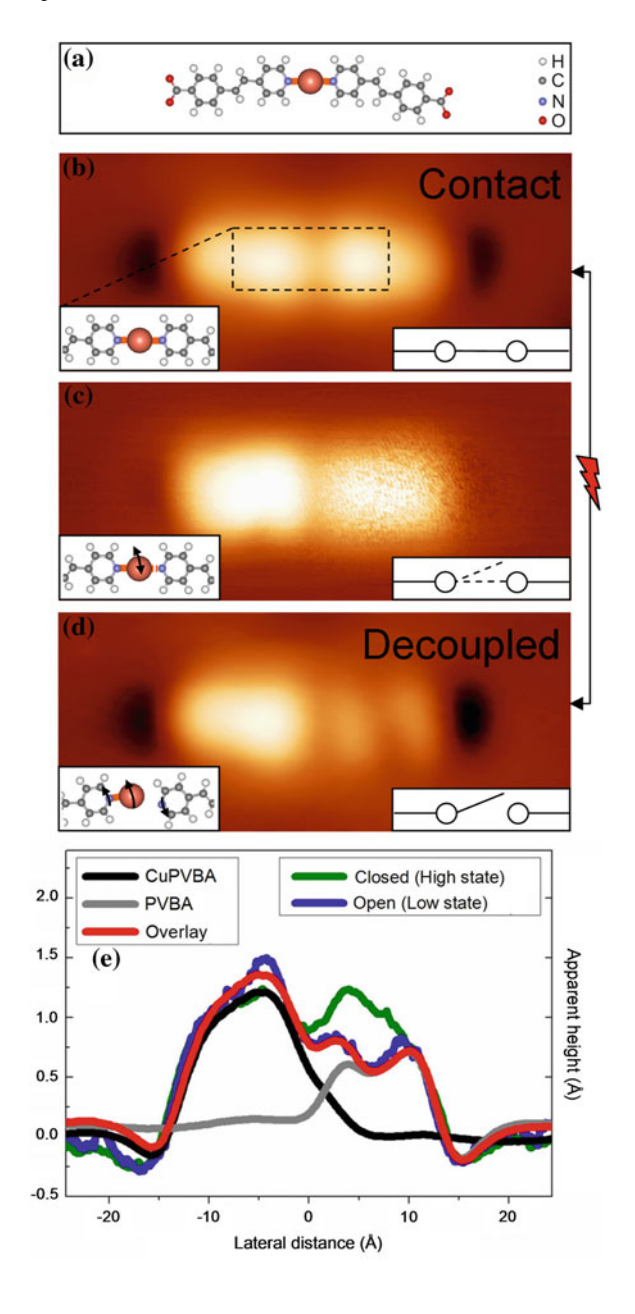
brought close together [27] and in some cases, this was followed by applying a voltage pulse [31]. Cases of nonreversible reactions have been characterized [31] and recently a subsequent breaking of an artificially created bond has been shown [11] by applying a voltage pulse. However, a study on the nature and efficiency of both reaction pathways of a reversible metal–ligand bond is still missing.

Additionally, as the electronic structure of reactants and products typically differs (see previous section), a controlled alternation between these, would allow to select and switch between specific conductance states. Compared to artificially created molecular systems, a control of individual bonds in a self-assembled formation is desirable in view of creating large arrays of functional units [3, 25]. By applying a voltage (up to 2 V) on the CuPVBA complex, the complex remained unchanged. However, for self-assembled Cu(PVBA)₂ complexes [23, 32], which occur besides the monomers of PVBA also on the surface, consisting of two PVBA molecules and one central Cu atom (see Fig. 3a), this differs. Applying an electrical bias acts as an external stimulus, which leads either to a bond formation or a bond breaking. A so-called transitory chemical bond, i.e., a bonding state which varies with time, between a copper adatom and coordinating organic molecules adsorbed on a metal surface has been discovered and is characterized in detail.

A typical STM topography image of a self-assembled $Cu(PVBA)_2$ complex acquired at a sample bias of -0.1 V is shown in Fig. 3b. In Fig. 3c, a topograph of the same complex taken at a higher bias voltage (0.8 V) is displayed. It can be seen that one side of the metal-organic coordination compound shows a "fuzzy" appearance. This is indicative of an instability of the imaged structure triggered by inelastic tunneling electrons [8, 16].

In order to understand this behavior, the tunneling current was measured in open feedback loop conditions as a function of time. Current traces recorded in the fuzzy area show an oscillation between two values (see Fig. 4a), which are labeled as low- and high-conductance state. The high-conductance state can be easily imaged at low voltages (see Fig. 3b). The low-conductance state, instead, can be accessed, if the applied sample bias overcomes a threshold voltage. This causes the system to alternate between the low- and high-conductance state. A slow reduction of the voltage allows the system to relax and to restore the high-conductance state suggesting this to be the most preferable state. However, by fast (faster than the lifetime of the low-conductance state) reducing the voltage, the bistable behavior can be quenched and the complex is blocked in the low state. The system remains then stable until a sufficiently large voltage reactivates the bistable fluctuations showing that the process is fully reversible.

As the metal complex can be either in a naturally occurring high-conductance state or been quenched in a low-conductance state, topographic images of both states can be taken (see Fig. 3b and d). Their appearance clearly indicates that the molecular configuration differs in the two cases. The apparent height profiles across the long axis in the two conductance states are shown in Fig. 3e. The high-conductance state (green line) shows a symmetric line profile expected for Cu(PVBA)₂ where two PVBA molecules are coordinated to a central Cu atom. The profile along the low-state (blue line) differs from the previous as the apparent



■ Fig. 3 STM topography images of a self-assembled nanoswitch and schemes illustrating the mechanism. a Scheme of the metal-organic complex Cu(PVBA)₂. b High-conductance state of the complex measured at low voltage (-0.1 V). c same area as b imaged at a higher voltage (0.8 V). One side appears fuzzy, which is characteristic of rapid changes in the conductance. d Read out of the low-state at the same voltage as (b). Prior to imaging the low-state, the complex in the high-state was brought into the low-state by applying a sufficiently high voltage on the fuzzy area (see text). In the low-state, one PVBA molecule is decoupled from the central Cu atom. Images are 51 by 22 Å². c Comparison of the apparent height profiles of the high- and low-state with the profile of a single PVBA molecule and a single PVBA molecule bonded to a Cu adatom fabricated by single-molecule chemistry using the STM (see previous section) (all profiles taken at comparable voltages across the long-axis) (taken from [24])

molecular height is reduced on the "fuzzy" side. To rationalize the profile of the low state, it is compared with the one of a single PVBA molecule and a PVBA molecule with a single Cu atom attached to the nitrogen side (grey and black line in Fig. 3e). The sum of these two line profiles (red line in Fig. 3e) reproduces the one achieved of the structure in the low-conductance state. The apparent height of the low state resembles thus an electronically decoupled PVBA monomer and an only onefold CuPVBA complex. These observations let conclude that by applying a voltage large enough a transitory metal–ligand bond is induced by attaching or detaching one PVBA molecule to or from the central Cu atom. As will be explained in more detail later, this process is largely governed by an asymmetric movement of the central Cu atom (see insets in Fig. 3b–d). In a broader sense, the high state visualizes a closed and the low state an open metal–organic nanocontact.

The bistable behavior of this metal-ligand bond can be controlled by several parameters. These are the tip-sample distance (i.e., setpoint current), bias voltage, and position of the tip across the plane of the complex. By analyzing the resulting characteristic current fluctuations, the switching rate R as well as the lifetime τ_{state} , the probability p_{state} and the quantum yield of each state can be obtained (Figs. 4, 5).

The switching rate, which is the number of complete switches per second, depends linearly on the tunneling current. This is experimentally confirmed for currents up to 10 nA and for various positive (Fig. 4c) and negative voltages (not shown). This indicates that it is a one electron process [8]. By recording the tunneling current for a sufficiently long time, histogram plots can be obtained as reported in Fig. 4b. These show two characteristic peaks, whose areas represent the time spent by the complex in the high- or in the low-conductance state. In other words the ratio of these areas, obtained from Gaussian fits, with respect to the total area defines the probability p_{state} to find the complex in one of the two conductance states. In Fig. 4d, this is plotted as a function of bias voltage. It can be seen that for voltages around the Fermi level, the compound stabilizes preferably in the highconductance state. By increasing the absolute value of the applied bias above a threshold value, the probability of the low-state increases smoothly. For negative voltage beyond -2 V it approaches unity becoming the preferred state. Acquiring a topographic image at these voltages provides then an alternative method to read out the low state. For positive voltages, the probability of the low-state smoothly

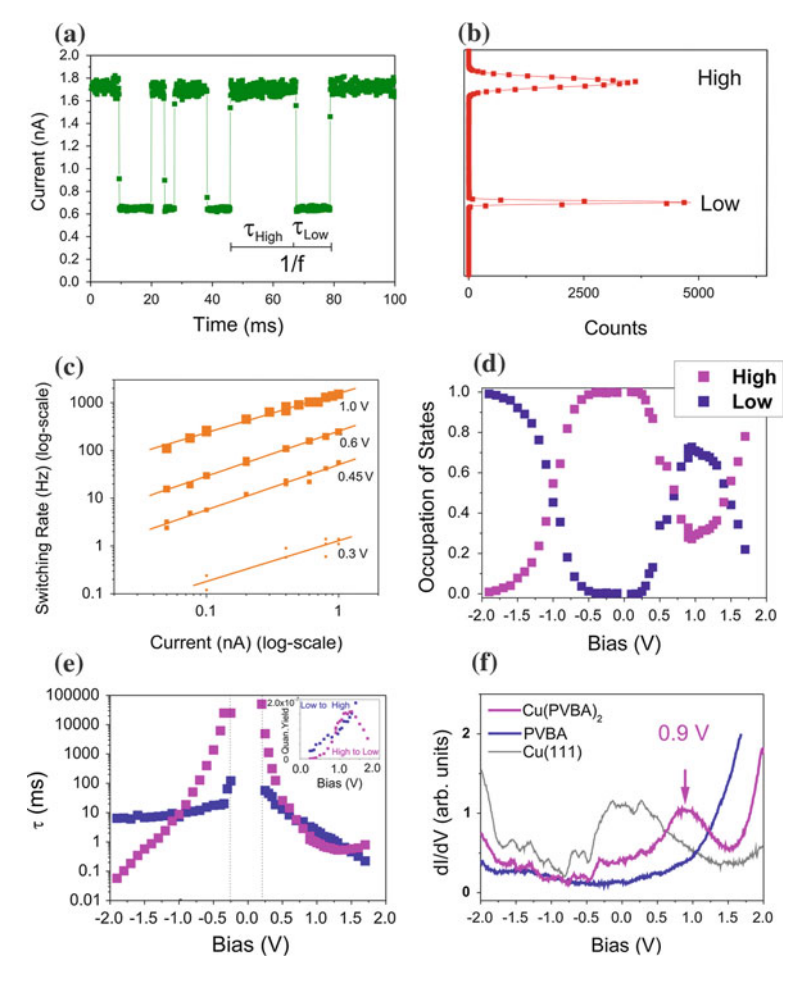


Fig. 4 Analysis of current versus time series. a Current as a function of time measured in open feedback loop conditions on top of one side of the complex showing the telegraph noise (Bias $= -1.3 \,\mathrm{V}$, Setpoint: 0.1 V, $I = 0.1 \,\mathrm{nA}$). b Corresponding histogram of the current distribution. c Switching rate as a function of current. d Probability of occupation of the low- and high-state as a function of bias voltage. e Lifetime of each state versus bias voltage. *Inset* shows the quantum yield for each transition in the positive voltage range. f Scanning tunneling spectra on the PVBA complex, an isolated PVBA monomer and the bare Cu(111) surface for comparison (taken from [24])

increases till it reaches a maximum around 1 V before it decreases again. This trend was observed on all twofold complexes investigated.

In the following, the response of the complex to tunneling electrons is related to its electronic properties. A good indicator of the bistable behavior is the quantum yield (see inset Fig. 4e), which is the probability of a transition (from high- to low- or low- to high-state) per tunneling electron and is given by $Re/(p_{\text{state}}I_{\text{state}})$, where

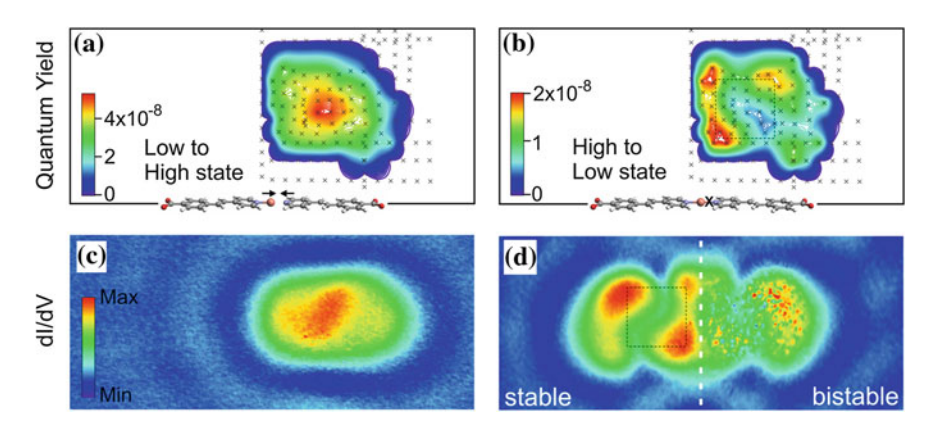


Fig. 5 Spatial correlation of quantum yield and the local density of states. **a** and **b** Contour plot of the quantum yield on the complex for the two different transitions low- to high- and high to low state. *Red areas* denote the largest quantum yield per tunneling electron. In the *white area* surrounding the colored area, no switching events were observed. The *gray crosses* indicate positions where the current traces were taken (Bias = 0.9 V, Setpoint: 0.1 V, $I = 0.1 \,\text{nA}$). The sketches of the molecules are drawn to scale. **c** and **d** are maps of the LDOS measured on an isolated PVBA monomer and on a PVBA complex at the same bias voltage (0.9 V). Given the molecular bistability, the LDOS can be better visualized at the stable side of the molecule. Measuring the LDOS at conditions of low-switching rates confirms a similar density of states at both sides of the complex. The *dotted square* in **b** and **d** is a guide for the eyes for easier comparison of the features seen in the quantum yield with the LDOS. All panels are 51 by 22 Å (taken from [24])

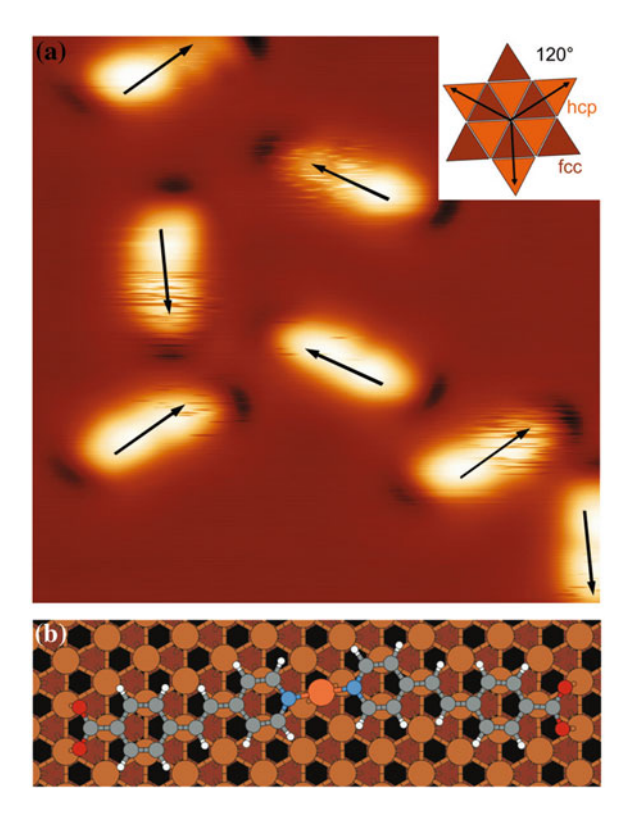
e is the elementary charge and I_{state} denotes the value of the measured current in the respective state. In Fig. 5a and b, we report the quantum yield for the two transitions mapped at the voltage corresponding to the peak observed in the LDOS on Cu(PVBA)₂ (Fig. 4f). At each point marked by a cross, a time series was taken and evaluated in terms of the quantum yield. The resulting contour plots indicate that the quantum yield is not uniform in space and is more prominent on the molecular ligand. As a consequence, the formation of a coordination bond to the copper adatom can hence be triggered several angstrom away from the bonding site. Additionally, the spatial dependence of the quantum yield for the forward and backward reaction differs significantly on the molecular plane. Whereas for the transition from the low to the high state one clear maximum (red area) is found, several maxima at different positions are observed for the transition from high- to low state. This can be understood by comparing the quantum yield to the local density of states. To measure unambiguously the density of states, a prerequisite is that the structure remains stable. This condition is met for a PVBA monomer and the other half of the PVBA complex. Their spatially resolved density of states are reported in Fig. 5c and d. Since in the low state the PVBA molecule is electronically decoupled from the central Cu atom as has been shown in Fig. 3d and e, the quantum yield for the low- to the high-state (Fig. 5a) is consequently compared to the electronic structure of an isolated PVBA monomer (Fig. 5c). Similar to the yield, the density of states shows one maximum. The quantum yield of the high- to the low-state (Fig. 5b) is compared with the more stable half of the complex (Fig. 5d), where the PVBA is bonded to the central Cu atom. Several maxima are observed in the conductance map, whose shape resemble the one in the yield map. Thus, both comparisons reveal clearly that the spatial dependence of the density of states matches the one of the quantum yield of each transition.

The average lifetime of each state, obtained by dividing the relative occupation of each state by the switching rate $\tau_{\text{state}} = p_{\text{state}}/R$ is shown in Fig. 4e as a function of voltage. For negative voltages, the lifetime of the high state covers a broad range extending over several orders of magnitude from below 0.1 ms to above 10 s, whereas the lifetime of the low state remains roughly constant. The dependence for positive voltages differs as the lifetime for the high state is reaching a minimum and then increases again reflecting the influence of the LDOS. The switching rate, which is the inverse of the sum of the lifetime of each state, ranges from a few events per minute to well above 1 kHz. For the higher frequencies, the time resolution of the electronics $> 20 \,\mu$ s limits the measurability of shorter lifetimes and hence higher frequencies. Nevertheless, the measured switching rate in the kHz-regime shows that it is a fast process compared to other known molecular-based functional units adsorbed on a surface [3, 15]. The quantum yield is also appreciable; the highest measured quantum yield was in the 10^{-6} range. Similar values have been achieved only for an electron-induced lateral movement of a single cobalt atom attached to a Cu chain [8]. Compared to molecular systems [12, 13], this is up to three orders of magnitude higher.

Given the symmetry of the metal complex (Fig. 3a) it may be surprising that only one of the PVBA molecules shows the described bistable behavior (see Figs. 3, 5). The asymmetry can be explained by taking the Cu substrate into account. A large-scale STM topography image shown in Fig. 6 illustrates that the long axis of the complex on Cu(111) follows well-defined orientations. Notably, the "fuzzy" appearing half is always facing in one specific direction as indicated by the arrows. Figure 6b reveals that the adsorption geometry of the two halves, calculated by means of density functional theory (DFT), differs with respect to lower lying Cu layers. This demonstrates that the second and subsequent layers affect the bonding of the complex at the surface and consequently the bistability of the metal complex.

The structural model also provides the basis to rationalize atomic scale movements of the molecular switch. As has been indicated by the insets in Fig. 3b–d, the bistable behavior can be assigned to a movement of the Cu adatom. The Cu atom is assumed to switch between the bridge position being bonded to both ligands and a nearby hollow site (favored for a single Cu adatom [33]) being bonded to only one. Following the displacement of the metal adatom, both PVBA molecules are slightly relaxed toward new energetically preferred positions. These are expected to be similar to adsorption positions of one single PVBA molecule and one CuPVBA compound. Whereas the actual displacements are too small to

Fig. 6 The role of the substrate in the switching mechanism. a Overview STM topography image showing several complexes in different orientations (Bias = -1.7 V). The arrows indicate directions from the quiet side to the fuzzy side. Their distribution is threefold symmetric. Image is 101 by 101 Å^2 . **b** Model of a PVBA complex on Cu(111) obtained from density functional theory calculations showing that the second atomic layer of the substrate imposes an asymmetry to the molecular structure (taken from [24])



be detected, the breaking of the chemical bond can be visualized via the conductance change. Metal–ligand bonds have generally precise bond length differing by only a few tenth of an angstrom [34]. Once the Cu adatom is in the hollow site, this geometry allows the bonding to one PVBA molecule only, whereas the distance to the other molecule is too large to form a bond. If the adatom resides in the bridge position bonding can occur to both molecules. The bistability can hence be ascribed to a competition between preferred adsorption positions of the single components and the whole metal–organic complex. The switching between both configurations is steered by tunneling into electronic states of the respective chemical species.

4 Summary

To mimic natural occurring reactions is tempting in order to gain a more detailed understanding of them. Here, a Cu atom was moved with the tip of an STM toward the N-terminated side of a PVBA molecule to assemble a metal–organic complex. The formed metal–ligand bond led to a significant change in the electronic

structure of the initial molecule. Hybridization of atomic and molecular orbitals were accounted for this modification.

Additionally, changing the conductance of a nanoscale object back and forth was demonstrated. Self-assembled twofold metal-organic complexes Cu(PVBA)₂ revealed a transitory metal-ligand bond [24]. By applying a voltage, the chemical bond between the central Cu atom and one of the ligands was continuously formed and broken. Given the distinct electronic structure of the bonded and non-bonded configuration, the conductance was switched on demand. The rapid alternations occurred on a time-scale down to milliseconds. The quantum yield for the reactions was experimentally determined from time-series taken at defined positions on the complex, revealing a strong correlation with the local density of states of the respective molecular structures. This opened a local view into the nature and efficiency of a chemical reaction, specifically showing the distinct properties of the forward and backward reaction. The investigated bistable nanoscale molecular system offers interesting prospects for designing large-scale assemblies of functional units. It provides a highly localized switch with a tunable rate up to the kHz regime. Furthermore, nanoelectromechanical devices could be envisioned based on injecting electrons with defined energies into bistable configurations triggering an opening or closing of a nanocontact.

Acknowledgments We thank Giacomo Levita for the theoretical input and Mario Ruben for synthesizing the PVBA.

References

- 1. Comstock, M.J., Levy, N., Kirakosian, A., Cho, J., Lauterwasser, F., Harvey, J.H., Strubbe, D.A., Fréchet, J.M.J., Trauner, D., Louie, S.G., Crommie, M.F.: Phys. Rev. Lett. 99, 038301 (2007)
- 2. Wu, S.W., Ogawa, N., Ho, W.: Science 312, 1362 (2006)
- 3. Wang, Y., Kröger, J., Berndt, R., Hofer, W.A.: J. Am. Chem. Soc. 131, 3639 (2009)
- 4. Kühne, D., Klappenberger, F., Krenner, W., Klyatskaya, S., Ruben, M., Barth, J.V.: Proc. Natl. Acad. Sci. U.S.A. 107, 21332-21336 (2010)
- 5. Alemani, M., Peters, M.V., Hecht, S., Rieder, K.-H., Moresco, F., Grill, L.: J. Am. Chem. Soc. 128, 14446 (2006)
- 6. Ohara, M., Kim, Y., Kawai, M.: Phys. Rev. B 78, 201405 (2008)
- 7. Eigler, D.M., Lutz, C.P., Rudge, W.E.: Nature **352**, 600 (1991)
- 8. Stroscio, J.A., Tavazza, F., Crain, J.N., Celotta, R.J., Chaka, A.M.: Science 313, 948 (2006) 9. Stipe, B.C., Rezaei, M.A., Ho, W.: Science 279, 1907 (1998)
- 10. Repp, J., Meyer, G., Paavilainen, S., Olsson, F.E., Persson, M.: Science 312, 1196 (2006)
- 11. Gaudioso, J., Ho, W.: Angew. Chem. Int. Ed. 40, 4080 (2001)
- 12. Lastapis, M., Martin, M., Riedel, D., Hellner, L., Comtet, G., Dujardin, G.: Science 308, 1000 (2005)
- 13. Iancu, V., Hla, S.-W.: Proc. Natl. Acad. Sci. U.S.A. 103, 13718 (2006)
- 14. Harikumar, K.R., Polanyi, J.C., Sloan, P.A., Ayissi, S., Hofer, W.A.: J. Am. Chem. Soc. 128, 16791 (2006)
- 15. Liljeroth, P., Repp, J., Meyer, G.: Science 317, 1203 (2007)

 Henningsen, N., Franke, K.J., Torrente, I.F., Schulze, G., Priewisch, B., Rück-Braun, K., Dokić, J., Klamroth, T., Sallfrank, P., Pascual, J.I.: J. Phys. Chem. C 111, 14843 (2007)

- 17. Repp, J., Meyer, G., Olsson, F.E., Persson, M.: Science 305, 493 (2004)
- 18. Eigler, D.M., Schweizer, E.K.: Nature 344, 524 (1990)
- 19. Stroscio, J.A., Eigler, D.M.: Sciene **254**, 1319 (1991)
- 20. Bartels, L., Meyer, G., Rieder, K.-H.: Phys. Rev. Lett. 79, 697 (1997)
- Nickel, A., Meyer, J., Ohmann, R.: Jacquot de Rouville, H.-P., Rapenne, G., Ample, F., Joachim, C., Cuniberti, G., Moresco, F. Journal of Physics: Condensed Matter 24, 404001 (2012)
- Nickel, A., Ohmann, R., Meyer, J., Grisolia, M., Joachim, C., Moresco, F., Cuniberti, G.: ACS Nano 7, 191 (2013)
- 23. Ohmann, R. Dissertation, Universität Konstanz (2010)
- 24. Ohmann, R., Vitali, L., Kern, K.: Nano Letters 10, 2995–3000 (2010)
- 25. Barth, J.V., Costantini, G., Kern, K.: Nature 437, 671 (2005)
- 26. Lee, H.J., Ho, W.: Science 286, 1719 (1999)
- 27. Nazin, G.V., Qiu, X.H., Ho, W.: Science 302, 77 (2003)
- Olsson, F.E., Persson, M., Borisov, A.G., Gauyacq, J.-P., Lagoute, J., Fölsch, S.: Phys. Rev. Lett. 93, 206803 (2004)
- 29. Stroscio, J.A., Celotta, R.J.: Science 306, 242 (2004)
- 30. Ohmann, R., Levita, G., Vitali, L., De Vita, A., Kern, K.: ACS Nano 5, 1360-1365 (2011)
- 31. Hla, S.-W., Bartels, L., Meyer, G., Rieder, K.-H.: Phys. Rev. Lett. **85**, 2777 (2000)
- 32. Vitali, L., Levita, G., Ohmann, R., Comisso, A., De Vita, A., Kern, K.: Nature Materials 9, 320 (2010)
- 33. Repp, J., Meyer, G., Rieder, K.-H., Hyldgaard, P.: Phys. Rev. Lett. **91**, 206102 (2003)
- Tait, S.L., Langner, A., Lin, N., Stepanow, S., Rajadurai, C., Ruben, M., Kern, K.: J. Phys. Chem. C 111, 10982 (2007)

SPM Imaging of Trinaphthylene Molecular States on a Hydrogen Passivated Ge(001) Surface

Marek Kolmer, Szymon Godlewski, Bartosz Such, Paula de Mendoza, Claudia De Leon, Antonio M. Echavarren, Hiroyo Kawai, Mark Saeys, Christian Joachim and Marek Szymonski

Abstract We report on studies concerning individual trinaphthylene molecules (Y molecules) deposited and anchored on the hydrogenated Ge(001):H surface. The characterization of single Y molecules has been performed by means of cryogenic temperature STM imaging using conventional STM tungsten tips and tuning fork-based sensors. In the latter case, a qPlus sensor facilitated simultaneous STM and NC-AFM measurements and thus molecular states were probed by both tunneling current and atomic forces concurrently. We show that the molecules are physisorbed, thus weakly interacting with the substrate. Contrary to the measurements on hydrogenated silicon, for planar aromatic molecules on the hydrogenated germanium, both empty and filled molecular states could be probed by STM.

M. Kolmer (⋈) · S. Godlewski · B. Such · M. Szymonski

Centre for Nanometer-Scale Science and Advanced Materials, NANOSAM, Faculty of Physics, Astronomy, and Applied Computer Science, Jagiellonian University, Reymonta 4, 30059 Krakow, Poland

e-mail: marek.kolmer@uj.edu.pl

P. de Mendoza · C. De Leon · A. M. Echavarren

Institute of Chemical Research of Catalonia (ICIQ), Avenida Països Catalans 16, 43007 Tarragona, Spain

H. Kawai · M. Saevs · C. Joachim

Institute of Materials Research and Engineering, 3 Research Link, Singapore 117602, Singapore

M. Saeys

Department of Chemical and Biomolecular Engineering, National University of Singapore, 4 Engineering Drive 4, Singapore 117576, Singapore

C. Joachim

Nanosciences Group & MANA Satellite, CEMES-CNRS, 29 rue Jeanne Marvig, F-31055 Toulouse, France

L. Grill and C. Joachim (eds.), *Imaging and Manipulating Molecular Orbitals*, Advances in Atom and Single Molecule Machines, DOI: 10.1007/978-3-642-38809-5_9, © Springer-Verlag Berlin Heidelberg 2013

106 M. Kolmer et al.

1 Introduction

Since further development of a conventional, CMOS-type electronic device is approaching fundamental limits at the nanoscale, several alternative routes are considered [1–3]. One possibility, called "monomolecular electronics," is considering a device in which states of a single organic molecule are altered by close contact with another atom or a molecule, which play the role of inputs [4]. In order to extract output information from such a molecular (quantum) device, spectroscopic control of individual molecular states is needed, so at first, imaging and spectroscopy of states of the prospective molecules should be performed with atomic precision. Furthermore, the effect of external input stimulation on the molecular states of the device, for example with atomic-size defects, should be characterized with similar level of precision.

In order to facilitate molecular orbital imaging and spectroscopy based on the state-of-the-art use of modern nanotechnology tools, such as Scanning tunneling microscopy (STM) and Non-contact atomic force microscopy (Nc-AFM), electronic decoupling of the molecule in question from the underlying substrate is required. It is expected that proper isolation of such molecular entities could be achieved by application of passivated semiconductor surfaces, e.g., Si(001):H and Ge(001):H. A monolayer of hydrogen atoms may decouple molecules from a semiconductor surface as recently demonstrated by Bellec et al. [5], who imaged physisorbed pentacene molecules on hydrogen passivated silicon surfaces. Recorded images closely resemble the HOMO orbital contour of molecules and the dI/dU spectra provide additional confirmation of weak molecule substrate interaction. The STM image of the pentacene on the Si(001):H is shown in Fig. 1.

Similarly, also functionalized molecular platforms adsorbed on hydrogenated surfaces could be probed by STM technique as reported by Gruyters et al. [6], who measured iron phthalocyanine molecules on passivated silicon Si(111):H. The images recorded with different bias voltages provide insight into the electronic structure and are shown in Fig. 2.

Fig. 1 STM image of the pentacene molecule anchored on a step of the hydrogenated Si(001) surface; the image closely resembles the contour of molecule HOMO orbital. Reprinted with permission from Bellec et al. [5]

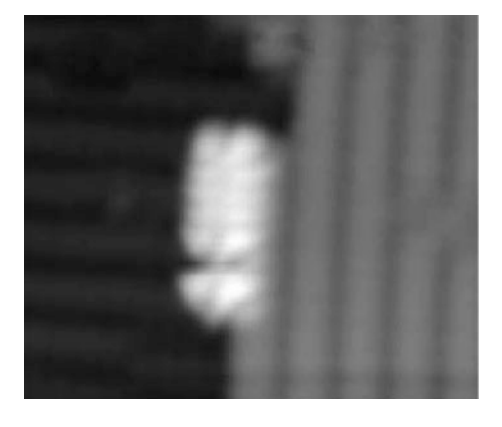
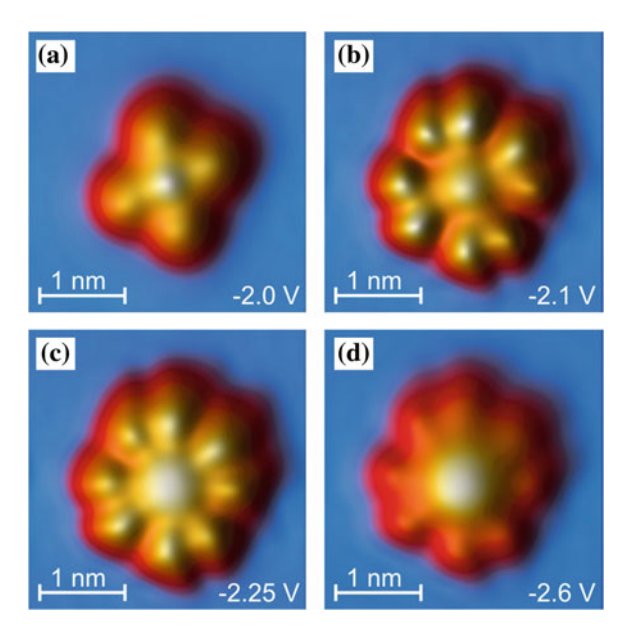


Fig. 2 STM filled-state images of the iron phthalocyanine molecule adsorbed on the hydrogenated Si(111) surface. Reprinted from Gruyters et al. [6] with permission



The application of passivated surfaces offers also the possibility to construct dangling-bond (DB) atomic-scale structures by STM tip-induced hydrogen desorption [7]. These DB structures may then serve as interconnects in molecular electronic devices. However, in principle the measurements of aromatic molecules on hydrogenated surfaces are extremely challenging due to high mobility of molecules. Moreover, the large band gap of the silicon substrate may hinder empty state probing especially if the states are hidden in the gap of the substrate. As a result only filled states are measured [5, 6].

Recent advances in quantum-chemical design and organic synthesis offer practical solutions toward fabrication of a suitable molecular logic gate. In general, we need planar aromatic molecules, which would physisorb on the passivated Ge(001):H and/or Si(001):H surface and should rather not be quite freely diffusing on those substrates but still the binding should allow for STM-tip induced manipulation over the surface. The molecules should have 3–4 branches allowing for anchoring them to dangling-bond defects (hydrogen monomer or dimer vacancies), so the lateral dimensions of the molecule branches should be correlated with a spacing of the reconstruction rows on the passivated surface.

One possibility is to use some symmetrical or non-symmetrical Y-shaped acenes, i.e., triphenylene-cored oligoacenes, as molecular gate building blocks. Therefore, in this study we decided to deposit a simple Y-shaped trinaphthylene, which could be considered as a prototypic molecule for the molecular logic gate devices. In our work, usage of hydrogen passivated Ge(001) allows for not only decoupling the molecules electronically (at least partially) from the low band gap substrate, but also offers an innovative way of producing interconnects by

108 M. Kolmer et al.

H-extraction with the STM tip, as described recently in Ref. [7]. The DB wires fabricated by STM-tip-induced H-extraction could also form logic structures providing specific input for the molecule device.

2 Ge(001) Surface Preparation and Molecule Deposition

The experiment was carried out in an ultra-high vacuum (UHV) system containing preparation and cryogenic microscope chambers. The STM measurements were performed with the Omicron low temperature scanning probe microscope (LT-STM/AFM). The base pressure was in the low 10^{-10} mbar range. The preparation chamber was supplied with a noble gas ion gun, a homebuilt hydrogen cracker, and an infrared pyrometer. The surface quality was monitored with a low energy electron diffraction (LEED) setup. The Ge(001) undoped wafers (TBL Kelpin Crystals) were mounted on sample holders and were heated by direct current flowing through the sample. The samples were first annealed for 6 h at 800 K, and subsequently the 15 min cycles of 600 eV Ar⁺ sputtering of the sample kept at 1040 K were repeated until a clean, well-defined surface was obtained, as checked by LEED and STM. The annealing temperature was controlled by the infrared pyrometer. Hydrogen passivation was performed with the use of a homebuilt hydrogen cracker providing atomic hydrogen. During passivation procedure the sample was kept at 485 K and the hydrogen pressure was maintained at 1×10^{-7} mbar. The STM imaging was carried out at reduced temperature of around 4 K (liquid helium) with etched tungsten tips used as probes. For image processing and STM data analysis SPIP and WSxM [8] software was used.

Figure 3 shows low temperature (liquid helium, 4 K) filled state STM images of Ge(001) (left panel) and hydrogen passivated Ge(001):H (right panel) surfaces. Ge(001) image exhibits clearly a mixed $c(4 \times 2)$ and $p(2 \times 2)$ surface

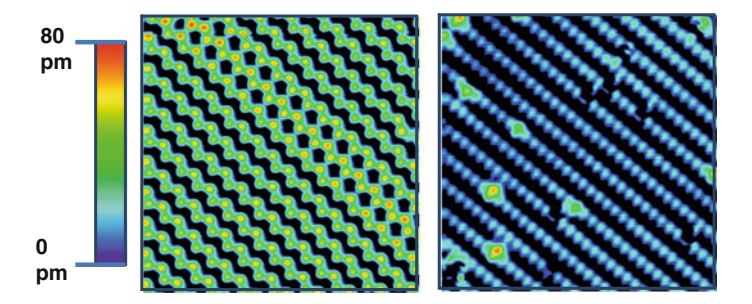
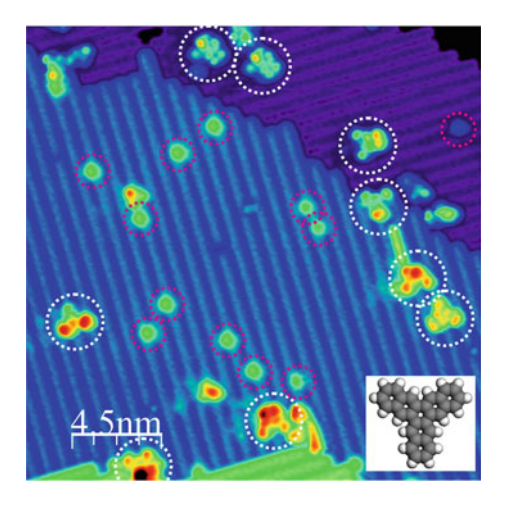


Fig. 3 Filled-state low temperature (4 K) STM images of the zig-zag dimer rows indicating mixed $c(4 \times 2)$ - and $p(2 \times 2)$ -Ge(001) surface reconstructions (*left panel*), and Ge(001)-(2 × 1):H (*right panel*) surfaces; scan size $10 \times 10 \text{ nm}^2$, STM parameters V = -0.5 V, and I = 1 nA

Fig. 4 LT STM image (25 × 25 nm) of the hydrogen passivated Ge(001) surface with individual trinaphthylene molecules (Y). White circles mark single Y molecules and red circles indicate individual DBs Tunneling current 2 pA, bias voltage -2.0 V. A scheme of the Y molecules is shown in the inset



reconstruction which arises from in-phase and out-of-phase buckling of neighboring Ge dimers. The hydrogenated surface is recorded as a ladder structure consisting of rows of Ge dimers passivated by hydrogen atoms. On the right panel image, one can distinguish three main types of intrinsic defects inevitably present on the surface. The brightest are attributed to surface double DBs (two dangling bonds on a Ge dimer), slightly smaller and less bright are single DBs (one dangling bond per Ge dimer). The third type recorded as dark depletion is ascribed to surface Ge atom vacancies. Note that the apparent height of surface double DBs is in principle identical to the height of surface Ge atoms on unpassivated surface.

In this work, low temperature scanning tunneling microscopy and non-contact atomic force microscopy (LT-STM/nc-AFM) measurements have been made on planar polyaromatic hydrocarbon molecules, namely the heptastarphene (trinaphthylene, Y) molecules deposited on the hydrogenated germanium surface. The Y molecules are prototypical 3 input/output molecules that could be applied in single molecule switches. The inset in Fig. 4 shows the scheme of Y molecule. Due to extremely high molecule mobility, Y molecules are evaporated on the sample which is removed from the microscope cryostat just before deposition. This procedure enables evaporation of molecules on the sample kept still at low temperature. The sample is inserted into the microscope cryostat immediately after molecule deposition. The molecules are evaporated at very low molecule flux with the evaporator kept at 450 K. A typical result of the deposition at relatively low dose is presented in Fig. 4, where LT-STM image $(25 \times 25 \text{ nm})$ of the hydrogen passivated Ge(001) surface with individual trinaphthylene molecules (Y) is shown.

110 M. Kolmer et al.

3 Molecular State Imaging of Heptastarphene Molecules Anchored on the Ge(001):H Surface with LT-STM

The molecules deposited on the hydrogenated germanium sample are physisorbed, and thus only weakly interact with the substrate. Therefore, after evaporation the molecules are mobile and move across the surface. This results in trapping of the molecules by surface defects and step edges. Some molecules are trapped by unidentified defects and are strongly interacting with these defects. Therefore these molecules could not be manipulated with the use of the STM tip. However, the vast majority of the molecules could be found immobilized by the well-known surface defects, i.e., characterized previously DB dimers [7]. These molecules do not interact very strongly with the defects and could be manipulated with the use of the STM tip. The procedure of the tip-induced lateral manipulation enables us to detach the molecules from the DB dimes and to place the molecules on the fully hydrogenated surface. Therefore, we can probe both the properties of molecules immobilized by surface DBs and molecules physisorbed on the surface without any defects in the vicinity.

At liquid helium temperature the molecules physisorbed on the hydrogenated surface prove to be stable during measurements allowing for acquisition of STM images with different bias voltages. In Fig. 5a the STM images obtained at different bias voltages are shown. The images obtained for -3.0 and +3.0 V voltage settings exhibit intramolecular contrast proving that the submolecular resolution of physisorbed molecules could be achieved. For bias voltages between -2.4 and +3.0 V almost no intramolecular contrast is recorded indicating that no molecule states are available for tunneling electrons and the recorded image is simply the image of the hydrogenated surface with the image contrast modulated by the molecule. To analyze the details of the molecule–substrate interaction and the electronic structure we performed extensive calculations. The density functional theory (DFT)-based calculations show that the HOMO–LUMO gap of free gas phase molecule reaches approximately 3.24 eV (HSE06 functional). In Fig. 5b calculated STM image of the molecule physisorbed on the Ge(001):H is shown. The image closely resembles the experimental images acquired for -2.0 V

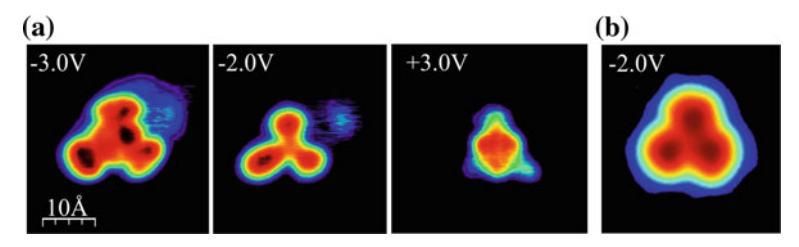


Fig. 5 a STM images of the physisorbed Y molecule acquired with different bias voltages denoted in the text. b Calculated STM image of Y molecule

indicating that the measurements are performed out of the resonances resulting in the imaging of the surface modified by the presence of the molecule.

4 3D Molecular State Probing with Simultaneous Tunneling Current and Force Imaging with a qPlus Sensor

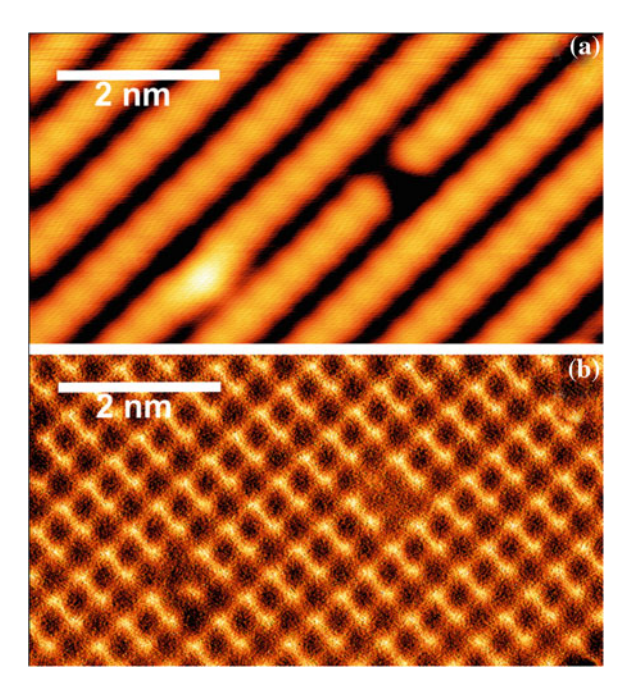
In recent years NC-AFM-related techniques have been developing very fast. One of the fields where fast progress is especially prominent is cryogenic NC-AFM. Following the footsteps of STM, for which going to low temperatures gave access to new fields in physics and chemistry, cryogenic NC-AFM is opening a range of new applications. There are some examples of highly successful NC-AFM experiments performed with the use of cantilever-based systems; however, the rapid growth of applications and accessibility of the field coincided with the introduction of quartz tuning forks as sensors. Additionally, a tuning fork can be equipped with a tip made of any material (for instance tungsten or Pt–Ir alloy) which can be connected to preamplifier by a separate lead allowing in principle for dual AFM/STM operation. Tuning forks are typically used in qPlus configuration—in which one of the prongs is glued to a ceramic holder while another, with a tip attached at its end, is oscillating freely.

Two consecutive images of the same area of the hydrogenated Ge(001):H surface taken with qPlus-based scanning probe microscope: topographic, constant current STM image, and constant height map of frequency shift are presented in Fig. 6a and b. The appearance of the STM image (Fig. 6a) is similar to the one presented in Fig. 3. The main features of the constant height image (Fig. 6b) are double rows of protrusions, i.e., positions where the tip had to adjust the frequency shift in order to maintain the required height. Note that Fig. 6b represents a map of the frequency shift, i.e., elevation indicates weaker attraction. The separation between the protrusions in a single row is about 0.37 nm, while the double rows are separated by 0.82 nm. Those values correspond quite closely to the postulated distances between hydrogen atoms adsorbed on a Ge dimer and the distance between dimer rows on the Ge(001) surface. Occasionally, defects can be observed on the surface, located over one of the hydrogen atoms in a dimer row. In the atomically resolved images, they are depicted as depressions.

Proper characterization of molecular adsorbates with the use of an NC-AFM based on qPlus sensor solution could provide an additional channel of information complementary to a standard STM study. In particular, possibility of simultaneous acquiring both the tunneling current and the detuning frequency maps for selected tip sensor heights above the surface opens new opportunities for 3D spectroscopy of molecular states. It is known that standard STS dI/dU spectroscopy for molecules adsorbed on surfaces provides information in which spatial distribution of the molecular state density is filtered by a specific surface band structure and the

112 M. Kolmer et al.

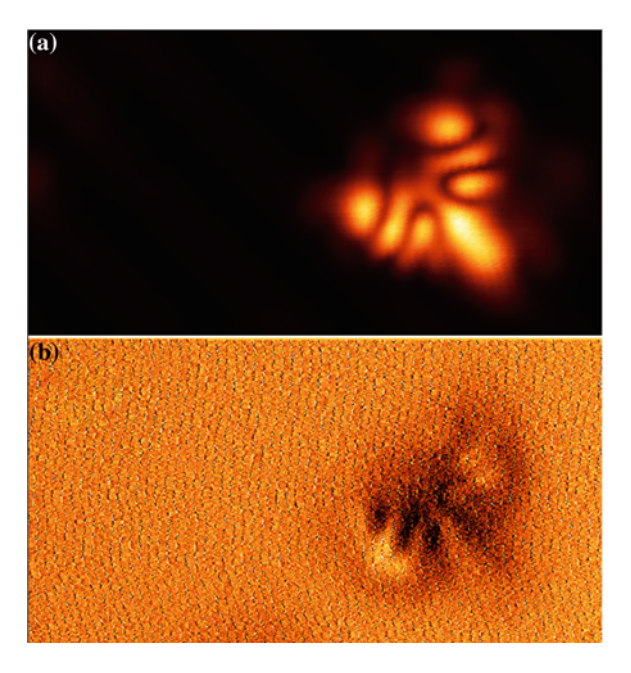
Fig. 6 Two consecutive images of the same area of hydrogenated Ge(001):H surface taken with qPlusbased scanning probe microscope; a topographic, constant current STM image, U = -0.5 V, the color scale spans over 0.15 nm; b constant height map of frequency shift $(f_0 = 22,970 \text{ Hz}, Q = 20,000, A = 500 \text{ pm})$, color scale corresponds to the range from -1.1 to -0.1 Hz



molecule-surface electronic coupling. For large surface band gaps and low level of coupling a large fraction of the density of states spectrum is not accessible in conventional STS measurements. This missing information could be retrieved by the proper analysis of the force maps measured by a qPlus sensor in parallel to tunneling current measurements.

In Fig. 7 the result of simultaneous STM/NC-AFM imaging of a single starphene molecule adsorbed at a defect on the Ge(001):H surface is shown. In this case, it is clear that the image is dominated by the interactions related to the density of electrons and hence is quite similar to the corresponding STM image. Till date it was impossible to approach the repulsive mode which could show the internal structure of a molecule, since binding to the surface is not strong enough and such an attempt resulted in uncontrolled manipulation of a molecule. However, since during the STM experiments a certain degree of control over location of the molecule on the surface (i.e. tip-induced manipulation) was achieved, further efforts will be undertaken to find a location stable enough to access molecular internal structure by the NC-AFM.

Fig. 7 Simultaneous imaging of "Y" molecule by STM and NC-AFM in constant height mode. a 5×2.7 nm current image, V = -0.5 V, color scale corresponds to currents from 0 to 3.1 nA; b 5×2.7 nm frequency shift image, color scale corresponds to frequency shift from -1.0 to 0.4 Hz



5 Concluding Remarks

In this report we showed that a symmetric Y-shaped starphene, a prototypic molecule for the molecular logic gate devices, could be successfully anchored and imaged on the passivated semiconductor surface, namely Ge(001):H, using an STM/NC-AFM scanning probe operating at cryogenic temperatures (4 K). It appears that a uniform monohydrate layer provides sufficient electronic decoupling of the molecular states from the semiconductor substrate providing insight into internal structure of the molecular orbitals by scanning tunneling current spectroscopy and force spectroscopy with an NC-AFM qPlus sensor. The physisorbed molecules could also be manipulated with the STM tip. This could be utilized in the future for sampling of various levels of the molecule coupling to the passivated surface defects, both native and at will, created by analyzing STM images of the molecules at the relevant locations. Finally, possibility of simultaneous acquiring of both the tunneling current and the detuning frequency maps for selected tip sensor heights above the surface has been successfully explored.

Acknowledgments This research was supported by the 7th Framework Programme of the European Union Collaborative Project ICT (Information and Communication Technologies) "Atomic Scale and Single Molecule Logic Gate Technologies" (ATMOL), Contract No. FP7-270028. The experimental part of the research was carried out with equipment purchased with financial support from the European Regional Development Fund in the framework of the Polish Innovation Economy Operational Program (Contract No. POIG.02.01.00-12-023/08).

114 M. Kolmer et al.

References

- 1. Fiurasek, J., et al.: Intramolecular Hamiltonian logic gates. Physica E 24(3–4), 161–172 (2004)
- Joachim, C., Gimzewski, J.K., Aviram, A.: Electronics using hybrid-molecular and monomolecular devices. Nature 408(6812), 541–548 (2000)
- 3. Prauzner-Bechcicki, J.S., Godlewski, S., Szymonski, M.: Atomic- and molecular-scale devices and systems for single-molecule electronics. Phys. Status Solidi (a) **209**, 603–613 (2012)
- Soe, W.-H., Manzano, C., Renaud, N., De Mendoza, P., De Sarkar, A., Ample, F., Hliwa, M., Echavarren, A.M., Chandrasekhar, N., Joachim, C.: Manipulating molecular quantum states with classical metal atom inputs: demonstration of a single molecule NOR logic gate. ACS Nano 5, 1436–1440 (2012)
- 5. Bellec, A., Ample, F., Riedel, D., Dujardin, G., Joachim, C.: Imaging molecular orbitals by scanning tunneling microscopy on a passivated semiconductor. Nano Lett. 9, 144–147 (2009)
- Gruyters, M., Pingel, T., Gopakumar, T.G., Néel, N., Schütt, Ch., Köhler, F., Herges, R., Berndt, R.: Electronic ground-state and orbital ordering of iron phthalocyanine on H/Si(111) unraveled by spatially resolved tunneling spectroscopy. J. Phys. Chem. C 116, 20882–20886 (2012)
- Kolmer, M., Godlewski, S., Kawai, H., Such, B., Krok, F., Saeys, M., Joachim, C., Szymonski, M.: Electronic properties of STM-constructed dangling-bond dimer lines on a Ge(001)-(2 × 1):H surface. Phys. Rev. B 86, 125307 (2012)
- Horcas, I., Fernández, R., Gómez-Rodríguez, J. M., Colchero, J., Gómez-Herrero, J., Baro, A. M.: WSXM: a software for scanning probe microscopy and a tool for nanotechnology. Rev. Sci. Instr. 78, 013705 (2007)

Part V STM Theory and Image Interpretation

Simulations of Constant Current STM Images of Open-Shell Systems

M. Kepenekian, R. Robles, R. Korytár and N. Lorente

Abstract In this chapter we review the main methods for simulating STM images, mainly the Tersoff–Hamman approximation based on the Bardeen approach and full-fledge Landauer calculations based on nonequilibrium Green's functions (NEGF). However, these methods are built on the electronic structure of the system as computed by density functional theory (DFT). This theory has important limitation for open-shell systems. As a matter of fact, an open-shell molecule on a metallic substrate can lead to correlations among the electrons of the metal. This gives rise to the Kondo effect. Hence, we briefly present a method to implement STM image simulations including the Kondo effect.

1 Introduction

Condensed matter theory has seen a fast evolution since the late 1970s. From being a qualitative theory where sometimes getting the right sign of the concern quantity was considered a remarkable achievement, it reached a status of being able to actually predict the quantities and, in general, to be within a factor of two of experiment [1]. This quantum leap was made possible by the advent of density functional theory (DFT). The 1970s saw the birth of many numerical methods devoted to the actual calculation of the Hohenberg-Kohn theorem [2] and the Kohn and Sham equations [3]. Surface science has been a great beneficiary of DFT, already from the early stages of development [4]. Later on, with the

M. Kepenekian (☒) · R. Robles · R. Korytár · N. Lorente Centro de Investigación en Nanociencia y Nanotecnología, CSIC-ICN, Bellaterra 08193, Spain

e-mail: mikael.kepenekian@cin2.es

R. Korytár

Institut für Nanotechnologie, Karlsruher Institut für Technologie, Hermann-von-Helmholtzplatz 1, 76344 Eggenstein-Leopoldshafen, Germany invention of the scanning tunneling microscope (STM), DFT-based methods were put in practice and simulations of STM images were soon realized [5, 6].

Limitations in the simulations are due to two different types of approximation: (1) approximations of the tunneling current, i.e., the Tersoff–Hamman approximation [5, 6] and (2) approximations of the underlying electronic structure, i.e., the used DFT approximation. There exist a hierarchy of approximations of the Schrödinger's equation improving on the current description and hence attacking the first type of limitations. The improvements range from including realistic tip and sample electronic structures using a tunneling formalism such as the Bardeen one [7], to proper electronic current calculations including a realistic voltage drop and a nonequilibrium formalism [8–10]. Obviously, the computational cost increases dramatically as the accuracy of the calculation improves.

But there are also limitations due to the approximate character of realistic DFT approaches. Hence, the electronic structure that enters the current calculation is already faulty at some degree. One of the most challenging cases for present implementations of DFT is the calculation of open-shell atoms and molecules on metallic surfaces. Indeed, in these cases, charge fluctuations become important. At low substrate temperatures, the fluctuations manage to correlate the sample's electrons [11], and the system can only be described using dynamical many-body theory. This is out of reach of present approaches of DFT that are based on a mean-field view of many-body correlations.

In this chapter, we review the most common approaches of STM image simulations based on DFT. We briefly expose the Bardeen and Tersoff–Hamman approaches and then move on to the more involved nonequilibrium Green's functions (NEGF) methods for current calculations. But the main objective of this chapter is to render an account of how to go beyond mean-field and correctly treat open-shell correlations. There are increasing scores of experimental work showing that indeed open-shell systems do exist and have important consequences in the STM data [12–14]. We pretend to give a first step towards the comprehension of these experimental data.

2 Simulation of Constant Current STM Images

The most popular approach to simulate tunneling currents is based on the tunneling transfer matrix developed by Bardeen [7]. It is based on the fact that the electronic structure of both tip and sample are not perturbed by each other. Hence, only the Shrödinger equation for each electrode needs to be solved. See Fig. 1 for a scheme of a tunneling junction in Bardeen's approach. This is obviously valid when the mutual interaction is indeed negligible, which is generally true in the case of tunneling currents. Here, we summarize the main steps of the Bardeen approach and direct the reader to a more complete account elsewhere [15].

The Hamiltonian is divided in two parts corresponding to the influence area of each electrode. Hence, there are two different sets of eigentsates, each of each region, $\{\psi_{u,L}\}$ and $\{\psi_{v,R}\}$:

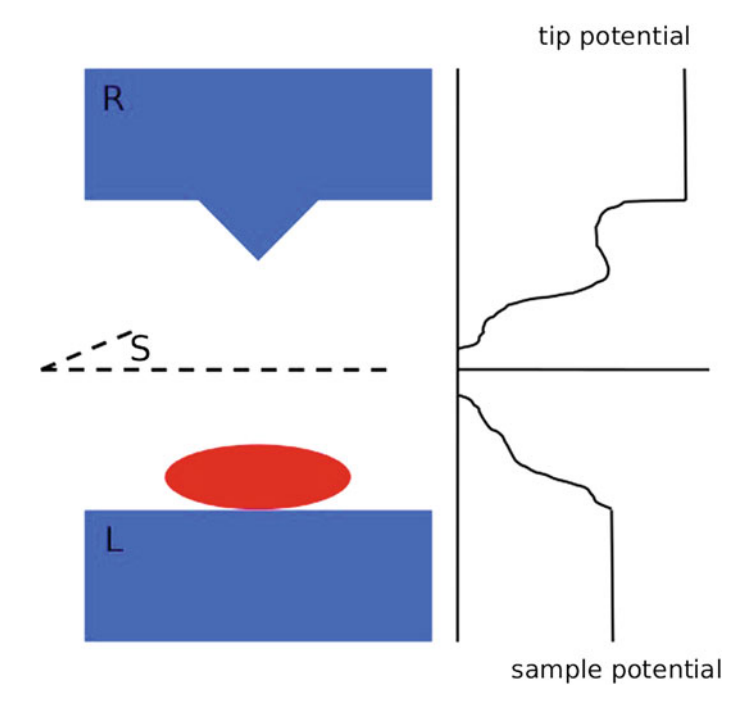


Fig. 1 Schematic picture of the division of the system into *left* and *right* regions. Both tip and sample potentials cannot be simultaneously non zero

$$egin{aligned} \left(-rac{\hbar^2
abla^2}{2m} + V_L
ight)\!\psi_{\mu,L} &= arepsilon_{\mu,L}\!\psi_{\mu,L} \ \left(-rac{\hbar^2
abla^2}{2m} + V_R
ight)\!\psi_{
u,R} &= arepsilon_{
u,R}\!\psi_{
u,R}. \end{aligned}$$

The total Hamiltonian being

$$\hat{H} = -\frac{\hbar^2 \nabla^2}{2m} + V_L + V_R + \Delta V.$$

The first step in Bardeen's approximation is to show that we can write a Fermi's Golden rule-like expression [16] for the transition rate of a left state into right states. For this, we write a wavepacket that is a combined time-dependent wavefucntion of both electrodes:

$$\psi(\mathbf{r},t) = \sum_{\nu} a_{\nu}(t)\psi_{\nu,R}(\mathbf{r})e^{-i\varepsilon_{\nu}t/\hbar} + \sum_{\mu} a_{\mu}(t)\psi_{\mu,L}(\mathbf{r})e^{-i\varepsilon_{\mu}t/\hbar}.$$
 (1)

Then, using the Schrödinger's equation with the initial condition

$$\psi(\mathbf{r},t=0) = a_0(t)\psi_{0,L}(\mathbf{r})e^{-i\varepsilon_0 t/\hbar},$$

we compute the probability to find the wavepacket on the final right state $\psi_{\alpha,R}$, $P_{0\to\alpha} = |\langle \psi(\mathbf{r},t) | \alpha, R \rangle|^2 = |a_{\alpha}(t)|^2$, that is:

$$P_{0\to\alpha} = \left| \frac{e^{i(\varepsilon_{\alpha}-\varepsilon_{0})t/\hbar}-1}{\varepsilon_{\alpha}-\varepsilon_{0}} \right|^{2} |\langle \alpha,R|V_{R}+\Delta V|0,L\rangle|^{2}.$$

And hence, the transition rate is:

$$\frac{1}{\tau} = \sum_{\alpha} \frac{\mathrm{d}P_{0\to\alpha}}{\mathrm{d}t}.$$

Finally, in the long time and continuum limits [16]:

$$rac{1}{ au} = rac{2\pi}{\hbar} \sum_{lpha} \left| \langle lpha, R | V_R + \varDelta V | 0, L \rangle \right|^2 \delta(arepsilon_lpha - arepsilon_0).$$

Now, the matrix element is evaluated using that the electrodes do not perturb each other and inverting the Schrödinger equation:

$$egin{aligned} V_R |lpha,R
angle &= \left(-rac{\hbar^2
abla^2}{2m} - arepsilon_lpha
ight) |lpha,R
angle \ V_L |0,L
angle &= \left(-rac{\hbar^2
abla^2}{2m} - arepsilon_0
ight) |0,L
angle. \end{aligned}$$

The matrix element can be approximated then by,

$$\langle \alpha, R | V_R + \Delta V | 0, L \rangle \approx \langle \alpha, R | -\frac{\hbar^2 \nabla^2}{2m} - \varepsilon_{\alpha} | 0, L \rangle_R + \langle 0, L | -\frac{\hbar^2 \nabla^2}{2m} - \varepsilon_0 | \alpha, R \rangle_R$$

$$\approx \int_R -\frac{\hbar^2}{2m} \nabla \cdot [\psi_{\alpha, \mathbf{R}} \nabla \psi_{\mathbf{0}, \mathbf{L}}^* - \psi_{\mathbf{0}, \mathbf{L}}^* \nabla \psi_{\alpha, \mathbf{R}}] \mathbf{d}^3 \mathbf{r}$$

$$\approx \hbar i \int_S \mathbf{J}_{\alpha, \mathbf{0}} \cdot \mathbf{dS}$$
(2)

Replacing the above expression in the rate calculation, we can compute the tunneling current using that it is the time rate of electron transfer times the charge of the electron:

$$I = -\frac{2\pi e}{\hbar} \sum_{\nu,\alpha} (f_L(\varepsilon_{\nu}) - f_R(\varepsilon_{\mu})) \times \left| \hbar \int_{S} \mathbf{J}_{\alpha,\nu} \cdot \mathbf{dS} \right|^2 \delta(\varepsilon_{\alpha} - \varepsilon_{\nu}). \tag{3}$$

Tersoff and Hamman [5, 6] reduced the tunneling current calculation to a simplified expression. Tersoff and Hamman considered a spherical tip retaining the s-wave of the tip's electronic wavefunction. Later on, Chen [17] gave a hierarchy of successive improvements by including higher terms in the wave expansion.

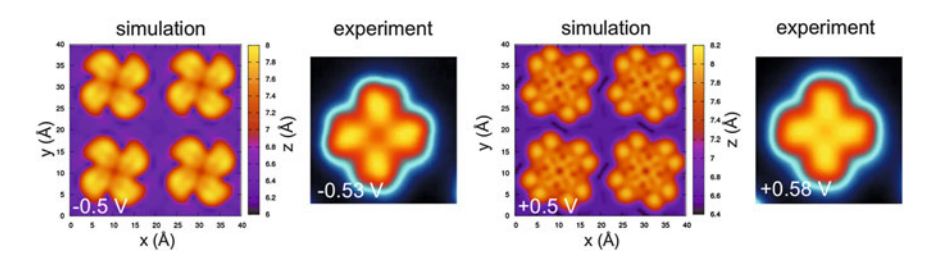


Fig. 2 Experimental and simulated constant current images of CuPc adsorbed on Ag(100) at -0.5 and +0.5 V. The simulated image is performed using the Tersoff-Hamman approach [22]

The Tersoff-Hamman approximation is based on the linear behavior of current with voltage and the spherical symmetry of the electronic structure of the tip's wave function. The first point implies that only the electronic structure of the substrate at the Fermi energy will create the STM image. The second is good for a tip electronic structure that is featureless.

The use of Tersoff–Hamman approximation from DFT calculations has been successful in the simulation of the STM imaging of closed-shell molecules [18, 19]. Recently, it has been shown to be also accurate in the description of constant current images of open-shell molecules [20, 21]. Here, we consider the case of a copper-phthalocyanine (CuPc) adsorbed on Ag(100) [22–24]. CuPc presents an open-shell d^9 electronic configuration on the metallic ion plus a closed-shell phthalocyanine. When adsorbed on Ag(100), a charge transfer of about 1 electron from the surface to the phthalocyanine ring occurs leading to an open-shell ligand with a half-spin [24]. Both magnetic moments of the phthalocyanine and the copper ion are ferromagnetically coupled leading to a triplet ground state.

In Fig. 2 we show the simulated STM image (left images) and the experimental ones [22] for two different biases. Here, the Tersoff–Hamman approximation is extended to include finite bias by adding up the contribution to the local density of states in an energy window corresponding to the applied voltage. We see that for negative bias the agreement is very good. Indeed, it clearly shows the chiral character of the hybridized molecule-surface electronic states [22]. However, the agreement is reduced for positive bias. Despite an overall agreement there is more molecular contrast in the theoretical image. The difference is actually due to a simplified calculation of the surface electronic states and not a failure of the Tersoff–Hamman approximation as more involved calculations have shown.

3 Beyond the Perturbative Approach

In the case that the interaction between tip and sample cannot be neglected, one must go beyond the perturbative Bardeen scheme. The way to do so is to take explicitly into account the tip and the sample. Then, the current can be calculated

122 M. Kepenekian et al.

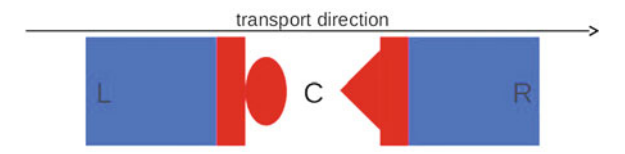


Fig. 3 Schematic picture of the division of the system into a central contact (C), and left (L) and right (R) electrode regions. The z axis corresponds to the transport direction

using one of the different schemes for computing ballistic currents. Here we choose the NEGF-based method. A more complete account of the method can be found in Ref. [25].

We consider the following situation (see Fig. 3): a left semi-infinite electrode (L), a contact region (C), and a right semi-infinite electrode (R). We use an atomic orbital basis set with a finite range as implemented in the SIESTA DFT code [26, 27]. This basis enables us to split the space into these regions. The electrode regions L and R are chosen so that all the disturbances in the C region are assumed to be screened out before the electrodes. Thus, the matrix takes the following form,

$$\mathcal{H} = \begin{pmatrix} \mathbf{H}_L & \mathbf{V}_L & 0 \\ \mathbf{V}_L^{\dagger} & \mathbf{H}_C & \mathbf{V}_R \\ 0 & \mathbf{V}_R^{\dagger} & \mathbf{H}_R \end{pmatrix}$$
(4)

where \mathbf{H}_L and \mathbf{H}_R are semi-infinite tridiagonal matrices identical to the corresponding Hamiltonian for the semi-infinitely repeated layer structure for the L or R electrodes, and can be calculated once and for all using periodic boundary conditions. We are only interested in the central region. Thus, we limit our inspection to the inversion of the corresponding finite matrix and take into account the effect of the electrodes thanks to the self-energies,

$$\mathbf{G}(E) = (E + i\delta - \mathbf{H}_C - \Sigma_L(E) - \Sigma_R(E))^{-1}$$
(5)

where the one electron self-energies, $\Sigma_{L,R}$, fully take into account the coupling of C to L and R. Thanks to the perfect semi-infinite layer structure of the electrodes, the self-energies can be calculated exactly using recursion-like methods. Roughly speaking, the real part of $\Sigma_{L,R}$ describes the change in energy levels in region C due to the bond formation with the L, R electrodes, whereas the imaginary part describes the decay (inverse lifetime) of electronic states located inside the C-region.

Defining $\Gamma_{L,R}(E)$ related to the imaginary part of the corresponding self-energies and hence to the inverse lifetimes of electronic states in the *C*-region (see Eq. 6), we can write the density matrix, which is related to the density inside region *C* resolved in electronic states,

$$\Gamma_L(E) = i \Big(\Sigma_L(E) - \Sigma_L^{\dagger}(E) \Big)$$
 (6)

Practically with the DFT approach, we calculate electronic density and potential by solving the Kohn–Sham and Poisson equations, the difference is that the electron density inside the central region is deduced from nonequilibrium set of Kohn–Sham equations [25]. As a consequence, we can evaluate the changes of the electron density in the sample and the tip due to the voltage drop. This can lead to forces and structural changes that are considered.

In the case of elastic electron transport, the conductance G can eventually be calculated following a Landauer-Büttiker-like formula [8],

$$G = G_0 \int dE \left(n_F (E - E_F^L) - n_F (E - E_F^R) \right) Tr[\Gamma_R \mathbf{G} \Gamma_L \mathbf{G}^*]$$
 (7)

where G_0 is the quantum of conductance $G_0 = 2e^2/h$.

In the previous section, we showed the good qualitative agreement of the Tersoff–Hamman approach. A more involved calculation as the one presented here, can give a quantitative agreement. In order to show an example, we compare the theoretical and experimental dI/dV, using the above theory. Figure 4 shows the computed transmission (like a simplified dI/dV, an excellent approximation in the absence of strong bias effects) compared with the experimental dI/dV taken from Ref. [24] The overall behavior is very well reproduced. Only the fine structure at 0 bias is missing. But this is related to Kondo features to be treated in the next section.

By considering both the tip and the sample explicitly in the DFT calculation, this approach allows one to reproduce the interaction between both electronic structures. The effect of the bias is also fully described. Unfortunately, the DFT-NEGF approach suffers from the limitations of the DFT treatment. In particular, when strong local correlation effects are to be considered. Such effect is expected in the case of open-shell molecules adsorbed on metallic surfaces. As an important example, the next section focuses on the Kondo resonance observed for some magnetic atoms and molecules associated with conductive surfaces.

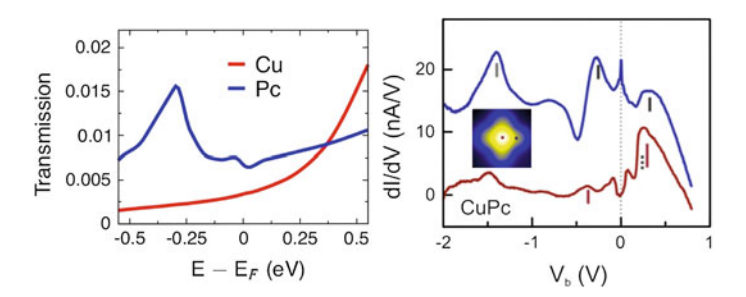


Fig. 4 Calculated transmission (left) and experimental [24] dI/dV (right) of CuPc on Ag(100). Blue and red lines correspond to the tip positioned on top of the phthalocyanine and copper ion, respectively

4 A NCA Approach to the Kondo Effect

The Kondo problem deals with the interaction of a magnetic moment (and hence of an open-shell molecule) with electronic conduction bands [11]. The historical motivation for studying this problem was the discovery of anomalies in the resistivity measurements of dilute alloys. Indeed, for some host metal, the doping with magnetic impurities such as cobalt or iron lead to a minimum in the temperature dependence of resistivity.

Jun Kondo [28] showed that the resistance minimum is due to a subtle mechanism nowadays known as Kondo effect. The mechanism relies on the ability of a magnetic impurity to induce spin flips of conduction electrons (see Fig. 5). The simplified Hamiltonian which captures this effect is known as the Kondo Hamiltonian and has the form

$$H_K = \sum_{\mathbf{k}\sigma} \varepsilon_{\mathbf{k}\sigma} c_{\mathbf{k}\sigma}^{\dagger} c_{\mathbf{k}\sigma} + J\mathbf{s}(\mathbf{0}) \cdot \mathbf{S}$$
(8)

The first term is the Hamiltonian of noninteracting Bloch electrons. The second term is due to a magnetic impurity having exchange coupling with conduction electrons. The impurity spin, represented by a spin operator S, is coupled to the spin of conduction electrons s(0) at the impurity site 0. The coupling between conduction electrons and the magnetic impurity is antiferromagnetic. Therefore, the constant J is taken positive. The spin-flip interaction in the Kondo Hamiltonian does not come from the Coulomb exchange, but is due to hybridization of conduction states and an impurity orbital, having strong on-site repulsion.

Besides the minimum in the resistivity dependence with temperature, the Kondo effect is accompanied by a sharp resonance on the Fermi level in the impurity spectral function. This feature has become the most popular signature of the Kondo effect since it can be easily seen in scanning tunneling spectroscopy experiences [12–14]. Indeed, at low temperature, one can observe a sharp resonance, the Kondo resonance, in the $\mathrm{d}I/\mathrm{d}V$ spectra when the tip is probing the magnetic impurity.

4.1 The Anderson Hamiltonian

Model Hamiltonians are extremely powerful tools of physics as they deliver a large amount of information in a simple form. One of the most used model Hamiltonian in the case of magnetic impurities is the Anderson Hamiltonian [29].



Fig. 5 Scheme of the spin-flip scattering of an incoming conduction electron (blue) off the localized magnetic impurity (red)

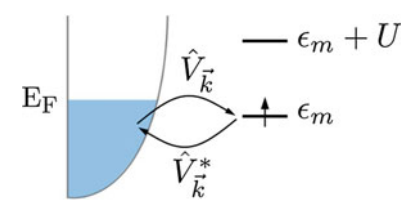


Fig. 6 The Anderson Hamiltonian. The impurity level ε_m is hybridized with the continuum through \hat{V}_k . The double occupancy of the impurity level leads to the Coulomb on-site repulsion U

The idea is that the impurity is weakly coupled to the continuum with its level ε_d well below the Fermi level, i.e., $\varepsilon_d < E_F$. The impurity conserves a single occupancy at the condition that the on-site Coulomb repulsion U is large enough, i.e., $\varepsilon_d + U > E_F$ (see Fig. 6). This leads to the following Hamiltonian:

$$\hat{H} = \sum_{n\mathbf{k}\sigma} \varepsilon_{n\mathbf{k}\sigma} \hat{c}_{n\mathbf{k}\sigma}^{\dagger} \hat{c}_{n\mathbf{k}\sigma} + \sum_{\sigma} \epsilon_{m} c_{m\sigma}^{\dagger} c_{m\sigma} + U c_{m\uparrow}^{\dagger} c_{m\uparrow} c_{m\uparrow} c_{m\downarrow} + \sum_{\mathbf{k}\sigma} \left(\hat{V}_{\mathbf{k}} \hat{c}_{m\sigma}^{\dagger} \hat{c}_{n\mathbf{k}\sigma} + \hat{V}_{\mathbf{k}}^{*} \hat{c}_{nk\sigma}^{\dagger} \hat{c}_{m\sigma} \right)$$

$$(9)$$

The first term is again the noninteracting Bloch electrons. n and \mathbf{k} are band index and k-vector of the Bloch states. Then is the impurity orbital m with the on-site energy ε_m . The double occupancy of m triggers the on-site Coulomb repulsion U. The last term is the hybridization of the impurity with the band states. The operator $\hat{c}_{m\sigma}^{\dagger}\hat{c}_{n\mathbf{k}\sigma}$ destroys an electron in the conduction band and creates a new one on the impurity with the same spin.

4.2 The Noncrossing Approximation

Our main goal here is to evaluate the impurity Green function and the spectral function showing the Kondo resonance. Indeed, this quantity can be directly related to STM experiments. This is achieved by a perturbation expansion on the hybridization. We consider the following Hamiltonian:

$$\hat{H} = \hat{H}_{\text{metal}} + \hat{H}_i + \hat{H}_{\text{hyb}} \tag{10}$$

$$\hat{H}_{\text{metal}} = \sum_{n \mathbf{k} \sigma} \varepsilon_{n \mathbf{k} \sigma} \hat{c}^{\dagger}_{n \mathbf{k} \sigma} \hat{c}_{n \mathbf{k} \sigma} \tag{11}$$

$$\hat{H}_{i} = \sum_{mm'} h_{mm'} |m\rangle\langle m'| \tag{12}$$

This Hamiltonian has a more general form and is referred to as the multi-orbital Anderson Hamiltonian. We will restrict ourselves to an impurity occupied by N and N+1 electrons. This means that only one electron is allowed to be transferred from the substrate to the molecule at the time. This is equivalent to making U tending to infinity. Therefore the hybridization is written as

$$\hat{H}_{\text{hyb}} = \sum_{\{N\}\{N+1\}} \sum_{n\mathbf{k}\sigma m} \langle m\sigma | \hat{V} | n\mathbf{k}\sigma \rangle \langle N+1 | \hat{c}_{m\sigma}^{\dagger} | N \rangle | N+1 \rangle \langle N | \hat{c}_{n\mathbf{k}\sigma} + h.c.$$
 (13)

where we take into account the one-body potential connecting impurity and substrate:

$$\hat{V} = \sum_{n \mathbf{k} \sigma n} \langle m \sigma | \hat{V} | n \mathbf{k} \sigma \rangle \hat{c}_{m\sigma}^{\dagger} \hat{c}_{n \mathbf{k} \sigma} + h.c.$$
 (14)

In the following we will consider: greek letters for the basis set of the impurity with N electrons, latin letters for the impurity with N+1 electrons, and $\{m, m', \ldots\}$ to denote single-electron orbitals. Hence,

$$\hat{H}_{\text{hyb}} = \sum_{\alpha i} \sum_{n \mathbf{k} \sigma m} \langle m \sigma | \hat{V} | n \mathbf{k} \sigma \rangle \langle i | \hat{c}_{m\sigma}^{\dagger} | \alpha \rangle | i \rangle \langle \alpha | \hat{c}_{n \mathbf{k} \sigma} + h.c.$$
 (15)

$$= \sum_{n\mathbf{k}\sigma m} \left(\sum_{\alpha i} V_{i\alpha}^{n\mathbf{k}\sigma} \hat{c}_{n\mathbf{k}\sigma} |i\rangle \langle \alpha| + h.c. \right)$$
 (16)

with

$$V_{i\alpha}^{n\mathbf{k}\sigma} = \sum_{m} \langle m\sigma | \hat{V} | n\mathbf{k}\sigma \rangle \langle i | \hat{c}_{m\sigma}^{\dagger} | \alpha \rangle \tag{17}$$

$$V_{\alpha i}^{n\mathbf{k}\sigma} = \sum_{m} \langle n\mathbf{k}\sigma | \hat{V} | m\sigma \rangle \langle \alpha | \hat{c}_{m\sigma}^{\dagger} | i \rangle.$$
 (18)

The noncrossing approximation (NCA) of Kuramoto [30] and Grewe [31] can be derived in different ways. Kroha and coworkers have exploited the slave-boson technique of Coleman [32] and produce a complete study of the multi-orbital NCA [33]. Here, we prefer to use the derivation by Bickers and co-workers [34]. In simple terms, we can picture the NCA as a self-consistent approach based on the change of the impurity's Green's function by the change of the impurity's charge state. Hence, we start by defining the impurity's Green's function (in this case, the resolvent) for fixed charge states, N and N+1:

$$\hat{R}^{(N)}(z) = \left[z\hat{\mathbb{I}} - \hat{h}^{(N)} - \hat{\Sigma}^{(N)}\right]^{-1}$$
(19)

$$\hat{R}^{(N+1)}(z) = \left[z\hat{\mathbb{I}} - \hat{h}^{(N+1)} - \hat{\Sigma}^{(N+1)}\right]^{-1}.$$
 (20)

Here, $\hat{h}^{(N)}$ is the impurity's Hamiltonian, Eq. (12), for N electrons. The fact that the charge state can change is reflected in the appearance of a self-energy that considers the other charge state made possible by the hybridization to the substrate. Intuitively then, we may expect that these self-energies are the square of the hybridization term times the resolvent of the *other* charge state. And, indeed, the more involved calculations by Bickers [34] yield something very close:

$$\Sigma_{\alpha\alpha'}^{(N)} = \sum_{ii} \sum_{n\mathbf{k}\sigma} f(\varepsilon_{n\mathbf{k}\sigma}) V_{\alpha j}^{n\mathbf{k}\sigma} R_{ji}^{(N+1)} (\omega + \varepsilon_{n\mathbf{k}\sigma}) V_{i\alpha'}^{n\mathbf{k}\sigma}$$
(21)

$$\Sigma_{ij}^{(N+1)} = \sum_{\alpha\alpha'} \sum_{n\mathbf{k}\sigma} f(-\varepsilon_{n\mathbf{k}\sigma}) V_{i\alpha}^{n\mathbf{k}\sigma} R_{\alpha\alpha'}^{(N)}(\omega - \varepsilon_{n\mathbf{k}\sigma}) V_{\alpha'j}^{n\mathbf{k}\sigma}$$
(22)

The fact that the self-energy depends on the resolvent of the other charge state generates an infinite sequence of powers on the hybridization term if we solve, self-consistently, the above sets of equations. As in all self-consistent generation of perturbation terms, even if the perturbation series is summed to all orders, many perturbation terms are not generated. Indeed, if drawn by diagrams, the perturbation terms that do not cross are the only one retained in the perturbation expansion.

In order to actually evaluate the NCA equations in a realistic system, we prefer to rewrite the self-energies using a Γ -function that permits us to express the self-energies as convolutions. Then, the convolution theorem can be used, and efficient fast-Fourier transforms renders the calculation very efficient. Hence, using the following definition of the Γ -function, the self-energies can be expressed as:

$$\Gamma_{j\alpha'}^{\alpha i}(\omega) = \sum_{n\mathbf{k}\sigma} V_{\alpha i}^{n\mathbf{k}\sigma} V_{j\alpha'}^{n\mathbf{k}\sigma} \delta(\omega - \varepsilon_{n\mathbf{k}\sigma})$$
(23)

$$\Sigma_{\alpha\alpha'}^{(N)}(\omega) = \sum_{ij} \int f(\omega') \Gamma_{j\alpha'}^{\alpha i}(\omega') R_{ij}^{(N+1)}(\omega + \omega') d\omega'$$
 (24)

$$\Sigma_{ij}^{(N+1)}(\omega) = \sum_{\alpha\alpha'} \int f(-\omega') \Gamma_{\alpha'j}^{i\alpha}(\omega') R_{\alpha\alpha'}^{(N)}(\omega - \omega') d\omega'$$
 (25)

It is straightforward to find the resolvents for fixed states by iteration of the above equations. However, we are searching for the Green's function of the full system. This means that the charge state of the impurity will be fluctuating as should be due to its open-shell electronic structure. In order to take this into

account, we perform a thermal average of the resolvents. This is immediately done if the thermal impurity's Green's function is considered:

$$G_{mm'}^{\sigma\sigma'}(\tau) = -\langle \operatorname{Tr}\{\hat{a}_{m}^{\sigma}(\tau)\hat{a}_{m'}^{\sigma'\dagger}(0)\}\rangle$$
 (26)

Let us notice here that $\hat{a}_{m}^{\sigma}(\tau)$ is not a standard fermionic operator. They are called Hubbard operators and can be expressed in terms of standard fermionic operators, \hat{c}_{m}^{σ} , in the following way:

$$a_m^{\sigma} = \sum_{\{N\}\{N+1\}} |N\rangle\langle N|\hat{c}_m^{\sigma}|N+1\rangle\langle N+1|$$
(27)

$$= \sum_{\alpha i} |\alpha\rangle\langle\alpha|\hat{c}_m^{\alpha}|i\rangle\langle i| \tag{28}$$

$$a_m^{\sigma\dagger} = \sum_{\{N\}\{N+1\}} |N+1\rangle\langle N+1|\hat{c}_m^{\sigma\dagger}|N\rangle\langle N|$$
 (29)

We can replace these expressions in the expression for the thermal Green's function, Eq. (26), and find:

$$G_{mm'}^{\sigma\sigma'}(\tau) = -\sum_{\alpha\alpha'} \sum_{ii} \langle \text{Tr}\{e^{H\tau}|\alpha\rangle\langle\alpha|\hat{c}_{m}^{\sigma}|i\rangle\langle i|e^{-H\tau}|j\rangle\langle j|\hat{c}_{m'}^{\sigma'\dagger}|\alpha'\rangle\langle\alpha'|\}\rangle$$
(30)

$$= -\sum_{\alpha\alpha'} \sum_{ij} \langle \text{Tr}\{e^{H\tau} | \alpha\rangle \langle i | e^{-H\tau} | j \rangle \langle \alpha | \hat{c}_m^{\sigma} | i \rangle \langle j | \hat{c}_{m'}^{\sigma'\dagger} | \alpha' \rangle \langle \alpha' | \} \rangle, \tag{31}$$

which is a practical form, since it will permit us to separate, at least partially, spin and orbital degrees of freedom. As a consequence, the spin of the impurity is reflected in the appearance of coefficients that depend on Clebsch–Gordan coefficients as we shall see later on. Hence, the final expression can be recasted as

$$G_{mm'}^{\sigma\sigma'}(\tau) = -\sum_{\alpha\alpha'ij} \langle \alpha | \hat{c}_m^{\sigma} | i \rangle \langle j | \hat{c}_{m'}^{\sigma'\dagger} | \alpha' \rangle G_{i\alpha',\alpha j}(\tau)$$
(32)

If we Fourier-transform [35] it into imaginary frequencies (remember we are dealing with thermal Green's functions), it can be easily transformed into real frequencies via analytical continuation:

$$G_{i\alpha',\alpha j}(\omega + i\eta) = \frac{1}{\mathscr{Z}_i} \int d\omega' e^{-\beta\omega'} \left[A_{\alpha'\alpha}^{(N)}(\omega') R_{ij}^{(N+1)}(\omega' + \omega + i\eta) - R_{\alpha'\alpha}^{(N)}(\omega' - \omega - i\eta) A_{ij}^{(N+1)}(\omega') \right]$$
(33)

with

$$A_{\alpha'\alpha}^{(N)}(\omega) = \frac{i}{2\pi} \left[R_{\alpha'\alpha}^{(N)}(\omega + i\eta) - R_{\alpha\alpha'}^{(N)*}(\omega + i\eta) \right]$$
(34)

The total impurity's Green's function in the frequency domain, and hence corresponding to real-time Green's functions (not the thermal ones) is, finally:

$$G_{mm'}^{\sigma\sigma'}(\omega+i\eta) = \sum_{\alpha\alpha'ij} \langle \alpha|\hat{c}_{m}^{\sigma}|i\rangle\langle j|\hat{c}_{m'}^{\sigma'\dagger}|\alpha'\rangle G_{i\alpha',\alpha j}(\omega+i\eta). \tag{35}$$

In order to be able to compute the impurity's Green's function, we would like to further the orbital-and-spin separation. The rational for this is that for most light open-shell systems, the orbital angular momentum will be quenched by the external interaction with the electrodes, hence only the spin is a good quantum number. Hence, it is interesting to explicitly express our equations in terms of the total spin of the system, since this last can be known by independent quantum chemistry calculations, for example. Hence, let us consider the spin coefficients appearing in Eq. (35): $\langle \alpha | \hat{c}_m^{\sigma} | i \rangle = \{ \langle \alpha | \otimes \langle m, \sigma | \} | i \rangle$. This expression can be interpreted as follows: starting from $|\alpha\rangle$ we add 1 electron in orbital m with spin σ and it becomes $|i\rangle$

We separate it in 2 parts, *orbital* and *spin*: $|\alpha\rangle = |L\rangle \otimes |S\rangle$, assuming that

- L is not necessarily an angular moment but rather the occupation of Hartree orbitals.
- (2) there is no magnetic anisotropy and more generally, no strong spin-orbit coupling.

Then,

$$\langle \alpha | \hat{c}_m^{\sigma} | i \rangle = f^{i\alpha}(m) \times \langle S^N, S_z^N; \frac{1}{2}, \sigma | S^{N+1}, S_z^{N+1} \rangle$$
 (36)

where $f^{i\alpha}(m)$ is the occupation of the orbital m in the configuration i and α such that $f^{i\alpha}(m)$ is different from zero only if the one-particle orbital "m" is the difference between the α and i configurations that are respectively electronic configurations of the N and N+1 Fock subspaces. Now, the spin part is indeed a Clebsch-Gordan coefficient under the above proviso. Hence, $S_z^{N+1} = S_z^N + \sigma$ and $S_z^{N+1} = S_z^N \pm \frac{1}{2}$.

We have just performed some important approximations that deserve deeper consideration. First, the approximation (2) is not very crude since it is just a matter of choosing the basis sets that will diagonalize $h^{(N)}$ in $R^{(N)}$. Here, we assume that that one can define S^N for N and S^{N+1} for each Green's function and that it can be done for the resolvent. Now, the absence of magnetic anisotropy permits us to maintain spherical symmetry and hence $G_{i\alpha',\alpha j} = G^{S^N,S^{N+1}}$ with 2 S^{N+1} for each S^N (or vice-versa). As one would expect from the spherical approximation, G does not depend on S_z any longer.

With these considerations, we can now re-express the physical impurity's Green's function, Eq. (35), to obtain:

$$G_{mm'}^{\sigma\sigma'}(\omega + i\eta) = f^{i\alpha}(m)f^{j\alpha'}(m')$$

$$\sum_{S^{N}S_{z}^{N}} \langle S^{N}, S^{N}_{z}; \frac{1}{2}, \sigma | S^{N+1}, S^{N+1}_{z} \rangle \langle S^{N} + \frac{1}{2}, S^{N+1}_{z} | S^{N}, S^{N}_{z}; \frac{1}{2}, \sigma \rangle G^{S^{N}, S^{N+1}}$$

$$+ f^{i\alpha}(m)f^{j\alpha'}(m')\langle S^{N}, S^{N}_{z}; \frac{1}{2}, \sigma | S^{N} - \frac{1}{2}, S^{N}_{z} + \sigma \rangle$$

$$\langle S^{N} - \frac{1}{2}, S^{N}_{z} + \sigma | S^{N}, S^{N}_{z}; \frac{1}{2}, \sigma \rangle G^{S^{N}, S^{N-\frac{1}{2}}}$$
(37)

One final remark is in order here, if we assume that $G_{mm'}^{\sigma\sigma'}=G^{\sigma}\delta_{\sigma\sigma'}$ then, by symmetry, $G^{\sigma}=G^{-\sigma}$, and the equations do not depend on σ which should simplify Eq. (37).

It is interesting to see how the spherical assumption and the orbit-spin separation affets Eq. (24). In particular, the hybridization terms, Eq. (18), contain the same matrix element $\langle i|\hat{c}_m^{\sigma\dagger}|\alpha\rangle$ as just discussed. If we keep spin dependence in V, we can describe magnetic substrates. But, by removing σ , we can easily compute Γ by factoring out the σ dependence.

$$\Gamma_{j\alpha'}^{\alpha i}(\omega) = \sum_{\sigma} \left[\Gamma_{j\alpha'}^{\alpha i}(\sigma, \omega) \right]$$
 (38)

$$\Gamma_{jz'}^{\alpha i}(\sigma,\omega) = \sum_{n\mathbf{k}mm'} f^{i\alpha}(m) f^{j\alpha'}(m') \langle S^{N+1} S_z^{N+1} | S^N, \frac{1}{2}; S_z^N, \sigma \rangle \langle S^N, \frac{1}{2}; S_z^N, \sigma | S^{N+1}, S_z^{N+1} \rangle$$

$$\times \langle m\sigma | \hat{V} | n\mathbf{k}\sigma \rangle \langle n\mathbf{k}\sigma | \hat{V} | m' \rangle \delta(\omega - \varepsilon_{n\mathbf{k}\sigma})$$
(39)

Hence, the Γ function becomes:

$$\Gamma_{j\alpha'}^{\alpha i}(\sigma,\omega) = \sum_{n\mathbf{k}mm'} f^{i\alpha}(m) f^{j\alpha'}(m') V_m^{n\mathbf{k}\sigma} V_{m'}^{n\mathbf{k}\sigma} \left[\langle S^N, \frac{1}{2}; S_z^N, \sigma | S^{N+1}, S_z^{N+1} \rangle \right]^2 \times \delta(\omega - \varepsilon_{n\mathbf{k}\sigma}).$$
(40)

In the case that only one S^N can be considered among the states constituting the $N \leftrightarrow N+1$ charge fluctuation, we can further simplify the expression to:

$$\Gamma_{j\alpha'}^{\alpha i}(\sigma,\omega,S^N,S^{N+1}) = \sum_{mm'} f^{i\alpha}(m) f^{j\alpha'}(m') \Gamma_{mm'}^{\sigma}(\omega) \left[\langle S^N, \frac{1}{2}; S_z^N, \sigma | S^{N+1}, S_z^{N+1} \rangle \right]^2$$

$$(41)$$

with
$$\Gamma_{mm'}^{\sigma}(\omega) = \sum_{n\mathbf{k}} V_m^{n\mathbf{k}\sigma} V_{m'}^{n\mathbf{k}\sigma} \delta(\omega - \varepsilon_{n\mathbf{k}\sigma})$$
.

Diagonalization of $\Gamma^{\sigma}_{mm'}(\omega)$ permits us to find the electron channels contributing to the Kondo effect. Continuing with the spherical symmetry approximation, we can now use that

$$R_{ij}^{N+1}(\omega) = R_{mm'}^{S^{N+1}} \delta_{S^{N+1}S^{N+1}} \delta_{S_{-}^{N+1}S^{N+1}}$$
(42)

which can be easily proved by starting from the from impurity's *R* with spherical symmetry for the spin and then solving the NCA equations. We can finally express the self-energies as:

$$\Sigma_{\alpha\alpha'}^{N}(\omega) = \sum_{mm'\sigma} \sum_{S^{N+1}} \int f(\omega') \Gamma_{mm'}(\omega') R_{mm'}^{S^{N+1}}(\omega + \omega') d\omega'$$

$$\sum_{\sigma S^{N+1}} \langle S'^{N+1}, S_{z}'^{N+1} | S'^{N}, \frac{1}{2}; S_{z}'^{N}, \sigma \rangle \langle S'^{N}, \frac{1}{2}, S_{z}'^{N}, \sigma | S^{N+1}, S_{z}^{N+1}, \sigma \rangle$$
(43)

By making use of the Clebsch-Gordan property

$$\begin{split} \sum_{\sigma S_{z}^{N+1}} \langle S^{N+1}, S_{z}^{N+1} | S^{N}, \frac{1}{2}; S_{z}^{N}, \sigma \rangle \langle S'^{N}, \frac{1}{2}; S_{z}'^{N}, \sigma | S^{N+1}, S_{z}^{N+1} \rangle \\ &= \frac{2S^{N+1} + 1}{2S^{N} + 1} \delta_{S^{N}S'^{N}} \delta_{S_{z}^{N}} \delta_{S_{z}^{N}}$$

we find that

$$\Sigma_{\alpha\alpha'}^{N}(\omega) = \sum_{mm'S^{N+1}} \int f(\omega') \Gamma_{mm'}^{\alpha\alpha'}(\omega') R_{mm'}^{S^{N+1}}(\omega + \omega')$$

$$\frac{2S^{N+1} + 1}{2S^{N} + 1} \delta_{S^{N}S^{N}} \delta_{S_{z}^{N}} \delta_{S_{z}^{N}} d\omega'$$
(44)

and

$$\Sigma_{ij}^{N+1}(\omega) = \sum_{\alpha\alpha'} \int f(-\omega') \Gamma_{\alpha'j}^{i\alpha}(\omega') R_{\alpha\alpha'}^{N}(\omega - \omega') d\omega'$$

$$= \sum_{\alpha\alpha'} \int f(-\omega') \Gamma_{mm'}^{\alpha\alpha'}(\omega') R_{\alpha\alpha'}^{S^{N}}(\omega - \omega') d\omega'$$
(45)

$$\underbrace{\sum_{\sigma S_z^N} \langle S'^{N+1}, S_z'^{N+1} | S'^N, \frac{1}{2}; S_z'^N, \sigma \rangle \langle S'^{N+1}, S_z'^{N+1} | S'^N, \frac{1}{2}; S_z'^N, \sigma \rangle}_{\delta_{S^NS'^N}}$$

$$(46)$$

Replacing the value of the above Γ functions, we obtain

$$\Sigma_{\alpha\alpha'}^{N}(\omega) = \sum_{mm'S^{N+1}} f^{i\alpha}(m) f^{\alpha'j}(m') \int f(\omega') \Gamma_{mm'}(\omega') R_{ji}^{S^{N+1}}(\omega + \omega')$$

$$\frac{2S^{N+1} + 1}{2S^{N} + 1} \delta_{S^{N}S^{N}} \delta_{S_{z}^{N}S_{z}^{N}} d\omega'$$
(47)

$$\Sigma_{ij}^{N+1}(\omega) = \sum_{\alpha \alpha' S^{N}} f^{i\alpha}(m) f^{\alpha'j}(m') \int f(-\omega') \Gamma_{mm'}(\omega') R_{ji}^{S^{N}}(\omega - \omega')$$

$$\delta_{S^{N+1}S^{N+1}} \delta_{S_{z}^{N+1}S^{N+1}} d\omega'$$
(48)

$$R^{S^{N}}(\omega) = \left[\omega \hat{\mathbb{I}} - \hat{h}^{S^{N}} - \hat{\Sigma}^{S^{N}}\right]^{-1} \tag{49}$$

$$R^{S^{N}}(\omega) = \left[\omega \hat{\mathbb{I}} - \hat{h}^{S^{N+1}} - \hat{\Sigma}^{S^{N+1}}\right]^{-1}$$
 (50)

which form the complete NCA equations plus. Performing the same type of operations over the physical Green's function, Eq. (35), we find:

$$G_{mm'}^{\sigma\sigma'}(\omega) = \sum_{\alpha\alpha'ij} f^{i\alpha}(m) f^{\alpha'j}(m') \langle S^N, \frac{1}{2}; S_z^N, \sigma | S^{N+1}, S_z^{N+1} \rangle$$

$$\langle S^{\prime N+1}, S_z^{\prime N+1} | S^N, \frac{1}{2}; S_z^{\prime N}, \sigma' \rangle G_{i\alpha'\alpha j}(\omega).$$
(51)

Again, the spin spherical symmetry permits us to simplify the expression to

$$G_{i\alpha'\alpha j}(\omega) = \delta_{\sigma\sigma'} \sum_{\alpha\alpha' ijS^NS^{N+1}} f^{i\alpha}(m) f^{\alpha' j}(m') \frac{2S^{N+1} + 1}{2} G_{S^N i\alpha'\alpha j}^{S^{N+1}}(\omega).$$
 (52)

Finally, the factor $e^{-\beta\omega}$, appearing in the expression of $G^{S^{N+1}}_{S^Ni\alpha'\alpha j}(\omega)$, see Eq. (33), is diverging at $\omega\to-\infty$. In order to deal with this divergence, a new propagator is defined, termed defect propagator by Kuramoto [30]:

$$a = \frac{i}{2\pi \mathcal{Z}_i} e^{-\beta\omega} (R - R^{\dagger}), \tag{53}$$

with \mathcal{Z}_i the impurity's partition function. After the same type of algebra as above, we find the final defect propagator expressions needed for the evaluation of the physical Green's function:

$$a_{ij}^{S^{N+1}} = \sum_{j_1 j_2} R_{ij_1}^{N+1} \times \left[\sum_{\alpha \alpha' S^N mm'} f^{j_1 \alpha}(m) f^{j_2 \alpha'}(m') \int d\omega' f(\omega') \Gamma_{mm'}(\omega') a_{\alpha \alpha'}^{S^N}(\omega - \omega') \right] R_{j_2 j}^{N+1*}$$
(54)

$$a_{\alpha\alpha'}^{S^{N}} = \sum_{\alpha_{1}\alpha_{2}} R_{\alpha\alpha_{1}}^{N} \times \left[\sum_{ijS^{N+1}mm'} f^{i\alpha_{1}}(m) f^{j\alpha_{2}}(m') \int d\omega' f(-\omega') \Gamma_{mm'}(\omega') a_{ij}^{S^{N+1}}(\omega + \omega') \frac{2S^{N+1} + 1}{2S^{N} + 1} \right] R_{\alpha_{2}\alpha'}^{N*}$$
(55)

We normalize a to avoid computing \mathcal{Z}_i , for each a:

$$\sum_{\gamma} \int a_{\gamma\gamma}(\omega) d\omega = \int \text{Tr}\{a(\omega)\} d\omega = 1$$
 (56)

The above procedure permits us to include the charge fluctuation in the impurity. However, the impurity will affect its environment. Then we use Dyson's equation to propagate the impurity's newly accounted for correlation to the rest of the electronic structure. We could also add a second electrode by modifying NCA to include the Fermi smearing of the tip.

Dyson's equation for the full system now reads:

$$G_{kk'}(\omega) = G_{kk'}^{0}(\omega) + \sum_{k,k} G_{kk_1}^{0} T_{k_1 k_2} G_{k_2 k'}^{0}$$
(57)

with the T-matrix given by:

$$T_{k_1 k_2} = \sum_{mm'} V_m^{n k_1 \sigma} G_{mm'}(\omega) V_{m'}^{n k_2 \sigma *}$$
(58)

And we can now compute an STM image for an open-shell system within the Tersoff-Hamman approximation using that the LDOS is

$$\rho(\mathbf{r},\omega) = -\frac{1}{\pi} \text{Im} G(\mathbf{r}_1, \mathbf{r}; \omega)$$
 (59)

$$G(\mathbf{r}_1, \mathbf{r}; \omega) = \sum_{kk'} \langle \mathbf{r} | \mathbf{k} \rangle \langle \mathbf{k}' | \mathbf{r} \rangle G_{kk'}(\omega)$$
(60)

M. Kepenekian et al.

and

134

$$\langle \mathbf{r} | \mathbf{k} \rangle = \sum_{i} \langle \mathbf{r} | \mathbf{w}_{i} \rangle \langle \mathbf{w}_{i} | \mathbf{k} \rangle = \sum_{i} \mathbf{w}_{i}(\mathbf{r}) \langle \mathbf{w}_{i} | \mathbf{k} \rangle \tag{61}$$

where $w_i(\mathbf{r})$ is a basis function located at each system's site. In the implementation that we performed they are maximally localized Wannier functions. These functions are particularly interesting because of its orthogonality and extreme localization that permits us to define a mathematically unambiguous Anderson Hamiltonian. We can go beyond the Tersoff–Hamman approximation using Büttiker-Landauer formula, which in the present case is easily written as:

$$I = \frac{2e}{h} \int (f_L - f_R) \operatorname{Tr} \underbrace{\left(\sum_{kk'} V_{kl}^{\operatorname{tip}} G_{kk'} V_{k'l'}^{\operatorname{tip}*} \right)}_{T_{n'}}$$
(62)

where l is the orbital of the tip. In general, $\text{Tr}\{T_{ll'}\}$ depends on various orbitals as shown in the above impurity-problem formalism.

Figure 7 shows preliminary results of the CuPc molecule. Instead of the LDOS, the PDOS have been plotted. The PDOS is given by,

$$PDOS(\omega) = -\frac{1}{\pi} Im \sum_{m,S^1,S^2} G_{m,m,S^1}^{S^2}(\omega)$$
(63)

where m is the doubly degenerated LUMO of the free CuPc molecule. The molecule is most of the time charged on the surface, hence the molecule fluctuates from two active electrons that constitute either a singlet, $S^2 = 0$, or a a triplet, $S^2 = 1$, to a single active electron, which is a doublet, $S^1 = 1/2$. The good agreement with the experiment is encouraging. For a deeper discussion of the Kondo physics of CuPc on Ag(100) please refer to Ref. [36].

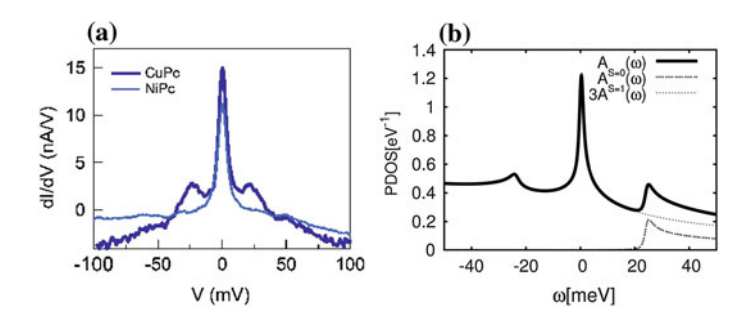


Fig. 7 a Experimental dI/dV of CuPc on Ag(100) (dark blue) and of NiPc on Ag(100) (light blue) [37]. b PDOS calculated from the NCA approach for the CuPc system. Notice that the intricate structure of the CuPc due to Kondo physics is reproduced in the NCA calculation and assigned to a triplet structure of the molecular spin [36]

5 Summary and Conclusions

In this article we have made a chronological presentation of the evolution of STM simulations of system's of increasing complexity. We have started from the simplified Bardeen approach that is at the origin of the ubiquitous Tersoff and Hamman approximation, and we have shown that this approximation if excellent in the qualitative understanding of STM images. The Bardeen approach permits us to improve the approximation by explicitly including a tip, but it necessarily fails when the tip enters in contact with the substrate or when bias effects become important. We have also briefly reviewed the NEGF implementation of the Landauer approach and showed that it can actually yield accurate results.

However, the above approaches necessarily fail when open-shell systems are involved. The reason for this is that at low temperatures, the open-shell character of the studied impurity on the substrate sets in a correlation among electrons of the substrate. This is the well known Kondo effect. In order to treat the Kondo problem correctly, we need to go beyond the above DFT approaches and include dynamical correlation in the electronic structure. We have presented for the first time how an implementation of one of the most successful methods to solve the Kondo problem can be done. The method is called NCA and it is very interesting because it permits us to go beyond density functional calculations. We have shown that the elusive Kondo peak of an open-shell molecule on a surface copper phthalocyanine on Ag(100) is reproduced within the presented approach.

The outlook of this work is to pursue this research until a complete transport study of the Kondo problem of atoms and molecules on surfaces have been realized, revealing the important features of open-shell systems as studied by the STM.

Acknowledgments Authors would like to thank the European Union Integrated Project AtMol for financial support.

References

- 1. Martin, R.M.: Electronic Structure. Basic theory and practical methods. (Cambridge, 2008).
- 2. Hohenberg, P., Kohn, W.: Phys. Rev. 136, B864 (1964)
- 3. Kohn, W., Sham, L.J.: Phys. Rev. 140, A1133 (1965)
- 4. Lang, N.D., Kohn, W.: Phys. Rev. B 1, 4555 (1970)
- 5. Tersoff, J., Hamman, D.R.: Phys. Rev. Lett. 50, 1998 (1983)
- 6. Tersoff, J., Hamman, D.R.: Phys. Rev. B 31, 805 (1985)
- 7. Bardeen, J.: Phys. Rev. Lett. 6, 57 (1961)
- 8. Datta, S.: Electronic Transport in Mesoscopic Systems (Cambridge University Press, 2007).
- Brandbyge, M., Mozos, J.L., Ordejón, P., Taylor, J., Stokbro, K.: Phys. Rev. B 65, 165401 (2002)
- Rocha, A.R., García-Suárez, V.M., Bailey, S., Lambert, C., Ferrer, J., Sanvito, S.: Phys. Rev. B 73, 085414 (2006)
- 11. Hewson, A.C.: The Kondo Problem to Heavy Fermions (Cambridge University Press, 1997).

- Madhavan, V., Chen, W., Jamneala, T., Crommie, M.F., Wingreen, N.S.: Science 280, 5363 (1998)
- 13. Li, J., Schneider, W.D., Berndt, R., Delley, B.: Phys. Rev. Lett. 80, 2893 (1998)
- 14. Ternes, M., Heinrich, A.J., Schneider, W.D.: J. Phys.: Condens. Matter 21, 053001 (2009).
- 15. Lorente, N.: Theory of tunneling currents and induced dynamics at surfaces in Dynamics. Handbook of Surface Science. (North Holland, 2008).
- 16. Cohen-Tannoudji, C., Diu, B.: Laloë. Quantum mechanics (Wiley-VCH, F. (1977)
- 17. Chen, C.J.: Introduction to Scanning Tunneling Microscopy (Oxford University Press, 2007).
- Olsson, F.E., Persson, M., Lorente, N., Lauhon, L.J., Ho, W.: J. Phys. Chem. B 106, 8161 (2002)
- Franke, K.J., Schulze, G., Henningsen, N., Fernández-Torrente, I., Pascual, J.I., Zarwell, S., Rück-Braun, K., Cobian, M., Lorente, N.: Phys. Rev. Lett. 100, 036807 (2008)
- 20. Alducin, M., Sánchez-Portal, D., Arnau, A., Lorente, N.: Phys. Rev. Lett. 104, 136101 (2010)
- 21. Robles, R., Lorente, N., Isshiki, H., Liu, J., Katoh, K., Breedlove, B.K., Yamashita, M., Komeda, T.: Nano Lett. 12, 3609 (2012)
- Mugarza, A., Lorente, N., Ordejón, P., Krull, C., Stepanow, S., Bocquet, M.L., Fraxedas, J., Ceballos, G., Gambardella, P.: Phys. Rev. Lett. 105, 115702 (2010)
- Mugarza, A., Krull, C., Robles, R., Stepanow, S., Ceballos, G., Gambardella, P.: Nature Commun. 2, 490 (2011)
- Mugarza, A., Robles, R., Krull, C., Korytár, R., Lorente, N., Gambardella, P.: Phys. Rev. B 85, 155437 (2012)
- 25. Kepenekian, M., Robles, R.: Lorente. First-principles simulations of electronic transport in dangling-bond wires (Springer, N. (2013)
- Soler, J.M., Artacho, E., Gale, J.D., García, A., Junquera, J., Ordejón, P., Sánchez-Portal, D.: J. Phys.: Condens. Matter 14, 2745 (2002).
- Artacho, E., Anglada, E., Diéguez, O., Gale, J.D., García, A., Junquera, J., Martin, R.M., Ordejón, P., Pruneda, J.M., Sánchez-Portal, D., Soler, J.M.: J. Phys.: Condens. Matter 20, 064208 (2008).
- 28. Kondo, J.: Prog. Theor. Phys. 32, 37 (1964)
- 29. Anderson, P.W.: Phys. Rev. 124, 41 (1961)
- 30. Kuramoto, Y.: Z. Phys. B 53, 37 (1983)
- 31. Grewe, N.: Z. Phys. B 53, 271 (1983)
- 32. Coleman, P.: Phys. Rev. B 29(6), 3035 (1984)
- 33. Kroha, J., Kirchner, S., Sellier, G., Wölfle, P., Ehm, D., Reinert, F., Hüfner, S., Geibel, C.: Phys. E **18**, 69 (2003)
- 34. Bickers, N.: Rev. Mod. Phys. 59, 845 (1987)
- 35. Korytár, R.: Molecular Kondo problem. First-principles approach for scanning-tunneling microscope studies. (Universitat Autònoma de Barcelona, 2011).
- 36. Korytár, R., Lorente, N.: J. Phys.: Condens. Matter 23, 355009 (2011).
- 37. Private communication from A. Mugarza, see also Refs. [23,24].

Electronic Transmission Through a Single Impurity in a Multi-configuration Scattering Matrix Approach

M. Portais and C. Joachim

Abstract A method is presented to calculate the scattering matrix of holes and electrons scattered by a molecular tunnel junction in a multi-configurational electronic approach. This is applicable for atomic scale systems where holes and electrons are delivered to the junction by metallic electrodes functioning in a ballistic regime of transport and where the full electronic structure of the molecular junction is considered. Applications of this CI-ESQC calculation technique demonstrates that the scattering resonances are built up from the superposition multi-configurational electronic states describing the virtual reduced or oxidized states of the molecular junction during the scattering process.

1 Introduction

With the invention of the scanning tunneling microscope (STM), we have now access to the details of the electronic properties of an isolated single atom (molecule) adsorbed on a surface [1–3]. One example is the mapping of the so-called (in the STM literature) molecular orbitals (MO) (see for example the chapter by W.Y. Soe in this volume). The theoretical challenge is to understand in detail those maps and to predict them for a new molecule. This goes with the more general problem of understanding the electronic transport properties through a single molecule tunnel junction since each pixel of an STM dI/dV map results from the conductance measurement of the STM molecular junction at the corresponding tip

M. Portais (⋈) · C. Joachim

Centre d'Elaboration de Matriaux et d'Etudes Structurales (CEMES-CNRS), 29 rue Jeanne Marvig 31055 Toulouse Cedex 4, BP 94347, France

e-mail: portais@cemes.fr

C. Joachim

e-mail: joachim@cemes.fr

apex location on the surface. The Landauer formula [4–6] allows to calculate the tunnel current intensity flowing through such a tunnel junction under the hypothesis that each charge transfer event through the junction can be viewed as a single effective particle scattering experiment. In this scattering experiment and depending of the bias voltage polarity of the junction, holes or electrons can be transferred through this molecular junction with at least the virtual participation of the reduced or oxidized states of the molecule.

In a mono-electronic description of this scattering process, the molecular junction contains no other particles than the incident one prepared in the contacting electrode for the scattering experiment to occur on the mono-electronic states of the molecular junction. In this approximation, the tunneling transmission coefficient through the molecular junction is equal to unity when the energy of the incident particle equals the energy of a given mono-electronic state [7]. A scattering resonance is here associated to the tunneling resonance through a MO state. Based on this approximation, STM images recorded at a tunnel resonance have been interpreted as "images" of given MOs [1, 8]. But the more accurate the recorded STM images, especially in a constant current dI/dV mode, the less this mono-electronic interpretation is efficient to interpret the recorded STM dI/dV images. Moreover, some STM images recorded low lying in energy resonances do not correspond to the spatial distribution of a given MO but to a mixing of several MOs of the molecule. The weight of each molecular states (or MO) in this mixing was till date very difficult to determine experimentally [9].

To go over this mono-electronic approximation, the full electronic structure of the molecular junction and of the interactions between the electrons of this junction and the transferred holes or electrons have to be taken into account. This cannot be done exactly because of the number of quantum particles involved. One solution to go over the mono-electronic approximation is to consider the average interactions between the scattered particles and the resident electrons in the molecular junction either using a self-energy approximation [10, 11] or using an SCF mean field approximation [12, 13]. Here, there is still one effective particle for describing the scattering process dressed by its interactions with the other electrons of the molecular junction [14]. But to be more precise in the calculation of a tunneling current intensity, the scattering matrix of the process must be obtained considering at the same time the scattered particles and the complete electronic structure of the molecular tunnel junction. A first approach in this direction has been proposed where the electrons in the junction are frozen in a particular electronic configuration [15, 16]. This allowed to study the effect of the scattered particle on the electrons localized in the junction. But in this first defrozen-like approach, the scattered particle has no possibility to benefit from the large multi-configurational quantum state space opened by its virtual occupation of the junction electronic states. Some full CI calculations have been attempted in order to work with a more exact multi-configuration electronic excitation spectrum of the molecular junction [17, 18]. But those approaches are considering multiconfiguration electron transfer processes in a Fermi golden rule like approximation with no calculation of a scattering matrix.

In this chapter, we demonstrate the generalization of the mono-electronic electron scattering quantum chemistry (ESQC) method to a multi-configurational (CI-ESQC) electronic approach. This approach allows to take into account the scattered particle, its interaction with the complete electronic structure of the molecular junction, and the virtual occupation of multi-configuration electronic states with one particle more in the molecular junction, this particle being the scattered hole or electron. In a first part, we justify the choice of a Slater determinant basis set for calculating this CI scattering matrix. Then, the calculation of this scattering matrix in a multi-configuration basis set is presented. Finally, Sects. 3 and 4 present very simple examples to illustrate the multi-electronic calculations as compared to the mono-electronic ones and the resulting changes in the T(E) elastic scattering transmission spectrum of the molecular junction.

2 The Multi-Configuration Basis Set

In general, a metal-molecule-metal tunnel junction contains a very large number of electrons. Therefore, an electron or hole scattering process on this junction cannot be treated exactly. Following the Landauer idea, the first approximation is to consider the electrodes contacting the junction as perfect conductors. Along the electrodes, the effective particles (hole or electron) to be scattered by this junction are propagating in a ballistic regime of transport and without interacting with each other. The electronic transparency of this junction is given by the T(E) transmission coefficient calculated from the scattering matrix of the corresponding scattering process.

A simple mono-electronic way to calculate this scattering matrix is to use a mono-electronic basis set where the electrodes are represented by a one-dimensional chain of atomic orbitals and the molecule by the set of its valence MOs. This approximation is at the basis of the mono-electronic ESQC approximation or to more elaborate ESQC-SCF methods where the electronic interactions of the scattered particles are determined in a mean field-like approach. Here, the many-body effects are not considered since the tunneling particles are simply scattered by the valence electronic structure of the molecular junction which in turn is not perturbed by the corresponding electron transfer process.

In order to accommodate the many-body effects occurring during a scattering process, calculations have to be performed in a multi-configuration electronic picture. In this case, the electronic transmission coefficient through the junction will depend on the different electronic configurations that can be formed with virtually one electron more (or less for a hole transfer process) in the molecular junction. The corresponding many-body electronic Hamiltonian will depend on the Coulomb and exchange interactions between all the considered electronic configurations of the junction. Notice that even if the scattered particle is far from the junction, different electronic configurations will have to be considered for describing the molecular junction due, for example, to exchange interactions. As a

consequence, the calculation of an elastic electronic transmission coefficient is possible for each electronic configuration of the molecular junction with the scattered particle located far away from the junction. As in any model of a scattering experiment, this condition permits to construct well-defined asymptotic states, one per molecular junction electronic configuration. This is essential to be able to calculate a scattering matrix on a multi-configuration electronic basis set. Following this condition, a model quantum state space for describing the electronic structure of the molecular junction and its electrodes can be constructed. It is spanned by a Slater determinant basis set including all the required electronic configurations for describing the scattering process in particular the configurations generated with one electron more or one electron less on the molecular junction.

In Fig.1, the incident particle q can either be an electron or a hole since two different types of charge transfer mechanisms contribute to the tunnel current intensity. When a positive bias voltage is applied between the right and the left electrodes of the junction, an electron can be transferred from the left to the right through the junction, i.e., $q = e^-$. When now a negative bias voltage is applied, an electron of the molecule can be first transferred to the left electrode and consequently an electron from the right electrode can occupy the hole left on the molecule electronic structure resulting in an effective hole transfer through the junction, i.e., $q = h^+$. Since it is easier to picture an electron than a hole transfer process, the scattering process worked out below will be an electron transfer process. But the CI-ESQC formalism presented here applies for both electron and hole scattering processes. The only difference can be found in the construction of the H many-body electronic Hamiltonian for a hole as compared with an electron transfer process.

The scattering process described Fig. 1 occurs between two semi-infinite electrodes in electronic interaction with a central molecule whose electronic structure contains m electrons. We are interested in the elastic scattering process of an electron coming from the left electrode transferred through the molecule and reaching or not the right electrode. There are m+1 particles in the system, and M_s is the projection on the z axis perpendicular to the electron propagation direction of the spin momentum of those m+1 electrons. Situations where $|M_s| = m+1$ or $|M_s| \neq m+1$ have to be treated separately because in the second case spins can flip and the configuration basis set has to include this possibility, contrary to the first case. The $|M_s| = m+1$ case is easily deduced from the $|M_s| \neq m+1$ case. In the following, only the second case will be considered.

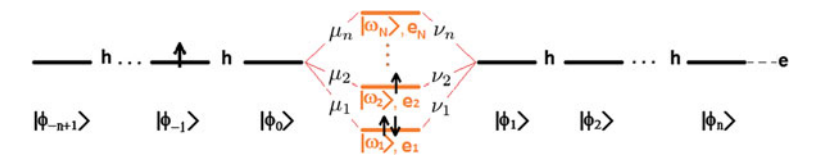


Fig. 1 Schematic representation of the system {electrodes, defect}, $q = h^+$ for hole transfer and $q = e^-$ for electron transfer

For an elastic scattering process, one has to solve the stationary Schrödinger equation to buildup the corresponding scattering matrix. On a given multi-configuration basis set, this equation can be written in its matrix form:

$$(H - E_T S)[\psi] = 0 \tag{1}$$

where the solution is supposed to be known far away from the molecular junction. E_T is the total electronic energy of the electronic system made of the two semi-infinite electrodes and of the central molecular junction. This hypothesis transforms the eigenvalue problem (1) in an initial value problem where H is the Hamiltonian of the m+1 electronic system considering the two electrodes and the central molecule and S is the overlap matrix on the multi-configuration basis set used for this m+1 electrons system. Applying the superposition principle, E_T is the sum of the mono-electronic energy of the incident electron E, [in effect the mono-electronic part of asymptotic solution of (1)] and of the energy Y_0 of the m electrons belonging to the central molecular junction supposed to be in its ground state.

The spatial atomic orbital basis set used to construct the Slater determinants for the description of the incident electron propagating along the electrodes (and not interacting with the molecule) are denoted $|\phi_i\rangle$ with $i\in\{-\infty,\ldots,0\}$ on the left electrode and $i\in\{1,\ldots+\infty\}$ on the right one. The MOs are denoted $|\omega_i\rangle$ with $i\in\{1,\ldots,n\}$. So the m electrons of the molecule are occupying the set $\mathscr{D}=\{|\omega_1\rangle\ldots|\omega_n\rangle\}$. h and s are the mono-electronic coupling and the overlap between two neighbor sites of the periodic part of the chain and e the on-site energy. The m-electron configurations with a spin momentum $M_s-1/2$ on the set $\mathscr D$ are denoted $\{\chi_i^-\}_{i=1\ldots N_m^-}$, the m-electron configurations with a spin momentum $M_s+1/2$ on the set $\mathscr D$ are denoted $\{\chi_i^+\}_{i=1\ldots N_m^+}$. So there are $N_m=N_m^++N_m^-$ possible configurations for the m-electrons on the molecule. Finally, the m+1 electron configurations are denoted $\{\alpha_i\}_{i=1\ldots N_{m+1}}$.

Two different types of Slater determinants are considered to buildup the basis set for (1): those with the scattered electron remaining on the electrodes and the electrons on the molecule, $||\phi_p\chi_i^-||\rangle$ and $||\overline{\phi_p}\chi_i^+||\rangle$ and those with both the scattered electron and the m electrons of the molecule on the molecular junction, $||\alpha_i||\rangle$. Therefore, the total basis set on which the scattering matrix will be calculated is given by:

$$\mathcal{B} = \{ \dots F_{-p} \dots F_0 \mid \alpha_1 \dots \alpha_{N_{m+1}} F_1 \dots F_p \dots \}$$
with : $F_p = \{ ||\phi_p \chi_i^-|\rangle \}_{i=1\dots N_m^-} \bigcup \{ ||\overline{\phi_p} \chi_i^+|\rangle \}_{i=1\dots N_m^+}$ (2)

To buildup the initial value problem in its matrix form, the Schrödinger equation (1) is projected on the model space spanned by (2). Parameters and calculation method for electron–electron interactions on this basis set are recalled in Appendix A. For example, the elements of the Hamiltonian and the overlap matrix between two m+1 particles Slater's determinants are given by:

$$\frac{1}{m+1!} \langle |u_1 u_2 \dots u_{m+1}| | \sum_{i} h(i) + \frac{1}{2} \sum_{ij} \frac{1}{r_{ij}} ||v_1 v_2 \dots v_{m+1}| \rangle$$

$$= \sum_{\sigma} \epsilon(\sigma) \left[\sum_{i} \langle u_i | h | v_{\sigma(i)} \rangle \prod_{k \neq i} \langle u_k | v_{\sigma(k)} \rangle + \frac{1}{2} \sum_{ij} \langle u_i u_j | \frac{1}{r_{12}} |v_{\sigma(i)} v_{\sigma(j)} \rangle \prod_{k \neq i,j} \langle u_k | v_{\sigma(k)} \rangle \right]$$
(3)

$$\frac{1}{m+1!} \langle |u_1 u_2 \dots u_{m+1}| | |v_1 v_2 \dots v_{m+1}| \rangle = \sum_{\sigma} \epsilon(\sigma) \prod_k \langle u_k | v_{\sigma(k)} \rangle$$
 (4)

In the following H_m and S_m are the Hamiltonian and the overlap matrix of dimension $N_m \times N_m$ for the m electrons of the molecular junction.

3 Calculation of the Scattering Matrix on a Multi-Configuration Basis Set

In a mono-electronic approximation, a well-known procedure to calculate a transmission coefficient from the mono-electronic simple version of (1) is to transform this equation into a spatial propagation equation. The spatial propagator relates the coefficients of the decomposition of an eigenstate of the mono-electronic approximation of (1) on the left of the molecular junction to the ones on the right thanks to a transfer matrix t(E) [7]:

$$\begin{bmatrix} C(E) \\ D(E) \end{bmatrix} = \mathbf{t}(E) \begin{bmatrix} A(E) \\ B(E) \end{bmatrix}$$
 (5)

Here, A(E) and B(E) are the amplitudes of incident and reflected plane waves on the left of the molecule, and C(E) and D(E) the amplitudes of incident and emergent plane waves on the right of the molecule. This is done by calculating the spatial propagator M(p,-p) which relies $C_p = C(E)e^{ikp} + D(E)e^{-ikp}$ and $C_{-p} = A(E)e^{ik(-p)} + B(E)e^{-ik(-p)}$, the amplitude along the states ϕ_p and ϕ_{-p} , k being the wave vector defined by $2\cos(k) = -\frac{E-e}{h-Es}$. M(p,-p) can be expressed using the local propagators for the periodic part of the chain, M(p,p-2), and the effective propagator of the defect, $M_{\rm eff}(2,-1)$. Using M(p,p-2) = U(p,p-1) $U(p-1,p-2)^{-1}$ with $U(p,p-1) = \begin{bmatrix} e^{ikp} & e^{-ikp} \\ e^{ik(p-1)} & e^{-ik(p-1)} \end{bmatrix}$, the transfer matrix is then given by $\mathbf{t}(E) = U(2,1)^{-1}M_{\rm eff}(2,-1)U(0,-1)$.

From this matrix $\mathbf{t}(E)$, the scattering matrix $\mathbf{s}(E)$ can be calculated. It relates the amplitudes of the emergent waves C(E) and B(E) to the amplitudes of the incident

waves A(E) and D(E). The transmission coefficient is then defined as $T(E) = |\mathbf{s}(E)_{11}|^2 = \frac{1}{|\mathbf{t}(E)_{11}|^2}$. This is the mono-electronic ESQC method which can easily be extended to two multi-channels electrodes or to a multiple electrodes molecular junction [19].

In the following, this spatial propagator technique is developed further in a many-body approach with a non-frozen electronic configuration description of the central molecular junction. Instead of propagating the coefficients of the decomposition of incident and transmitted electron quantum state along the electrodes from $|\phi_p\rangle$ to $|\phi_{p+1}\rangle$, a m+1 particles quantum state is propagated from the subspace of dimension N_m generated by F_p (i.e., all the electronic configurations with one electron in $|\phi_p\rangle$) to the one generated by F_{p+1} (i.e., all the electronic configurations with one electron in $|\phi_{p+1}\rangle$). The importance of the localization hypothesis appears here because it ensures that the state spatial propagation is performed between finite size subsystems. Using the Slater determinant basis set described in Sect. 1, any solution of the stationary Schrödinger equation (1) can now be decomposed on this $\mathcal B$ basis set leading to:

$$\begin{aligned} |\psi\rangle &= \sum_{p=-\infty}^{0} \left(\sum_{i=1}^{N_{m}^{-}} D_{pi}^{-} ||\phi_{p}\chi_{i}^{-}|\rangle + \sum_{i=1}^{N_{m}^{+}} D_{pi}^{+} ||\overline{\phi_{p}}\chi_{i}^{+}|\rangle \right) + \sum_{i=1}^{N_{m+1}} A_{i} ||\alpha_{i}|\rangle \\ &+ \sum_{p=1}^{\infty} \left(\sum_{i=1}^{N_{m}^{-}} D_{pi}^{-} ||\phi_{p}\chi_{i}^{-}|\rangle + \sum_{i=1}^{N_{m}^{+}} D_{pi}^{+} ||\overline{\phi_{p}}\chi_{i}^{+}|\rangle \right) \end{aligned}$$
(6)

In this decomposition, the coefficients of the asymptotic electronic quantum states on the subset F_p can be easily identified and rewritten in a vector-like form:

$$\mathbf{D}_{p} = egin{bmatrix} D_{p1}^{+} \ dots \ D_{pN^{-}}^{+} \ D_{pN^{-}}^{-} \ dots \ D_{pN^{-}} \ \end{pmatrix} = egin{bmatrix} D_{p1} \ dots \ D_{pN_{m}} \ \end{bmatrix}$$

The positive integer l was chosen in such a way that if $|p| \ge l$, the propagating electron in $|\phi_p\rangle$ or $|\phi_{-p+1}\rangle$ is not interacting with the m electrons belonging to the molecular junction. The spatial propagation technique of solving (1) consists now in relating $\mathbf{D_p}$ to $\mathbf{D_{-p}}$ via a transfer matrix for |p| > l. We note \mathbf{A} the vector of the coordinates of $|\psi\rangle$ on $\{F_{-l+2}F_0 \mid \alpha_1\alpha_{N_{m+1}}F_1F_{l-1}\}$, and $N_1=2N_m(l-1)+N_{m+1}$ the length of \mathbf{A} .

Using this vector-like representation of the left and right asymptotic states, (1) can then be rewritten in the matrix form:

with $H_0 = S_m h + H_m s - E s S_m$, $E_0 = H_m + (e - E) S_m$, and the other blocks are calculated using (3) and (4).

A Slater determinant can be spatially propagated from D_p to D_{p-2} leading to:

$$\begin{bmatrix} \mathbf{D}_{p} \\ \mathbf{D}_{p-1} \end{bmatrix} = \begin{bmatrix} -\mathbf{H}_{0}^{-1} \mathbf{E}_{0} & -\mathbf{I}_{\mathbf{N}_{m}} \\ \mathbf{I}_{\mathbf{N}_{m}} & 0 \end{bmatrix} \begin{bmatrix} \mathbf{D}_{p-1} \\ \mathbf{D}_{p-2} \end{bmatrix}$$
(8)

When X is the eigenstate matrix of Hm and Y the corresponding diagonal matrix, (7) is equivalent to (see the relations in Appendix B):

$$\begin{bmatrix} \mathbf{D}_{p} \\ \mathbf{D}_{p-1} \end{bmatrix} = \begin{bmatrix} \mathbf{X} & \mathbf{0} \\ \mathbf{0} & \mathbf{X} \end{bmatrix} \begin{bmatrix} -Y_{H}^{-1}Y_{E} & -I_{N_{m}} \\ I_{N_{m}} & \mathbf{0} \end{bmatrix} \begin{bmatrix} \mathbf{X} & \mathbf{0} \\ \mathbf{0} & \mathbf{X} \end{bmatrix}^{-1} \begin{bmatrix} \mathbf{D}_{p-1} \\ \mathbf{D}_{p-2} \end{bmatrix}$$
(9)

As compared to the mono-electronic ESQC calculation technique and because the scattering process is elastic, each electronic configuration of energy Y_{ii} of the m electrons (Y_0 is the ground state one) serves for the definition of a peculiar scattering process. Therefore, each electronic excitation of the central molecular junction described by a given Slater determinant is opening its own Slater determinant spatial propagation. At a given incident energy E, the quantum superposition principle is used to superpose the contributions of each of those channels opened at this energy E with K_{ii} the corresponding propagation wave vector for the channel corresponding to Y_{ii} . In the following, a diagonal wave vector matrix K for this superposition of elastic channels is defined as:

$$\forall i \in [1, Nm], \ 2\cos(K_{ii}) = [-Y_H^{-1}Y_E]_{i,i} = \frac{E - e - Y_{ii}}{h - s(E - Y_{ii})}$$
(10)

is used for the spatial propagator along the periodic part of a given electrode to have a form similar to the one in the mono-electronic spatial propagation case:

$$\begin{bmatrix} \mathbf{D}_{p} \\ \mathbf{D}_{p-1} \end{bmatrix} = \begin{bmatrix} X & 0 \\ 0 & X \end{bmatrix} & \underbrace{\begin{bmatrix} e^{iKp} & e^{-iKp} \\ e^{iK(p-1)} & e^{-iK(p-1)} \end{bmatrix}}_{\begin{bmatrix} e^{iK(p-1)} & e^{-iK(p-1)} \\ e^{iK(p-2)} & e^{-iK(p-2)} \end{bmatrix}^{-1}}_{\begin{bmatrix} e^{iK(p-1)} & e^{-iK(p-1)} \end{bmatrix}^{-1}} \begin{bmatrix} X & 0 \\ 0 & X \end{bmatrix}^{-1} \begin{bmatrix} \mathbf{D}_{p-1} \\ \mathbf{D}_{p-2} \end{bmatrix}$$

$$\begin{bmatrix} X & 0 \\ 0 & X \end{bmatrix} & U(p, p-1) & U(p-1, p-2)^{-1} & \begin{bmatrix} X & 0 \\ 0 & X \end{bmatrix}^{-1} \begin{bmatrix} \mathbf{D}_{p-1} \\ \mathbf{D}_{p-2} \end{bmatrix}$$
(11)

Performed by iterations, it becomes:

$$\begin{bmatrix} \mathbf{D}_p \\ \mathbf{D}_{p-1} \end{bmatrix} = \begin{bmatrix} X & 0 \\ 0 & X \end{bmatrix} U(p, p-1) U(l+1, l)^{-1} \begin{bmatrix} X & 0 \\ 0 & X \end{bmatrix}^{-1} \begin{bmatrix} \mathbf{D}_{l+1} \\ \mathbf{D}_l \end{bmatrix}$$
(12)

Using the same procedure, a determinant can be propagated from \mathbf{D}_{l+1} to \mathbf{D}_{l+1} :

$$\begin{bmatrix} \mathbf{D}_{l+1} \\ \mathbf{D}_{l} \end{bmatrix} = \begin{bmatrix} -H_{0}^{-1}E_{0} & -H_{0}^{-1}\mathcal{H}_{2} \\ I_{N_{m}} & 0 \end{bmatrix} \\
\times \begin{bmatrix} -\mathcal{H}_{D}^{-1}\mathcal{H}_{-1} & -\mathcal{H}_{D}^{-1}\mathcal{H}_{-2} \\ I_{N_{m}} & 0 \end{bmatrix} \begin{bmatrix} \mathbf{D}_{-l+1} \\ \mathbf{D}_{-l} \end{bmatrix}$$

$$= \mathcal{M} \times \begin{bmatrix} \mathbf{D}_{-l+1} \\ \mathbf{D}_{-l} \end{bmatrix}$$
(13)

Finally, and combining the two, it becomes:

$$\begin{bmatrix} \mathbf{D}_{p} \\ \mathbf{D}_{p-1} \end{bmatrix} = \begin{bmatrix} X & 0 \\ 0 & X \end{bmatrix} U(p, p-1) U(l+1, l)^{-1} \begin{bmatrix} X & 0 \\ 0 & X \end{bmatrix}^{-1} \mathcal{M} \begin{bmatrix} X & 0 \\ 0 & X \end{bmatrix}$$

$$\times U(-l+1, -l) U(-p+1, -p)^{-1} \begin{bmatrix} X & 0 \\ 0 & X \end{bmatrix}^{-1} \begin{bmatrix} \mathbf{D}_{-p+1} \\ \mathbf{D}_{-p} \end{bmatrix}$$
(14)

For $|p|\gg 1$ and because the propagating electron does not interact electronically with the central molecule in this case, it propagates independently along both left and right electrodes. The spatial representation of its quantum state is a plane wave. In this case, the electrons on the molecule are assumed to fill up the molecule MOs leading to the multi-electronic ground state of this *m*-electrons molecular subsystem. Therefore and still far from the molecule and when the propagating electron is on the left electrode (respectively on the right one), the *m*-electron subsystem is considered to be in the eigenstate j_0 (resp. l_0) and it comes directly:

$$p \to \infty, \quad \mathbf{D}_{-pi} = C_{-p}(j_0) X_{ij_0}$$
 (15)

$$\mathbf{D}_{pi} = C_p(l_0) X_{il_0} \tag{16}$$

with $C_p(j_0)$ the amplitude of the plane wave along the electrode. Since E is the mono-electronic energy of the propagating electron far from the defect, one can take $E = E(i) = E_T - Y_{ii}$ and it becomes:

(19)

$$p \to \infty$$
 $C_{-p}(E, j_0) = A(E, j_0)e^{iK_{j_0j_0}(-p)} + B(E, j_0)e^{-iK_{j_0j_0}(-p)}$ (17)

$$C_p(E, l_0) = C(E, l_0)e^{iK_{l_0 l_0} p} + D(E, l_0)e^{-iK_{l_0 l_0} p}$$
(18)

with $2\cos(K_{ii}) = \frac{E-e}{h-Es} = \frac{E_T - Y_{ii} - e}{h - (E_T - Y_{ii})s}$.

Multiplying (14) to the left by $\begin{bmatrix} X & 0 \\ 0 & X \end{bmatrix}^{-1}$ and using (15) and (16), the infinite limit in p leads to:

$$\begin{bmatrix} 0 \\ \vdots \\ C_{p}(E, l_{0}) \\ \vdots \\ 0 \\ 0 \\ \vdots \\ C_{p-1}(E, l_{0}) \\ \vdots \\ 0 \end{bmatrix} = U(p, p-1)U(l+1, l)^{-1} \begin{bmatrix} X & 0 \\ 0 & X \end{bmatrix}^{-1} \mathscr{M} \begin{bmatrix} X & 0 \\ 0 & X \end{bmatrix}$$

$$\times U(-l+1,-l)U(-p+1,-p)^{-1} \begin{bmatrix} 0 \\ \vdots \\ C_{-p+1}(E,j_0) \\ \vdots \\ 0 \\ 0 \\ \vdots \\ C_{-p}(E,j_0) \\ \vdots \\ 0 \end{bmatrix}$$
(19)

and using (17) and (18):

$$\begin{bmatrix} 0 \\ \vdots \\ C(E, l_0) \\ \vdots \\ 0 \\ 0 \\ \vdots \\ D(E, l_0) \\ \vdots \\ 0 \end{bmatrix} = U(l+1, l)^{-1} \begin{bmatrix} X & 0 \\ 0 & X \end{bmatrix}^{-1} \mathscr{M} \begin{bmatrix} X & 0 \\ 0 & X \end{bmatrix} U(-l+1, -l) \begin{bmatrix} 0 \\ \vdots \\ A(E, j_0) \\ \vdots \\ 0 \\ 0 \\ \vdots \\ B(E, j_0) \\ \vdots \\ 0 \end{bmatrix}$$

$$(20)$$

Therefore, the transfer matrix through the central molecule reads as

$$\mathbf{t}(E) = U(l+1, l)^{-1} \begin{bmatrix} X & 0 \\ 0 & X \end{bmatrix}^{-1} \mathcal{M} \begin{bmatrix} X & 0 \\ 0 & X \end{bmatrix} U(-l+1, -l)$$
 (21)

The scattering matrix $\mathbf{s}(E, j_0)$ of our scattering problem which relates B and C to A and D can now completely be written starting from the transfer matrix $\mathbf{t}(E) =$

$$\begin{bmatrix} T_{11} & T_{12} \\ T_{21} & T_{22} \end{bmatrix}$$
 where the T_{ij} are $N_m \times N_m$ matrices:

$$\mathbf{s}(E) = \begin{bmatrix} T_{11} - T_{12}T_{22}^{-1}T_{21} & T_{12}T_{22}^{-1} \\ -T_{22}^{-1}T_{21} & T_{22}^{-1} \end{bmatrix}$$
(22)

Therefore, the elastic transmission coefficient from $E_T = E(j_0) + Y_{j_0,j_0}$ to $E_T = E(l_0) + Y_{l_0,l_0}$ is given by $\left(T_{11} - T_{12}T_{22}^{-1}T_{21}\right)_{l_0,j_0}$. This leads to a transmission process superposing the contribution of several channels, each one corresponding to an eigenstate of the m-electron subsystem when the delocalized particle is far from the molecular junction. A complete calculation of the tunneling current intensity would ask for the description of the detailed statistical occupation of each channel. But in this chapter, only the transmission coefficient is of interest to detail the multiple contributions of the complete many-body description of a scattering process. Therefore, in the following, we will limit the transmission coefficient calculation and discussion to the tunnel process from the channel corresponding to X_0 , i.e., to the one corresponding to the ground state of the m-electron subsystem (with $X_{j_0} = X_{i_0} = X_0$).

Our multi-configuration scattering model is applicable to many scattering situations. In practice, it is limited by numerical considerations. The scattering matrix (22) is valid for any many-body electronic system. But the submatrices involved in such scattering matrix calculations can be of very large dimension. The larger one is H_D , the coupling between site -l+1 and the whole part of the electrode where the electron–electron interactions are existing. Its size is $(l-1)N_m+N_{m+1}+(l-1)N_m$. Notice also that the calculations presented in this section are only valid for $|Ms| \neq \frac{m+1}{2}$. The other case can be deduced by changing F_p in $\{||\phi_p \chi_i^-||\rangle\}_{i=1...N_m}$ or $\{||\overline{\phi_p}\chi_i^+||\rangle\}_{i=1.N_m^+}$.

4 Application to a Weakly Coupled Two-States Molecule Filled Up with Two Electrons

The transmission coefficient for electrons and holes are calculated here for the simple model electronic system shown in Fig. 2. The MOs used in the calculations are simple 1s Gaussian functions. They are sufficient to lighten the effects of a many-body calculation as compared to a simple mono-electronic ESQC one. The MOs $|\omega_1\rangle$, $|\omega_2\rangle$ are the ones obtained by an Hartree Fock (HF) calculation, the first one being symmetric relative to the center of the extended system and the second being its anti-symmetric. When the propagating particle is interacting with those two electrons, the corresponding ground state can only be described using an electronic multi-configuration basis set. Here, our HF calculated MOs give the best mono-electronic description of these two electron systems. Therefore, the state $|\omega_1\overline{\omega_1}\rangle$ is the Slater determinant closest to the exact ground state. Below, the presented calculations are made in the Ms=1/2 subspace. The electron–electron interactions are modified in the same ratio starting from the exact value of $U=\langle \omega_1\overline{\omega_1}|\frac{1}{I_{12}}|\omega_1\overline{\omega_1}\rangle$.

4.1 The Simple U=0 eV Non-interacting Case

Figure 3 gives the calculated transmission coefficients in the simple case where U=0, i.e., with no interaction between the electrons of the molecular junction. Since we are working with a Slater determinant basis set, electronic

$$\frac{\mathsf{q}_{\bullet}}{|\phi_{-n+1}\rangle}\,\mathsf{h}\,\cdots\,\frac{\mathsf{q}_{\bullet}}{|\phi_{-1}\rangle}\,\,\mathsf{h}\,\frac{\epsilon_2}{|\phi_0\rangle}\underbrace{\epsilon_1}_{\epsilon_1}\underbrace{\epsilon_2}_{\epsilon_1}\underbrace{\epsilon_2}_{|\phi_1\rangle}\,\mathsf{h}\,\frac{\mathsf{h}}{|\phi_2\rangle}\,\cdots\,\mathsf{h}\,\frac{\mathsf{h}}{|\phi_n\rangle}_{--0}$$

Fig. 2 A schematic representation of the simple {electrode, two-states molecule, electrode} molecular junction considered in this section

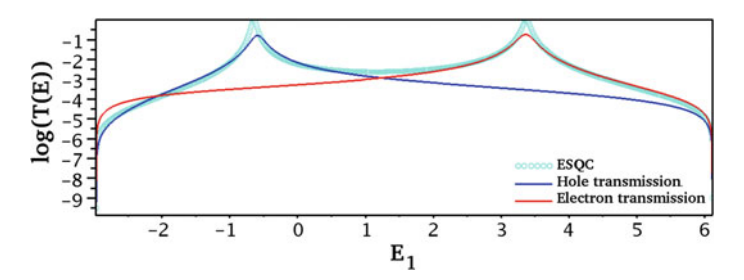


Fig. 3 The transmission coefficients as a function of E the asymptotic energy of the delocalized electron, without bi-electronic interactions ($U=0~{\rm eV}$). The on-site energy on the electrodes is e=0. The solid line is the transmission coefficient for holes, the dotted line is the transmission coefficient for electrons

indiscernibility and antisymmetry are still taken into account. Without these interactions, the ground state of the molecular junction obtained by the HF calculations is exact. So when the propagating particle is scattered by this molecular junction, $|\omega_1\rangle$ is doubly occupied and $|\omega_2\rangle$ is empty. Thus, for an electron scattering on the junction, the already doubly occupied orbital $|\omega_1\rangle$ cannot be filled up more. Therefore, the incident electron cannot be fully transmitted at this energy and there is no tunneling resonance in this case. A scattered electron can still occupy $|\omega_2\rangle$ creating a tunneling resonance at an energy very close to e_2 . The same process occurs for a hole scattering. Since $|\omega_2\rangle$ is empty, a hole cannot be created on this state and there is no resonance for a hole at incident energy e_2 . But an incident hole can occupy the ground state $|\omega_1\rangle$. This introduces a tunneling resonance at an energy very close to e_1 . Therefore, and for both an electron or a hole scattering process, there is only one resonance per type of particle instead of two in mono-electronic ESQC calculations on the same system. After a quantum superposition of the two processes, the hole and electron tunneling resonances lead to the expected T(E) spectrum with two tunneling resonances, each one near the energy of a MO resonance. These resonances have the same shape as ESQC monoelectronic calculations. So in the non-interacting case, there is apparently a good agreement between the mono-electronic ESQC and the CI-ESQC T(E) spectra.

With ESQC, the energy of the T(E) tunneling resonances are usually slightly shifted as compared to the position of the exact MO energy position because of the perturbation due to the coupling with the electrodes. But with CI-ESQC, those couplings, for instance between state $||\omega_1\overline{\omega_1}\omega_2|\rangle$ and state $||\omega_1\overline{\omega_1}\phi_0|\rangle$ depend not only on the mono-electronic coupling between $|\phi_0\rangle$ and $|\omega_2\rangle$, ϵ_2 but also on the mono-electronic coupling between $|\phi_0\rangle$ and $|\omega_1\rangle$, ϵ_1 . Therefore, the relative shift between the T(E) resonance and the MO energy is not the same as compared to the mono-electronic ESQC case even if this difference here is quite small.

Another difference between multi-electronic CI-ESQC and the mono-electronic T(E) spectra is the value of the T(E) resonance maximum. With CI-ESQC and as presented in Fig. 3, no T(E) resonance reaches unity contrary to the mono-electronic case which reaches unity for a symmetric tunnel junction. This is due to the

fact that only the principal transmission channel is represented in Fig. 3 because it corresponds to the initial choice of an incident particle access to the molecular junction scattering center with the molecular junction in its ground state. However, corresponding to the different electronic configurations of the molecular junction than its ground state, all the other channels are elastically open due to the quantum superposition principle leading to the fact that there is more than one output channel accessible at a given incident energy E. In Fig. 3 and for simplicity, we have only represented the T(E) for output channel corresponding to the central molecule in its ground state. As presented in Fig. 3, this is the essential part of the transparency of the Fig. 2 molecular junction. At the same energy E, the transmission spectrum of the other channels can also be studied since the scattering matrix (22) is unitary.

4.2 A Large U = 4 eV Electron-Electron Interaction Case

Figure 4 gives the transmission coefficients for a large U=4 eV electronic interaction. Therefore, and in addition to the Pauli exclusion principle, there are now interactions between all the particles involved in the molecular junction. In the hole transmission case, the interactions between the scattered hole and the electrons localized on the molecule are calculated by subtracting the interactions existing if there was one electron more instead of a hole on the molecule.

To compare the CI-ESQC with the mono-electronic ESQC T(E) spectra, we pay particular attention in the following and for large U to the choice of the mono-electronic electronic interaction parameters. Indeed, if the mono-electronic parameters are not modified in between the two approaches, the electron-electron interactions will be considered twice in the CI-ESQC case: first in the many-body interactions and second, in average in the mono-electronic parameters. So, we have imposed that the HF calculated MOs in the interacting case are the same as compared to the ones obtained with U=0. This was done by subtracting the bielectronic part of the Fock operator (calculated in the MOs of the non-interacting

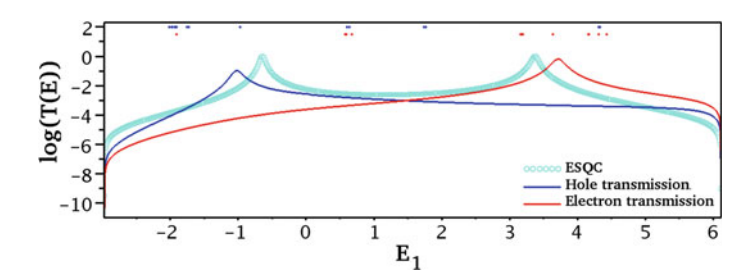


Fig. 4 Transmission coefficients as a function of E the asymptotic energy of the delocalized electron, for U=4 eV. The on-site energy on the electrodes is e=4 eV. The *solid line* is the transmission coefficient for holes, the *dotted line* is the transmission coefficient for electrons

case) from the mono-electronic Hamiltonian in the interacting case. Electronic interactions along the electrodes or from the electrodes to the molecular junction have also been renormalized, i.e., averaged interactions have been subtracted from the mono-electronic parameters. This average is calculated when the localized electrons are frozen in the HF fundamental state. HF is not an exact way to get these average interactions. Therefore, and when comparing with the exact interacting case, we are aware that the position of the T(E) resonances in the mono-electronic case is dependent on this choice.

In Fig. 4, the series of points located above the T(E) spectra indicates the eigenvalue energy positions of the Hamiltonian of the molecular junction, including the part of the electrodes where the incident and transmitted particle interact with the electrons of the molecular junction. A few of these eigenvalues can be associated with a given T(E) resonance. The correspondence Fig. 5 gives the renormalized decomposition of the associated eigenvectors for each of the two resonances on the subspace generated by the Slater determinants with all the particles on the molecule, i.e., the Slater determinants with one electron in the molecule for a hole scattering process and three electrons for an electron scattering process. This decomposition is using only two Slater determinants. For an electron transmission process, it simply corresponds to two electrons in the HF fundamental $|\omega_1\overline{\omega_1}\rangle$ state plus one electron in the $|\omega_2\rangle$ state. For a hole transmission process, one hole is created in the $|\overline{\omega_1}\rangle$ state. This seems to correspond exactly to a mono-electronic transmission picture where a particle is simply tunneling through the HOMO or LUMO orbitals. But here, the exact fundamental state of the two-electrons subsystem is given by the quantum superposition $0.979||\omega_1\overline{\omega_1}|\rangle - 0.202||\omega_1\overline{\omega_1}|\rangle$. This is different from the simple $||\omega_1\overline{\omega_1}|\rangle$ determinant. Therefore, the state describing the two electrons electronic ground state is modified by the transferred particle. This explains the difference in energy between a resonance in a full CI-ESQC calculation and in a simple ESQC calculation. Another consequence is that, for example, at E=4.65 eV, i.e., for an electron transfer process not only ω_2 but also ω_1 are participating to the transmission mechanism. Finally, the tunneling process through the Fig. 2 quantum system with a large U can be viewed as supported by a "HOMO-like" resonance and a "LUMOlike" resonance because of the small number of electronic states involved in the model quantum state space used. But it cannot be reduced to a simple frozen-heart like picture.

Resonance energie	Composition
-1.70 eV	100%
4.65 eV	100%

Fig. 5 Renormalized decompositions of the Hamiltonian's eigenvectors associated with each resonances projected on the configurations with one electron on MMM for hole transfer and the configurations with three electrons on MMM for electron transfer

5 Application to a Weakly Coupled Four-States Molecule with a Four Electrons Closed Shell Structure

In the previous section, it was shown how a scattering process required a model quantum state space spanned by multi-configuration electronic states involving both the incident particle and the resident electrons. But this previous two-states molecule is very specific since these two states are of opposite symmetry relative to the center of the system and thus the only two possible electronic configurations with three or one electrons in the molecule during the scattering process are of opposite symmetry and therefore cannot mix. To explore further the consequence of a CI-ESQC calculation, a four-states molecular junction is considered in this section. This system is shown in Fig. 6 where the spatial orbitals are still here 1s Gaussian functions for simplicity and with $q = e^-$ for electron transfer, $q = h^+$ for hole transfer and $M_s = 1/2$. The orbitals $|\omega_1\rangle$ and $|\omega_3\rangle$ are symmetric relative to the center and the orbitals $|\omega_2\rangle$ and $|\omega_4\rangle$ anti-symmetric.

Figure 7 gives the CI-ESQC calculated transmission coefficients for holes (solid line) and electrons (dotted line) together with the transmission coefficient obtained after a simple ESQC calculation (circles) for reference. In the top T(E) curves (a), there are no bi-electronic interactions and in the bottom T(E) curves (b) U=2.5 eV for these electronic interactions. In (b), U was chosen smaller as compared to the previous two-states case since the MOs are more widespread in energy because of the larger quantum state space as compared with the two-states case.

In the U=0.0 eV non-interacting case, the CI-ESQC and ESQC calculated T(E) have the same resonance shape and the same T(E) curvature in between the resonances. As discussed previously, the resonance energies are shifted from ESQC to CI-ESQC and the resonance maxima are not reaching unity with CI-ESQC. For U=2.5 eV, the T(E) resonance are largely shifted in energy and there are new resonances as compared to ESQC. As discussed below, these new resonances are introduced by the electronic configurations built up with the molecule in an excited state. Indeed, these resonances are not of high interest here since they are always outside the central ground and first excited T(E) resonances. Below, we focus on the four central T(E) resonances located at E=-1.12, -0.62, 3.16, 4.34 eV.

The state decomposition of each resonance is shown in Fig. 8. Now and contrary to what was obtained in the previous section, those decompositions do not lead to single Slater determinants. For each resonance, a principal determinant can

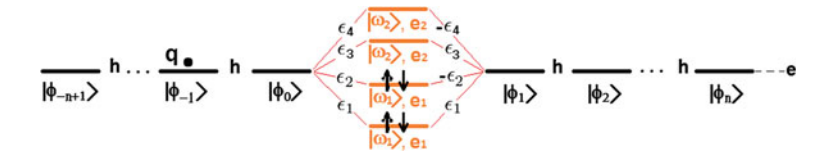


Fig. 6 Schematic representation of the system {electrodes, two-states defect}

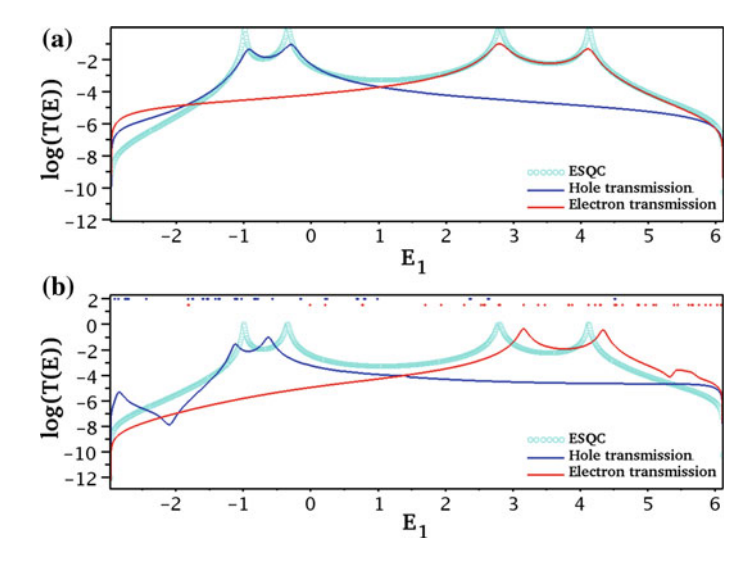


Fig. 7 Transmission coefficients as a function of E the asymptotic energy of the delocalized electron. In (a) there is no electron–electron interaction and e = 0, and in (b) U = 2.5 eV and e = 4.9 eV. The *solid line* is the transmission coefficient for holes, the *dotted line* is the transmission coefficient for electrons

Energy	λ-y _o	Renormalized decomposition			
-1.12eV		78.8%			
		8.5% + 0.2% + 0.7% + 0.7% + 8.9% + 1.3% + 0.9% + 0.1% +			
-0.62eV -0.5	-0.57eV	90.2% ——			
		3.9% + 0.6% + 1.4% + 0.7% + 0.7% + 0.9% + 0.1% + 1.4%			
3.16eV		95.8% ++			
		0.3% ++ , 0.1% ++ , 0.8% ++ , 0.7% ++ , 0.4% ++ , 1% ++ , 0.8% ++			
4.34eV	4.22eV	91.6% ++++++++++++++++++++++++++++++++++++			
		$0.4\% \stackrel{\longleftarrow}{\stackrel{\longleftarrow}{\longleftarrow}} , 1.5\% \stackrel{\longleftarrow}{\stackrel{\longleftarrow}{\longleftarrow}} , 1.8\% \stackrel{\longleftarrow}{\stackrel{\longleftarrow}{\longleftarrow}} , 0.9\% \stackrel{\longleftarrow}{\stackrel{\longleftarrow}{\longleftarrow}} , 1.2\% \stackrel{\longleftarrow}{\stackrel{\longleftarrow}{\longleftarrow}} , 0.9\% \stackrel{\longleftarrow}{\stackrel{\longleftarrow}{\longleftarrow}} , 0.7\% \stackrel{\longleftarrow}{\stackrel{\longleftarrow}{\longleftarrow}} , 0.9\% \stackrel{\longleftarrow}{\stackrel{\longleftarrow}{\longleftarrow}}$			

Fig. 8 Renormalized decompositions of the Hamiltonian's eigenvectors associated with two of the resonances projected on the configurations with three electrons on MMM for hole transfer and the configurations with five electrons on MMM for electron transfer

still be identified with a determinant weight much larger than the others in the superposition. However, many other Slater determinants contribute to each resonance. For example and with a weight of 95.8 %, the principal determinant of the E = 3.16 eV resonance corresponds to an electronic configuration with two electrons in HOMO-1, two electrons in HOMO, plus one electron in the LUMO. But seven other Slater determinants are required to properly reconstruct this resonance. In a mono-electronic ESQC interpretation, this resonance would have been called the "LUMO" resonance of the junction since the transferred process would have been described by only passing through this LUMO mono-electronic state. But the Slater determinant $||\omega_1\overline{\omega_1}\omega_2\overline{\omega_2}|\rangle$ is not the exact ground state of the four-electrons molecule subsystem. Therefore, it is perturbed by the incident electron and a large state superposition results. This also explains the large difference in energy between the CI-ESQC and the ESQC resonances.

6 Conclusion

A new method was presented to calculate the electronic transmission coefficient through a molecular junction from an electronic multi-configuration point of view. The first step was to choose a quantum state basis set of Slater determinants to perform the CI-ESQC calculations. This basis set describes a tunneling junction where an effective particle (electron or hole) is scattered on a molecule described by its full electronic structure. In a second step, the mono-electronic ESQC calculation technique was generalized using this Slater determinant basis set. In a third step, the electronic transmission coefficient through the molecular junction was calculated. It depends on the electronic configuration of the molecule when the incident and transferred particle is far from it. Each possible configuration opens a tunneling channel and it is the quantum superposition of those channels which describe the full CI tunneling process through the molecular junction. Then, the scattering process analysis was restricted to the case of a ground state molecule channel. This CI-ESQC model was applied to two cases, focusing on the electronic multi-configuration mechanisms responsible for the tunneling resonances observed in the calculated transmission coefficient. In a two-states molecule case, it can be simply shown how a mono-electronic interpretation of a particle transmission is distorted by the many-body effects. Indeed, no single MO can describe a twoelectron subsystem in its ground state such as one of the orbital is totally empty or occupied and with electronic configuration where the incident particle occupies also instantaneously the molecule. For the case of a four-states molecule, the fourelectrons electronic ground state is modified by the scattered particle because no orbital is totally empty or occupied during a scattering process. The mechanisms at work for the resonances do not simply correspond to a simple occupation, for example, of the LUMO. It is a full quantum superposition of many Slater determinants describing different configurations of the molecule electronic system by considering also the scattered particle (electron or hole). This demonstrates that the actual identification of the dI/dV resonance (and map) of STM resonances as, for example, HOMO and LUMO resonances is not exact. Those resonances are a mix of many electronic configurations of the molecular junction, including electronic configurations taking into account the transferred particle. Therefore, the STM dI/dV maps must be interpreted with care.

Appendix A: Parameters and Calculation Method for the Electron–Electron Interactions

To calculate the electron–electron interactions a basis set of localized spatial orbitals is required. In this chapter, 1s Gaussian functions were used whose exponent parameters are noted α_i . The following table provides the different numerical values of those Gaussian functions and the parameters on which they depend:

		Parameters
$\overline{\langle \phi_i \phi_j \rangle, \langle \phi_i \omega_j \rangle, \langle \omega_i \omega_j \rangle}$	Overlap integrals	d_i, α_i
$egin{aligned} raket{\phi_i h_{ ext{mono}} \phi_j angle,raket{\phi_i h_{ ext{mono}} \omega_j angle} } \ raket{\omega_i h_{ ext{mono}} \omega_j angle} \end{aligned}$	Mono-electronic interactions	h, e, μ_i, v_i, e_i
$egin{array}{l} \left\langle \phi_i \omega_j \middle rac{1}{r_{12}} \middle \phi_k d_l ight angle, \left\langle \phi_i \omega_j \middle rac{1}{r_{12}} \middle \omega_l \phi_k ight angle \\ \left\langle \omega_i \omega_j \middle rac{1}{r_{12}} \middle \omega_k \omega_l ight angle \end{array}$	Coulomb and exchange integrals	$d_i, lpha_i, \lambda$

Here, d_i is the position of site i and λ is the screening length for Coulombian interactions: to mimic the Colombian decay due to the electrons of the environment, an exponential factor $e^{-\lambda|r|}$ was introduced in the Coulomb and exchange integrals [15].

To simplify the calculations of the two bodies integrals, we use Fourier transformations to express them in the form of a one-dimension integral [20]:

$$p = \alpha_i + \alpha_k \quad q = \alpha_i + \alpha_l \tag{23}$$

$$R_p = \frac{\alpha_i d_i + \alpha_k d_k}{p} \quad R_q = \frac{\alpha_j d_j + \alpha_l d_l}{q}$$
 (24)

if $R_{\rm p} \neq R_{\rm q}$:

$$\langle \phi_{i}^{GF} \phi_{j}^{GF} | \frac{e^{-\frac{r_{12}}{\lambda}}}{r_{12}} | \phi_{k}^{GF} \phi_{l}^{GF} \rangle = \frac{e}{4\pi_{0}} \left(\frac{2\alpha_{i}}{\pi} \right)^{\frac{3}{4}} \left(\frac{2\alpha_{j}}{\pi} \right)^{\frac{3}{4}} \left(\frac{2\alpha_{k}}{\pi} \right)^{\frac{3}{4}} \left(\frac{2\alpha_{l}}{\pi} \right)^{\frac{3}{4}} \times e^{-\frac{\alpha_{i}\alpha_{k}}{p} (d_{i} - d_{k})^{2} - \frac{\alpha_{j}\alpha_{l}}{q} (d_{j} - d_{l})^{2}} \left(\frac{\pi^{2}}{pq} \right)^{\frac{3}{2}} \frac{1}{|R_{p} - R_{q}|} \times \frac{2}{\pi} \int_{0}^{+\infty} e^{-\frac{p+q}{4pq}k^{2}} \sin\left(\frac{k}{|R_{p} - R_{q}|} \right) \frac{k}{k^{2} + \lambda^{2}} dk$$
(25)

if $R_{\rm p} = R_{\rm q}$:

$$\langle \phi_{i}^{GF} \phi_{j}^{GF} | \frac{e^{-\frac{r_{12}}{\lambda}}}{r_{12}} | \phi_{k}^{GF} \phi_{l}^{GF} \rangle = \frac{e}{4\pi_{0}} \left(\frac{2\alpha_{i}}{\pi} \right)^{\frac{3}{4}} \left(\frac{2\alpha_{j}}{\pi} \right)^{\frac{3}{4}} \left(\frac{2\alpha_{k}}{\pi} \right)^{\frac{3}{4}} \left(\frac{2\alpha_{l}}{\pi} \right)^{\frac{3}{4}} \times e^{-\frac{\alpha_{i}\alpha_{k}}{p} (d_{i} - d_{k})^{2} - \frac{\alpha_{j}\alpha_{l}}{q} (d_{j} - d_{l})^{2}} \left(\frac{\pi^{2}}{pq} \right)^{\frac{3}{2}} \times \frac{2}{\pi} \int_{0}^{+\infty} e^{-\frac{p+q}{4pq}k^{2}} \frac{k^{2}}{k^{2} + \lambda^{2}} dk$$
(26)

Appendix B: Some Useful Relations

The following relations were used throughout this chapter:

$$X^{\dagger} \begin{bmatrix} Sm^{+} & 0\\ 0 & Sm^{-} \end{bmatrix} X = I_{N_{m}}$$
 (27)

$$E_0 X = \begin{bmatrix} Sm^+ & 0 \\ 0 & Sm^- \end{bmatrix} x Y_E = \begin{bmatrix} Sm^+ & 0 \\ 0 & Sm^- \end{bmatrix} X (Y - E)$$
 (28)

$$H_0X = \begin{bmatrix} Sm^+ & 0 \\ 0 & Sm^- \end{bmatrix} XY_H = \begin{bmatrix} Sm^+ & 0 \\ 0 & Sm^- \end{bmatrix} X(h + s(Y - E))$$
 (29)

References

- Repp, J., Meyer, G., Stojkovic, S.M., et al.: Molecules on insulating films: Scanning-tunneling microscopy imaging of individual molecular orbitals. Phys. Rev. Lett. 94, 026803 (2005)
- Gimzewski, J.K., Joachim, C.: Nanoscale science of single molecules using local probes. Science 283, 1683–1688 (1999)
- 3. Moresco, F., Meyer, G., Rieder, K.H., et al.: Conformational changes of single molecules induced by scanning tunneling microscopy manipulation: a route to molecular switching. Phys. Rev. Lett. **86**, 672–675 (2001)
- 4. Landauer, R.: IBM J. Res. Dev. 1, 233 (1957)
- 5. Landauer, R.: Philos. Mag. 21, 863 (1970)
- Datta, S.: Electronic Transport in Mesoscopic Systems. Cambridge University Press, Cambridge (1995)
- Sautet, P., Joachim, C.: Electronic transmission coefficient for the single-impurity problem in the scattering-matrix approach. Phys. Rev. B 38, 12238 (1988)

- 8. Soe, W.H., Manzano, C., De Sarkar, A., Chandrasekhar, N., Joachim, C.: Direct observation of molecular orbitals of pentacene physisorbed on Au(111) by scanning tunneling microscope phys. Rev. Lett. **102**, 176102 (2009)
- Soe, W.H., Wong, H.S., Manzano, C., Grisolia, M., Hliwa, M., Feng, X., Mullen, K., Joachim, C.: Mapping the excited states of single hexa-peri-benzocoronene oligomers. ACS Nano 6, 3230 (2012)
- Lippmann, B.A., Schwinger, J.: Variational principles for scattering processes. I. Phys. Rev. 79, 469 (1950)
- Cerd, J., Van Hove, M.A., Sautet, P., Salmeron, M.: Efficient method for the simulation of STM images. I. Generalized Green-function formalism. Phys. Rev. B 56, 1588515899 (1997)
- 12. Wang, Y., Wang, J., Guo, H., Zaremba, E.: Many-electron effects on ballistic transport. Phys. Rev. B **52**, 4 (1995)
- 13. Towie, E.A., Watling, J.R., Barker, J.R.: Remotely screened electron-impurity scattering model for nanoscale MOSFETs. Semicond. Sci. Technol. 26, 055008 (2011)
- 14. Meir, Y., Wingreen, N.S.: Landauer formula for the current through an interacting electron region. Phys. Rev. Lett. **68**, 2512 (1992)
- Toyama, F.M., Nogami, Y.: Effect of a trapped electron on the transmission characteristic of a quantum wire. Phys. Lett. A 196, 237–241 (1994)
- Malysheva, L.I., Onipko, A.I.: Linear and nonlinear resonnant tunneling through a minimalsize resonnant structure in quantum molecular wires. Phys. Rev. B 46, 7 (1991)
- Vérot, M., Borshch, S.A., Robert, V.: Importance of a multiconfigurational description for molecular junctions. Chem. Phys. Lett. 519520, 125–129 (2012)
- Toroz, D., Rontani, M., Corni, S.: Visualizing electron correlation by means of ab-initio scanning tunneling spectroscopy images of single molecules. J. Chem. Phys. 134, 024104 (2011)
- 19. Ami, S., Hliwa, M., Joachim, C.: Molecular OR and AND logic gates integrated in a single molecule. Chem. Phys. Lett. **367**, 662 (2003)
- Szabo, A., Ostlund, N.S.: Modern Quantum Chemistry, pp. 410–416. Dover Publications, New York (1996)

Electron Transport Through a Molecular Junction Using a Multi-configurational Description

Martin Vérot, Serguei A. Borshch and Vincent Robert

Abstract The importance of the electronic description of the junction electronic structure is investigated in quantum transport through molecular devices. Using an accurate wave-function-based description of the low-energy spectroscopy, transport through a 2-electron/2-molecular orbital prototype is evaluated. The contributions arising from the presence of competing singlet and triplet states in magnetic systems are analyzed. It is shown that the electronic conductivity provides a signature of the full multiplet energy spectrum, as well as of the multideterminant structure of wave-functions. We then inspected the current-potential characteristics as a function of the differential magnetization of the electrodes. From the wave-function description, a modulation of the magnetoresistance ratio is anticipated and both direct and inverse regimes are observed depending on the electronic structure of the junction.

1 Introduction

Since the pioneering conjecture on the use of molecules as an alternative to silicon materials [1], miniaturization is at reach and has opened a whole new range of new physical effects for molecular-based electronic devices. Challenges are numerous from both experimental and theoretical points of view: miniaturization at the molecular scale for conduction questions simultaneously spectroscopic techniques, as well as the quantum description of systems where it cannot be discarded.

M. Vérot (⋈) · S. A. Borshch

Laboratoire de Chimie, École Normale Supérieure de Lyon, CNRS, 46 allée d'Italie

F-69364 Lyon, France

e-mail: martin.verot@ens-lyon.fr

V. Robert

Laboratoire de Chimie Quantique, Université de Strasbourg, 4 rue Blaise Pascal F-67000 Strasbourg, France

Yet, a wide range of applications such as molecular diodes, transistors, and molecular switches have already been fabricated [2–4]. The most striking aspect of molecular junctions conductance are effects such as negative differential resistance [5–7]. or single molecular Kondo effect [8]. Development of molecular electronics and molecular spintronics now stimulates experimental chemists to synthesize new molecules, which can manifest unique features in molecular junctions. Some guiding principles establishing correlations between the fine details of the electronic structure of a molecular system and its conductivity are necessary for to go beyond a mere trial and error process.

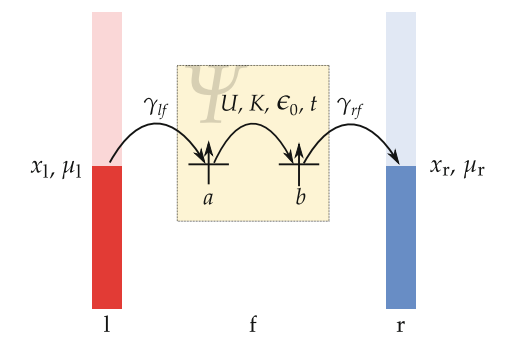
Very often the single-molecule conductance is analyzed on the basis of the composition and energetics of molecular orbitals as they are considered as conducting channels from a monoelectronic point of view [9]. It is usually assumed that the molecular orbitals positions with respect to electrodes's Fermi energies are of prime importance to achieve resonant transmission and the so-called "level alignment problem" has been much discussed [10]. However, even a molecule with closed electronic shells goes through an open-shell state during the electron transmission process. And the multi-configurational description is the most adequate to describe open-shell molecules [11]. In particular, the multi-electronic treatment becomes crucial for magnetic molecules [12, 13]. Over the last years, many efforts have been devoted to include multi-electronic effects into the description of molecular conduction, either with DFT approaches or explicit correlation treatments. Both types of electron transfer through molecular junctions, namely sequential and coherent tunnelings, have been considered in the literature [9, 14–18]. However, earlier works usually focus on the shapes and energies of the molecular orbitals to explain the details of the observed conductance even if Nelectron energies and wave-functions might be more appropriate to describe correlation effects when transport is investigated [19].

Here, our goal is to investigate the relationship between key factors resulting from explicit multi-configuration calculations of molecular electronic states and the molecular junction behavior. We first concentrate on a system with nonmagnetic electrodes before investigating magnetoresistive effects when electrodes are spin-polarized.

2 Theoretical Approach

It is known that electron correlation effects can dramatically impact the electronic properties of molecular systems. As a consequence, density functional theory (DFT) methods may not be well-adapted to describe systems where the presence of quasi-degenerate molecular orbitals could imply a prime importance of static correlation effects. The latter is usually inexactly described by approximate exchange correlation functionals. Thus, we decided to fully describe the multi-electronic states spectrum of a 2-electrons/2-orbitals *a* and *b* system using explicitly correlated methods (*ab initio* configuration interaction (or CI)

Fig. 1 Schematic representation of electron hopping process controlled by the spin states of the molecular junction. From the wave-functions, the relevant integrals involved in the model are extracted from CI calculations and indicated



calculations). We then injected the extracted information into a sequential tunneling transport description [16].

The left (1) and right (r) Fermi energies of the electrodes are μ_l , μ_r , respectively. The coupling coefficients $\gamma_{l,a}$ and $\gamma_{b,r}$ (see Fig. 1) of the fragment (f) with the electrodes are assumed to be small compared to temperature. Even though inelastic effects can modify conducting properties [20–24] we here focus on purely electronic effects.

Therefore, the full electronic Hamiltonian is split as the following:

$$\hat{H} = \hat{H}_{f} + \hat{H}_{l} + \hat{H}_{r} + \hat{H}_{fl} + \hat{H}_{fr}$$

where \hat{H}_f is the Hamiltonian of the isolated molecule, \hat{H}_l and \hat{H}_r stand for the electrodes Hamiltonians and $\hat{H}_{\rm fl}$, $\hat{H}_{\rm fr}$ correspond to the coupling Hamiltonians. Within our model, we assumed that only monoelectronic jumps are allowed. Thus, $\hat{H}_{\rm fl}$ can be written as $\hat{H}_{\rm fl} = \hat{H}_{\rm fl,anionic} + \hat{H}_{\rm fl,cationic} = \sum_{f,l,\sigma} \gamma_{l,f} f_{\sigma}^{\dagger} l_{\sigma} + \sum_{f,l,\sigma} \gamma_{l,f} l_{\sigma}^{\dagger} f_{\sigma}$ where

f stands for the fragment orbitals, l for the electrode orbitals, and $\sigma = \uparrow$ or \downarrow ($\hat{H}_{\rm fr}$ is defined accordingly). Higher order terms are not considered as it is unlikely to have a double charge transfer occurring in the tunneling regime. The first term defines what we name "anionic" paths since the fragment temporarily holds one more electron as compared to the initial two-electron state on the connected molecule. Similarly, the second term defines "cationic" paths, the fragment being temporarily deprived of one electron.

2.1 Isolated Fragment Low-Energy Spectroscopy

Let us briefly recall that the 2-electrons/2-orbitals picture can describe a much wider range of situation than the simple molecule of H₂-like molecules. The low-energy spectroscopy accessible through multireference configuration interaction methods (MRCI) [25, 26]. With these MRCI methods, we can obtain the spectroscopy of polynuclear magnetic systems with an accuracy of the order of a few

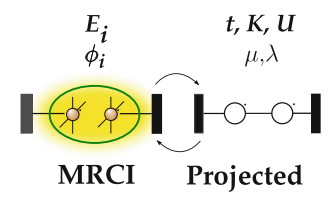


Fig. 2 Effective Hamiltonian theory: starting from the initial system holding a large number of electrons and orbitals, the procedure concentrates the relevant information in a two-electron-two-orbital picture which captures the energetics and electronic details of the exact system

tens of wavenumbers (cm⁻¹) [27]. *Via* the theory of effective hamiltonians, the spectroscopy can then be reduced to a simple 2-electrons/2-orbitals picture [28].

Here we consider a symmetric system with two degenerate, localized, atomic orbitals a and b with an energy ε_0 . The symmetry-adapted molecular orbitals are the normalized in-phase (g) and out-of-phase (u) linear combinations:

$$g = \frac{a+b}{\sqrt{2}} \qquad u = \frac{a-b}{\sqrt{2}} \tag{1}$$

Using the effective Hamiltonians theory, one can rigorously derive an effective Hamiltonian \hat{H}^{eff} . The construction of the latter has been previously reported [13]. It relies on the projection of the MRCI eigenfunctions of the exact Hamiltonian onto the four $M_s = 0$ configurations $|a\bar{b}|$, $|b\bar{a}|$, $|a\bar{a}|$ and $|b\bar{b}|$ defining the so-called model space. Since the spin-projections $M_s = -1, 0, +1$ of the triplet are degenerate, this effective Hamiltonian fully defines the investigated part of the spectrum. This procedure allows one to map the exact Hamiltonian with a limited set of physical parameters, namely the resonance $t = \langle a\bar{a}|\hat{H}^{\mathrm{eff}}|a\bar{b}\rangle$, one-site repulsion $U = \langle a\bar{a}|\hat{H}^{\mathrm{eff}}|a\bar{a}\rangle$ and exchange $K = \langle a\bar{b}|\hat{H}^{\mathrm{eff}}|b\bar{a}\rangle$ integrals. The full problem is reduced to physical quantities without omitting the electronic variety of molecules which can be considered as biradicals (vanadium(IV) or copper(II) dimers and organic radicals for example). The key point is that we exploit simultaneously both the energies and the projection of the wave-functions to extract relevant parameters. This amount of information could not be extracted only with the energies, which is a possible limitation of monodeterminental methods.

First, one can recover the ground state of the "neutral" junction

$$|N=2,2S+1=1,M_S=0\rangle_{g}=\lambda|g\overline{g}|+\mu|u\overline{u}| \qquad (2)$$

where λ and μ are given by $\mu/\lambda=-(4t+\sqrt{U^2+16t^2})/U$ (the normalization commands $\lambda^2+\mu^2=1$), N, S and M_s are the number of electrons standing on the molecule, the spin of the fragment and its projection, respectively. Thus, in the non-correlated limit (i.e., Hückel, U=0): $\lambda=1$ and $\mu=0$, whereas, in the strong correlated limit $(U\to\infty)$: $\lambda\to1/\sqrt{2}$ and $\mu\to-1/\sqrt{2}$. The orthogonal excited singlet states read $|2,1,0\rangle_{\rm g}^*=-\mu|g\overline{g}|+\lambda|u\overline{u}|$ and $|2,1,0\rangle_{\rm u}=(|g\overline{u}|+|u\overline{g}|)/\sqrt{2}$.

$(3,2,1/2\rangle_u, 3,2,1/2\rangle_g) \text{ and anionic } (1,2,1/2\rangle_g, 1,2,1/2\rangle_u) \text{ states of the molecular junction}$					
$ 2,1,0\rangle_{g}$	$ 2,1,0\rangle_{\mathrm{g}}^{*}$	$ 2,3,1\rangle_{ m g}$	$ 2,1,0\rangle_{\mathrm{u}}$		
$K + \frac{U - \sqrt{U^2 + 16t^2}}{2}$	$K + \frac{U + \sqrt{U^2 + 16t^2}}{2}$	-K	-K + U		
$ 3, 2, 1/2\rangle_{\rm u}$	$ 3,2,1/2\rangle_{\rm g}$	$ 1,2,1/2\rangle_{\mathrm{g}}$	$ 1,2,1/2\rangle_u$		
$\varepsilon_0 + U + t - K$	$\varepsilon_0 + U - t - K$	$-\varepsilon_0 + t$	$-\varepsilon_0 - t$		

Table 1 Corresponding energies for neutral $(|2,1,0\rangle_g, |2,1,0\rangle_g^*, |2,3,1\rangle_g, |2,1,0\rangle_u)$, cationic $(|3,2,1/2\rangle_u, |3,2,1/2\rangle_g)$ and anionic $(|1,2,1/2\rangle_g, |1,2,1/2\rangle_u)$ states of the molecular junction

Their energies are summarized in Table 1. The full space spanned by the occupations of g and u also gives rise to a triplet state with degenerate spin-projections $M_s = +1, 0, -1: |2, 3, 1\rangle_n = |gu|, |2, 3, 0\rangle_n = (|g\overline{u}| - |u\overline{g}|)/\sqrt{2}$ and $|2, 3, -1\rangle_n = |\overline{gu}|$.

At this stage, 2-electron configurations have been considered to extract the different parameters from MRCI calculations. Nevertheless, intermediate states $(|I\rangle)$ with one added (anion) or withdrawn (cation) electron must also be considered to account for electron transport. The corresponding electronic states of the cation with $M_s = +1/2$ spin projection are $|3, 2, 1/2\rangle_g = |g|$ and $|3, 2, 1/2\rangle_u = |u|$, whereas the anionic ones read $|3, 2, 1/2\rangle_{u} = |g\overline{g}u|$ and $|3, 2, 1/2\rangle_{g} = |gu\overline{u}|$. Assuming that the relevant parameters are not modified when ionization of the junction occurs, the energies of these states are easily evaluated (see Table 1). Even though the parameters included into the energy expressions refer a priori to an isolated molecule, they can be modified to account for the environment effects such as charge polarization phenomenon. Such procedure is often used in MRCI calculations of magnetic exchange coupling constants [29]. Let us stress that whatever the strategy, DFT or MRCI, the calculated levels should be renormalized, for instance through many-body perturbation theory to include the polarization effects from metallic electrodes [30]. Our contribution lies in the mapping of ab initio calculations into a phenomenological model (see Fig. 2) which not only reproduces the energetics of the full spectrum (t, K, U) but also the structure of the wave-functions (λ, μ) .

2.2 Transport Through Magnetic Molecular Devices

In a two-step hopping process, two channels are to be considered. The first one consists in transferring one electron from the left electrode to the fragment in the initial step. This channel is called "anionic" path since the fragment temporarily holds a negative charge. The second channel goes first through the removal of one electron from the fragment and is thus referred to as a "cationic" path (see Fig. 3).

Let us detail the equations for the anionic pathway. Similar equations are obtained for the cationic one. While the fragment is depicted with a many-body approach, the electronic structure of each electrode is given by a tight-binding model. In the weak coupling regime, the electronic structure of the fragment is not deeply modified by the presence of the electrodes. At this stage, let us stress that

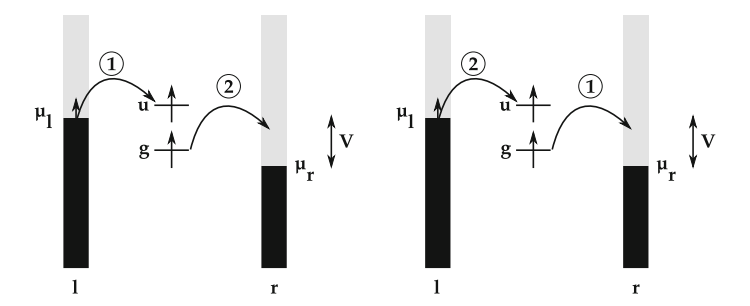


Fig. 3 Schematic representation of the anionic (left) and cationic (right) channels

such regime implies that the multi-electronic structure is not strongly affected by the electrostatic distribution of the electrodes. As mentioned before, the quality of the parameters can be improved by embedding the molecule in an appropriate bath to depict the environment.

The kinetic equation for the molecular fragment population for each intermediate state n_I under stationary regime can be written as:

$$\frac{\mathrm{d}\,n_I}{\mathrm{d}\,t} = (w_{\rm rI} + w_{\rm II})(1 - n_I) - n_I(w_{II} + w_{Ir}) = 0 \tag{3}$$

where $w_{\rm rI}$, $w_{\rm II}$ (w_{II} , w_{Ir}) stand for the electron transfer probabilities from electrodes to the molecular fragment (from the fragment to the electrodes, respectively). Since inelastic effects are ignored, the electronic energy is constant. Therefore, the energy loss or gain between the N and N+1 states is exactly compensated by the energy of the incoming or outgoing electron. The probabilities include the electronic details of the junction holding N or $N\pm 1$ electrons with corresponding states $|N,S,M_s\rangle$ and $|N\pm 1,S',M_s'\rangle$.

Those terms derive from the Fermi's golden rule and can be written as:

$$w_{lI^{-},\sigma} = x_{l,\sigma} \frac{2\pi}{\hbar Z} \sum_{I} \rho_{l} (E_{N} - E_{N+1}) \hat{D}(E_{N} - E_{N+1})$$

$$\times \sum_{f} \left| \gamma_{l,f} \langle I^{-} | f_{\sigma}^{\dagger} l_{\sigma} | I \otimes l \rangle \right|^{2} \exp\left(-\frac{E_{N+1}}{k_{B}T} \right)$$
(4)

where l is a one-electron state localized on the left electrode such that the total energy is conserved. The expression of the other coefficients appearing in Eq. 3 is similar. They are detailed in the appendix A. Z is the partition function which accounts for the vibrational states distribution at temperature T. $x_{l,\sigma}$ stands for the spin-polarization of the left electrode. $x_{l,\sigma}$ was introduced by varying the fractions of \uparrow electrons ($x = N_{\uparrow}/(N_{\uparrow} + N_{\downarrow})$) on the left and right electrodes, x_{l} and x_{r} . The $x_{l,r}$ parameters correspond to the experimentally controlled magnetizations of the electrodes. We first studied situations with nonmagnetized electrodes for which all the different $x_{l/r,\sigma}$ parameters are taken equal to 1/2. We then examined transport

properties when magnetic electrodes are involved and more particularly two different cases: the parallel situation where $x_{l,\sigma} = x_{r,\sigma}$ and the antiparallel one where $x_{l,\sigma} = 1 - x_{r,\sigma}$

The Fermi distributions ρ_{α} of electrode α are the only voltage-dependent quantities,

$$\rho_{\alpha}(E) = \frac{1}{1 + \exp\left(\frac{E - \mu_{\alpha}}{k_B T}\right)}$$

 $\hat{D}(E)$ is the density of states of the electrode and is supposed to be constant. The coupling is ruled by the hopping integrals $\gamma_{l,f}$ and $\gamma_{l,f}$ depicted in Fig. 1 and n_l along each intermediate state can, therefore, be determined. Finally, the current is written as:

$$i(V) = e(w_{II}(1 - n_I) - w_{II}n_I). (5)$$

3 Impact of the Electronic Structure of the Fragment

We first studied the impact of the electronic structure on the current with non-magnetic electrodes. We evaluated the current as a function of the fragment parameters. For all simulations, the temperature was fixed to 10 K and the $\gamma_{1/r,I,\sigma}$ coefficients were set to 1 cm⁻¹. Unless stated otherwise, we always chose as default parameters $\epsilon_0 = -15,000 \, \mathrm{cm^{-1}}$, $t = -3,000 \, \mathrm{cm^{-1}}$, $K = 10 \, \mathrm{cm^{-1}}$ and $U = 25,000 \, \mathrm{cm^{-1}}$). The channel with the lowest energy defines the energy reference for the Fermi energies. A bias voltage V is then applied from 0 to 50,000 cm⁻¹ (50,000 cm⁻¹ corresponds to 6.2 V). The parameters were continuously varied to trace the conduction changes with respect to the electronic states of the junction. Let us remind that a one-to-one correspondance between MRCI calculations and the set of parameters can be made using the effective Hamiltonian theory.

3.1 Influence of the Coulomb On-Site Repulsion U

Starting from a singlet-character junction, U was varied from $0~\rm cm^{-1}$ to $40,000~\rm cm^{-1}$, a standard range for magnetic molecules [31, 32]. First, let us mention that the $t=-3,000~\rm cm^{-1}$ value pushes the anionic states $|3,2\pm1/2\rangle_{\rm g}$ much higher in energy than the $|3,2\pm1/2\rangle_{\rm g}$ ones and there contribution at low-voltage is absent.

The voltage at which a channel opens is directly controlled by the spectroscopic features of the fragment. The length of the steps is equal to energy differences

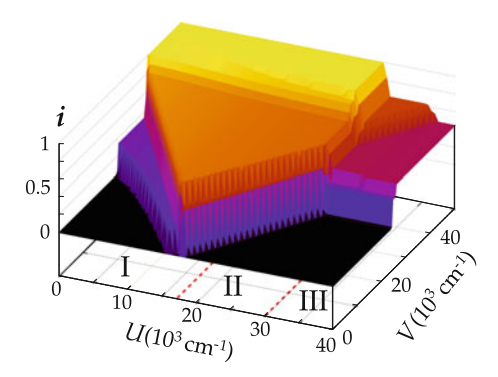


Fig. 4 Influence of the on-site repulsion U (cm⁻¹) on the i-V characteristic. The current is normalized (i) with respect to the voltage (V). $t=-3,000\,\mathrm{cm^{-1}}$, $K=10\,\mathrm{cm^{-1}}$, $\varepsilon_0=-15,000\,\mathrm{cm^{-1}}$. Three different regions can be distinguished: for the zones (I) and (II), the anionic pathway is preferred while the cationic one is preferred in region (III). The difference between the zone (I) and (II) resides into the different relative placement of the states

between the neutral and intermediate states. Thus, as it can be tedious to obtain theoretically the energetic ordering of the different states for a magnetic system, it confirms that the accuracy of methods such as wave-function-based ones is of prime importance. Here, U acts like a gate voltage by controlling the spectroscopy of the fragment and the traditional "diamond-like" shape observed for conductance originates from level-crossing between ionic and neutral energy states, favoring either one channel or another.

Then, one can analyze the successive steps observed in Fig. 4. At high voltages where the triplet and three singlet states contribute to the current, their contributions are rigorously equal. Besides, the ratio of the contributions arising from the triplet $|2,3,(0,\pm 1)\rangle_{\rm u}$ and singlet $|2,1,0\rangle_{\rm u}$ channels (see steps 2 and 3 in Fig. 5a) is equal to the ratio of their degeneracies, namely 3. Therefore, the sum of the currents through $|2,1,0\rangle_{\rm g}$ and $|2,1,0\rangle_{\rm g}^*$ channels is exactly 2/3 of the one through the triplet state. Such decomposition allows one not only to split the current into different contributions but also to clarify the low-energy spectroscopy of the junction. Indeed, for larger U values, the first step (1 in Fig. 5b, bottom) corresponds to the triplet channel, suggesting a paramagnetic junction. At this stage, we can notice that the relative heights of the $|2,3,(0,\pm 1)\rangle_{\rm u}$ and $|2,1,0\rangle_{\rm u}$ channels depend only on their degeneracies. The situation is more complicated for the singlets of g symmetry where correlation factors such as the ratio t/U are determinant. This is further analyzed in the next section.

Let us now focus on the current value i as a function of the voltage V and the on-site repulsion U (i-V characteristic, Fig. 4). In the low-U regime (Fig. 5a, zone (I) and (II)), $E(|3,2,\pm 1/2\rangle_{\rm u}) < E(|1,2,\pm 1/2\rangle_{\rm g})$. Thus, the conduction through the anionic channels dominates whereas the opposite holds in the high-U regime (zone (III)). This can be easily understood: the anionic channels must overcome the energetic cost of accommodating two electrons on the same site

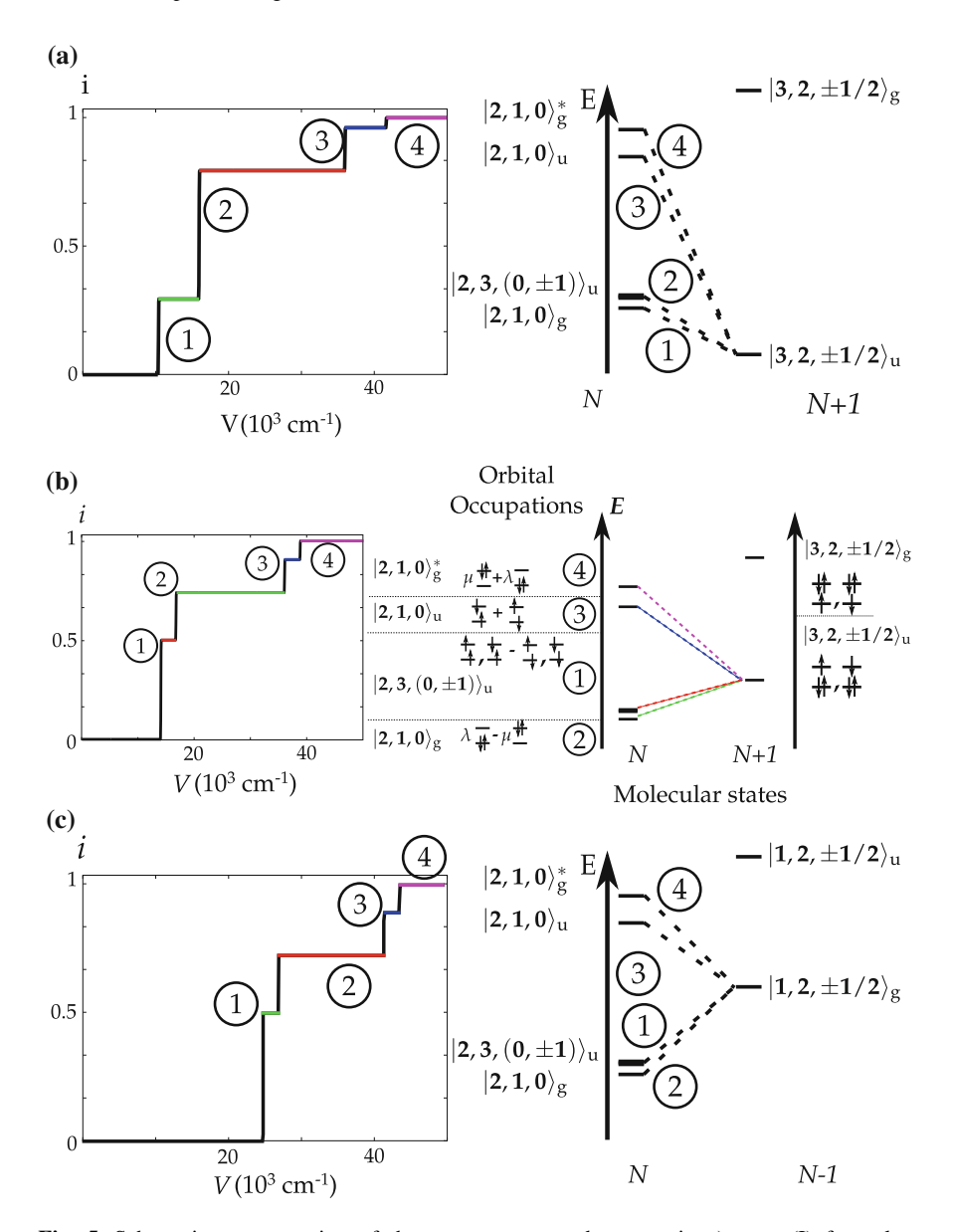


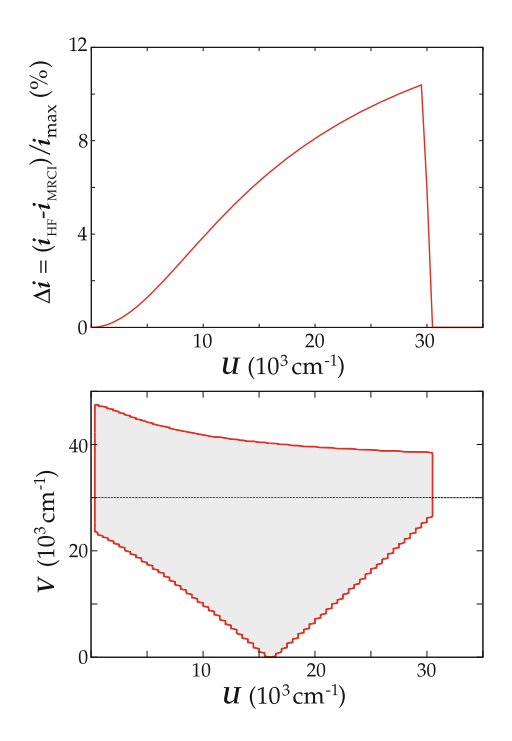
Fig. 5 Schematic representation of the spectroscopy and current in a) zone (I) for a low correlated regime ($U=10,000~{\rm cm^{-1}}$), b) zone (II) for a moderately ($U=25,000~{\rm cm^{-1}}$) correlated regimes and c) zone (III) for a highly correlated regime ($U=32,000~{\rm cm^{-1}}$) is given to stress the successive opened channels. The ratio between the steps due to $|2,3,(0,\pm 1)\rangle_{\rm u}$ and $|2,1,0\rangle_{\rm u}$ is equal to 3, in agreement with the spin multiplicities of the u channels

while such double occupation is absent in the cationic channels. As their energies do not depend on U, cationic channels are not sensitive to the Coulomb repulsion. Furthermore, cationic channels are more numerous than anionic ones since the spin σ of the electrons standing on the electrodes can take all the different possible values. That is why current is reduced as the overall partition function increases.

3.2 Influence of the Multideterminantal Structure of the Wave-Function

Since many reported descriptions of transport are based on mono reference frameworks, the multiderminental nature of the wave-function was also investigated. To do so, we described the first singlet as a double occupation of the lowest-lying MO ($|2,1,0\rangle_g^{\rm HF}=|g\overline{g}|$), and the third singlet as a double occupation of the second MO ($|2,1,0\rangle_g^{*,\rm HF}=|u\overline{u}|$). Thus, the current was calculated using either a multireference electronic structure $i_{\rm MRCI}$ or a mono reference wave-function (Hartree-Fock type, HF) $i_{\rm HF}$ and $\Delta i=i_{\rm HF}-i_{\rm MRCI}$ was computed (see Fig. 6). Evidently, differential contributions arising from the open-shell singlet $|2,1,0\rangle_u$ and triplet $|2,3,(0,\pm1)\rangle_g$ channels are strictly zero in the light of their monodeterminantal character.

Fig. 6 (top) For a given voltage, the relative error $\Delta i/i_{\rm max} = (i_{\rm HF} - i_{\rm MRCI})/i_{\rm max}$ is plotted with respect to U. (bottom) Top view of the error for U and the applied voltage V, inside the highlighted zone, the error at a given U corresponds to the percentage given above. Outside the highlighted zone, the results are identical $t = -3,000 \, {\rm cm}^{-1}, K = 10 \, {\rm cm}^{-1}, \varepsilon_0 = -15,000 \, {\rm cm}^{-1}$



The overall landscape is not changed but the relative heights of the steps are deeply modified by the multi-electronic approach with enhanced modifications as U increases. Actually, at low-voltage the first step height is determined by $\left| {}_{\mathbf{u}}\langle 3,2,\pm 1/2|\hat{H}_{\mathbf{f},\mathbf{r}/\mathbf{l}}|2,1,0\rangle_{\mathbf{g}} \right|^2 = \lambda^2\gamma_\alpha^2/2$. Therefore, the contribution is reduced by a factor λ^2 when a multireference wave-function is used: full resonance is lost.

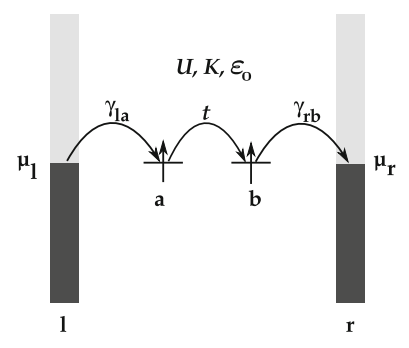
At higher voltages, the $|2,1,0\rangle_g^*$ channel is turned on, the MRCI approach and zero in the HF one. Since $\lambda^2 + \mu^2 = 1$, the difference between the total currents Δi is strictly zero. In the many-body description, two channels are partially resonating while a single one is active in the monodeterminantal description. Our conclusion is in agreement with previous works [16], stating that the heights of the plateaus are governed by the internal electronic structure. The main advantage of our approach lies in evidencing the explicit relationship between the conductivity features and the structure of the multi-electronic wave-functions (λ , μ parameters) and energies (t, K, U parameters).

Since a 20 % difference can be reached, the relevance of a mondeterminantal approach is questionable. The information which is correctly extracted from the relative heights can also be very insightful into the elucidation of electronic structures.

4 Impact of the Spin-Polarization of the Electrodes

As a magnetoresistive effect can appear when a material is sandwiched between two magnetic layers, we then focused on molecular spintronics issues. As with a macroscopic system, the electrical conductance of the device can be modified, depending on the magnetic configuration of the electrodes. In particular, the possible implementation of such devices has opened new pathways in miniaturization and offered an alternative to standard lithography technologies. A typical device uses two ferromagnetic electrodes (e.g., $La_{1-x}Sr_xMnO_3$ or Co) holding different coercive fields that allow one to fix the relative magnetization directions to parallel or antiparallel (see Fig. 7).

Fig. 7 Schematic representation of a junction contacted between two magnetic leads. The spinvalve effect can be triggered by some external magnetic field



By sweeping the external magnetic field, the resistance of the junction can be deeply modified. The extent of the modification is usually measured by the magnetoresistance ratio MR defined as

$$MR = \frac{R_{AP} - R_P}{R_{AP}},\tag{6}$$

where R_{AP} and R_P denote the resistance value in the antiparallel and parallel magnetization alignments, respectively. Based on the tunneling transport assumption [33], the MR can be expressed as a function of the left (1) and right (r) electrodes spin-polarizations P_1 and P_r as:

$$MR = \frac{2P_1P_r}{1 + P_1P_r} \tag{7}$$

Since the observation of magnetoresistance effects for sandwiched metallic layers [34], researchers have followed two main axes for the development of magnetoresistive effect. One was to change the type of sandwiched material between oxides [35, 36], alloys [37], polymers [38], and purely organic molecules [39–41]. The other was to reduce the size of the sandwiched materials. After using layers, carbon nanotubes sandwiched between two La_{1-x}Sr_xMnO₃ magnetic layers have been considered as target devices [42]. More recently, supramolecular spin valves were prepared with the addition of single molecule magnets on nanotube junctions [43, 44]. Such experimental realization was decisive since it demonstrated that there is apparently no absolute need to use magnetic leads. Indeed, the spin filtering manifestation can be ascribed to magnetic quantum dots holding singlemolecule magnet properties. In the absence of magnetic leads with a TbPc₂ (Pc = phtalocyanine) molecule, the spin valve effects arise because of the interaction between the nanotube and a single-molecule magnet. The latter exhibits an uniaxial anisotropic spin localized on the rare earth and a delocalized spin density over the π systems of the phtalocyanine. Such reduction at the molecular scale prompted the study of magnetic objects and their transport properties [45]. Following this development, we thus studied single molecules contacted between magnetic electrodes.

We particularly focused on the link between the observed current for a system with magnetic electrodes and the multideterminental description of the wavefunction. For that, two situations are considered: one where the magnetic of the two different electrodes are aligned and one where they have opposite directions (see Figure 7). We then studied the magnetoresistance observed and how much the multideterminental approach may impact its value.

For the chosen parameters values, only anionic pathways between the two lowest anionic states and the four neutral states occurs. Since the transferred electron is either \uparrow or \downarrow , two successive hops and two electrodes are to be considered, at most $2^4=16$ different transfer coefficients are anticipated. We focused primarily on two quantities (i) the total current $i_{\text{total}}=\sum_I i_I(V)=i_\uparrow+i_\downarrow$ where i_σ

indicates the spin of the transferred electron, and (ii) the polarization of the current $P^i = \frac{i_{\uparrow} - i_{\downarrow}}{i_{\uparrow} + i_{\downarrow}}$ as a function of the left electrode magnetization $(0 \le x_l \le 1)$.

4.1 Parallel Magnetization

First, let us concentrate on a parallel magnetization of the electrodes defined as $x = x_1 = x_r$. The overall shape of the total conductance is unchanged with respect to the electrode magnetization x

In this case, there is a symmetry between the $M_s=1/2$ and $M_s=-1/2$ components of the intermediate doublet state of u symmetry. It implies that the electron transfer probabilities $w_{1/2,\uparrow}$ and $w_{-1/2,\downarrow}$ are equal. For this situation, it can be analytically shown (see Appendix B) that the total current $i_{\uparrow}+i_{\downarrow}$ is constant with respect to x for parallel magnetizations.

On the other hand, the current polarization P^i is equal to $2x - 1 = P_1$, a value which does not depend on any other coefficient and is uniquely controlled by the injected electrons spin-polarization P_1 . This behavior is mainly governed by the coupling coefficients between the electrode and the fragment appearing in the expression (5) which are linear functions of x while the different fragment populations do not play any role. The polarization of the current P^i in such situation is fully controlled by the common spin-polarization value of the electrodes. Despite the presence of the molecule, the electron-hop from the left to the right lead is not spin filtered, a reflection of the symmetry of the device.

Since the conductance properties do not depend on the magnetization of the electrodes, no further information about the electronic structure of the molecule can be deduced under such condition. One could try to lift the symmetry by using two different leads. However, other difficulties might arise since the densities of states would differ from one electrode to the other. A simpler way to bring information upon the relationship between spin filtering and the electronic structure of the molecular fragment is to reverse the magnetization of one of the electrode to obtain an antiparallel configuration.

4.2 Antiparallel Magnetization

Thus, we then examined the antiparallel configuration of the electrodes magnetization, $x_1 = x$, $x_r = 1 - x_1 = 1 - x$ (i.e., $P_r = -P_1$).

First, the current is unpolarized (i.e., $P^i = 0$) for all x values. One can qualitatively anticipate that a favored spin orientation for the first hop is disfavored for the second one. As a consequence, there are no more \uparrow than \downarrow electrons flowing through the junction because of this balance. The transfer processes involving a spin flip through the junction are favored. Therefore, the amplitudes of the

electronic configurations involved in the different wave-functions of the molecular junction directly control the opened channels. Such manifestation evidently stems from the multideterminantal description of the sequential tunneling and questions the relevance of other approaches to examine open-shell junctions.

In contrast with the parallel situation, the relative heights of the peaks are functions of the electrode magnetization x. One can show that the latter are parabolic functions (see Appendix C). Indeed, the different n_l explicitly contribute on top of the linear dependence of the coupling coefficients. Thus, a spin filtering effect occurs for this antiparallel situation whereas it was absent in the parallel one. Since the steps heights vary with the magnetization, one can anticipate magnetoresistance effects.

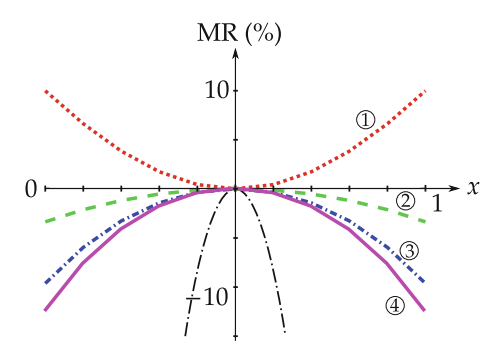
4.3 Magnetoresistance

After examining parallel and antiparallel configurations, we computed the magnetoresistance as defined in Eq. (6) with respect to the electrode magnetization to stress the importance of a wave-function description. Figure 8 exhibits the MR ratio along the four different steps generated by the presence of a 2 electron/ 2 MO junction. The magnetoresistance value can reach up to 11 % and more importantly, direct and inverse regimes are identified.

The observations of both positive and negative signs in the MR have been reported recently [46]. However, such manifestation has been mostly attributed to interfacial distance modifications. Even though our description does not include these important changes, the spin-value of the contributing states affects differently the evolution of the MR amplitude and sign. The different contributions cannot be decoupled one from the other if the population of the transient state is determined by all possible channels.

However, one can evaluate the contribution of a given channel by inspecting the MR changes it produces when it gets involved in the tunneling process. As seen in Fig. 8, the opening of the triplet channel enhances the MR value, whereas all singlet ones tend to favor an inverse MR regime. For large enough bias voltages

Fig. 8 Magnetoresistance MR as a function of the left electrode magnetization *x*. The *circled* numbers indicate the steps for which the magnetoresistance is calculated. The *black dash-dotted line* corresponds to the MR values in the absence of a contacted molecule



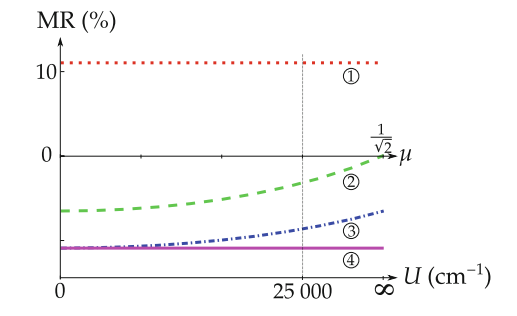
 $V (\sim 17,000 \text{ cm}^{-1} \text{ with the chosen set of parameters, see Fig. 5b), the first singlet$ (step 2) participation is switched on. The emerging negative MR contribution is large enough to result in a net inverse MR. In this case, one can show that the MR manifestation and sign come from the difference between the number and nature of available channels for ↑ and ↓ electrons (see Appendix C). Our results demonstrate that not only metal-molecule interface modulations [46] but also the reconstruction of molecule spin states spectrum (similar to spin transition) can result in the inversion of the MR sign. For comparison purposes, the MR value was finally plotted in the absence of a molecular junction (see Fig. 8, black dash-dotted line). Such analysis is rather instructive and stresses the importance of the molecular fragment. Indeed, the addition of a molecular junction strongly impacts the magnetoresistance since the magnetic molecule acts as a spin filter for the hopping electrons. The divergence that one would anticipate when $P_1 = -P_r = \pm 1$ is suppressed in the limits x = 0 and x = 1. The finite value stems from pathways through the junction that allow the spin flipping of tunneling electrons. From our inspection, the electronic structure and multideterminantal character of the wavefunctions directly control the coupling coefficients and the resulting conductance.

4.4 Impact of the Multideterminantal Approach

Thus, the magnetoresistance was finally studied with respect to the multideterminantal structure of the molecular junction states. The μ parameter, defined in Eq. (2), which is controlled by the electron correlation was smoothly varied from zero to $1/\sqrt{2}$, to span the non-correlated to strongly correlated regime range. Such inspection allows one to stress the impact of the multideterminantal structure of the wave-function on the magnetoresistance. The energies of the different states were kept constant to concentrate on this particular issue.

Figure 9 stresses the relationship between the electronic structure of the successive states and the expected magnetoresistance effect. Changing μ does not

Fig. 9 Evolution of the MR value for x = 1 as a function of the on-site repulsion parameter U, or equivalently on the μ parameter. The *circled numbers* indicate the steps for which the magnetoresistance is calculated. The U scale is not linear but the μ one is



affect the electronic structure of the triplet state. Thus, step 1 is not sensitive to μ variations (see Fig. 9). A similar behavior is observed when all four channels are involved (step 4 in Fig. 9). As expected, the electron correlation strength leaves the MR constant when all the electronic configurations are involved. In contrast, the participation of the first g symmetry singlet state leads to a U/μ -dependent MR value. This is a reflection of the multideterminantal character of this particular spin state. Finally, the opening of the u symmetry singlet state channel, which electronic structure is U-independent for symmetry reason, does not alter the evolution of the magnetoresistance but only its absolute value.

Let now us concentrate on the low U regime. Whatever the step considered, the MR derivative is zero in the non-correlated limit (see Fig. 9). Quantitatively, the evaluation of the MR value based on a monodeterminantal description deviates from the exact value by less than 10 % as long as $\mu < \mu_0 = \frac{1}{4\sqrt{2}}$. Beyond μ_0 , the validity of the monodeterminantal picture becomes questionable. In our calculations where $U = 25,000 \, \mathrm{cm}^{-1}$, the error would already be of approximately 30 %.

Inspection of the high U regime deserves more attention. Indeed, the third and fourth steps lie too high in energy ($\sim U$) to be experimentally probed with acceptable bias-voltage V values. Thus, the only accessible molecular junction states are the triplet and open-shell singlet of g symmetry (steps 1 and 2). For the second step, the calculated MR value becomes strictly zero in this regime (see Fig. 8). Such behavior cannot be reproduced by a monodeterminantal approach (i.e., $\mu=0$) which would predict a negative MR, a qualitatively unacceptable result. This discrepancy arises because a Hartree-Fock like framework overestimates the so-called ionic forms (i.e., structures where both electrons are localized on the same site). Thus, Coulomb blockade situations are favored and a positive MR value is observed. In contrast, a full multideterminantal wave-function tends to reduce the weight of these configurations. As a consequence, the Coulomb blockade phenomenon is reduced, the MR value is lowered.

5 Conclusion

The importance of a detailed description of the electronic structure was stressed out in electronic junctions. Our approach tends to complement previous theoretical works which mostly use a monodeterminantal representation of the junction.

First, with a 2-electrons/2-orbitals model, the i-V characteristic was investigated with respect to the relevant multi-electronic parameters governing the spectroscopy. Our treatment allows one to contact molecular conductivity with key electronic structure parameters which can be extracted for synthetic systems. In

¹ Here, only symmetry-adapted states were considered since our goal was to emphasize the importance of the molecular junction spectroscopy. No broken-symmetry states were introduced to avoid nonproper spin eigen-states.

that sense, the mapping of MRCI calculations into a phenomenological model ruled by a limited number of parameters can be used as a possible guide for experiment works. It was shown that depending on the energy states ordering, different conduction channels are selectively turned on. Such phenomenon results in the presence of steps in the i-V characteristic. Our inspection demonstrates that the steps length is directly linked to the spectroscopy of the sandwiched system. As a consequence, the accuracy of the method used to determine this spectroscopy is of prime importance. Multireference technique are particularly indicated for magnetic systems as the energetic ordering is subtle and requires a proper account of the static correlation. On the other hand, the height of the peaks is a direct reflection of two different aspects of the channels involved. First, their degeneracy which is a simple indication of the spin state involved. Second, the wave-function structure which can be used to extract meaningful parameters to measure the correlation strength or could be indicative of the structure of the contact.

Second, the use of a multireference Coulomb blockade situations -description of the conductivity of spin-polarized systems can highlight phenomena which could not be obtained by monodeterminental methods. For a parallel magnetization, the molecule does not induce any further spin-polarization into the injected spin-polarized current. As a consequence, we cannot extract information about the electronic structure of the involved states. In contrast, a magnetoresistive effect of the order of 10 % was calculated for an antiparallel magnetization. The sign of the magnetoresistance depends on the various solicited states. Depending on the different channels opened or closed by the multi-electronic structure, both direct or inverse magnetoresistive effects can be observed. On top of that, we suggest that the evolution of the current with respect to the magnetization is deeply changed with the correlation strength. The magnetoresistance reaches a finite value with a zero slope when correlation goes to zero. However, the discrepancy between monodeterminantal and multideterminantal approaches becomes rapidly nonnegligible. The limitation becomes even more acute in the $U \to \infty$ since the qualitative behavior characterized by a zero magnetoresistance is missed. As a major conclusion, the amplitude of the correlation effects fully governs the approach to be used to tentatively describe magnetoresistive effects. The multideterminantal character of the wave-function for systems where correlation is effective (e.g., contacted magnetic molecules) cannot be discarded in the description of spin-polarized electron transfers.

We focused here on a system with only two orbitals and a limited number of electrons. Nevertheless, this procedure can be generalized directly using multiconfigurational calculations. Either directly for systems reducible to a two-electron in two-orbital scheme —such as biradicals or binuclear transition metal complexes (copper(II) and V(IV) systems)— or it can be expanded to more complex systems involving more electrons and orbitals.

A. Coefficients

$$\begin{split} w_{\mathbf{r}I^{-},\sigma} &= x_{\mathbf{r},\sigma} \frac{2\pi}{\hbar Z} \sum_{I} \rho_{\mathbf{r}} (E_{N} - E_{N+1}) \hat{D}(E_{N} - E_{N+1}) \\ &\times \sum_{f} \left| \gamma_{r,f} \langle I^{-} | f_{\sigma}^{\dagger} r_{\sigma} | I \otimes r \rangle \right|^{2} \exp\left(-\frac{E_{N+1}}{k_{B}T} \right) \end{split}$$

$$w_{I^{-1},\sigma} = x_{1,\sigma} \frac{2\pi}{\hbar Z} \sum_{I} (1 - \rho_1 (E_N - E_{N+1})) \hat{D}(E_N - E_{N+1})$$
$$\times \sum_{f} \left| \gamma_{l,f} \langle I \otimes l | l_{\sigma}^{\dagger} f_{\sigma} | I^{-} \rangle \right|^2 \exp\left(-\frac{E_{N+1}}{k_B T} \right)$$

$$\begin{split} w_{I^-r,\sigma} &= x_{r,\sigma} \frac{2\pi}{\hbar Z} \sum_{I} (1 - \rho_r (E_N - E_{N+1})) \hat{D}(E_N - E_{N+1}) \\ &\times \sum_{f} \left| \gamma_{r,f} \langle I \otimes r | r_\sigma^\dagger f_\sigma | I^- \rangle \right|^2 \exp\left(-\frac{E_{N+1}}{k_B T} \right) \end{split}$$

B. Cancellation of Coefficients in \mathbf{i}_{tot} and \mathbf{P}^i for a Parallel Magnetization

All coefficients can be factored depending on the corresponding spin and the electrode involved. All the w_{\uparrow} coefficients can be factorized as $w = \bar{w}x_1$. While all w_{\downarrow} coefficients can be factorized as: $w = \bar{w}(1 - x_1)$.

As the difference between $w_{I^-r,l,\sigma}$ and $w_{r,1I^-,\sigma}$ is only the proportionality to $1 - \rho_{1,r}$ or $\rho_{1,r}$. We have:

$$A_1 + A_2 = B_1 + B_2$$

$$= \frac{2\pi}{\hbar Z} \sum_{l} \hat{D}(E_N - E_{N+1}) \sum_{f} \left| \gamma_{l,f} \langle I \otimes l | l_{\sigma}^{\dagger} f_{\sigma} | I^{-} \rangle \right|^2 \exp\left(-\frac{E_{N+1}}{k_B T} \right)$$

and
$$C_1 + C_2 = D_1 + D_2$$

Using equations (3) and (5) we can show that the polarization P^i is equal to 2x - 1 and the total current is constant.

		$1I^-$	$I^{-}1$	I^- r	rI^-
$ 3, 1, 1/2\rangle$	↑	A_1x	A_2x	B_1x	B_2x
	\downarrow	$C_1(1-x)$	$C_2(1-x)$	$D_1(1-x)$	$D_2(1-x)$
$ 3,1,-1/2\rangle$	↑	C_1x	C_2x	D_1x	D_2x
	1	$A_1(1-x)$	$A_2(1-x)$	$B_1(1-x)$	$B_2(1-x)$

Table 2 Simplified expression of the different coupling coefficients for the parallel situation

Table 3 Simplified expression of the different coupling coefficients for the antiparallel situation

		$1I^-$	$I^{-}1$	I^{-} r	${ m r}I^-$
$ 3, 1, 1/2\rangle$	↑	A_1x	A_2x	$B_1(1-x)$	$B_2(1-x)$
	\downarrow	$C_1(1-x)$	$C_2(1-x)$	D_1x	D_2x
$ 3, 1, -1/2\rangle$	↑	C_1x	C_2x	$D_1(1-x)$	$D_2(1-x)$
	\downarrow	$A_1(1-x)$	$A_2(1-x)$	B_1x	B_2x

8 C. Origin of the Quadratic Term in the Total Current for an Antiparallel Situation

For the antiparallel situation, only the proportionality to x or 1-x is changed for the coefficients involving the right electrode.

Using Eqs. (3) and (5) we can show that the quadratic term in the total current is the following:

$$\frac{1}{A_1 + A_2 + C_1 + C_2} ((A_1 - C_1)(D_1 - B_1) + (A_2 - C_2)(B_2 - D_2))$$

As a consequence everything is controlled by the difference between \uparrow and \downarrow coefficients deprived of their dependence upon x.

References

- Aviram, A., Ratner, M.A.: Molecular rectifiers. Chem. Phys. Lett. (1974). doi:16/0009-2614(74)85031-1
- Reed, M.A., Zhou, C., Muller, C.J., Burgin, T.P., Tour, J.M.: Conductance of a molecular junction. Science (1997). doi:10.1126/science.278.5336.252
- Tao, N.J.: Electron transport in molecular junctions. Nat. Nano. (2006). doi:10.1038/ nnano.2006.130
- Meisner, J.S., Kamenetska, M., Krikorian, M., Steigerwald, M.L., Venkataraman, L., Nuckolls, C.: A single-molecule potentiometer. Nano Lett. (2011). doi:10.1021/n1104411f
- Chen, J., Reed, M.A., Rawlett, A.M., Tour, J.M.: Large on-off ratios and negative differential resistance in a molecular electronic device. Science (1999). doi:10.1126/ science.286.5444.1550
- Simonian, N., Li, J., Likharev, K.: Negative differential resistance at sequential singleelectron tunnelling through atoms and molecules. Nanotechnology (2007). doi:10.1088/0957-4484/18/42/424006

- 7. Crivillers, N., Paradinas, M., Mas-Torrent, M., Bromley, S.T., Rovira, C., Ocal, C., Veciana, J.: Negative differential resistance (NDR) in similar molecules with distinct redox behaviour. Chem. Commun. (2011). doi:10.1039/c1cc10677e
- 8. Korytár, R., Lorente, N.: Multi-orbital non-crossing approximation from maximally localized wannier functions: the kondo signature of copper phthalocyanine on Ag(100). J. Phys.: Condens. Matter (2011). doi:10.1088/0953-8984/23/35/355009.
- 9. Herrmann, C., Solomon, G.C., Ratner, M.A.: Organic radicals as spin filters. J. Am. Chem. Soc. (2010). doi:10.1021/ja910483b
- Solomon, G.C., Reimers, J.R., Hush, N.S.: Single molecule conductivity: The role of junction-orbital degeneracy in the artificially high currents predicted by ab initio approaches. J. Chem. Phys. (2004). doi:10.1063/1.1791011
- 11. Robert, V.: Electron tunneling: A scattering problem and a chemical approach. interpretation of STM O₂ image. J. Phys. Chem. A (1999). doi:10.1021/jp990488u.
- Calzado, C.J., Cabrero, J., Malrieu, J.-P., Caballol, R.: Analysis of the magnetic coupling in binuclear complexes. I. physics of the coupling. J. Chem. Phys. (2002). doi:10.1063/ 1.1430740
- Calzado, C.J., Cabrero, J., Malrieu, J.-P., Caballol, R.: Analysis of the magnetic coupling in binuclear complexes. II. derivation of valence effective hamiltonians from ab initio CI and DFT calculations. J. Chem. Phys. (2002). doi:10.1063/1.1446024
- Leijnse, M., Sun, W., Brøndsted Nielsen, M., Hedegård, P., Flensberg, K.: Interactioninduced negative differential resistance in asymmetric molecular junctions. J. Chem. Phys. (2011). doi:10.1063/1.3560474
- Gauyacq, J.P., Lorente, N.: Excitation of spin waves by tunneling electrons in ferromagnetic and antiferromagnetic spin-1/2 heisenberg chains. Phys. Rev. B (2011). doi:10.1103/ PhysRevB.83.035418
- Muralidharan, B., Ghosh, A.W., Datta, S.: Probing electronic excitations in molecular conduction. Phys. Rev. B (2006). doi:10.1103/PhysRevB.73.155410
- 17. Hettler, M.H., Schoeller, H., Wenzel, W.: Non-linear transport through a molecular nanojunction. Europhys. Lett. (2002). doi:10.1209/epl/i2002-00500-3
- Parida, P., Lakshmi, S., Pati, S. K.: Negative differential resistance in nanoscale transport in the coulomb blockade regime. J. Phys.: Condens. Matter (2009). doi:10.1088/0953-8984/21/ 9/095301.
- 19. Meir, Y., Wingreen, N.S.: Landauer formula for the current through an interacting electron region. Phys. Rev. Lett. (1992). doi:10.1103/PhysRevLett.68.2512
- Bominaar, E.L., Achim, C., Borshch, S.A., Girerd, J.-J., Münck, E.: Analysis of exchange interaction and electron delocalization as intramolecular determinants of intermolecular electron-transfer kinetics. Inorg. Chem. (1997). doi:10.1021/ic961298q
- Smit, R.H.M., Noat, Y., Untiedt, C., Lang, N.D., van Hemert, M.C., van Ruitenbeek, J.M.: Measurement of the conductance of a hydrogen molecule. Nature (2002). doi:10.1038/ nature01103
- 22. Galperin, M., Ratner, M.A., Nitzan, A.: Inelastic electron tunneling spectroscopy in molecular junctions: Peaks and dips. J. Chem. Phys. (2004). doi:10.1063/1.1814076
- Galperin, M., Ratner, M. A., Nitzan, A.: Molecular transport junctions: vibrational effects. J. Phys.: Condens. Matter (2007). doi:10.1088/0953-8984/19/10/103201.
- Härtle, R., Benesch, C., Thoss, M.: Vibrational nonequilibrium effects in the conductance of single molecules with multiple electronic states. Phys. Rev. Lett. (2009). doi:10.1103/ PhysRevLett.102.146801
- Miralies, J., Malrieu, J.-P., Caballol, R.: Observable-dedicated molecular orbitals. i. method and illustrations. Chem. Phys. (1991). doi:10.1016/0301-0104(91)90003-C.
- 26. Ben Amor, N., Maynau, D.: Size-consistent self-consistent configuration interaction from a complete active space. Chem. Phys. Lett. (1998). doi:10.1016/S0009-2614(98)00104-3
- 27. Le Guennic, B., Petit, S., Chastanet, G., Pilet, G., Ben Amor, N., Robert, V.: Antiferromagnetic behavior based on quasi-orthogonal MOs: synthesis and characterization of a Cu₃ oxidase model. Inorg. Chem. (2011). doi: 10.1021/ic701758x

- Bloch, C.: Sur la théorie des perturbations des états liés. Nuclear Physics (1958). doi:10.1016/ 0029-5582(58)90116-0
- Lepetit, M.-B., Suaud, N., Gelle, A., Robert, V.: Environment effects on effective magnetic exchange integrals and local spectroscopy of extended strongly correlated systems. J. Chem. Phys. (2003). doi:10.1063/1.1540620
- Neaton, J.B., Hybertsen, M.S., Louie, S.G.: Renormalization of molecular electronic levels at metal-molecule interfaces. Phys. Rev. Lett. (2006). doi:10.1103/PhysRevLett.97.216405
- 31. Vérot, M., Rota, J.-B., Kepenekian, M., Le Guennic, B., Robert, V.: Magnetic and conduction properties in 1D organic radical materials: an ab initio inspection for a challenging quest. Phys. Chem. Chem. Phys. (2011). doi:10.1039/c0cp02124e
- 32. Rota, J.-B., Le Guennic, B., Robert, V.: Toward verdazyl radical-based materials: Ab initio inspection of potential organic candidates for spin-crossover phenomenon. Inorg. Chem. (2010). doi:10.1021/ic902197f
- 33. Julliere, M.: Tunneling between ferromagnetic films. Phys. Lett. A (1975). doi:10.1016/0375-9601(75)90174-7
- 34. Baibich, M., Broto, J., Fert, A., Van Dau, F., Petroff, F., Etienne, P., Creuzet, G., Friederich, A., Chazelas, J.: Giant magnetoresistance of (001)Fe/(001)Cr magnetic superlattices. Phys. Rev. Lett. (1988). doi:10.1103/PhysRevLett.61.2472
- Moritomo, Y., Asamitsu, A., Kuwahara, H., Tokura, Y.: Giant magnetoresistance of manganese oxides with a layered perovskite structure. Nature (1996). doi:10.1038/380141a0
- 36. Liao, Z.-M., Li, Y.-D., Xu, J., Zhang, J.-M., Xia, K., Yu, D.-P.: Spin-filter effect in magnetite nanowire. Nano Lett. (2006). doi:10.1021/nl052199p
- Gould, C., Rüster, C., Jungwirth, T., Girgis, E., Schott, G.M., Giraud, R., Brunner, K., Schmidt, G., Molenkamp, L.W.: Tunneling anisotropic magnetoresistance: A spin-valve-like tunnel magnetoresistance using a single magnetic layer. Phys. Rev. Lett. (2004). doi:10.1103/ PhysRevLett.93.117203
- 38. Lachinov, A.N., Genoe, J., Vorob'eva, N.V., Lachinov, A.A., Garifullina, F.F., Kornilov, V.M.: Magnetoresistance phenomena in ferromagnetic/wide band gap polymer system. Synth. Met. (2011). doi:10.1016/j.synthmet.2010.12.010
- 39. Xiong, Z.H., Wu, D., Vardeny, Z.V., Shi, J.: Giant magnetoresistance in organic spin-valves. Nature (2004). doi:10.1038/nature02325
- Barraud, C., Seneor, P., Mattana, R., Fusil, S., Bouzehouane, K., Deranlot, C., Graziosi, P., Hueso, L., Bergenti, I., Dediu, V., Petroff, F., Fert, A.: Unravelling the role of the interface for spin injection into organic semiconductors. Nat. Phys. (2010). doi:10.1038/nphys1688
- 41. Grünewald, M., Wahler, M., Schumann, F., Michelfeit, M., Gould, C., Schmidt, R., Würthner, F., Schmidt, G., Molenkamp, L.W.: Tunneling anisotropic magnetoresistance in organic spin valves. Phys. Rev. B (2011). doi:10.1103/PhysRevB.84.125208
- Hueso, L.E., Pruneda, J.M., Ferrari, V., Burnell, G., Valdés-Herrera, J.P., Simons, B.D., Littlewood, P.B., Artacho, E., Fert, A., Mathur, N.D.: Transformation of spin information into large electrical signals using carbon nanotubes. Nature (2007). doi:10.1038/nature05507
- 43. Urdampilleta, M., Klyatskaya, S., Cleuziou, J.-P., Ruben, M., Wernsdorfer, W.: Supramolecular spin valves. Nat. Mater. (2011). doi:10.1038/nmat3050
- 44. Sanvito, S.: Organic spintronics: Filtering spins with molecules. Nat. Mater. (2011). doi:10.1038/nmat3061
- 45. Iacovita, C., Rastei, M.V., Heinrich, B.W., Brumme, T., Kortus, J., Limot, L., Bucher, J.P.: Visualizing the spin of individual cobalt-phthalocyanine molecules. Phys. Rev. Lett. (2008). doi:10.1103/PhysRevLett.101.116602
- 46. Mandal, S., Pati, R.: What determines the sign reversal of magnetoresistance in a molecular tunnel junction? ACS Nano (2012). doi:10.1021/nn3006569

Visualizing Electron Correlation in Molecules Using a Scanning Tunneling Microscope: Theory and Ab Initio Prediction

Massimo Rontani, Dimitrios Toroz and Stefano Corni

Abstract Scanning tunneling spectroscopy (STS) is able to image a single molecule decoupled from its supporting substrate. The obtained images are routinely interpreted as the square moduli of molecular orbitals, dressed by the mean-field electron–electron interactions. Here, we demonstrate that the effect of electron correlation beyond the mean field qualitatively alters the uncorrelated STS images. After developing the proper many-body theoretical framework, we present the coupled-cluster calculation of the STS images of a planar molecule with a metal center, copper-(deh-salen). We find that many-body correlations alter significantly the image spectral weight close to the copper ion. This change is large enough to be assessed experimentally and survives to molecule–substrate interactions.

1 Introduction

Scanning tunnelling spectroscopy (STS) visualizes electron states in both extended systems and nanoobjects, such as quantum dots or molecules [1]. Whereas extended quantum states are insensitive to electron number fluctuations, an energy gap opens each time a new electron is injected by the STS tip into a nanoobject. This gap originates from the interaction of the next incoming electron with the others already present in the system. Under this Coulomb blockade condition, STS maps the wave function modulus of the electron injected by the tip into the nanoobject. The obtained image is routinely interpreted as the atomic-like [2] or molecular [3] orbital of the added electron, that experiences the mean field of the other electrons already populating the system. A fundamental question is whether features of the tunneling map may appear due to electron–electron correlation beyond the mean field [4–8].

M. Rontani (⊠) · D. Toroz · S. Corni CNR-NANO Research Center S3, Via Campi 213a 41125 Modena, MO, Italy e-mail: massimo.rontani@nano.cnr.it 182 M. Rontani et al.

In this paper, we illustrate the many-body theoretical framework fit to include the effects of correlation into the ab initio calculation of STS images. We accomplish this task by computing the quasiparticle wave function [4, 7]—the many-body generalization of the molecular-orbital concept. As an application based on a high-level (post-Hartree-Fock) quantum chemistry approach, we present the coupled-cluster [9] evaluation of the STS image of a planar molecule with a copper center, copper-(deh-salen) (cf. Fig. 1). With respect to the Hartree-Fock calculation, the key improvement of coupled cluster as well as other post-Hartree-Fock methods is that the molecular wave function is computed as a linear superposition of different electronic configurations (Slater determinants). Our main result is that the image predicted by this many-body calculation differs qualitatively from its uncorrelated Hartree-Fock counterpart. We find in the STS maps resolved at the Fermi energy that correlation alters significantly the spectral weight around the copper ion. This change may be experimentally quantified by contrasting the altered STS images to those of molecules unaffected by correlation that are used as benchmarks (in the present case, divinyl benzene). Besides, we show that this novel many-body effect survives to molecule-substrate interactions (a NaCl layer in our simulations).

Many-body phenomena such as the Kondo effect [10, 11] have already been observed in molecules. Moreover, quasiparticle calculations have been used to predict the alignment of molecular levels with respect to the extended states of the supporting substrate [12–14]. Whereas the above effects are induced by various types of interactions between the molecules and either the substrate or the STS tip, here we focus on the intrinsic few-body behavior of almost isolated molecules. A prerequisite is the electrical decoupling of the molecule from the conductive substrate that may be achieved either by inserting a thin insulating over layer [3] or by physisorbing the molecule [15]. We stress that our aim is not to propose yet another method to simulate and interpret experimental STS images. Our aim is instead to show how the electronic correlation intrinsic to the molecule can be revealed in terms of distortion of STS images, providing a theoretical and computational apparatus to quantify and visualize such distortions. A summary of our results was previously given in [16].

Fig. 1 The structure of copper-(deh-salen). The geometry has been optimized at the Hartree–Fock level. Color code: *cyan* C, *white* H, *red* O, *blue* N, *orange* Cu



The structure of this paper is the following: Sect. 2 shows the link between STS images and quasiparticle wave functions (QPWFs), Sect. 3 explains how we compute the QPWF, and Sect. 4 reports our predictions for copper-(deh-salen).

2 Many-Body Theory of STS with an Ideal Tip

In this section, we derive, in the limit of zero temperature and small applied bias voltages, the differential conductance dI/dV originating from the transport resonance between two many-body ground states of a molecule with N and N-1 electrons, respectively, as measured by STS [7]. By assuming that the STS tip has an s-wave wave function, we extend the well-known Tersoff–Hamman mean-field treatment [17] to the many-body realm.

The many-body time-dependent perturbation theory at first order in the tip-molecule tunneling matrix element predicts that:

$$\frac{dI}{dV} = \frac{2\pi e^2}{\hbar} \sum_{\xi,i} \left| M_{\xi,i} \right|^2 \delta(\varepsilon_{\xi} - \mu) \delta(E_i(N) - E_{\xi}(N-1) - \mu). \tag{1}$$

Here $M_{\xi,i} = \langle \xi | \hat{M} | i \rangle$ is the matrix element of Bardeen's tunneling operator \hat{M} [4] between the two many-body states $|i\rangle$ and $|\xi\rangle$, which are both direct products of the tip state times the molecule–substrate state:

$$|i\rangle = |N, i\rangle \otimes |N_{\text{tot}} - N\rangle_{\text{tip}},$$
 (2)

$$|\xi\rangle = |N-1,\xi\rangle \otimes |N_{\text{tot}} - N + 1\rangle_{\text{tip}}.$$
 (3)

Both states $|i\rangle$ and $|\xi\rangle$ [Eqs. (2) and (3), respectively] conserve the total number of electrons, N_{tot} , which is the sum of the electrons in the tip, molecule, and substrate. Furthermore, Dirac's delta appearing in Eq. (1) ensures that $|i\rangle$ and $|\xi\rangle$ have the same energy. $|N,i\rangle$ is the many-body ith excited state of the N-electron molecule–substrate system, $|N_{\text{tot}} - N\rangle_{\text{tip}}$ is the tip state with $N_{\text{tot}} - N$ noninteracting electrons, and the final many-body state $|N-1,\xi\rangle$ is obtained by $|N,i\rangle$ by removing an electron and transferring it into the empty single-particle state of the tip whose energy is ε_{ξ} . Since the tip state is not interacting, the level ε_{ξ} is univocally determined by the difference between the energies of the interacting molecule with N and N-1 electrons, respectively $E_i(N)$ and $E_{\xi}(N-1)$. Such difference (chemical potential) equals the Fermi energy μ at vanishing bias. Note that in Bardeen's approach, the tip and molecule states are not mutually orthogonal. The explicit form of Bardeen's operator is:

$$\hat{M} = \frac{\hbar^2}{2m} \int \left[\hat{\Psi}^+(\mathbf{r}) \frac{\partial \hat{\Psi}(\mathbf{r})}{\partial z} - \frac{\partial \hat{\Psi}^+(\mathbf{r})}{\partial z} \hat{\Psi}(\mathbf{r}) \right] \delta(z - z_{\text{vacuum}}) d\mathbf{r}, \tag{4}$$

where m is the electron mass, z is the coordinate perpendicular to the substrate (lying in the plane xy) which originates from the center of the locally spherical tip and increases as it approaches the substrate, z_{vacuum} is any coordinate placed in the vacuum region between the tip and the molecule adsorbed on the substrate.

We now write the annihilation Fermi field operator $\hat{\Psi}(\mathbf{r})$ as the sum of tip and molecule + substrate parts, $\hat{\Psi}_T(\mathbf{r})$ and $\hat{\Psi}_S(\mathbf{r})$, respectively:

$$\hat{\Psi}(\mathbf{r}) = \hat{\Psi}_T(\mathbf{r}) + \hat{\Psi}_S(\mathbf{r}). \tag{5}$$

We explicit the tip part $\hat{\Psi}_T(\mathbf{r})$ as

$$\hat{\Psi}_T(\mathbf{r}) = \sum_{\xi} \hat{c}_{\xi} \phi_{\xi}(\mathbf{r}), \tag{6}$$

where the operator \hat{c}_{ξ} destroys an electron occupying the single-particle state ξ of the tip, whose orbital wave function $\phi_{\xi}(\mathbf{r})$ in the region of interest may be approximated as the asymptotic s-wave form:

$$\phi_{\xi}(\mathbf{r}) = \frac{1}{\sqrt{\Omega_T}} A_T R \kappa e^{\kappa R} \frac{e^{-\kappa r}}{\kappa r}.$$
 (7)

Here κ is the minimum inverse decay length fixed by the tip work function W, $\kappa = \hbar^{-1}(2mW)^{1/2}$, R is the tip radius, Ω_T is a normalization volume, and A_T is a normalization factor of order one [17]. We also expand the molecule + substrate part $\hat{\Psi}_S(\mathbf{r})$ on the set of two-dimensional plane waves with wave vector \mathbf{q} :

$$\hat{\Psi}_{S}(\mathbf{r}) = \frac{1}{\sqrt{\Omega_{S}}} \left(\frac{L}{2\pi}\right)^{2} \int d\mathbf{q} e^{i\mathbf{q}\cdot\mathbf{r}} e^{z\left(\kappa^{2}+q^{2}\right)^{1/2}} \hat{c}_{\mathbf{q}}.$$
 (8)

Here Ω_S is the normalization volume of the molecule, L^2 is the area of the substrate on which the molecule is adsorbed, the operator $\hat{c}_{\mathbf{q}}$ destroys an electron filling the plane wave of vector \mathbf{q} in the xy plane, and we have assumed the same work function as for the tip.

We now evaluate $M_{\xi,i} = \langle \xi | \hat{M} | i \rangle$ by using Eqs. (2–8) together with the following two-dimensional decomposition for the expression $e^{-\kappa r}/(\kappa r)$ entering Eq. (7):

$$\frac{e^{-\kappa r}}{\kappa r} = \frac{1}{2\pi} \int d\mathbf{q} \frac{1}{\kappa (\kappa^2 + q^2)^{1/2}} e^{-(\kappa^2 + q^2)^{1/2} |z|} e^{i\mathbf{q} \cdot \mathbf{r}}.$$
 (9)

The result is

$$M_{\xi,i} = \frac{\hbar^2}{2m} \frac{4\pi}{\sqrt{\Omega_T}} \kappa^{-1} A_T R \kappa e^{\kappa R} \frac{1}{\sqrt{\Omega_S}} \left(\frac{L}{2\pi}\right)^2 \int d\mathbf{q} \langle N-1, \xi | \hat{c}_{\mathbf{q}} | N, i \rangle$$
$$= \frac{\hbar^2}{2m} \frac{4\pi}{\sqrt{\Omega_T}} \kappa^{-1} A_T R \kappa e^{\kappa R} \langle N-1, \xi | \hat{\Psi}_S(0) | N, i \rangle. \tag{10}$$

Therefore, if only the ground states $|N\rangle$ and $|N-1\rangle$ of the adsorbed molecule are involved in the sums, respectively, over i and ξ of Eq. (1)—a typical situation for low-temperature STS—we obtain that dI/dV is directly proportional to the square modulus of the molecule + substrate quasiparticle wave function $\phi(\mathbf{r})$ evaluated at the frame origin, which is the center of the tip \mathbf{r}_0 :

$$\frac{dI}{dV} \propto |\varphi(\mathbf{r}_0)|^2 \tag{11}$$

Here the (hole) quasiparticle wave function (h-QPWF) entering Eq. (11), also known as Dyson orbital, is defined as

$$\varphi(\mathbf{r}) = \langle N - 1 | \hat{\Psi}_{\mathcal{S}}(\mathbf{r}) | N \rangle \tag{12}$$

The h-QPWF $\varphi(\mathbf{r})$ is the probability amplitude of finding a hole—created in the neutral ground state $|N\rangle$ by subtracting an electron at position \mathbf{r} —in the positively ionized molecule ground state $|N-1\rangle$. In the absence of correlation, $|N\rangle$ and $|N-1\rangle$ are single Slater determinants and the h-QPWF is reduced to the Hartree–Fock (HF) highest occupied molecular orbital (HOMO) as a consequence of Koopmans' theorem. This observation endows the HF HOMO with a clear physical meaning, amenable to experimental measurement when electron correlation is weak. In the correlated case, the h-QPWF must be computed through Eq. (12) from the knowledge of both correlated ground states $|N\rangle$ and $|N-1\rangle$. Similar considerations hold for the electron QPWF (e-QPWF), $\varphi(\mathbf{r}) = \langle N+1|\hat{\Psi}^+(\mathbf{r})|N\rangle$.

We conclude this section by recalling that the above approach, based on the perturbative treatment of the tip-molecule coupling, is unable to treat phenomena such as the Kondo effect. In the latter case, a many-body state coherent over the whole tip + molecule + substrate system sets in requiring the knowledge of the global spectral density [18, 19]. Hereafter, we will assume that the molecule under study is in the Coulomb blockade regime and significantly decoupled from the substrate, hence the QPWF of Eq. (12) is evaluated by taking $|N\rangle$ and $|N-1\rangle$ as many-body ground states of the isolated molecule.

3 Ab Initio Evaluation of the Quasiparticle Wave Function

In order to compute the h-QPWF, we perform a restricted HF calculation on the N-1 ground state, that is a closed-shell system for the investigated copper-(deh-salen) molecule. We save and then employ the HF molecular orbitals, with no further changes, for the calculations of the N-1 and N molecular many-body states entering Eq. (12) by using the coupled-cluster method with single and double excitations (CCSD). For the e-QPWF, the procedure is the same but we use the N+1 state instead of N-1. We perform all quantum mechanical calculations with Gaussian 09 suite of codes [20], using the Lanl2DZ basis set and effective core. We compute QPWFs by means of an in-house parallel code.

The differences between the h-QPWF and the HF HOMO are caused by the interference among the orbitals $\phi_{\alpha}(\mathbf{r})$ of different electronic configurations that contribute to $\phi(\mathbf{r})$, according to [7]

$$\varphi(\mathbf{r}) = \sum_{i,j} (C_j^{N-1})^* C_i^N \sum_{\alpha} \phi_{\alpha}(\mathbf{r}) \left\langle \Phi_j^{N-1} \middle| \hat{c}_{\alpha} \middle| \Phi_i^N \right\rangle.$$
 (13)

Here the coefficients C_i^N are obtained by the CCSD expansion of $|N\rangle$ in terms of Slater determinants $|\Phi_i^N\rangle$, $|N\rangle = \sum_i C_i^N |\Phi_i^N\rangle$, retaining only those coefficients with nonnegligible magnitude, $|C_i^N| > 10^{-7}$, and including determinants up to double excitations. The matrix element $\langle \Phi_j^{N-1} | \hat{c}_\alpha | \Phi_i^N \rangle$ is nonzero only when the operator \hat{c}_α destroys an electron in the α th orbital that is occupied in $|\Phi_i^N\rangle$ but empty in $|\Phi_j^{N-1}\rangle$. In the absence of correlation, only the HOMO survives with unitary weight. Correlation mixes orbitals of different energies—but like symmetries—which typically interfere destructively and reduce both weight and extension of $\varphi(\mathbf{r})$.

We then obtain the constant-current STS maps, s(x,y), by arbitrarily choosing a set-point threshold t and then defining s(x,y) = z with z such that $|\varphi(\mathbf{r})|^2 = t$. As the value of the STS current is proportional to $|\varphi(\mathbf{r})|^2$, choosing t is equivalent to choose a set point current. Examples of STS maps are provided in Figs. 2 and 3. In those plots, the values of contour lines in the xy plane signify the apparent height of the molecule, i.e., the distance z from the molecule plane at which the square modulus of the QPWF assumes a given value. Such value is proportional to the current flowing through the STS tip if the transport energy window includes only the resonance between the ground states of the N and N+1 (or N-1) molecule.

4 Predicted STS Images of Copper-(deh-salen)

Molecules with metal centers are targets of choice to investigate effects of correlation, as they sustain different electronic configurations of comparable energies. We focus on a planar molecule in order to simplify the analysis of STS maps, copper-(deh-salen), that is a Cu complex with the dehydrogenated salen ligand whose chemical structure is shown in Fig. 1 [21].

The STS images from the HF HOMO and the corresponding hole quasiparticle wave function are reported in Fig. 2, together with those of a reference molecule that we studied previously [7], divinyl benzene. The images obtained from the HF LUMO and the electron quasiparticle wave function are reported in Fig. 3. Since the ground state of copper-(deh-salen) is a spin doublet, the HF highest (singly) occupied molecular orbital (bottom image in Fig. 2a) is very similar to the lowest unoccupied one (bottom image in Fig. 3a), with small discrepancies arising from the spin-unrestricted character of the calculation [9]. The top of the hole

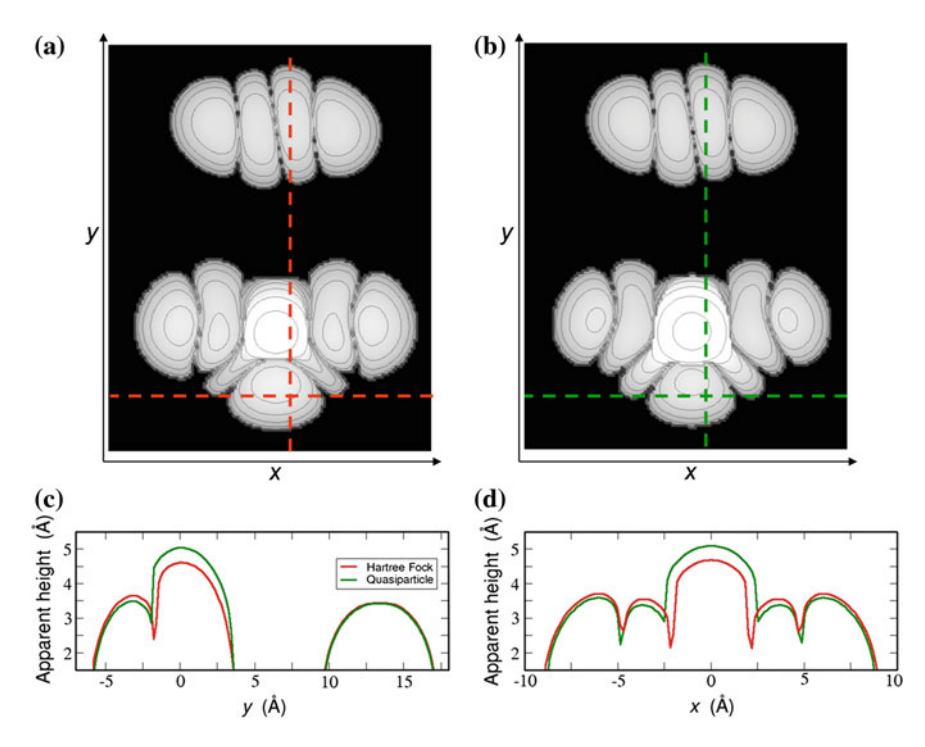


Fig. 2 Simulated constant-current STS images of positively ionized copper-(deh-salen) and divinyl benzene. The density threshold is $6.7 \cdot 10^{-7} \text{ Å}^{-3}$. **a** Contour plot in the *xy* plane of the STS images obtained by HF HOMOs. **b** Contour plot of the STS images obtained by h-QPWFs. **c** Slice of the HF (*red curve*) and quasiparticle (*green curve*) STS images obtained along the vertical dashed line shown in panels (**a**) and (**b**). **d** Slice of the HF (*red curve*) and quasiparticle (*green curve*) STS images obtained along the horizontal dashed line shown in panels (**a**) and (**b**). After Ref. [16]

quasiparticle map of copper-(deh-salen) (bottom image in Fig. 2b), located over the central Cu site, is patently higher than in the uncorrelated image (bottom image in Fig. 2a), whereas the eminence of the remaining lobes is slightly lower. On the other hand, the HF (top image in Fig. 2a) and quasiparticle (top image in Fig. 2b) maps of divinyl benzene are identical. Therefore, one may use divinyl benzene as a reference, by comparing its height, unperturbed by correlation, to the height of copper-(deh-salen), sensitive to many-body effects.

This is best illustrated by cutting the contour STS maps along the y axis (dashed vertical lines in Fig. 2a and b). Figure 2c allows to compare the hole quasiparticle profiles of copper-(deh-salen) and divinyl benzene along y (green lines) with their uncorrelated images (red lines). Correlation changes the apparent height of copper-(deh-salen) non homogeneously along the axis, with an increase of ≈ 0.5 Å over the Cu site and a slight decrease elsewhere. The joint imaging of the two molecules provides an absolute reference to assess the height of copper-(deh-salen) profile. An analogous cut along the x axis (Fig. 2d) further supports the above

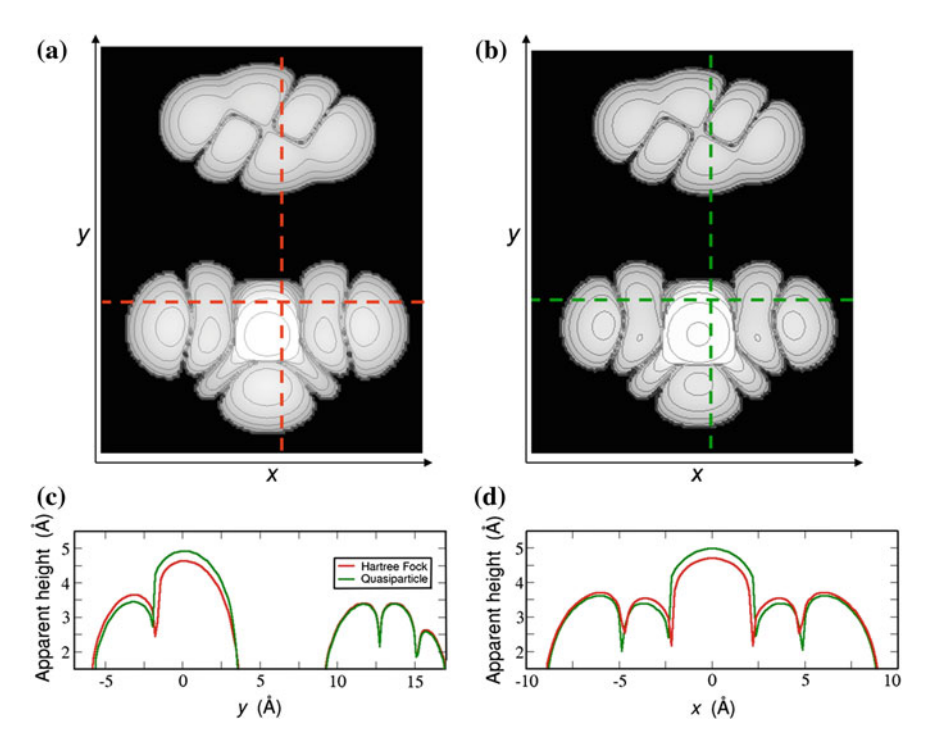


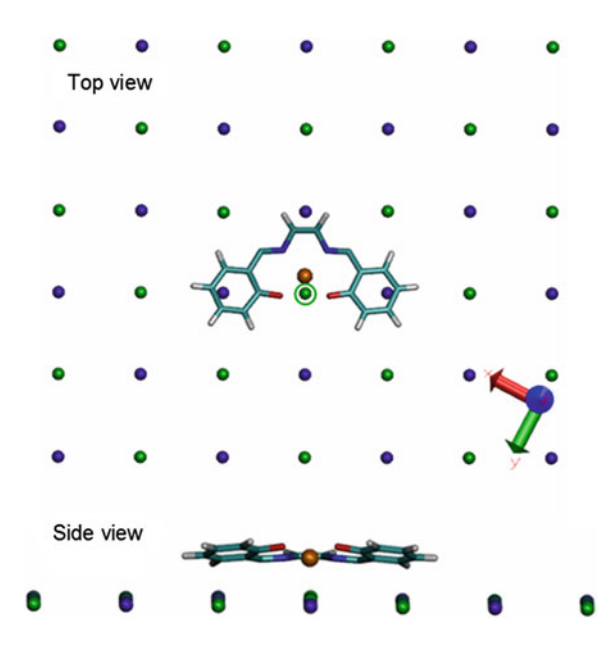
Fig. 3 Simulated constant-current STS images of negatively ionized copper-(deh-salen) and divinyl benzene. **a** Contour plot in the *xy* plane of the STS images obtained by HF LUMOs. **b** Contour plot of the STS images obtained by e-QPWFs. **c** Slice of the HF (*red curve*) and quasiparticle (*green curve*) STS images obtained along the vertical dashed line shown in panels (**a**) and (**b**). **d** Slice of the HF (*red curve*) and quasiparticle (*green curve*) STS images obtained along the horizontal dashed line shown in panels (**a**) and (**b**). After Ref. [16]

conclusion. The choice of divinyl benzene here has illustrative purposes, since there is a broad class of molecules that are unaffected by correlations, including pentacene that has been thoroughly investigated [7].

Correlation strongly affects also the electron-like excitation of copper-(deh-salen), as shown in Fig. 3. The effect is very similar to that emerging from hole images, with the divinyl benzene LUMO still unaffected by correlation, while the STS electron map of copper-(deh-salen) being basically the same as the hole map.

To verify whether the presence of a substrate may hide correlation effects on STS images of copper-(deh-salen), we have considered this molecule on a typical experimental substrate, NaCl (100) [3]. We have relaxed the structure of the molecule using the so-called QM/MM approach. Specifically, copper-(deh-salen) has been placed on a single NaCl (100) layer composed of 12 Na⁺ and 12 Cl⁻ ions. Then, the molecule plus the Cl⁻ ion closest to the Cu ion (see Fig. 4) has been considered in the quantum mechanical (QM) part of the calculation, whereas the rest of the NaCl layer is treated at the classical level (MM) as a set of point charges

Fig. 4 Geometrical arrangement of copper-(dehsalen) on a NaCl (100) monolayer. The geometry has been obtained by optimization at the HF level, using a QM description of copper-(deh-salen) and the closest Cl- ion (circled in the upper panel) and a MM description of the rest of the NaCl monolayer. Color code: green Cl, violet Na, cyan C, white H, red O, blue N, orange Cu. After Ref. [16]



(+1 for Na⁺ and -1 for Cl⁻). Geometry optimization has been performed at the HF level, freezing the NaCl layer. Different optimizations have been started by different initial positions, converging to qualitatively similar structures (the most stable was chosen for the calculations). The obtained geometry is plotted in Fig. 4.

The distortion from planarity of the molecular geometry is due to the interaction of Cu with the underlying Cl⁻ ion. NaCl, therefore, is not an ideal substrate for this class of molecules, as the nonplanar arrangement and the coupling with the substrate make the interpretation of STS results more complex. Nevertheless, NaCl provides a convenient test to check whether correlation effects in STS survive to relatively strong interactions with the substrate.

The inspection of Fig. 5 shows that this is indeed the case: The STS maps of copper-(deh-salen) on the substrate calculated respectively from the HF HOMO (Fig. 5a) and from the hole QPWF (Fig. 5b) show clear differences. Here, the QPWFs are calculated at the level of configuration interaction with singles and doubles [9] (CISD), as the superior CCSD calculation is unattainable due to the size of the system.

The central region of the STS map, around the Cu center, is much higher for the uncorrelated image than for the correlated one. Height differences amount to approximately 2 Å. Here, the uncorrelated STS map is the highest, whereas for the isolated molecule it was the opposite (Fig. 2). Nevertheless, the differences between quasiparticle and HF images remain significant and measurable. Overall, we find significant many-body effects, that remain large and measurable even when the extrinsic effect of the substrate is taken into account.

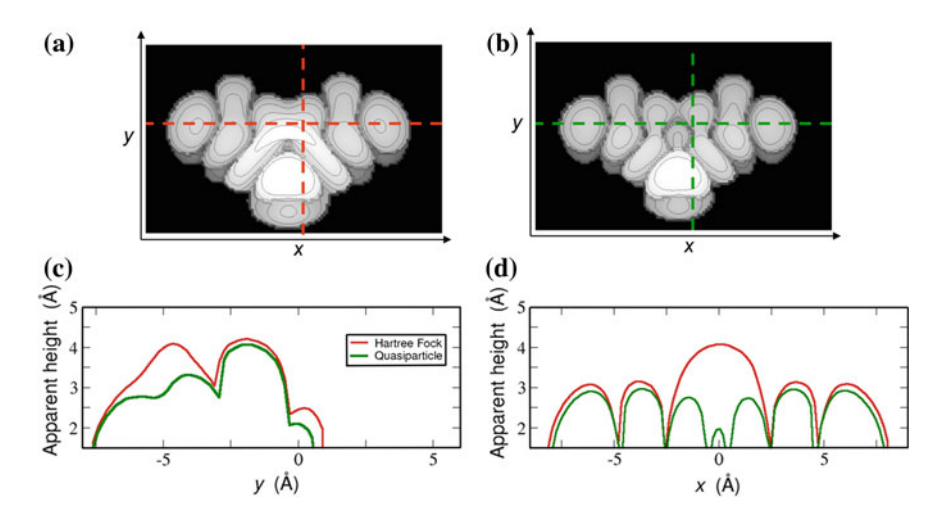


Fig. 5 Simulated constant-current STS images of positively ionized copper-(deh-salen) on an NaCl (100) monolayer. **a** Contour plot in the *xy* plane of the STS images obtained by HF HOMOs. **b** Contour plot of the STS images obtained by h-QPWFs. The level of the theory is CISD for copper-(deh-salen) and the closest Cl- ion, MM for the rest. **c** Slice of the HF (*red curve*) and quasiparticle (*green curve*) STS images obtained along the vertical *dashed line* shown in panels (**a**) and (**b**). **d** Slice of the HF (*red curve*) and quasiparticle (*green curve*) STS images obtained along the horizontal *dashed line* shown in panels (**a**) and (**b**). After Ref. [16]

5 Conclusions

In conclusion, by obtaining the quasiparticle wave function through quantum-chemical methods, we have demonstrated that many-body effects may profoundly affect the STS images of molecules with metal centers. Our results highlight the still unexplored potential of STS as a probe of electron correlation in molecules and nanoobjects. So far, the importance of electron correlation in molecules has been inferred indirectly through structural and energetic properties (e.g., bond energies, geometries, and optical spectra). Our work shows that STS directly images the effects of electron correlation on the wave function. We hope that our findings may stimulate further STS experiments along this path.

Acknowledgments Funding from INFM under the Young Researcher Seed Project 2008 initiative and Fondazione Cassa di Risparmio di Modena under the project COLDandFEW is gratefully acknowledged. Computer time has been provided by CINECA under the CINECA-ISCRA supercomputer project grants IscrB_FERMIFEW, IscrC_FEW1D, and IscrC_QUASIPAR.

References

- Wiesendager, R.: Scanning probe microscopy and spectroscopy. Cambridge University Press, Cambridge (1994)
- Venema L.C., Wildöer J.W.G., Janssen J.W., Tans S.J., Temminck Tuinstra H.L.J., Kouwenhoven L. P., Dekker, C.: Imaging electron wave functions of quantized energy levels in carbon nanotubes. Science 283, 52–55 (1999). doi:10.1126/science.283.5398.52
- 3. Repp, J., Meyer, G., Stojkovic, S.M., Gourdon, A., Joachim, C.: Molecules on insulating films: Scanning-tunneling microscopy imaging of individual molecular orbitals. Phys. Rev. Lett. **94**, 026803 (2005). doi:10.1103/PhysRevLett.94.026803
- Rontani, M., Molinari, E.: Imaging quasiparticle wave functions in quantum dots via tunneling spectroscopy. Phys. Rev. B 71, 233106 (2005). doi:10.1103/PhysRevB.71.233106
- Maruccio, G., Janson, M., Schramm, A., Meyer, C., Matsui, T., Heyn, C., Hansen, W., Wiesendanger, R., Rontani, M., Molinari, E.: Correlation effects in wave function mapping of molecular beam epitaxy grown quantum dots. Nano Lett. 7, 2701–2706 (2007). doi:10.1021/ nl071133m
- Bester, G., Reuter, D., He, L., Zunger, A., Kailuweit, P., Wieck, A.D., Zeitler, U., Maan, J.C., Wibbelhoff, O., Lorke, A.: Experimental imaging and atomistic modeling of electron and hole quasiparticle wave functions in InAs/GaAs quantum dots. Phys. Rev. B 76, 075338 (2007). doi:10.1103/PhysRevB.76.075338
- Toroz, D., Rontani, M., Corni, S.: Visualizing electron correlation by means of ab initio scanning tunneling spectroscopy images of single molecules. J. Chem. Phys. 134, 024104 (2011). doi:10.1063/1.3520567
- 8. Secchi A., Rontani M.: Spectral function of few electrons in quantum wires and carbon nanotubes as a signature of Wigner localization. Phys. Rev. B **85**, 121410(R) (2012). doi:10.1103/PhysRevB.85.121410
- Helgaker, T., Jørgensen, P., Olsen, J.: Molecular electronic structure theory. Wiley, Chichester (2000)
- Park, J., Pasupathy, A.N., Goldsmith, J.I., Chang, C., Yaish, Y., Petta, J.R., Rinkoski, M., Sethna, J.P., Abruña, H.D., McEuen, P.L., Ralph, D.C.: Coulomb blockade and the Kondo effect in single atom transistors. Nature 417, 722–725 (2002). doi:10.1038/nature00791
- Liang, W., Shores, M.P., Bockrath, M., Long, J.R., Park, H.: Kondo resonance in a single-molecule transistor. Nature 417, 725–729 (2002). doi:10.1038/nature00790
- Neaton, J.B., Hybertsen, M.S., Louie, S.G.: Renormalization of molecular electronic levels at metal-molecule interfaces. Phys. Rev. Lett. 97, 216405 (2006). doi:10.1103/ PhysRevLett.97.216405
- Thygesen, K.S., Rubio, A.: Renormalization of molecular quasiparticle levels at metalmolecule interfaces: Trends across binding regimes. Phys. Rev. Lett. 102, 046802 (2009). doi:10.1103/PhysRevLett.102.046802
- Freysoldt, C., Rinke, P., Scheffler, M.: Controlling polarization at insulating surfaces: Quasiparticle calculations for molecules adsorbed on insulator films. Phys. Rev. Lett. 103, 056803 (2009). doi:10.1103/PhysRevLett.103.056803
- Soe, W.-H., Manzano, C., De Sarkar, A., Chandrasekhar, N., Joachim, C.: Direct observation of molecular orbitals of pentacene physisorbed on Au(111) by scanning tunneling microscope. Phys. Rev. Lett. 102, 176102 (2009). doi:10.1103/PhysRevLett.102.176102
- Toroz, D., Rontani, M., Corni, S.: Proposed alteration of images of molecular orbitals obtained using a scanning tunneling microscope as a probe of electron correlation. Phys. Rev. Lett. 110, 018305 (2013). doi:10.1103/PhysRevLett.110.018305
- 17. Tersoff, J., Hamman, D.R.: Theory of the scanning tunneling microscope. Phys. Rev. B 31, 805–813 (1985). doi:10.1103/PhysRevB.31.805
- 18. Rontani, M.: Friedel sum rule for an interacting multiorbital quantum dot. Phys. Rev. Lett. 97, 076801 (2006). doi:10.1103/PhysRevLett.97.076801

 Rontani, M.: Exchange and correlation effects in the transmission phase through a fewelectron quantum dot. Phys. Rev. B 82, 045310 (2010). doi:10.1103/PhysRevB.82.045310

- 20. Frisch M.J. et al.: Gaussian 09, Revision B.01. Gaussian Inc., Wallingford CT (2010)
- Suresh, E., Bhadbhade, M.M., Srinivas, D.: Molecular association, chelate conformation and reactivity correlations in substituted o-phenylenebis(salicylidenato)copper(//) complexes: UV-visible, EPR, and X-ray structural investigations. Polyhedron 15, 4133–4144 (1996). doi:10.1016/0277-5387(96)00178-7

Part VI NC-AFM

Submolecular Resolution Imaging of C_{60} : From Orbital Density to Bond Order

Philip Moriarty

Abstract I review a number of advances and milestones in the acquisition of submolecular resolution scanning probe microscope images of the buckminster-fullerene (C_{60}) molecule. Scanning tunneling microscopy essentially provides an image derived from the local density of states of the electronic structure of a molecule within an energy window defined by the tip-sample bias voltage. These measurements of the local density of states, which are generally interpreted in terms of molecular orbital probability density, have now been complemented by non-contact atomic force microscopy (NC-AFM) images of the internal structure of the molecule. The NC-AFM images yield either atomic resolution (if imaging occurs in the attractive regime of the tip-sample potential), or, in the Pauli exclusion regime, remarkable maps of the charge density of the interatomic bonds. This combination of scanning probe techniques is exceptionally powerful in elucidating the correlations between atomic structure, bond order, and the submolecular distribution and symmetry of electron density.

1 Introduction

Despite never quite living up to the over-hyped expectations of its potential for world-changing applications in fields as diverse as commercial molecular electronics and drug delivery, C_{60} nonetheless continues to appear with remarkable regularity as an essential 'ingredient' of ground-breaking developments in nanoscience. In particular, the fullerenes have played a central role in advancing the state of the art in high resolution scanning probe microscope (SPM) imaging. From the early 1990s onwards, C_{60} and the fullerene family (comprising the higher

School of Physics and Astronomy, University of Nottingham, Nottingham NG7 2RD, UK e-mail: philip.moriarty@nottingham.ac.uk

P. Moriarty (⊠)

fullerenes such as C_{70} and C_{84} , and endohedral, substitutional, and doped derivatives) have formed the bedrock of a series of scanning probe microscopy experiments, supported by theoretical analyses, which focussed on attaining images of the electronic and/or geometric structure of the fullerene cage.

Here I review just a few of the advances in submolecular resolution imaging of C_{60} which spans a two decade period from the early 1990s, and the observation of intramolecular contrast in chemisorbed buckyballs on Si(111) [1], up to late 2012, when Gross and coworkers, in a pioneering, elegant, and immensely challenging experiment, succeeded in resolving the differences in Pauling bond order associated with the two types of inter-carbon bond in the molecular framework [2]. State-of-the-art scanning probe microscopy represents a remarkably powerful tool for the analysis of intramolecular electron density (in a variety of systems, although I shall focus solely on C_{60}). Before discussing the evolution of submolecular imaging of C_{60} , however, and given that a theme I will return to throughout this chapter will be the unique ability of scanning probes to access, in a single technique, information on occupied and unoccupied molecular orbital densities, geometric structure, and charge, it is worth taking the time to clarify just what is meant when scanning probe microscopists loosely speak of "imaging molecular orbitals".

2 Do We See Orbitals?

In a lucid and entertaining article [3], Scerri has robustly countered the suggestion that orbitals have ever been observed via scanning tunneling microscopy or any other technique. His arguments are clear and convincing, and his primary motivation in writing the paper was to ask that the scientific community pays more careful attention to the lexicon and fundamental postulates of quantum mechanics. First, an orbital, i.e., a wavefunction for a single particle (or pair of particles), is a mathematical construct. A wavefunction is a complex-valued 'entity' whose internal phase is not an experimental observable (although phase information can be extracted in STM via the exploitation of isospectral nanostructures, as pioneered by Moon et al. in a ground-breaking experiment in 2008 [4]). Coupled with this is the important question of the status of an orbital within quantum theory and it is worth quoting Scerri at length on this point:

According to accepted theory atomic orbitals serve merely as basis sets, that is, as types of coordinate systems that can be used to expand mathematically the wavefunction of any particular physical systems. Just as the coordinate system of x, y, and z used to describe any particular experiment in classical physics is unobservable, so too atomic orbitals are completely unobservable even in principle.

The basic point is therefore this: STM measures a flow of electrons which derives from the electron density of the system (where the system comprises the tip, the surface, including any subsurface region involved in carrier transport, and,

if relevant, adsorbate, under investigation). The terms "electron density" and "orbital" are clearly not synonymous. Looking at the issue from the point of view of fundamental quantum mechanics (QM), an orbital is a *state* in Hilbert space, not a physical entity, i.e., not an observable (in the strict QM sense of the term).

Scerri's strong words regarding the conflation of the terms "orbital" and "electron density" were, however, met by a measured response from Spence et al. [5]. They argued that while Scerri was indeed correct to point out that orbitals were physically unobservable mathematical constructs strictly only valid in terms of single particle wavefunctions, "The continued use of one-electron terms by all authorities in the field simply indicates that this theory is too useful an approximation to be abandoned". In the following sections, we shall see a number of examples of where experimental STM data are interpreted directly in terms of tunneling to and from specific molecular orbitals [usually the highest occupied molecular orbital (HOMO) and the lowest unoccupied molecular orbital (LUMO)]. Moreover, and as noted above, it is very common practice to speak of "imaging molecular orbitals" in the scanning probe community. The reasons why, rightly or wrongly, this terminology has become so widespread - and why quantum mechanical language with a very specific meaning (such as the term "observable") is arguably used rather loosely in certain fields—are covered in a recent fascinating article by Mulder [6].

3 STM Observations of Intramolecular Contrast in C_{60}

It is not appropriate to provide here an exhaustive review of the observation of intramolecular contrast in adsorbed C_{60} molecules, particularly as the adsorption of fullerenes on semiconductor surfaces has been reviewed elsewhere relatively recently [7]. Instead, I will focus on just a relatively small subset of instructive examples (and offer my apologies to the authors of the very many other equally important studies which I have not selected for discussion).

In the context of this volume, the paper by Pascual et al. [8] entitled "Seeing Molecular Orbitals" and a related publication by Hou et al. [9] on imaging of C_{60} adsorbed on the $Si(111)-(7\times7)$ surface are particularly relevant. Figure 1 shows a comparison of STM images of different C_{60} molecules adsorbed on $Si(111)-(7\times7)$, where each has adopted a different adsorption geometry and orientation with respect to the surface normal. Underneath each experimental image is plotted an isosurface (of constant $\Sigma |\psi_i(r)|^2$) derived from the highest occupied molecular orbital of C_{60} which has been calculated using density functional theory. It is important to note that a surface slab is not included in the calculations, so there is no 'atomistic' consideration of the underlying substrate.

¹ This measurement is weighted, of course, by the density of states of the tip and the details of the tunneling process itself, including the variation in tunnel probability for electrons with different energies.

Instead, the authors applied a slight strain to the molecule in the simulations in order to mimic the symmetry-breaking effects of adsorption on the $Si(111) - (7 \times 7)$ surface. (A similar strategy has also been very successfully adopted by Dunn and coworkers [10], as described below.)

In each case in Fig. 1 there is good qualitative agreement between the experimental STM images and the calculated shape of the highest occupied molecular orbital (HOMO) of the distorted C_{60} molecule. Pascual et al. [8] point out that other molecular orbitals, or mixtures of orbital contributions, do not reproduce the experimental images as successfully as the HOMO isosurface. This is despite the fact that intramolecular contrast arises in principle from a complicated mixture of different tunneling channels due to different molecular resonances coupled to surface, interface, and tip states. Pascual et al. explain the close similarity of the shape of the HOMO to the experimental STM images as being due to the strong covalent coupling of C_{60} to the Si(111) surface. (Note that the C_{60} -Si(111) interaction is, however, most likely best described as ionocovalent [9, 11]) This coupling effectively accentuates the contribution of the HOMO to the image.

Pascual et al. also did not observe a strong bias dependence for their experimental images. This was very much at odds with Hou et al.'s STM images, and associated calculations, of the submolecular structure of C_{60} on $Si(111)-(7\times7)$. Hou et al. instead observed that positive bias imaging, i.e., tunneling into unoccupied states, was less affected by the molecule–substrate interaction (i.e., gave intramolecular contrast closer to that expected for the free fullerene molecule) than for negative bias imaging, which maps filled state density. They argued that the 'stripe-like' features often observed in high resolution images of C_{60} (see Moriarty [7] for a review) arose fundamentally from the surface–molecule interaction.

One consideration lacking, however, from both the work of Hou et al. and Pascual et al. is the role of the electronic structure of the tip on the patterns of

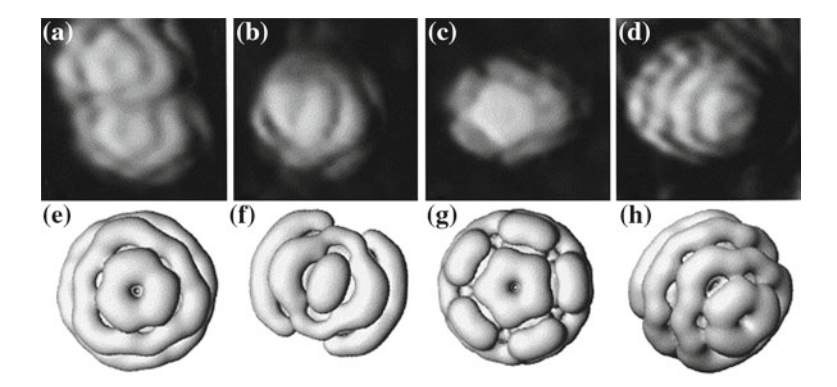


Fig. 1 a–d STM images of C_{60} molecules adsorbed in different orientations on the $Si(111)-(7\times7)$ surface; e–h Isosurfaces of the highest occupied molecular orbital for a free C_{60} molecule subject to a 5 % compressive uniaxial strain which serves to mimic the degeneracy-lifting effects of adsorption on the silicon surface. Taken from Pascual et al. [8]. ©Elsevier (2000)

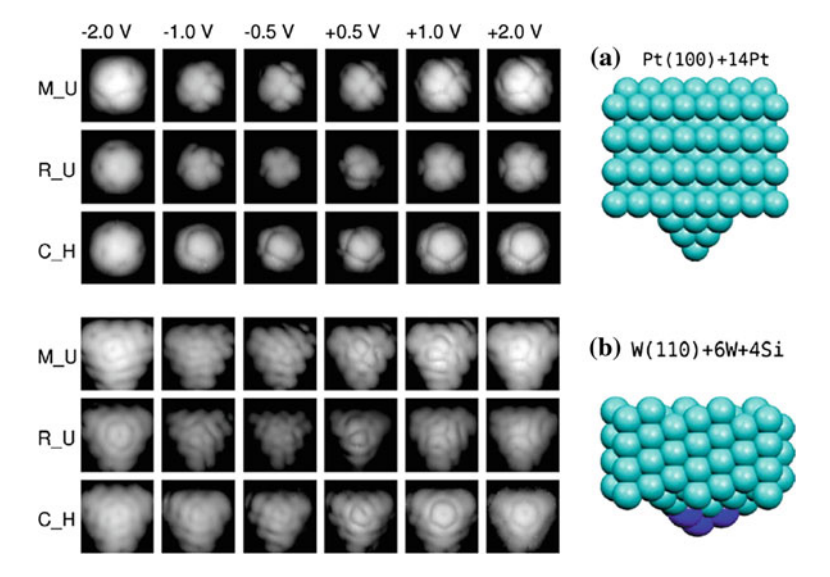


Fig. 2 Simulated STM images for C_{60} molecules adsorbed at various sites within the $Si(111) - (7 \times 7)$ unit cell and for different bias voltages ranging from -2 to +2V. The set of images shown in (a) was calculated using a simulated Pt tip, whereas those in (b) arise from a WSi tip. Adapted from Rurali et al. [12]. ©American Physical Society (2010)

submolecular contrast observed in the STM images. Rurali et al. [12] have carried out a careful and comprehensive study of the influence of different tip types, namely Pt and WSi, on simulated STM images (Fig. 2). The WSi tip, in particular, is an important choice as it is very likely that in many experiments the scanning probe—which is often a W (or tungsten oxide) tip to begin with—will become inadvertently terminated with silicon (or indeed C_{60}) particularly if voltage pulsing and/or gentle crashing of the tip is carried out by the experimentalists to (re)gain atomic resolution. Very strong differences in intramolecular contrast were observed in the simulated STM images as a result of changing the tip type and topography. I return repeatedly to the issue of the precise probe structure in the following sections.

4 Probing the Probe

There is a fundamental "reciprocity" principle at the heart of scanning probe microscopy, which is easily understood. Generally, we assume that the tip is sharper, i.e., has a smaller radius of curvature, than the features under investigation and so the tip images the sample. But, of course, the opposite case is just as true: if features at the sample surface are sharper than the tip than those surface structures will image the tip.

In many cases this can be a major irritation as, when it is the sample surface that is of interest (as is generally the case), tip imaging of this type represents a

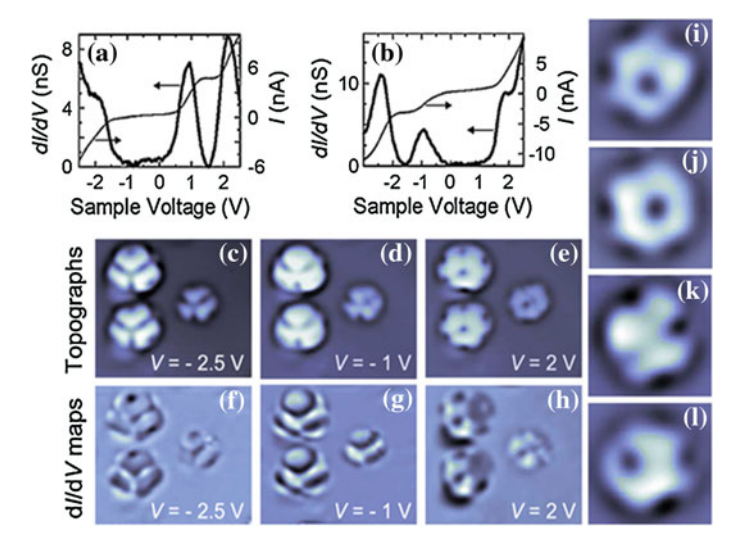


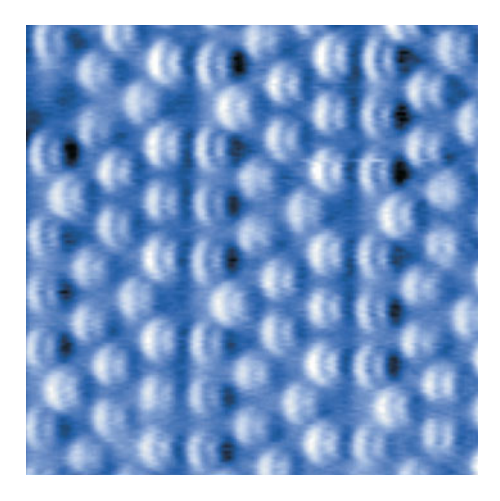
Fig. 3 Imaging molecular orbital density of an 'on-tip' C_{60} molecule. (a) and (b) are dI/dV spectra acquired above a C_{60} molecule with a metal tip, and a Au(111) surface with a C_{60} -terminated tip, respectively. (c-e) and (f-h) are STM and dI/dV images, respectively, of a C_{60} -terminated tip whose molecular orbital density is probed using Au clusters on the Au(111) surface. (i-l) show the reorientation of the on-tip C_{60} due to the application of high currents through the molecule-sample junction. Taken from Schull et al. [13]. ©American Physical Society (2009))

particularly irksome artifact in SPM. As a tool to provide direct information on the tip structure (usually a key experimental unknown), however, this type of inverse imaging process is immensely valuable. In a recent series of careful and challenging experiments, coupled with theoretical interpretation of the results, Schull, Berndt, and coworkers have elegantly demonstrated the extent to which single adsorbed atoms on metal surfaces can be used to image the state of a tip terminated with a single C_{60} molecule [13–15]. Figure 3 shows a particularly powerful example of the type of detailed information on the tip which can be extracted using this protocol. As the imaging mode in this case is STM, it is the density of states associated with the HOMO or LUMO of the molecule which accounts for the overall topography and symmetry of the images of the C_{60} -terminated tip.

Over a decade ago, Giessibl et al. applied the inverse imaging approach to non-contact atomic force microscopy (NC-AFM). Before discussing this work, it is worth taking a moment to highlight one of the key differences between STM and NC-AFM imaging.² As Hembacher et al. have pointed out [16], while STM

² "Non-contact" is something of a misnomer, given that many of the highest resolution images to date have been acquired in the Pauli exclusion, i.e., strongly repulsive, regime of the tip-sample potential as described later in this chapter. Dynamic force microscopy is a somewhat more appropriate description, but the NC-AFM term is now firmly embedded in the field and so, for consistency, I will also use it here.

Fig. 4 'Sub-atomic' resolution NC-AFM imaging of the $Si(111) - (7 \times 7)$ surface. The lobes observed in the image of each atom arise from the orbital structure of the tip apex. From Giessibl et al. [18]. ©American Association for the Advancement of Science (2000)



images are generated from the electron density of states which is accessible for tunneling within an energy window defined by the sample bias, NC-AFM is sensitive to the *total* electron density. This is a crucial distinction because, as first highlighted by Feynman [17], interatomic and intermolecular (and, indeed, intraatomic and intramolecular) forces depend on the total charge density. Thus, significantly higher resolution images are in principle, and, as recently shown, in practice, possible with NC-AFM.

By exploiting the relatively large separation and narrow spatial extent of the dangling bond orbitals of the $Si(111)-(7\times7)$ surface, Giessibl et al. [18] succeeded in imaging features derived from the orbital structure of the NC-AFM tip. While this result and the associated interpretation have not been without their critics, and the precise interpretation of the 'sub-atomic' contrast a matter of some debate, the experimental protocol is basically sound due to the reciprocity principle mentioned above. A comprehensive theoretical study by Campbellová et al. [19] lends support, however, to the idea that the sub-atomic structure in Giessibl et al.'s images arose from a dimerized tip apex, rather than from a single atom tip terminated by two dangling bonds (Fig. 4).

The question we sought to address in a set of experiments in 2011 was whether the approach developed by Schull et al. for STM imaging of the molecular orbital structure of a C_{60} functionalized probe (notwithstanding the discussion in Sect. 2) could be extended via the Giessibl et al. protocol to acquiring atomic resolution images of the fullerene cage structure. We were also keen to determine the extent to which STM and NC-AFM images of the same molecule at the tip apex could be combined to provide detailed information on the relationship between the energy window-specific STM data and the NC-AFM images which derive from the total, rather than partial, electron density.

As noted above, C_{60} forms a relatively strong ionocovalent bond to the $Si(111)-(7\times7)$ surface. Despite this, the molecule is relatively easy to transfer to an STM tip using any one of a number of strategies including fast scanning with

202

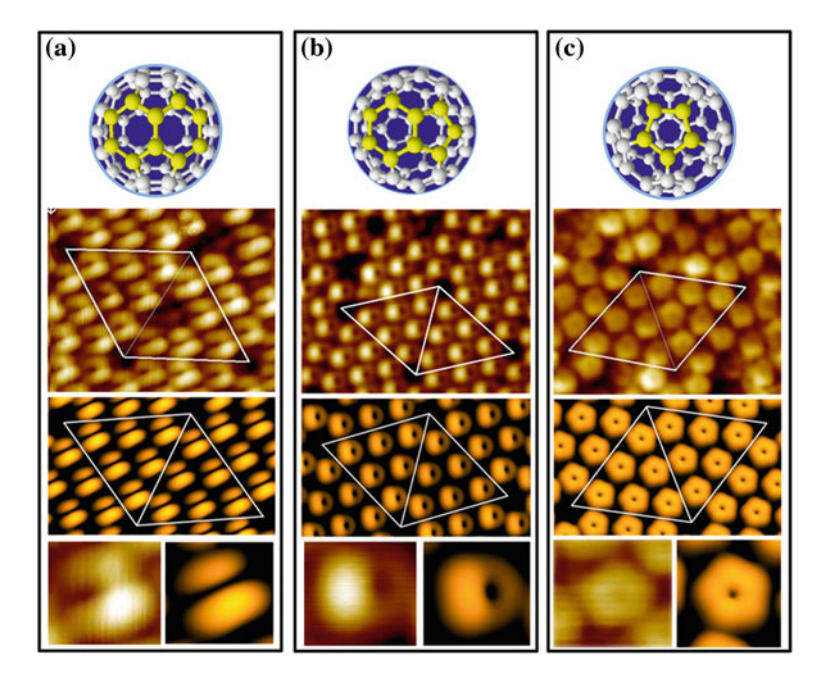


Fig. 5 Using Si dangling bonds to image the orientation of a C_{60} -terminated probe. Each panel, (a–c), comprises a model of the C_{60} orientation; an experimental dynamic STM image showing the (7×7) unit cell; the corresponding simulated image from Hückel molecular orbital (HMO) theory calculations; and a comparison of a single dangling bond feature as measured experimentally and calculated using HMO theory. From Chiutu et al. [20]. ©American Physical Society (2012)

low feedback gains, I(z) spectroscopy, or df(z) measurements. This ease of transfer is likely because, in our case at least, the Si-coated tip presents a number of highly reactive sites for molecular adsorption at its apex. We have indirect evidence, however, that more than one C_{60} molecule may well adsorb at the tip apex such that the terminating molecule is "back-bonded" not to silicon but to other C_{60} molecules.

We show in Fig. 5 one example of the effects of C_{60} transfer to a tip (taken from Chiutu et al. [20]) where, following transfer, the adatoms of the $Si(111) - (7 \times 7)$ surface no longer appear round as in 'traditional' STM images. Instead, the shape of each adatom is determined by the orientation of the C_{60} molecule terminating the tip apex. A 'trial-and-error' process involving modification of the tip apex via interaction with a chemisorbed C_{60} molecule on the underlying silicon substrate enables a rudimentary selection of the orientation of the tip-terminating molecule.

Figure 5 also shows a comparison of the experimental STM data with the results of Hückel molecular orbital (HMO) theory calculations. A key advantage of the HMO approach, as compared to density functional theory (DFT) calculations, is that it is computationally inexpensive: results can be obtained in a few

minutes on a standard desktop or laptop machine. A similar approach to that of Pascual et al. [8] mentioned above is used in the HMO calculations to model the surface-molecule or tip-molecule interaction: the effects of molecular adsorption are modeled via symmetry breaking, which lifts the degeneracies of the molecular orbitals. Although the HMO calculations, therefore, do not provide the detailed atomistic information on adsorbate–surface interactions which is available via DFT, this level of detail is not essential in order to identify molecular orientation.

5 Imaging Atoms and Bonds in C_{60}

The STM data shown in Figs. 3 and 5 represent a 'sampling' of the orbital density integrated in a relatively narrow energy window defined by the tip-sample bias. By moving to the NC-AFM imaging mode (which, with the qPlus technique, is straightforward using the same metallic probe) significantly higher resolution is possible. As shown in Fig. 6 (previously published in Chiutu et al. [20]), NC-AFM with a qPlus sensor is capable of resolving the individual atoms comprising the fullerene cage structure. In this case, the experiment was carried out such that the frequency shift used as the set-point value for the NC-AFM feedback loop represents an attractive interaction. It has been known since the early days of NC-AFM imaging of semiconductor surfaces that the acquisition of atomic resolution images on semiconductor surfaces depends on the ability to form a chemical bond

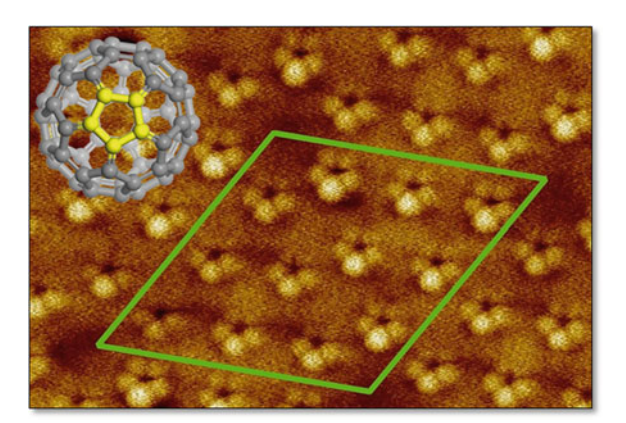


Fig. 6 NC-AFM image (taken using a qPlus sensor) of the $Si(111) - (7 \times 7)$ surface using a C_{60} -terminated tip apex. The *pentagon-down* orientation of the molecular probe can be ascertained from the five lobes which comprise each of the 12 adatoms in the (7×7) unit cell (outlined in *green*.) Note that not only are the five atoms of the *pentagonal* face visible but the molecule is clearly tilted toward the surface. In addition, the difference in chemical reactivity of the two sides of the unit cell is also visible as a small difference in average brightness of the adatoms on each side. Note that the image is a larger scan area version of Fig. 2a of Chiutu et al. [20]

between the tip and underlying substrate atoms [21]. The importance of the reactivity of the tip in NC-AFM imaging has recently been revisited by Ondracek et al. [22] in the context of imaging of carbon nanostructures. This work is of particular relevance to the data shown in Fig. 6 where atomic resolution arises due to the strong propensity of C_{60} (and other fullerenes) to form ionocovalent Si-C bonds. (Indeed, the interaction of C_{60} with the $Si(111) - (7 \times 7)$ surface is so strong that a thermal desorption experiment, traditionally used to determine adsorption energies, is not possible. As the $C_{60}/Si(111)$ sample is annealed, the molecules form an increasing number of Si-C bonds, up to the point where the cage cracks open and silicon carbide is formed).

As was also predicted by Hobbs and Kantorovich [23] some time ago, C atoms in the C₆₀ cage can, therefore, be resolved by NC-AFM. What is intriguing, however, is that despite repeated attempts we have failed to date to resolve a hexagonal, rather than pentagonal, face of the molecule. Although more data are required in order to provide a statistically robust analysis, it is interesting nonetheless that atomic resolution images of the hexagonal face of the molecule prove so elusive. In their DFT

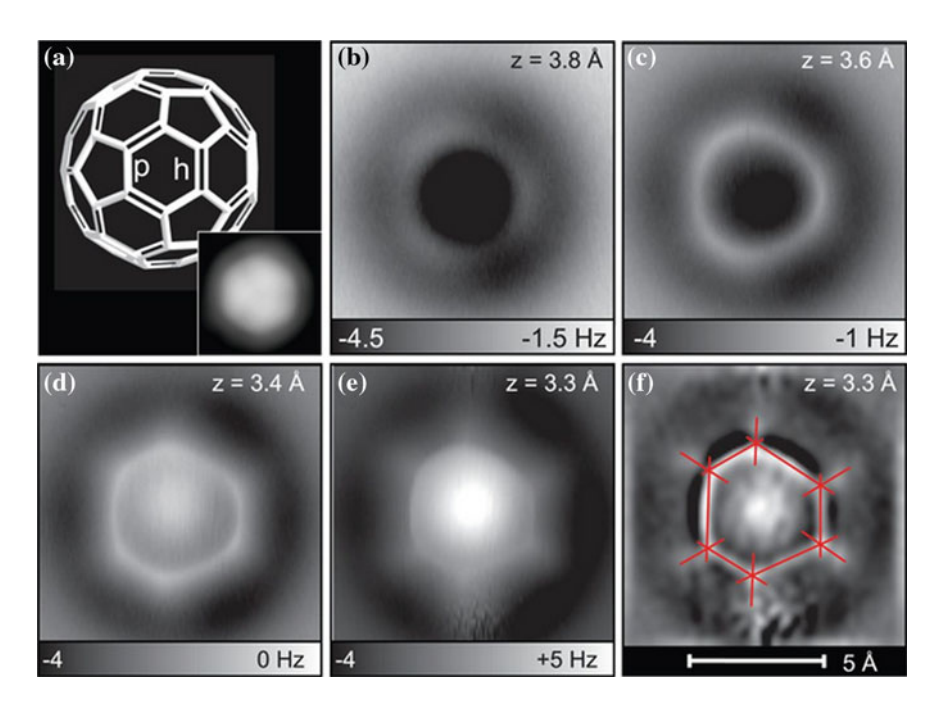


Fig. 7 Variation in bond order in C_{60} as probed by qPlus NC-AFM in the Pauli exclusion regime of the tip-sample interaction. **a** Ball and stick model of C_{60} showing difference between p and h bonds. The inset is an STM image of a C_{60} molecule adsorbed on Cu(111). **b–e** NC-AFM images taken at decreasing tip-sample separations showing the evolution of sharp bond contrast. The difference between p and h bonds (which have a different Pauling bond order) is clear throughout the sequence of images. **f** High pass filtered image of E to highlight differences in bond lengths. From Gross et al. [2]. ©American Association for the Advancement of Science (2012)

calculations (using the local density approximation) Masenelli et al. [24] found that a silicon atom preferentially binds to a hexagon–hexagon edge within the C_{60} molecule but that a geometry involving bonding to a pentagonal face is metastable. Moreover, they find that a silicon atom will not bond to an hexagonal face of the molecule. While those calculations were for an isolated silicon atom, rather than for an adatom at the $Si(111)-(7\times7)$ surface with only one free dangling bond (as in our NC-AFM experiments), it is nonetheless intriguing that bonding to the hexagonal face was found to be unstable whereas the silicon atom adopted a metastable bonding geometry at the pentagonal face.

But can we go beyond atomic resolution? Is it possible to image the interatomic bonds, i.e., the detailed chemical structure, of C_{60} ? This question was first addressed by Pawlak et al. [25] in 2011 using the Pauli repulsion imaging approach pioneered by Gross et al. [26], which involves reducing the tip-sample separation such that the regime of repulsive forces due to Pauli exclusion is probed and leads to extremely high resolution. Pawlak et al. [25] showed that intramolecular contrast in C_{60} was indeed possible, interpreting their data in terms of C–C bond imaging. Most recently, Gross et al. [2] have extended the Pauli repulsion imaging strategy to the determination of Pauling bond order (Fig. 7). This is an elegant extension of the technique which has clear and exciting potential in the analysis of a wide range of adsorbed organic molecules.

6 Conclusions

The capabilities of scanning probe microscope continue to develop apace. As I have discussed in this chapter, it is now possible to combine maps of molecular orbital density (if, as discussed in Sect. 2, the loose usage of that term can be excused) with not only atomic resolution imaging but chemical bond sensitivity. This is a remarkably powerful set of tools to bring to bear on a variety of problems in single molecule mechanics and electronics including the development of the single molecule computing devices at the core of the AtMol project.

Acknowledgments The results of the Nottingham Nanoscience group described in this chapter stem from the work of many researchers with whom it has been my pleasure to collaborate including, in particular (and in alphabetical order): Joseph Bamidele (King's College, London (KCL)), Cristina Chiutu, Rosanna Danza, Janette Dunn, Sam Jarvis, Lev Kantorovich (KCL), Andrew Lakin, Andrew Stannard, Peter Sharp, Adam Sweetman, and Richard Woolley. We are very grateful for financial support from the UK Engineering and Physical Sciences Research Council in the form of a fellowship (EP/G007837), from the Leverhulme Trust (through grant F/00114/BI), from the European Commission's ICT-FET programme via the Atomic Scale and Single Molecule Logic gate Technologies (AtMol) project (www.atmol.eu), Contract No. 270028, and the ACRITAS Marie Curie Initial Training Network (www.acritas.eu). We are also very grateful for the support of the University of Nottingham High Performance Computing Facility.

References

- 1. Wang, X.D et al., Jpn. J. Appl. Phys., 31, L983 (1992)
- Gross, L., Mohn, F., Moll, N., Schuler, B., Criado, A., Guitián, E., Pena, D., Gourdon, A., Meyer, G.: Science 337, 1326 (2012)
- 3. Scerri, E.: J. Chem. Ed. 77, 1492 (2000)
- Moon, C.R., Mattos, L.S., Foster, B.K., Zeltzer, G., Ko, W., Manoharan, H.C.: Science 319, 782 (2008)
- 5. Spence, J.C.H., O'Keefe, M., Zuo, J.M.: J. Chem. Ed. 78, 877 (2001)
- 6. Mulder, P.: Int. J. Phil. Chem. 17, 21 (2011)
- 7. Moriarty, P.: Surf. Sci. Rep. 65, 175 (2010)
- Pascual, J.I., Gomez-Herrero, J., Rogero, C., Baro, A.M., Sanchez-Portal, D., Artacho, E., Ordejon, P., Soler, J.M.: Chem. Phys. Lett. 321, 78 (2000)
- Hou, J.G., Yang, J., Wang, H., Li, Q., Zeng, C., Lin, H., Wang, B., Chen, D.M., Zhu, Q.: Phys. Rev. Lett. 85, 2654 (2000)
- 10. Hands, I.D., Dunn, J.L., Bates, C.A.: Phys. Rev. B 81, 205440 (2010)
- Sánchez-Portal, D., Artacho, E., Pascual, J.I., Gómez-Herrerom, J., Martin, R.M., Soler, J.M.: Surf. Sci. 482–485, 39 (2001)
- 12. Rurali, R, Cuadrado, JI and Cerdá, J.I., Phys. Rev. B 81, 074519 (2010).
- 13. Schull, G., Frederiksen, T., Brandbyge, M., Berndt, R.: Phys. Rev. Lett. 103, 206803 (2009)
- Schull, G., Frederiksen, T., Arnau, A., Sánchez-Portal, D., Berndt, R.: Nat. Nanotech. 6, 23 (2010)
- 15. Schull, G., Dappe, Y.J., González, C., Hulou, H., Berndt, R.: Nano Lett. 11, 3142 (2011)
- 16. Hembacher, S., Giessibl, F.J., Mannhart, J.: Proc. Natl. Acad. Sci. 100, 12539 (2009)
- 17. Feynman, R.: Phys. Rev. 56, 340 (1939)
- 18. Giessibl, F.J., Hembacher, S., Bielefeldt, H., Mannhart, J.: Science 289, 422 (2000)
- 19. Campbellová, A., Ondrácek, M., Pou, P., Pérez, R., Klapetek, P., Jelínek, P.: Nanotechnology 22, 295710 (2011)
- Chiutu, C., Sweetman, A.M., Lakin, A.J., Stannard, A., Jarvis, S., Kantorovich, L., Dunn, J.L., Moriarty, P.: Phys. Rev. Lett. 108, 268302 (2012)
- 21. Perez, R., Payne, M.C., Stich, I., Terakura, K.: Phys. Rev. Lett. 78, 678 (1997)
- 22. Ondrácek, M., Pou, P., Rozsíval, R., González, C.: Jelínek1, P, and Pérez, R. Phys. Rev. Lett. **106**, 176101 (2011)
- 23. Hobbs, C., Kantorovich, L.: Surf. Sci. 600, 551 (2006)
- 24. Masenelli, B., Tournus, F., Melinon, P., Blase, X., Perez, A., Pellarin, M., Broyer, M., Flank, A.M., Lagarde, P.: Surf. Sci. **532**, 875 (2003)
- 25. Pawlak, R., Kawai, S., Fremy, S., Glatzel, T., Meyer, E.: ACS Nano 5, 6349 (2011)
- 26. Gross, L., Mohn, F., Moll, N., Liljeroth, P., Meyer, G.: Science 325, 1110 (2009)